Interactions between electrons, mesoscopic Josephson effect and asymmetric current fluctuations

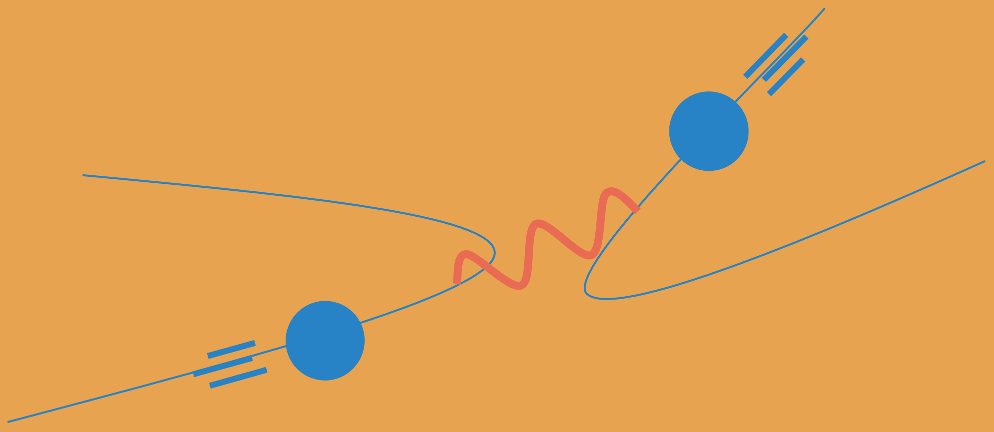

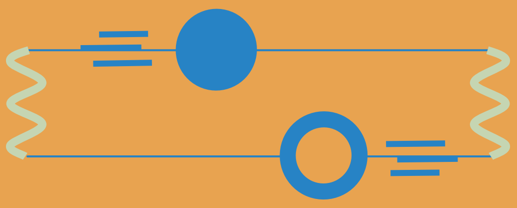

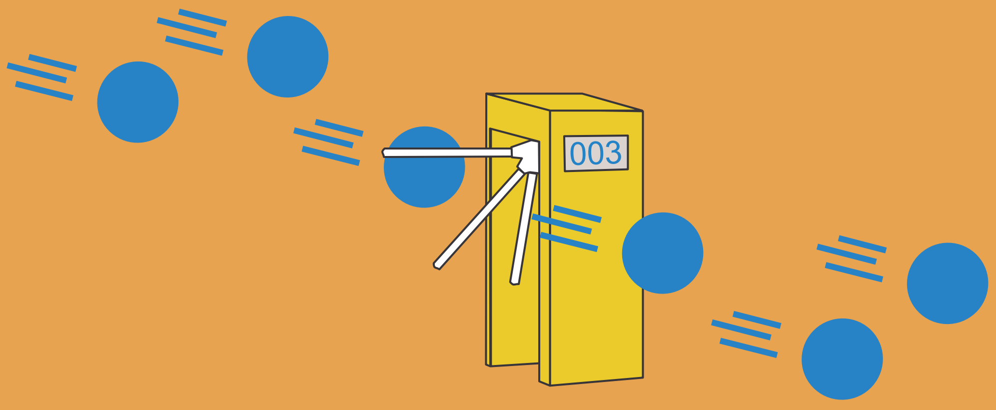

Benjamin Huard
Quantronics Group
SPEC – CEA Saclay

THESE DE DOCTORAT DE L'UNIVERSITE PARIS 6

Spécialité :

Physique des Solides

Présentée par

Benjamin HUARD

Pour obtenir le grade de DOCTEUR DE L'UNIVERSITE PARIS 6

Sujet de la thèse :

INTERACTIONS ENTRE ELECTRONS, EFFET JOSEPHSON MESOSCOPIQUE ET FLUCTUATIONS ASYMETRIQUES DU COURANT

préparée au sein du

SERVICE DE PHYSIQUE DE L'ETAT CONDENSE, CEA-SACLAY

soutenue le 22 septembre 2006
devant le jury composé de:

H. Bouchiat
R. Combescot
A. Georges
L. Glazman (rapporteur)
H. Pothier (directeur de thèse)
C. Strunk (rapporteur)

À ma belle

Remerciements

Je me souviens aujourd'hui de mon premier contact avec la Physique. Comme pour beaucoup de chercheurs, mon intérêt pour ce domaine s'est révélé au contact d'une personne exceptionnelle. Avec Yvette Casini, mon professeur au lycée, j'ai compris pour la première fois que l'édifice mathématique fournit un cadre conceptuel idéal pour appréhender les lois de la nature. Nos multiples discussions m'ont présenté une science vivante d'une grande richesse bien que bâtie sur un nombre restreint de principes élémentaires. Le fait qu'un cerveau humain puisse prédire la vitesse d'un skieur, la trajectoire d'une comète, la dilatation d'un gaz ou encore identifier les constituants élémentaires de la matière me stupéfie encore aujourd'hui. Yvette m'a rendu passionné de Physique à vie.

Cette thèse représente une étape importante dans ma relation à la Physique. Pour la première fois, l'approfondissement de ma compréhension des lois de la nature passait non seulement par la communication avec des érudits, mais aussi en participant personnellement à l'effort de recherche. Il n'est pas du tout évident de trouver la bonne façon de conduire des travaux de recherche. La vie d'un chercheur est une longue ascension vers la compréhension des lois de la nature. Au début de ma thèse, je partais pieds nus pour cette escalade. Ces trois années et demie passées au sein du groupe Quantronique m'ont non seulement fourni de bonnes chaussures et tout l'équipement nécessaire à la suite de mes recherches mais m'ont de plus permis de prendre le téléphérique.

Le groupe Quantronique est constitué de scientifiques de très haut niveau, modestes et à la bonne humeur contagieuse. Travailler avec eux fût un bonheur intense tant au niveau scientifique que personnel. Je remercie tout particulièrement mon guide de montagne Hugues Pothier qui est tout ce que je désire devenir. Merci pour m'avoir donné les clefs pour aborder un problème scientifique ouvert du point de vue théorique et expérimental, merci pour sa confiance précoce lorsqu'il m'envoyait en conférence et merci pour sa bonne humeur, ses blagues et sa façon d'égayer rapidement une journée mal commencée. Merci enfin pour sa générosité dans la correction de ce manuscrit. Je remercie Daniel Estève pour sa confiance et son affection, pour consacrer autant de temps à ses “récréations” pendant lesquelles il m'expliquait des notions très variées de Physique ou pendant lesquelles il venait tourner les boutons de l'expérience en cours. Sa double identité de super-héros lui permet de remplir à la fois des charges administratives importantes, d'être parfaitement au courant des expériences en cours, de nous donner les bonnes impulsions au bon moment, de donner une bonne leçon de courage et de jouer le rôle d'un père protecteur. Merci aussi à Norman Birge dont l'ouverture d'esprit, les qualités pédagogiques et l'envie de comprendre ont été particulièrement motivantes. J'ai beaucoup apprécié le recul de Cristian Urbina sur la science et sur les rapports humains en général, ses points de vue m'ont permis de relier les différentes branches de mes nouvelles connaissances en un arbre cohérent. Merci à Maria Luisa Della Rocca et Martin Chauvin dont les sourires ensoleillaient le labo du sous-sol, et avec qui j'ai pris un grand plaisir à collaborer. Merci à Anne Anthore pour avoir si bien préparé le terrain et qui a pris soin de partager ses connaissances au début de ma thèse. Merci à Denis Vion pour son enthousiasme sans égal lors de mes exposés et pour son dévouement pour rendre la vie plus simple au labo. Merci à Pief Orfila et Pascal Senat pour m'avoir simplifié la tâche si souvent. Merci aussi à Philippe Joyez, Grégoire Ithier, Peter Vom Stein, Eddy Collin, Hélène Le Sueur, Nicolas Boulant, Patrice Bertet, François Nguyen, Phil Meeson et Abdel Aassime pour avoir contribué à la formidable ambiance du groupe. Merci à tout le groupe pour les félicitations et encouragements permanents et la confiance qui me fut prêtée. Merci aussi à Sandrine Thunin, Nathalie Royer, Pierre Janvier et Eric Vincent qui permettent au service de bien fonctionner.

Enfin, je tiens à remercier les nombreuses personnes avec qui j'ai eu l'occasion de discuter pendant ma thèse et qui m'ont permis d'améliorer la qualité du manuscrit. Parmi elles : Gilles Montambaux, Joachim Ankerhold, Xavier Waintal, Hermann Grabert, Hélène Bouchiat, Frédéric Pierre, Bertrand Reulet, Marco Aprili, Christian Glattli, Boris Altshuler, Igor Aleiner, Yuri Nazarov, Juan Carlos Cuevas, Michel Devoret et Marcelo Goffman.

Je remercie chaleureusement Leonid Glazman, Christoph Strunk, Hélène Bouchiat, Antoine Georges, Roland Combescot et Hugues d'avoir fait partie du jury. Ce manuscrit serait d'ailleurs de bien moins bonne qualité sans les commentaires avisés d'Hugues Pothier, Daniel Estève, Cristian Urbina, Norman Birge, Gilles Montambaux et Hélène Bouchiat.

Je remercie mes parents pour leur amour et leur soutien sans borne. Merci à Gilberte, Antoinette, Jacqueline et Maurice pour leur affection et merci à mes beaux-parents de m'avoir si vite accepté dans la famille. Enfin, merci à celle qui se reconnaîtra.

Paris, Octobre 2006 *Benjamin Huard*

Contents

Part I Interactions between electrons in metals

Part II Mesoscopic Josephson effects

Part III Asymmetric current fluctuations

Part IV Experimental techniques

Chapter 1

Introduction

Contents

The understanding of electron transport in metals has improved continuously since Drude's model was established in 1900. The advent of quantum mechanics has clarified the microscopic model of charge transport, and amazing effects were predicted and observed experimentally. Characteristic length scales for a conductor were determined to draw a zoology of the behavior of electrons in metals, among them the phase coherence length L_φ, which sets the maximal distance on which electrons may be considered as quantum coherent particles [1, 2]. This length has been probed in experiments in which the conductance of a metallic conductor depends on electron interference effects.

In this work, we address three modern questions on electron transport in mesoscopic conductors and present conclusive experiments for each one of them.

What is the rate of energy exchange between electrons in a metal ?

The understanding of the mechanisms which limit the extension of phase coherence is a central issue in mesoscopic physics. The largest part of this work deals with the quantitative investigation of the processes limiting the phase coherence length L_φ. In particular, we investigate Coulomb electron-

electron interactions in weakly disordered metallic wires, and the complex interplay between electrons and magnetic impurities at a small concentration, in the Kondo regime.

In conductors of length shorter than L_φ, it was proposed by Landauer as early as 1957 that electrons could be described as waves propagating through the conductor [3, 4]. Due to the quantization of the electronic wave vector, the number M of modes participating to the transport is given by the product $M = k_F^2 S$ where k_F is the Fermi wave vector and S is the cross-section area. Transport through short conductors is therefore determined by an $M \times M$ matrix, whose eigenvalues squared τ_i are called the transmissions of the independent conducting channels. The celebrated Landauer-Büttiker relation expresses the conductance G in terms of the sum of all transmissions τ_i:

$$G = 2G_K \sum_{i=1}^{M} \tau_i \tag{1.1}$$

where $G_K = e^2/h$ is the quantum of conductance, and the factor 2 takes into account spin degeneracy. The full power of Landauer formalism has been widely exploited in systems with a few channels, mostly in two dimensional electron gases where it predicts the transport properties of the edge states in the Quantum Hall effect, or of electrons through quantum point contacts as proven by beautiful experiments on conductance and noise [5, 6, 7, 8]. In metals, this formalism was used to predict current noise properties in wires and atomic contacts[9, 10, 11], and more recently to predict Josephson effects in weak links between superconductors systems. While the current noise has been measured in wires and atomic contacts [12, 13, 14], the predictions on Josephson effects based on Landauer formalism have never been thoroughly investigated.

What is the current-phase relation for a weak link between two superconductors ?

In 1962, Josephson predicted that if the phase difference δ between the two superconductors connected through a weak link is fixed, a dissipationless supercurrent flows [15, 16]. In the 1990's, the amplitude of this supercurrent was expressed in terms of the set of transmissions, or Personal Identifying Number (PIN), of the short weak link [17, 18, 19, 20]. Despite its central importance for mesoscopic superconductivity, this relation was never thoroughly investigated. We present in the second part of this paper experiments started in collaboration with Martin Chauvin [21] which test this prediction quantitatively.

Is the non-Gaussian part of the current noise in mesoscopic conductors detectable with a Josephson junction ?

In 1993, Levitov et al. showed that the generating function of the moments of the current fluctuations through a mesoscopic conductor can be calculated [22]. One of the particular outcome of this calculation is the non-

Gaussian part of the current noise. On the experimental side, only very few measurements of this non-Gaussian characteristics have been performed, and most of them focus on the third moment of the current noise only [23, 24, 25, 26]. In the third part of this work, we investigate the possibility to measure properties of the non-Gaussian part of the current noise using a Josephson junction acting as a threshold detector, as proposed by Tobiska and Nazarov [27].

1.1 Interactions between electrons in metals

1.1.1 Theoretical and experimental status before this work

Weakly disordered metals with weak interactions

The simplest picture of electrons in metals is the independent electron gas in a periodic lattice, in which electrons are described by Bloch states. However, interactions make the independent electron picture inadequate. Indeed, as all electrons interact strongly, the dynamics of a single electron is a many body problem. Landau proposed the following elegant solution to that question in the middle of the 20^{th} century [28]. By branching adiabatically the interactions between electrons in a Gedanken experiment, each Bloch electronic eigenstate evolves continuously into a new eigenstate of the interacting many body system. Thus, electrons are mapped onto new particles which are nearly independent and form a Fermi liquid. Each of these quasi-particles can be seen as an electron dressed by a screening cloud of other electrons, which screens the Coulomb interaction[1] over a very small distance, of the order of the Fermi wavelength λ_F. In the following of this article, "electron" always means quasi-particle.

Actually, in real conductors, electrons do not solely interact one with another but also feel the disorder introduced by finite size and defects in the periodic lattice like grain boundaries or vacancies. The Fermi liquid theory can be extended to the case of disordered metals. In a three dimensional metal, disorder is characterized by the average distance traveled by an electron between two elastic scattering events. This length, called the mean free path l_e, is related to the diffusion constant D of the electrons by the Einstein relation $D = v_F l_e/3$ where v_F is the velocity of the electrons at the Fermi level.

Of course, this picture has some limits. If l_e becomes as small as λ_F, the conductor enters in the Anderson localization regime and becomes an insulator

---

[1] The Coulomb interaction between two electrons at a distance R in vacuum is $U(R) = \frac{e^2}{4\pi\epsilon_0 R}$. In a metal, the approximation of Thomas-Fermi [29] gives $U(R) = \frac{e^2}{4\pi\epsilon_0 R}\mathrm{e}^{-\kappa_s R}$ where the inverse screening length κ_s is given by $\kappa_s^2 = e^2\nu_F/\epsilon_0$ with ν_F the density of states per volume for both spin directions. In copper, for example, $\kappa_s \approx 1.5k_F$.

[30]. In this work, we consider the case of good conductors ($k_F l_e \gg 1$), which is valid for most thin films and bulk metals. Besides, the Fermi liquid picture is valid for a particular range of interactions. For interactions much stronger than the kinetic energy, quasi-particles do not form a Fermi liquid but more complex states like the Wigner crystal [31]. However, such strong interactions are not observed in three dimensional metals, and the experiments presented in this paper can be understood within the Fermi liquid theory.

Phase coherence time and interactions between electrons

The intensity of the interactions between electrons and their environment is characterized by the average distance L_φ traveled by an electron at the Fermi level before changing its quantum state, all other electrons being at equilibrium. In a given state, the quantum phase of the electron increases linearly in time. A change in quantum state can be seen as an abrupt change in the phase. For this reason, L_φ is called the phase coherence length and $\tau_\varphi = L_\varphi^2/D$ the phase coherence time. In 1982, Altshuler and Aronov, using a diagrammatic theory, predicted the influence on τ_φ of electron-electron and electron-phonon interactions [1, 2]. According to this theory, in disordered metallic wires, electron-phonon coupling prevails at temperature $T \gtrsim 1$ K, whereas at $T \lesssim 1$ K, electron-electron interaction is the main dephasing process. Besides, τ_φ diverges at $T = 0$ as does the electron lifetime in the Fermi liquid theory. Each process contributes to a different temperature dependence of τ_φ, and this behavior has been confirmed experimentally for the first time in 1986 by Prober *et al.* [32] through Weak Localization experiments (WL).

However, in 1997, Mohanty *et al.* reported WL experiments performed at lower temperatures (down to tens of mK), in which an apparent saturation of τ_φ was observed [33] in contradiction with the theory of Altshuler and Aronov. This saturation caused a strong controversy as the question was raised wether the existing theory was properly describing electron-electron interactions at low energies.

In parallel, a new type of experiments based on tunneling spectroscopy (called in the following *Relax experiments* because they probe the energy relaxation of electrons) was developed and used in the Quantronics group for the measurement of the energy distribution function of electrons in voltage-biased diffusive wires [34]. The higher the voltage bias, the more energetic the electrons. The redistribution of the energy between electrons, probed at different bias voltages, contains then information on the inter-electron energy exchange rates [35, 36]. Only in the samples obtained from sources of the purest metals did this experiment confirm the predicted dependence of the intensity of Coulomb interaction on the exchanged energy. In all other cases, the intensity depends on the exchanged energy in a different way.

Magnetic impurities modify the interactions between electrons

A few years later, Kaminski and Glazman proposed [37] an explanation for this behavior based on the presence of a tiny concentration of magnetic impurities. At first order, the interactions between an electron and an impurity spin cannot exchange any energy (at zero magnetic field). Yet, the second order process by which two electrons interact with the same impurity spin can redistribute energy between electrons and lead qualitatively to the observed behavior. Yet, the rate of such a process would be much too small without the Kondo effect. Kondo discovered that the coupling between a local magnetic moment and the Fermi liquid is resonant at an energy $k_B T_K$, where the Kondo temperature T_K depends on material properties only [38]. Kaminski and Glazman suggested that the presence of a tiny concentration of magnetic impurities with the appropriate Kondo temperature could explain the Relax experiments [37]. Later on, Göppert *et al.* have derived a quantitative expression for the intensity of electron-electron interactions mediated by magnetic impurities in a finite magnetic field [39]. In 2003, experiments in which the magnetic field dependence of the anomalous interaction was investigated confirmed that magnetic impurities were playing a major role [40, 41].

WL experiments [42, 43] showed also that the presence of magnetic impurities, at a very small concentration, could result in an apparent saturation of τ_φ similar to that observed by Mohanty *et al.*. Such a situation occurs when the Kondo temperature of the magnetic impurities in the host metal lies in the investigated sub-Kelvin temperature range.

At the beginning of this work, two issues on electron-electron interactions had yet to be clarified. The first one was a discrepancy between the predicted and the measured values of the intensity of Coulomb interaction in diffusive wires. The second one was the quantitative understanding of the influence of magnetic impurities on the energy exchange between electrons.

1.1.2 Intensity of Coulomb interaction

In the Altshuler-Aronov theory, the rate of energy exchange between electrons due to Coulomb interaction in diffusive metallic wires is entirely described by a parameter κ that depends on material and geometric properties only

$$\kappa = \left(\pi\sqrt{2D}\hbar^{3/2}\nu_F S_e\right)^{-1} \tag{1.2}$$

where ν_F is the density of states for both spin directions and S_e is the cross-section of the wire. Relax experiments give an indirect measurement of κ. Besides, the temperature dependence of τ_φ can also be predicted from the knowledge of κ only. Therefore, both Relax and WL experiments give access to κ.

It is noticeable that the parameters κ deduced from WL experiments are much closer to the theoretical values than those deduced from Relax experiments (see Fig. 1.1). Possible explanations for this discrepancy are investigated

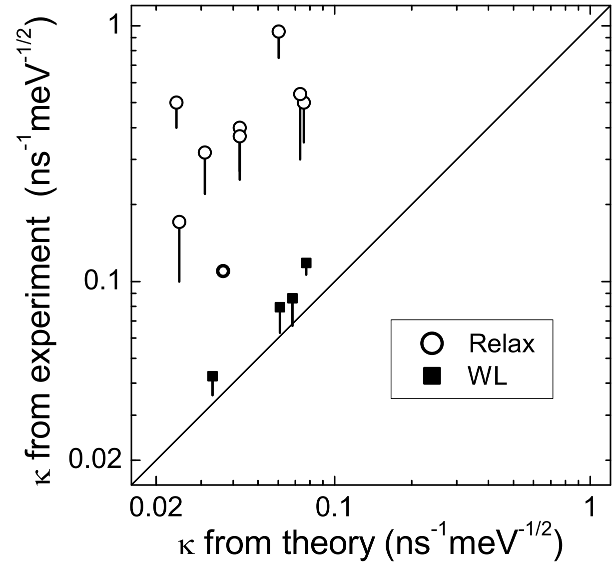

Fig. 1.1. Comparison of the measured value of κ with the theoretical prediction, for several WL experiments (■) and Relax experiments (○) on different wires (all but one were already discussed in [36, 41]). If one assumes that a small amount of magnetic impurities can be present in the metal, this extra fit parameter can allow to lower the fit values of κ down to the bottom of the lines below the symbols.

in this work (section 3.4.3). In particular, we performed a new experiment to explore the hypothesis that the theory of Altshuler and Aronov may not apply to an out-of-thermodynamic-equilibrium Fermi liquid. This experiment allows measurements of energy exchange between electrons in a situation close to thermodynamic equilibrium. We show that the measured interaction parameter κ is the same as in the standard setup with a larger departure from equilibrium. At this point, no satisfactory answer exists about the disagreement on the actual intensity of Coulomb interactions between electrons.

1.1.3 Effect of magnetic impurities on energy exchange between electrons

As stated above, work by Anthore *et al.* showed in 2003 that the unexpected energy exchange rates observed in dirtier metals could be explained by assuming the presence of magnetic impurities [40, 41]. However, a quantitative measurement of the rates of energy exchange between electrons induced by magnetic impurities had not been performed.

In order to perform such a test, two pure Ag wires were fabricated altogether on the same wafer. Then, only one of them was implanted with Mn atoms (which are magnetic) at a concentration of 0.65 ppm (parts per million).

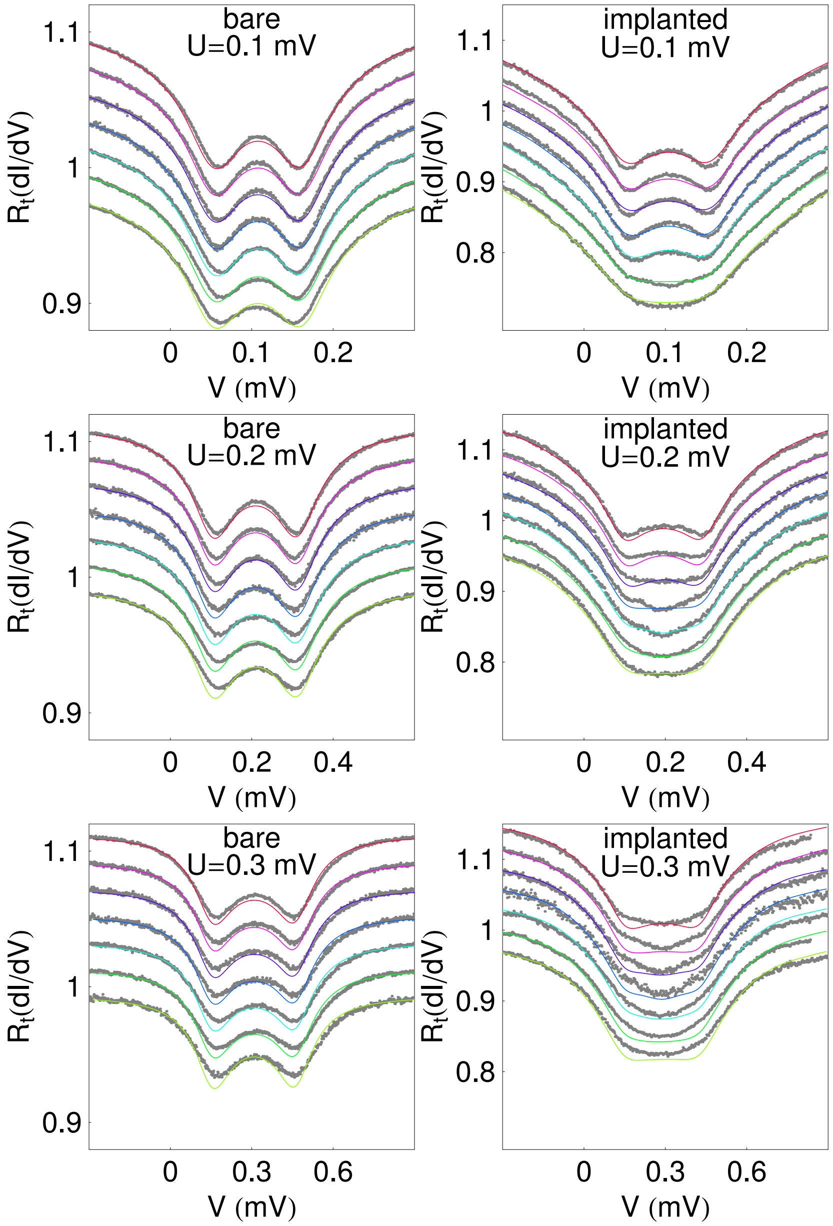

Fig. 1.2. Differential conductance $\mathrm{d}I/\mathrm{d}V(V)$ of the tunnel junction for the bare (left) and implanted (right) Ag wires, for $U = 0.1$ mV, 0.2 mV and 0.3 mV (top to bottom panels), and for $B = 0.3$ to 2.1 T by steps of 0.3 T (bottom to top in each panel). The curves were shifted vertically for clarity. Symbols: experiment. Solid lines: calculations using Mn concentrations $c_b = 0.02$ ppm for the bare wire, $c_i = 0.65$ ppm for the implanted one and $\kappa_{ee} = 0.05$ ns^{-1}meV$^{-1/2}$ for both.

Finally a tunnel junction in series with a long resistive Al wire was fabricated on both wires to perform the spectroscopy of the distribution function in the Ag wire.

First, the tunnel junction was not used and WL measurements were performed. The temperature dependence of $\tau_\varphi(T)$ exhibited a different behavior in both wires. Both behaviors were in good agreement with a theory using the amount of added Mn atoms in one of the wires. Then, in order to access the energy exchange rates, we performed Relax experiments at finite magnetic field. The tunneling conductance measurements are plotted on Fig. 1.2 for various magnetic fields and bias voltages U across each wire. In order to compare the measurements with the predictions using the inelastic processes involving magnetic impurities, three steps were followed.

- We start from the distribution function f in the wire computed using Coulomb interaction between electrons only.
- From the theory by Göppert *et al.* [39] we calculated the energy exchange rates between electrons in presence of magnetic impurities at a finite magnetic field using f. For each sample, we used the magnetic impurity concentration deduced from the WL experiments. We then used the Boltzmann equation [34] to recalculate the distribution function f in the wire from the theoretical rates of the different energy exchange mechanisms. We iterated this self-consistent calculation until f converges.
- The tunnel conductance was then calculated using the theory of dynamical Coulomb blockade as in Ref. [40].

Using the intensity of Coulomb interaction κ as the only fit parameter, we obtain the curves shown on Fig. 1.2. These experiments show that the rate of energy exchange between electrons in presence of magnetic impurities is quantitatively understood. However, as in all Relax experiments shown in Fig. 1.1, the theory underestimates the value of κ, in this case by a factor 3.

1.2 Josephson effect through a short coherent conductor

Superconductivity arises when an attractive interaction between electrons leads to the formation of bosons (the Cooper pairs) falling all in the same ground state. This ground state is defined by a complex parameter $\Delta e^{i\varphi}$ where φ is the phase of the superconductor. The Josephson effect develops when two superconductors are coupled through a weak link: in 1962, Josephson predicted that if the phase difference δ between the two superconductors is fixed, a dissipationless supercurrent flows [15, 16]. Besides, he predicted that when a constant bias voltage V is applied between two superconductors, an oscillating supercurrent develops at a frequency $\nu = V/\phi_0$, where $\phi_0 = \frac{h}{2e}$ is the flux quantum. This effect was first observed in a tunnel junction by Shapiro in 1963 [44].

In the 1990's, a new theoretical approach was built to tackle the Josephson effect in two superconductors coupled through coherent conductors shorter than the extension of the Cooper pairs $\xi = \sqrt{\hbar D/\Delta}$ [17, 18, 19, 20]. This approach is based both on the Landauer formalism and on the fundamental mechanism of Andreev reflection, a process by which electrons get reflected as holes (and *vice versa*) in superconductors. Within this picture, the supercurrent is carried through two states per channel, localized in the conductor. These so-called Andreev bound states have an energy lying inside the superconducting gap, and given by

$$E_{\pm}(\delta) = \pm\Delta\sqrt{1-\tau\sin^2(\delta/2)} \qquad (1.3)$$

where τ is the transmission of the channel. At zero temperature, the system is in the ground state $|\tau_-\rangle$ and the supercurrent flowing through the channel is proportional to the derivative of $E_-(\delta)$ at the phase difference δ between the superconductors:

$$I_{T=0}(\delta) = \frac{2\pi}{\phi_0}\frac{\partial E_-}{\partial\delta} = \frac{e\Delta}{2\hbar}\frac{\tau\sin\delta}{\sqrt{1-\tau\sin^2(\delta/2)}}. \qquad (1.4)$$

Starting from this expression for the supercurrent in one channel, the supercurrent can be predicted analytically in any short coherent conductor whose PIN is known, by summing the currents in each channel independently.

In order to test this central prediction of the modern theory of the Josephson effect, we have performed experiments using atomic contacts. Atomic contacts are perfect devices for that purpose, since they carry a few channels whose transmissions can be altered and measured *in situ* [45, 46]. More importantly, their highly non linear I-V characteristics[2] allows to measure their PIN [47].

Before the beginning of this work, several experiments that take advantage of these model systems had been performed in the Quantronics group. In particular, the existence of multiple charge transfer processes was evidenced through shot noise measurements [14, 48]. There have been also experiments on the supercurrent peaks which can be explained by the Andreev bound states dynamics [49, 48]. Furthermore, the fractional Shapiro steps predicted by the theory for highly transmitted channels could be observed [50, 21].

The experiment discussed in this work, and initiated by M. Chauvin, was designed to directly measure the current-phase relation $I(\delta)$ of an atomic contact, for which the PIN $\{\tau_i\}$ is known [21]. This requires also to measure the I-V characteristics. However, measuring both $I(\delta)$ and $I(V)$ on the same contact without changing it at the atomic level is challenging. Phase biasing an atomic contact requires to enclose it in a superconducting loop threaded by a magnetic field, while such a loop forbids voltage biasing because the contact is then shunted. In the experiment, an electrically controllable switch was implemented with a big tunnel junction in the loop (Fig. 1.3). This Josephson

---

[2] In case of superconducting electrodes only, due to multiple Andreev reflections.

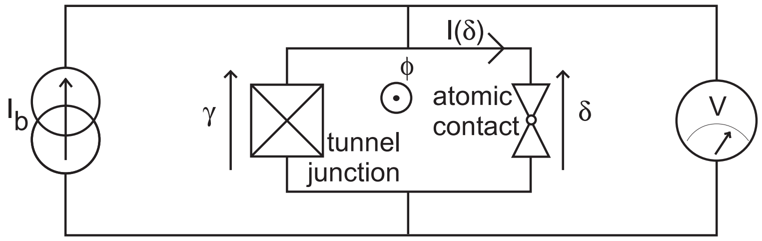

Fig. 1.3. Scheme of the atomic contact experiment. A superconducting loop encloses the atomic contact and a Josephson junction. The junction is biased by a current source I_b and the voltage V across is monitored.

junction can sustain a dissipationless current at zero voltage as long as the current is smaller than a so-called critical current I_0 (at zero temperature), allowing hence for a phase bias of the atomic contact. Ideally, as soon as the current increases beyond I_0, the junction "switches" and a finite voltage develops. By measuring the switching current I_b^{sw} as a function of the magnetic field in the loop, one directly measures the $I(\delta)$ relation, only shifted by a constant current. Moreover, at finite voltages V below twice the gap Δ of the superconductor, the tunnel junction acts ideally as an open circuit, thus the current is just that of the atomic contact alone.

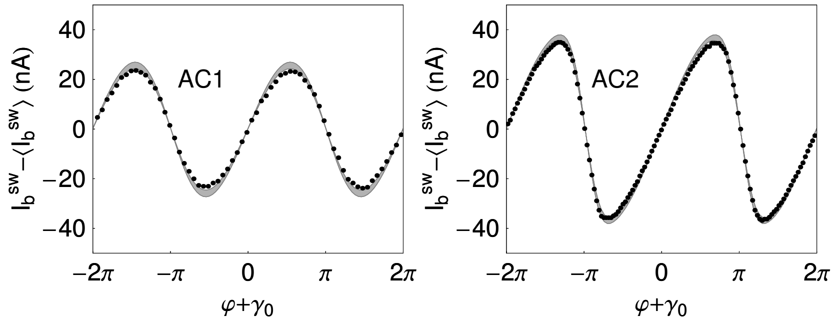

Fig. 1.4. Dots: Measured switching current I_b^{sw} depending on the reduced flux $\varphi = \phi/\phi_0$ in the loop for two atomic contacts denoted by AC1 and AC2. Data have been shifted from their average value $\langle I_b^{\text{sw}} \rangle$ which corresponds to the switching current of the Josephson junction alone. Grayed bands: Theoretical prediction for the same current at finite temperature using current-phase relation Eq. (1.4) with the PIN $\{\tau_i\}$ deduced from the I-V characteristics (see Fig. 5.23). The width of the band comes from the uncertainty in the measurement of the PIN. The PIN of AC1 is $\{\tau_i\} = \{0.62 \pm 0.01; 0.12 \pm 0.015; 0.115 \pm 0.01; 0.11 \pm 0.01; 0.11 \pm 0.01\}$ and for AC2, $\{\tau_i\} = \{0.957 \pm 0.01; 0.185 \pm 0.05\}$.

In the experiment, various contacts were measured with as few as one single channel with transmission as high as 0.992. A good agreement with the theoretical prediction for $I(\delta)$ was obtained (see Fig. 1.4). Yet, a finite discrepancy between theory and experiment remains. We discuss the possibility to explain this discrepancy by an excitation of the Andreev bound states. In a complementary experiment, we performed a measurement of the Josephson inductance as a function of δ, which could be compared quantitatively to the second derivative of the ground state spectrum Eq. (1.3). This whole set of data strongly supports the general theory of the Josephson effect [51].

1.3 Asymmetric current fluctuations

In another set of experiments, we focused on the detection of the non-Gaussian character of the electrical noise in mesoscopic conductors. The most common type of noise in electrical devices, called Johnson-Nyquist noise, is due to thermal fluctuations. Its characteristic properties are its frequency spectrum[3] and a Gaussian distribution of the current values. When a current flows in a conductor, the granularity of electrical current provides a source for another type of noise, called shot noise[4], with an intensity and a behavior in frequency that depend on the specific conductor. For decades, experiments and theory concentrated on the second moment of current fluctuations only (see [52] for a review on the flurry of theoretical and experimental works). In 1993, a seminal theory paper by Levitov and Lesovik [22] demonstrated the possibility to calculate all moments of current fluctuations analytically. In mesoscopic conductors, cumulants of higher order than 2 are finite and current fluctuations are not Gaussian. This theory also proved efficient in the calculation of the second moment of the current fluctuations in some systems where a standard perturbative approach fails (e.g. [53]). In 2001, Nazarov and Belzig, using Keldysh techniques, derived a general formula for the full counting statistics of any coherent conductor [54] based on Landauer formalism. In the mean time, Nagaev *et al.* developed a semiclassical method to calculate the frequency dependence of all moments of current noise even in the case where coherence is lost due to electron-electron interactions [55, 56].

Although the body of theoretical works on Full Counting Statistics is large, experiments in which signatures of non-Gaussian current fluctuations are evidenced are still extremely rare, and they have only focused on the existence of a third cumulant [23, 24], except in circuits where current is due to sequential

---

[3] The spectrum depends on the frequency ω as

$$S(\omega) = \frac{4}{R}\hbar\omega(1 - \mathrm{e}^{-\hbar\omega/k_B T})^{-1}.$$

[4] Proportional to the electrical current.

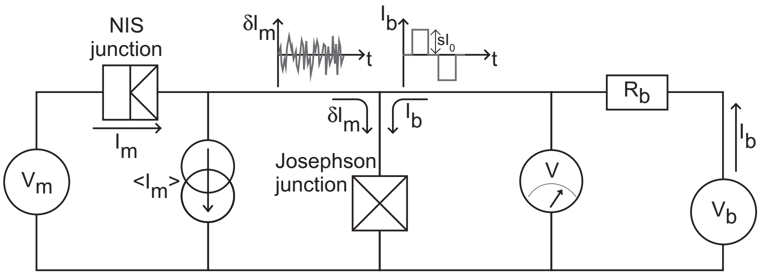

Fig. 1.5. Scheme of the counting experiment. The current fluctuations δI_m of a mesoscopic conductor (an NIS tunnel junction in our experiment) pass through a Josephson junction. A bias line sends current pulses $I_b(t)$ on top of the fluctuations δI_m in the junction. The switching probability of the junction during one pulse can then be related to the properties of the current fluctuations.

tunneling [25, 26]. Theoretically, a few set-ups have been proposed and analyzed. One of them considered the use of a Josephson junction as a current threshold detector. Using threshold detectors could let one have access to statistical quantities for the current fluctuations which have never been observed, like the statistics of the extreme values of the fluctuations, or even the full distribution of the current fluctuations [27, 57]. Though in a regime different to that discussed in [27], we performed a preliminary experiment with a Josephson junction as a threshold detector (see Fig. 1.5). Our experiment was designed to test the feasibility of such noise measurements with a Josephson junction. Therefore, a tunnel junction was chosen as the noisy mesoscopic device. The noise through a tunnel junction is well known, and can be used to calibrate this detector.

The Josephson junction acts, in a sense, as a fuse similarly to what it does in the experiment on atomic contacts. Indeed, if the current in the junction exceeds a given threshold of the order of the critical current I_0, a finite voltage develops across the junction and remains till the junction is reset by lowering again the current down to zero. During a pulse in the bias current I_b, large enough current fluctuations δI_m have the current in the junction exceed that threshold, and a finite voltage V develops. Doing the statistics of the switching events depending on the height of the pulses sI_0, one measures the statistics of the amplitude of the fluctuations δI_m.

It is well known that the presence of a resistive environment at sufficiently high temperature changes the switching rate because of Johnson-Nyquist noise (see Ref. [58] for a review). In presence of an arbitrary noise, one can define the escape temperature T_{esc} as the temperature that an ohmic environment with the same resistance R_{env} should have in an ideal experiment to reproduce the actual switching rate at best. In our experiment, the first order effect of the current fluctuations is then to increase the escape temperature T_{esc} when the voltage V increases. This increase can be understood by considering only the shot noise through the tunnel junction. Neglecting the Johnson-Nyquist noise due to thermal fluctuations of the current, one has by definition of T_{esc}:

$$\frac{4k_B T_{\text{esc}}}{R_{\text{env}}} \approx 2e\langle I_m \rangle. \tag{1.5}$$

We observe clearly such a behavior in our experiment, thus proving that Josephson junctions can probe current noise, as was also found by Pekola *et al.* in another regime [59].

Besides, as the current fluctuations are produced by a tunnel junction, the statistics of δI_m is not Gaussian[5] and has a finite third order moment $\langle \delta I_m^3 \rangle$. Therefore, the current distribution is asymmetric. In case of a tunnel junction, large positive (in the same direction as $\langle I_m \rangle$) current fluctuations occur more often than large negative ones[6]. This asymmetry in the current fluctuations should yield in an asymmetry in the switching probabilities of the Josephson junction for opposite values of I_b. More precisely, the switching rates Γ_+ during positive pulses of I_b should be higher than the switching rates Γ_- during negative pulses of the same amplitude.

Such an asymmetry in the switching rates is observed in the experiment. In order to be quantitative, we measured the relative difference R_Γ between the switching rates Γ_+ and Γ_- for various values of the average current $\langle I_m \rangle$, of the pulse height and of the temperature. Our experiment shows that, as the current $\langle I_m \rangle$ departs from zero, the asymmetry R_Γ in the rates increases monotonously starting from zero.

In this work, we present these results in great details. We also discuss preliminary comparison to a theory developed by Joachim Ankerhold [60] and to numerical simulations performed by one of our colleagues, Xavier Waintal.

In the near future, other mesoscopic devices could be probed with this method, in order to get more physical insight on the correlations between charge carriers.

---

[5] It is exactly a Poisson distribution.

[6] On the opposite, small positive fluctuations occur more rarely than small negative ones.

Part I

Interactions between electrons in metals

Chapter 2

Phase coherence and weak localization

Contents

In a typical metal, electrons scatter elastically on defects, performing a diffusive motion. An external voltage gradient induces an average drift of the electrons on top of this diffusive motion. Within a classical scheme, where electrons are just particles whose speed and position are well defined, the average conductance of a metallic conductor is given by the Drude value. Yet, quantum physics attributes to the electrons also a wave-like behavior, so that a single electron, which has a specially extended wave function, can interfere with itself after multiple scattering events. Such interferences modify slightly the Drude result for the average conductance. In the simplest case, we will see that interferences decrease the conductance from its classical value, so that this effect is called the *weak localization effect.* As quantum interferences are essential to this phenomenon, weak localization depends strongly on the time τ_φ after which electrons lose some information needed to interfere: their phase coherence. The loss of coherence, as any information exchange in quantum physics, results from a coupling to dynamic degrees of freedom. In particular, τ_φ is limited by the interactions between electrons and phonons, magnetic impurities, or more simply among electrons. Each of these interaction processes limits τ_φ in a manner which depends differently on temperature T, so that it is possible to identify the interaction rate of each process from the dependence of τ_φ on temperature. Knowing what determines the rates of those interaction is the key to controlling the extent of coherence in nanostructures.

In a first part, we introduce the tools needed to describe the effect of weak localization. Along the way, fundamental quantities are defined to characterize quantum coherence in a metal. For a more formal and comprehensive review, the reader should refer to Ref. [61]. In a second part, we present a set of experiments which illustrate the role of each dynamic degree of freedom on phase coherence. In the experiment, samples were designed to investigate both their role on phase coherence and energy exchange between electrons (*Relax* experiments, see § 3).

2.1 Weak Localization

2.1.1 Diffuson and Cooperon

The general formalism used to deal with phase-coherence in disordered metals was introduced in the 1980's by Al'tshuler, Aronov and Khmelnitsky [2, 1]. In this formalism, electrons are Fermi quasi-particles and scatter elastically on defects, grain boundaries or metal edges. It applies to metals verifying two conditions: weak disorder (Fermi wavelength λ_F much smaller than the mean free path l_e [30]) and not too strong interactions (interactions between quasi-particles much weaker than the kinetic energy). Weak localization comes from a quantum correction to the probability[1] $Z(t)$ for an electron to return to its

---

[1] The normalization of this probability is not obvious. Using the probability $P(\boldsymbol{r},\boldsymbol{r'},t)$ to go from $\boldsymbol{r}$ to $\boldsymbol{r'}$ in a time t, whose normalization is given by $\int P(\boldsymbol{r},\boldsymbol{r'},t)\mathrm{d}\boldsymbol{r'} = 1$, $Z(t)$ is defined by $\Omega Z(t) = \int P(\boldsymbol{r},\boldsymbol{r},t)\mathrm{d}\boldsymbol{r}$ where Ω is the volume of the system.

original position at time t. This return probability is the sum of the contributions of all possible loops followed by electrons in a time t. If the electron were a classical particle, $Z(t)$ would just be the sum of the probabilities for each loop $\mathcal{C}$ to be traveled in a time t. Because electrons are quantum objects, this is not true, and instead the probability amplitudes[2] $\mathcal{A}_\mathcal{C}$ of each path $\mathcal{C}$ must be summed before taking the square. Finally,

$$Z(t) = \left|\textstyle\sum_\mathcal{C} \mathcal{A}_\mathcal{C}\right|^2 = \textstyle\sum_{\mathcal{C}',\mathcal{C}} \mathcal{A}_\mathcal{C}\mathcal{A}^*_{\mathcal{C}'} = \underbrace{\sum_{\mathcal{C}} \mathcal{A}_\mathcal{C}\mathcal{A}^*_\mathcal{C}}_{Z_d(t)} + \underbrace{\sum_{\mathcal{C}'\neq\mathcal{C}} \mathcal{A}_\mathcal{C}\mathcal{A}^*_{\mathcal{C}'}}_{Z_c(t)} \tag{2.1}$$

where the sum extends over all possible paths starting and ending at the same point after time t. Obviously, $Z(t)$ is the sum of two terms of very different nature. The first one $Z_d(t)$, called the *Diffuson*, corresponds to the classical contribution to $Z(t)$, which is just the sum of the probabilities $\mathcal{A}_\mathcal{C}\mathcal{A}^*_\mathcal{C}$ of each path $\mathcal{C}$. The second one $Z_c(t)$, called the *Cooperon*, corresponds to interferences between different paths. Each particular interference term $\mathcal{A}_\mathcal{C}\mathcal{A}^*_{\mathcal{C}'}$ has a phase given by the product of the Fermi wavevector k_F by the length difference between both paths $\mathcal{C}$ and $\mathcal{C}'$. There are various strategies to take into account disorder when calculating $Z(t)$. One of these considers that scattering events are possible on a finite set of points $\{\boldsymbol{r_1}, \ldots, \boldsymbol{r_N}\}$ with no particular symmetry, each path $\mathcal{C}$ being identified by the ordered list of its q scattering events, its starting, and its ending points $\mathcal{C} = \big(\boldsymbol{r}, \boldsymbol{r_{p_1}}, \ldots, \boldsymbol{r_{p_q}}, \boldsymbol{r'}\big)$. Since $Z(t)$ is the probability for going back to the same position after a time t averaged on all starting points $\mathbf{r} = \mathbf{r}'$, most of the terms in $Z_c(t)$ die out by *disorder averaging*, that is by taking the average value on all $\mathbf{r}$. Indeed, depending on $\mathbf{r}$, the length $\ell_\mathcal{C}$ of a path $\mathcal{C} = \big(\boldsymbol{r}, \boldsymbol{r_{p_1}}, \ldots, \boldsymbol{r_{p_q}}, \boldsymbol{r}\big)$ varies on a much bigger scale than the Fermi wave length λ_F. And since, for any paths $\mathcal{C}$ and $\mathcal{C}'$, $\mathcal{A}_\mathcal{C}\mathcal{A}^*_{\mathcal{C}'}$ is proportional to a phase term $\mathrm{e}^{ik_F(\ell_\mathcal{C}-\ell_{\mathcal{C}'})}$, the only terms in $Z(t)$ which do not average out to zero are those for which $\ell_\mathcal{C} = \ell_{\mathcal{C}'}$ whatever the value of $\mathbf{r}$. Given a path $\mathcal{C}$, only two paths $\mathcal{C}'$ satisfy this condition: the path $\mathcal{C}$ itself, which enters in the Diffuson, and its time-reversal symmetric, meaning the path $\mathcal{C}$ gone along in reverse order, which enters in the Cooperon. In the following, we will denote a generic closed path $\mathcal{C}$ by $\circlearrowleft$ and its time-reversed symmetric by $\circlearrowright$ (see Fig. 2.1). In absence of magnetic field, spin-orbit scattering and interactions between electrons, the Cooperon is equal to the Diffuson:

$$Z_c(t) = \sum_{\circlearrowleft} \mathcal{A}_{\circlearrowleft}\mathcal{A}^*_{\circlearrowright} = \sum_{\circlearrowleft} \mathcal{A}_{\circlearrowleft}\mathcal{A}^*_{\circlearrowleft} = Z_d(t) \tag{2.2}$$

In a diffusive metal of dimensionality[3] d and diffusion constant D, assuming that the volume Ω of the system is big enough so that side effects are negligible, one gets

---

[2] Formal definitions for these quantities exist through Green functions,see [61].

[3] The effective dimensionality depends on the energies ε (times t) considered. For a diffusive metal with diffusive constant D, dimensions of length L are called

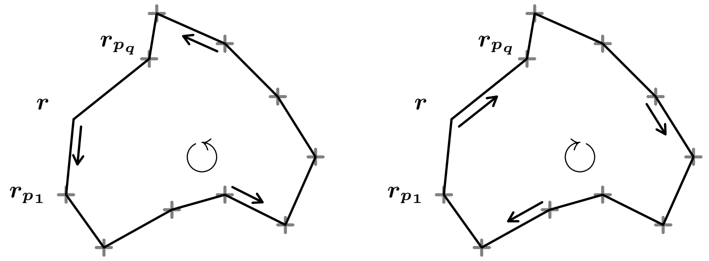

Fig. 2.1. Interfering paths followed by an electron. Each elastic scattering event is represented as a cross and results in a change of momentum. Formally, ↺$=(\boldsymbol{r}, \boldsymbol{r}_{\boldsymbol{p}_1}, \ldots, \boldsymbol{r}_{\boldsymbol{p}_q}, \boldsymbol{r})$ and ↻$=(\boldsymbol{r}, \boldsymbol{r}_{\boldsymbol{p}_q}, \ldots, \boldsymbol{r}_{\boldsymbol{p}_1}, \boldsymbol{r})$.

$$Z_d(t) = \frac{1}{(4\pi D t)^{d/2}}. \tag{2.3}$$

In the $d = 1$ case,

$$L Z_d(t) = \left(\frac{\tau_D}{4\pi t}\right)^{1/2} \tag{2.4}$$

where $\tau_D = L^2/D$ is the time needed to diffuse across the whole conductor. In our experiments on 40 μm-long silver wires, $\tau_D \approx 80$ ns.

2.1.2 Basic weak localization effect

The conductance is proportional to the probability to go from one end of a conductor to the other [2, 61]. This probability reads $\mathcal{P} = \left|\sum_{\mathcal{C}} \mathcal{A}_{\mathcal{C}}\right|^2$ where $\mathcal{C}$ can be any path across the conductor. Similarly to the calculation of $Z(t)$, terms $\mathcal{A}_{\mathcal{C}} \mathcal{A}^*_{\mathcal{C}'}$ vanish by disorder averaging as soon as paths $\mathcal{C}$ and $\mathcal{C}'$ differ by more than λ_F. Since, for most paths $\mathcal{C}$, no other path $\mathcal{C}'$ exists with the same length whatever the position of the starting point is, terms $\mathcal{A}_{\mathcal{C}} \sum_{\mathcal{C}'} \mathcal{A}^*_{\mathcal{C}'}$ reduce to the classical probabilities $\mathcal{A}_{\mathcal{C}} \mathcal{A}^*_{\mathcal{C}}$. This is why, the total probability is approximately the sum of classical terms

$$\mathcal{P} \approx \sum_{\mathcal{C}} \mathcal{A}_{\mathcal{C}} \mathcal{A}^*_{\mathcal{C}}. \tag{2.5}$$

Through the Kubo formula, the Drude formula for conductivity $\sigma_0 = e^2 \nu_F D$ can be derived within this approximation, where ν_F is the density of states per volume unit for both spin directions at the Fermi level.

---

effective only if $\varepsilon > E_{\mathrm{Th}}$ ($\hbar/t > E_{\mathrm{Th}}$), where $E_{\mathrm{Th}} = \hbar D/L^2$ is the Thouless energy relative to this dimension (see section 3.4.1 for more details). Thus, $d = 1$ does not mean real one-dimensional systems of section λ_F^2, for which Luttinger liquids theory must be used instead.

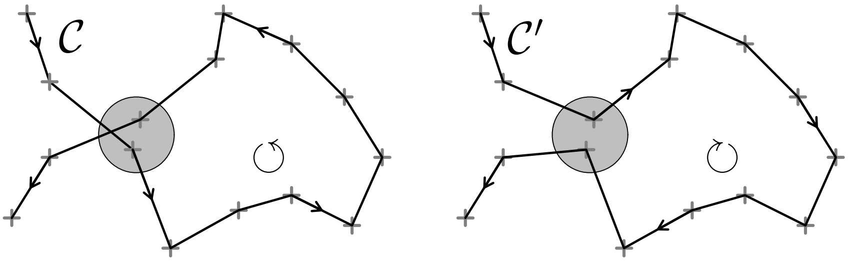

Fig. 2.2. Path $\mathcal{C}$ is said to contain a *quantum crossing* when two non successive scattering events are much closer than the mean free path l_e. Thus, for any configuration of disorder, $\mathcal{C}$ has about the same length than another path in which the loop $\circlearrowleft$ is traveled in reverse order $\circlearrowright$.

In order to go further, and calculate quantum corrections to Drude formula, the so-called weak[4] localization corrections, one needs to identify which terms have been neglected in the sum. It turns out that all paths containing *quantum crossings* (see Fig. 2.2) have a non-classical contribution to $\mathcal{P}$. Considering the path $\mathcal{C}$ of Fig. 2.2, the sum $\mathcal{A}_{\mathcal{C}} \sum_{\mathcal{C}''} \mathcal{A}^*_{\mathcal{C}''}$ does not reduce to the Drude contribution $\mathcal{A}_{\mathcal{C}}\mathcal{A}^*_{\mathcal{C}}$ alone, because the term $\mathcal{A}_{\mathcal{C}}\mathcal{A}^*_{\mathcal{C}'}$ does not vanish by disorder averaging. One gets

$$\left\langle \mathcal{A}_{\mathcal{C}} \sum_{\mathcal{C}''} \mathcal{A}^*_{\mathcal{C}''} \right\rangle = \langle \mathcal{A}_{\mathcal{C}}\mathcal{A}^*_{\mathcal{C}} \rangle + \langle \mathcal{A}_{\mathcal{C}}\mathcal{A}^*_{\mathcal{C}'} \rangle \,. \tag{2.6}$$

For any path $\mathcal{C}$ containing a quantum crossing one can define a loop $\circlearrowleft$ such as in Fig. 2.2. If this loop takes a time t to be traveled, all paths obtained by replacing $\circlearrowleft$ by another loop taking the same time t interfere with $\mathcal{C}$. Therefore, the total probability $\mathcal{P}$ can be calculated through the return probability $Z(t)$. One shows that in a non interacting metal without spin-orbit coupling, this weak localization correction, given by the probability for a path to contain a quantum crossing, reads

$$\frac{\sigma - \sigma_0}{\sigma_0} = -\frac{1}{\pi \hbar \nu_F} \int_{\tau_e}^{+\infty} Z_c(t) \mathrm{d}t \tag{2.7}$$

with $\tau_e = l_e / v_F$ the characteristic time interval between two elastic collisions. The cutoff at small times is due to the fact that the diffusion approximation is meaningless in the ballistic regime where $t < \tau_e$, as the probability for an electron to be reflected back to its departure point in a time shorter than τ_e is zero.

---

[4] as opposed to the strong localization regime where the metal is insulating (see 1.1.1)

Till now, we have only considered the simplest case where the terms $\mathcal{A}_{\mathcal{C}}\mathcal{A}^*_{\mathcal{C}'}$ depend only on the phase difference $k_F(\ell_{\mathcal{C}} - \ell_{\mathcal{C}'})$. In fact, this assumption requires that no external process can modify the phase of $\mathcal{A}_{\mathcal{C}}$ during transport. The next section will show how, in real metals, such processes limit the Cooperon drastically.

2.1.3 Coupling to dynamic degrees of freedom: phase coherence time

Along their trajectory, electrons can interact with phonons, electrons or other dynamic degrees of freedom. The Cooperon $Z_c(t)$ gets modified by those processes. Indeed, an electron undergoing such a process on a path $\circlearrowleft$ almost never suffers it in the exact same conditions on the reverse path $\circlearrowright$. Thus, both trajectories $\circlearrowleft$ and $\circlearrowright$ do not interfere anymore. Assuming that these events are uncorrelated, $Z_c(t)$ decreases exponentially with time[5].

$$Z_c(t) \leftarrowtail Z_c(t)\mathrm{e}^{-t/\tau_\varphi} \tag{2.8}$$

where the time τ_φ is called the *phase coherence time*. Hence, assuming $\tau_\varphi \gg \tau_e$, the weak localization correction becomes

$$\frac{\sigma - \sigma_0}{\sigma_0} = -\frac{1}{\pi\hbar\nu_F}\int_{\tau_e}^{+\infty} Z_c(t)\mathrm{e}^{-t/\tau_\varphi}\mathrm{d}t \tag{2.9}$$

In a finite length system, the return probability $Z_c(t)$ can be calculated by assuming that electrons coming into the leads never come back, and that those hitting an edge are reflected. In a quasi-one dimensional wire of length L, one can show that this results in a correction to the conductance $G = \sigma S_e/L$ [62]

$$G - G_0 = -2\frac{L_\varphi}{LR_K}\left(\coth\left(\frac{L}{L_\varphi}\right) - \frac{L_\varphi}{L}\right) \tag{2.10}$$

where $L_\varphi = \sqrt{D\tau_\varphi}$ is the phase coherence length and $R_K = h/e^2$ is the resistance quantum. In the case where $L \gg L_\varphi$, this reduces to $G - G_0 \sim -2L_\varphi/LR_K$.

As emphasized in section 1.1, the determination of L_φ is crucial. Measuring the quantum correction to the average conductance presents several advantaged to probe this length: it is sensible to any value of the phase coherence length, does not require any particular geometry for the conductor and depends on a few fit parameters. In the following, we will first present important corrections to the simple expression of the conductance (2.10), and then show how the magnetoresistance exhibits in a very simple way this quantum correction.

---

[5] We will see later that this assumption is too strong, but the resulting exponential law remains a good approximation in our experiments.

2.1.4 Spin-orbit coupling

As electrons move with a velocity $\boldsymbol{v}$ in the static potential $U(\mathbf{r})$ due to the ion lattice, they feel an effective electrostatic field $\mathbf{E} = -\nabla U(\mathbf{r})/e$, to which is also associated a magnetic field $\mathbf{B} = -\mathbf{v} \times \mathbf{E}/c^2$ (where c is the light velocity), that acts on their spin. Therefore, the Hamiltonian contains a term $-\mu_B \mathbf{B}.\sigma$ which depends on the position and velocity operators, where $\mu_B = e\hbar/2m_e$ is the Bohr magneton and σ is the vector formed by the Pauli matrices. This term rotates the electron spin and results, for a trajectory $\circlearrowleft$, in a rotation matrix $R_t^{\circlearrowleft}$ at time t which depends only on the path $\circlearrowleft$. Hence, terms in $Z(t)$ become spin-dependent. As Diffuson terms are interferences $\mathcal{A}_{\circlearrowleft}\mathcal{A}^*_{\circlearrowleft}$ between two identical paths, spin-orbit has the same effect on both paths and the Diffuson is not affected by spin-orbit coupling. However, the time-reversed trajectories of the Cooperon are affected by different spin factors. Given initial spin s_0 and final spin s_t for the electrons (see Fig. 2.3), each amplitude $\mathcal{A}_{\circlearrowleft}$ is multiplied by a factor $\langle s_0|R_t^{\circlearrowleft}|s_t\rangle$. Eventually, $Z_c(t)$ is modified by a global factor

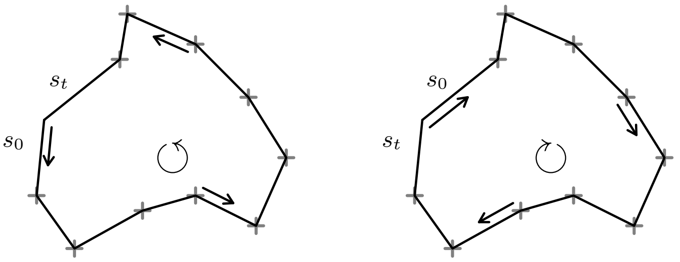

Fig. 2.3. Interfering paths followed by an electron starting in spin state s_0 at time 0 and ending in spin state s_t at time t.

$$Z_c(t) \longleftarrow Z_c(t)\overline{Q_{\mathrm{so}}(t)} \tag{2.11}$$

where

$$Q_{\mathrm{so}}(t) = \sum_{s_t \in \pm} \langle s_0|R_t^{\circlearrowright}|s_t\rangle^* \langle s_0|R_t^{\circlearrowleft}|s_t\rangle = \sum_{s_t \in \pm} \langle s_t|R_t^{\circlearrowright}|s_0\rangle \langle s_0|R_t^{\circlearrowleft}|s_t\rangle \tag{2.12}$$

and where $\overline{\cdots}$ denotes the average on all paths $\circlearrowleft$. One can show [63, 64] that the average on all possible rotation axes of R_t reads $\overline{R_t} = \mathrm{e}^{-\frac{t}{6\tau_{\mathrm{so}}}\sigma^2}$ where τ_{so} is the so-called spin-orbit time and σ the spin operator. In the tensorial product of the spin state spaces, any spin state $|s^{\circlearrowleft}\rangle \otimes |s^{\circlearrowright}\rangle$ can be written in terms of the singlet $|T_0\rangle$ and triplet states $|T_1\rangle$,$|T_2\rangle$ and $|T_3\rangle$ (which are eigenstates of the spin operator $\sigma^{\circlearrowleft} + \sigma^{\circlearrowright}$)using the closure relation

$$\sum_{i=0}^{3} |T_i\rangle\langle T_i| = \mathbf{1}$$

Hence,

$$\overline{Q_{\mathrm{so}}(t)} = \sum_{s_t \in \pm} \sum_{i=0}^{3} \langle s_t| \otimes \langle s_0|T_i\rangle\langle T_i|\mathrm{e}^{-\frac{t}{6\tau_{\mathrm{so}}}(\sigma^{\circlearrowleft}+\sigma^{\circlearrowright})^2}|T_i\rangle\langle T_i|s_0\rangle \otimes |s_t\rangle \tag{2.13}$$

Finally, using Eqs. (A.1-A.4) (see Appendix), different contributions to the factor $\overline{Q_{\mathrm{so}}(t)}$ exist depending if it is in the singlet state or in the triplet state, and one gets

$$\overline{Q_{\mathrm{so}}(t)} = \underbrace{\frac{3}{2}\mathrm{e}^{-4t/3\tau_{\mathrm{so}}}}_{\text{Triplet}} \underbrace{-\frac{1}{2}}_{\text{Singlet}} \tag{2.14}$$

Is spin-orbit really important for weak-localization experiments ?

As expressed by Eq. (2.9), the phase coherence time τ_φ acts as a cutoff in the integral on the Cooperon (2.7) expressing in the weak localization correction. If $\tau_{\mathrm{so}} \gg \tau_\varphi$, the spin-orbit correction $\overline{Q_{\mathrm{so}}(t)}$ is of order 1 and has no effect. In the opposite limit, spin-orbit has a strong effect on weak localization as soon as $\tau_{\mathrm{so}} \precsim \tau_\varphi$, and in the limit where $\tau_{\mathrm{so}} \ll \tau_\varphi$, $\overline{Q_{\mathrm{so}}(t)} \approx -1/2$. In the later case, one talks about weak anti-localization as the sign of the correction is reversed. It has long been argued that spin-orbit effects can always be neglected in light metals. Indeed, spin-orbit rate $1/\tau_{\mathrm{so}}$ increases roughly as

Material	Z number	τ_{so} (ps)	$\tau_e/Z^4\alpha^4$ (ps)
silver (Ag)	47	$10-50$	3
copper (Cu)	29	$20-40$	20
gold (Au)	79	0.5	0.3

Table 2.1. Spin orbit times τ_{so} extracted from weak localization measurements in [43, 65]. Simple theory [66] for evaluating τ_{so} gives almost the right order of magnitude.

$$1/\tau_{\mathrm{so}} = Z^4\alpha^4/\tau_e \tag{2.15}$$

with the atomic number Z, where $\alpha = \frac{e^2}{4\pi\epsilon_0 c\hbar} \approx 1/137$ is the fine structure constant[66, 67]. But, even for light metals, τ_{so} eventually becomes smaller than τ_φ, because τ_φ diverges at low temperatures. In our experiments τ_{so} is always smaller than τ_φ, and we observe weak anti-localization.

2.1.5 Magnetoresistance: a direct way of measuring the weak localization effect.

The Cooperon is strongly affected by an external uniform magnetic field $\mathbf{B}$. The Hamiltonian takes into account this field through a shift of the electron momentum $\mathbf{p} \leftarrowtail \mathbf{p} - e\mathbf{A}$ where $\mathbf{A}$ is the vector potential. Therefore, the phase acquired[6] on a loop $\circlearrowleft$ is $\phi(B, \circlearrowleft) = -e/\hbar \int_{\circlearrowleft} \mathbf{A}\mathrm{d}\mathbf{r} = -e\mathbf{B}.\mathbf{S}_{\circlearrowleft}/\hbar$, where $\mathbf{S}_{\circlearrowleft}$ is the oriented surface enclosed by the loop $\circlearrowleft$. Thus, in the Cooperon, terms in $\mathcal{A}^*_{\circlearrowleft}\mathcal{A}_{\circlearrowleft}$ are affected by a factor $\mathrm{e}^{2i\phi(B,\circlearrowleft)}$. Finally, the only terms in the Cooperon $Z_c(t)$ which do not average out to zero are those for which $\phi(B, \circlearrowleft)$ is small compared to 1. This dephasing introduces a new length in the system: the characteristic length of the longest loops contributing to the Cooperon, $L_B = \sqrt{\hbar/eB}$.

It turns out that this dephasing process can be taken into account in the same way as the coupling to dynamic degrees of freedom, and one just has to replace L_φ by a new length that combines L_φ and L_B. For example, in quasi-one dimensional wires of section S_e,

$$\frac{1}{L_\varphi^2} \leftarrowtail \frac{1}{L_\varphi^2} + \frac{S_e}{3L_B^4}. \tag{2.16}$$

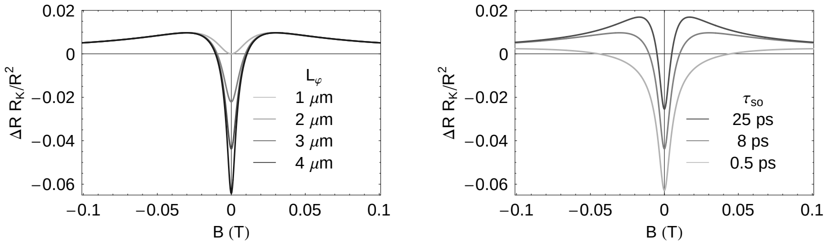

Fig. 2.4. Theoretical magnetoresistance curves using Eq. (2.17) for a 40 μm long wire with section $S_e = 230 \times 40$ nm^2 and diffusion constant $D = 200$ cm^{2}s^{-1}. Left panel: Assuming a spin-orbit time $\tau_{\mathrm{so}} = 8$ ps, each curve corresponds to a different L_φ going from 1 to 4 μm from light to dark. Right panel: Assuming $L_\varphi = 3$ μm, each curve corresponds to a different spin-orbit time τ_{so} going through 0.5, 8 and 25 ps from light to dark.

Finally, using Eqs. (2.10),(2.14), and (2.16), the magnetoresistance of a diffusive wire of length L reads

---

[6] We neglect the curvature of electronic paths due to the Lorentz force. This is equivalent to assume that the cyclotron frequency $\omega_c = eB/m$ is such that $l_e \ll v_F/\omega_c$. In metallic thin films, the mean free path l_e is about 50 nm, and this condition, equivalent to $B \ll 100$ T, is always fulfilled in practice.

$$\frac{\Delta R}{R} \equiv \frac{R(B)-R(B=\infty)}{R(B=\infty)} = \frac{R}{R_K}\left(3\xi(\mathit{\Lambda}^{(\mathrm{T})}(B)) - \xi(\mathit{\Lambda}^{(\mathrm{S})}(B))\right) \tag{2.17}$$

with $\xi(x) = x\coth(1/x) - x^2$, $\mathit{\Lambda}^{(\mathrm{T})}$ and $\mathit{\Lambda}^{(\mathrm{S})}$ the triplet and singlet normalized lengths describing weak localization given by

$$\begin{aligned} \mathit{\Lambda}^{(\mathrm{T})}(B) &= \tfrac{1}{L}\left(\frac{1}{\left(L_\varphi^{(\mathrm{T})}\right)^2} + \frac{4}{3L_{\mathrm{so}}^2} + \frac{S_e}{3L_B^4}\right)^{-1/2} \\ \mathit{\Lambda}^{(\mathrm{S})}(B) &= \tfrac{1}{L}\left(\frac{1}{\left(L_\varphi^{(\mathrm{S})}\right)^2} + \frac{S_e}{3L_B^4}\right)^{-1/2} \end{aligned} \tag{2.18}$$

where $L_\varphi^{(\mathrm{T,S})} = \sqrt{D\tau_\varphi^{(\mathrm{T,S})}}$ are the phase coherence lengths in the triplet (T) and singlet (S) channels, and $L_{\mathrm{so}} = \sqrt{D\tau_{\mathrm{so}}}$ the spin-orbit length.

In the noble metal we investigate in this work, $\tau_{\mathrm{so}} \sim 10$ ps is always much smaller than $\tau_\varphi^{(\mathrm{T})}$ by orders of magnitude (as will be proven in section 2.2.1). Therefore, only the singlet term $\tau_\varphi^{(\mathrm{S})}$ can be accessed in the magnetoresistance and we will call it τ_φ in the following, except for particular notices. The objective is now to measure this phase coherence times τ_φ.

2.1.6 Magnetoresistance measurements

In this section, we illustrate the above general picture on magnetoresistance measurements we have performed on two silver wires, and show how to extract the phase coherence time from them. These experiments will be described in more details in section 3.4.6 where Ref. [65] is reproduced. The two silver wires differ only by the addition of a known amount (0.65 ppm) of Mn atoms (see section 8.4 for technical details) in one of them, called *implanted* in the following, the other one being called *bare*. These wires were designed in such a way that both the phase coherence time and the rate of energy exchange between electrons can be measured (see chapter 3). For this reason, the length of the wires was not chosen very long compared to the maximal phase coherence

Wire	Length L (μm)	Width w (nm)	Thickness t (nm)	Resistance R (Ω)	Diff. const. D (cm^{2}s^{-1})
bare	40.3	237	42	53.4	287
implanted	38.9	230	42	55.9	273

Table 2.2. Geometrical and electrical characteristics of the wires investigated in [43, 65].

length expected at low temperature, as is usually the case for weak localization experiments. In the following, we first describe the difficulties inherent to the measurement of τ_φ in such short wires.

Measuring weak localization in short wires

The biggest trouble coming from the short length of the wires ($L \lesssim L_\varphi$) comes from another mesoscopic effect than weak localization: conductance fluctuations. As seen on the experimental curves on Fig. 2.7 and 2.8, the measured magnetoresistance shows strong fluctuations. Only part of those fluctuations is noise: most features are reproducible and even in magnetic field. They are due to interferences of electronic paths which are modified by magnetic field [68] and are a unique signature of the disorder potential. In the limit $L \gg L_T = \sqrt{\hbar D/k_B T}$, the variance of the conductance fluctuations is given by [61]

$$(\delta G)^2 \equiv \overline{G^2} - \overline{G}^2 = \tfrac{2\pi}{3R_K^2}(L_T/L)^2 \, [\underbrace{2\xi(L_\varphi^{(\mathrm{S})}/L)}_{\text{Diffuson}} + \underbrace{3\xi(\Lambda^{(\mathrm{T})}(B)) - \xi(\Lambda^{(\mathrm{S})}(B))}_{\text{Cooperon}}] \, . \tag{2.19}$$

Therefore, the signal to fluctuations ratio $\Delta R/R^2\delta G$ of the weak localization dip grows like L^2 and for short wires like in our experiment, this ratio can be of order 1 (see Fig. 2.5). Besides, the magnetic field scale of the correlations of these fluctuations is about the width of the weak localization dip, and both phenomena cannot be treated separately. Therefore, the precision of the determination of τ_φ in short wires is not as good as in experiments on longer wires.

Another modification to the standard picture of magnetoresistance in long wires is described by the finite length formula Eq. (2.17), which had to be used instead of the approximation $\xi(x) \approx x$. In fact, in Ref. [65], we had taken for finite length correction the following expression:

$$\frac{\Delta R^{\text{Ref. [65]}}}{R} = \frac{R}{R_K}\left(\frac{L_\varphi^{(\mathrm{S})}}{L}\xi(L_\varphi^{(\mathrm{S})}/L)\right)\left(3\Lambda^{(\mathrm{T})}(B) - \Lambda^{(\mathrm{S})}(B)\right) \tag{2.20}$$

instead of Eq. (2.17). This led to a slight underestimation (compare Fig. 3.26 with Fig. 2.9)of both τ_{so} and the phase coherence time. In the following, we use the correct formula (2.17).

Determination of the spin-orbit time

In the analysis of the magnetoresistance measurements, we first determine the spin-orbit time τ_{so}, since it is expected to be identical for both wires. We proceed as follows: for various values of τ_{so}, we calculate the best fit of all the magnetoresistance curves taken at $1\ \mathrm{K} < T < 6\ \mathrm{K}$, in order to be insensitive

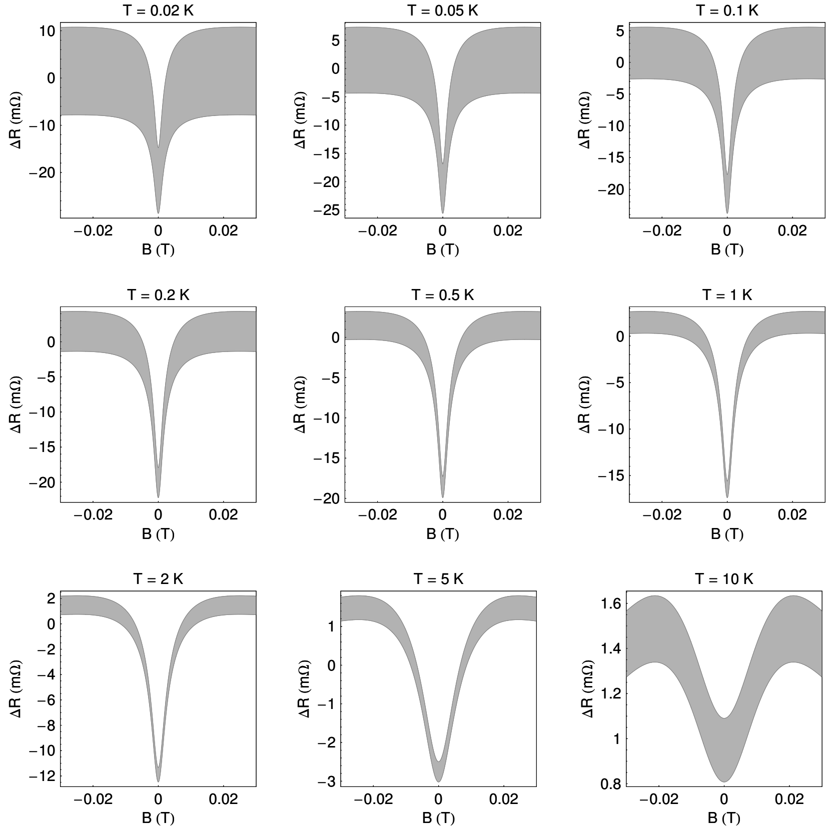

Fig. 2.5. Prediction for the characteristic window for the conductance fluctuations (width $2\delta R = R^2\delta G$), using the geometrical parameters of the two wires (bare and implanted) and assuming that τ_φ sticks to its theoretical prediction given later in Eq. (2.48) with the parameters given in Ref. [65].

to conductance fluctuations (Fig. 2.5). The fit parameters are the resistance R and the coherence length L_φ. For each magnetoresistance curve, we then calculate the sum of the squared difference between experiment and theory. A global estimation is obtained by calculating an average $Var(\tau_{\mathrm{so}})$ on all the resulting curves, each one normalized to its minimum value (see Fig. 2.6). We take for τ_{so} the value that minimizes[7] this global variance: $\tau_{\mathrm{so}} \approx 10 \pm 1$ ps. The value given in Ref. [65], $\tau_{\mathrm{so}} \approx 8$ ps, slightly differs from that one because a slightly different procedure was followed.

---

[7] The error bar is estimated from the distribution of the variance curves.

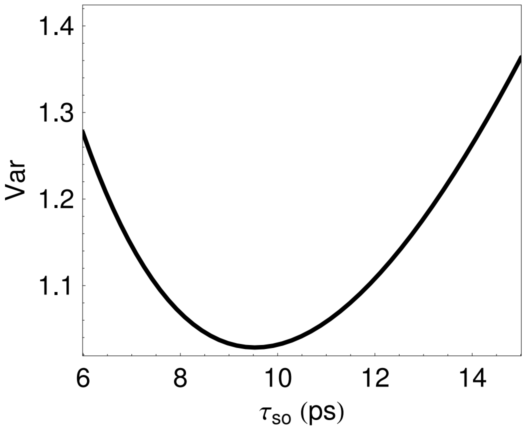

Fig. 2.6. Variance of the difference between experimental and theoretical magnetoresistance curves depending on the spin-orbit time $\tau_{\rm so}$. The best fit is around $\tau_{\rm so} = 10$ ps for both wires.

Extraction of the phase coherence time

The best fit curves obtained with $\tau_{\rm so} = 10$ ps are shown on Fig. 2.7 and 2.8. The corresponding values of $\tau_\varphi(T)$ are plotted on Fig. 2.9. The highest phase coherence time τ_φ is approximatively 10 ns. It means that at the lowest temperatures, electrons travel on a typical length of 15 μm without phase decoherence. This clarifies the order of magnitude one might expect for the maximal length of a coherent metallic conductor. The signal to noise ratio (due to a longer acquisition time) is worse for the implanted wire than for the bare wire, so that the symmetry of the conductance fluctuations by magnetic field reversal is clear for the bare wire only.

Furthermore, Fig. 2.9 shows that the two wires have different phase coherence times at low temperature. Since the only difference between them is the presence of 0.65 ppm of Mn atoms in the implanted wire, this curve proves that magnetic impurities can lead to a dramatic increase of phase decoherence. It is noteworthy that less than 1 ppm of magnetic impurities can have such an effect, especially knowing that the highest guaranteed purity of commercial metal sources is 1 ppm of impurities (altogether magnetic or not). In the next section, we will show how the coupling between electrons and dynamical degrees of freedom affects the phase coherence time τ_φ. Using Coulomb interactions between electrons, electron-phonon interactions and electron-magnetic impurity interaction, we will see how we can account for the data shown on Fig. 2.9.

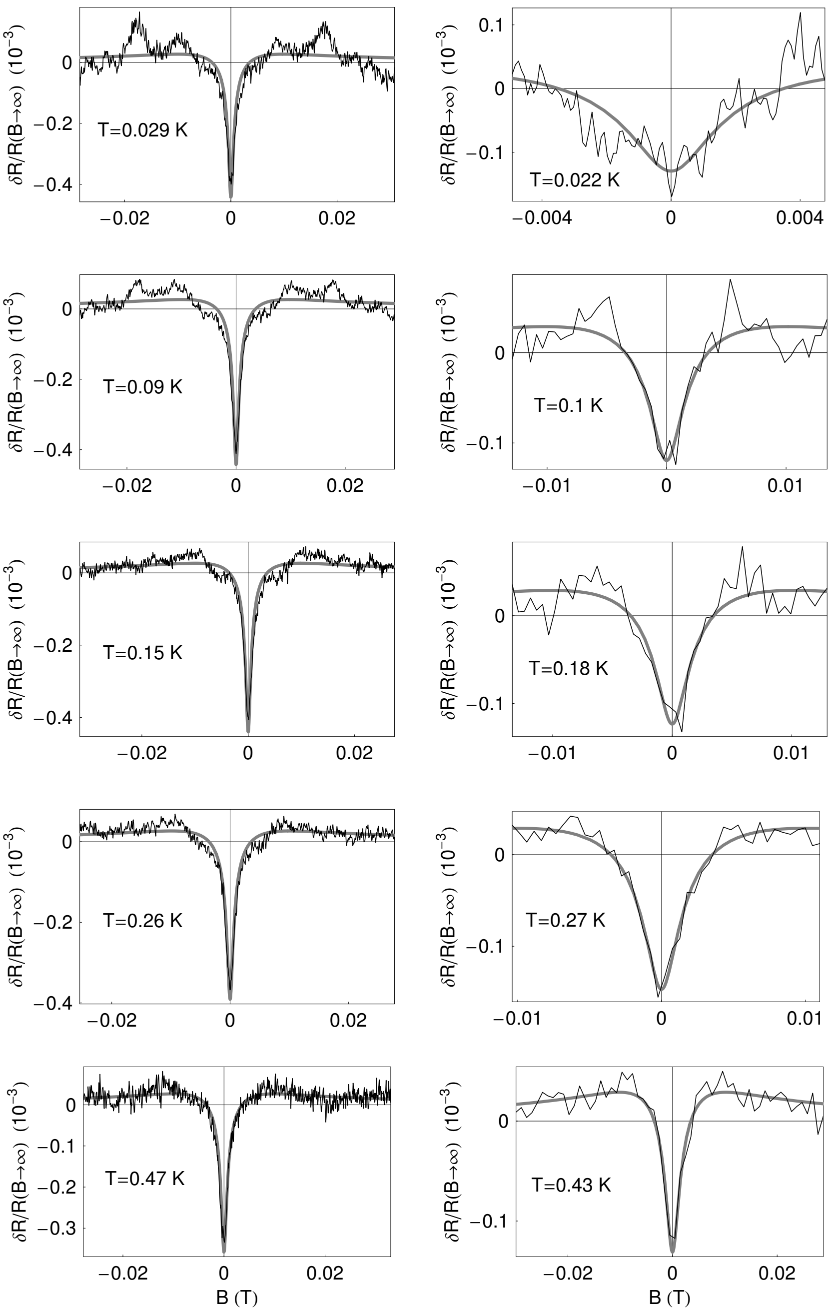

Fig. 2.7. Magnetoresistance (thin lines) of the bare wire (left column) and implanted wire (right column) for 20 mK $< T <$ 0.5 K. Thick grayed lines are plotted using theory of weak localization Eq. (2.17) with $\tau_{\mathrm{so}} = 10$ ps and using τ_φ as a fit parameter.

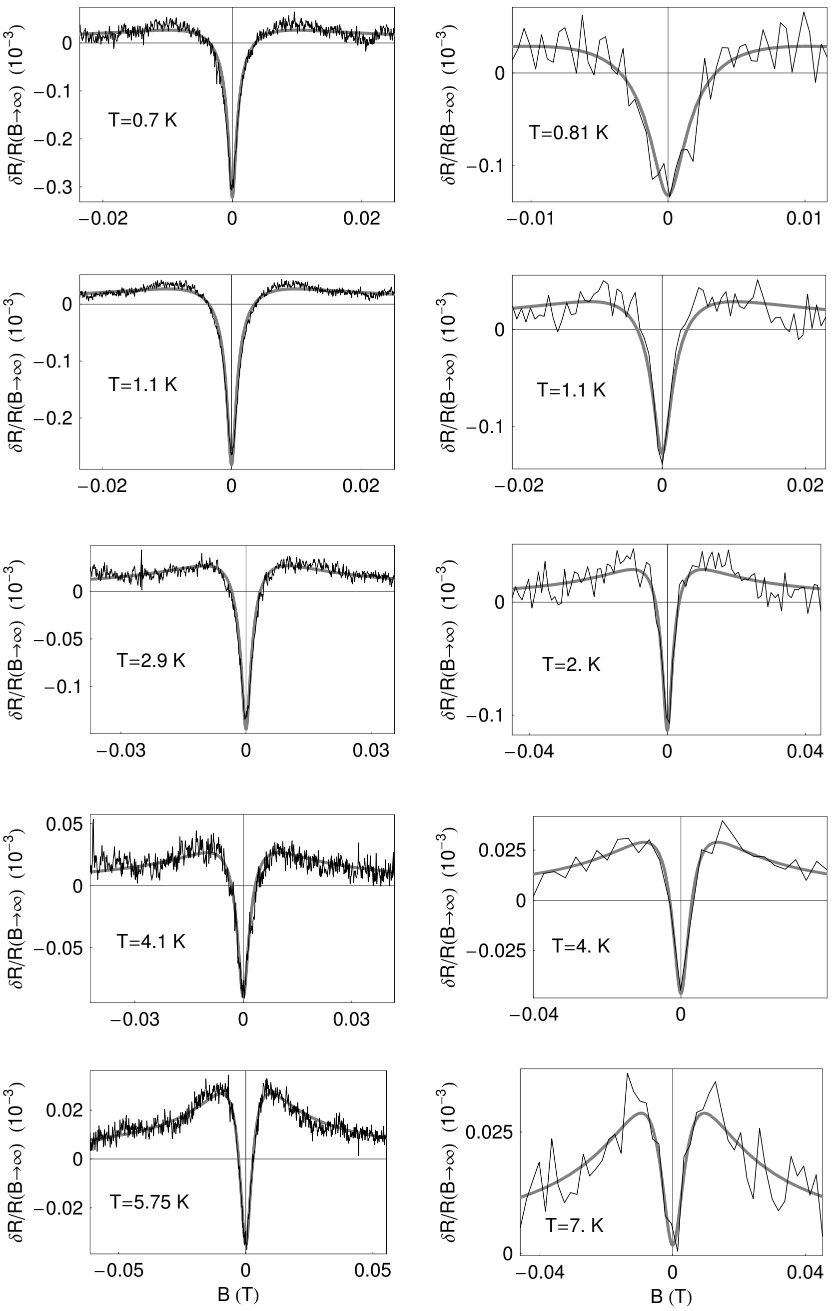

Fig. 2.8. Magnetoresistance (thin lines) of the bare wire (left column) and implanted wire (right column) for 0.5 K $< T <$ 7 K. Thick grayed lines are plotted using theory of weak localization Eq. (2.17) with $\tau_{\mathrm{so}} = 10$ ps and using τ_φ as a fit parameter.

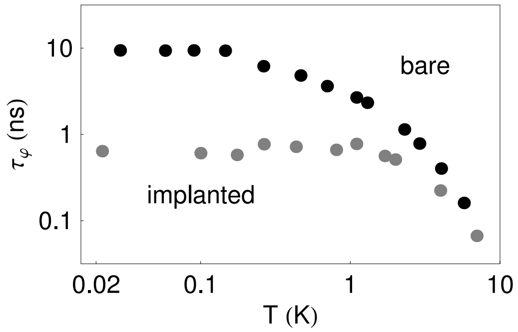

Fig. 2.9. Phase coherence times measured in each wire as a function of temperature. Black dots correspond to the bare wire and Grey dots to the implanted one. The addition of manganese impurities has significantly reduced the phase coherence time.

2.2 Phase coherence time limitations due to interactions

In this section, we review the limitations of τ_φ due to interactions between electrons and their environment. To each channel (singlet or triplet) and to each dephasing process "dp" can be attributed a rate $1/\tau_\varphi^{(\mathrm{dp})}$ contributing to the Cooperon $Z_c(t)$ along Eq. (2.8), so that all processes together modify the Cooperon by[8]

$$Z_c(t) \longleftarrow Z_c(t) \prod_{\mathrm{dp}} \mathrm{e}^{-t/\tau_\varphi^{(\mathrm{dp})}} = Z_c(t)\mathrm{e}^{-t(\sum_{\mathrm{dp}} 1/\tau_\varphi^{(\mathrm{dp})})} \equiv Z_c(t)\mathrm{e}^{-t(1/\tau_\varphi)} \tag{2.21}$$

Phase coherence time abides by a Matthiessen rule: the inverse phase coherence time $1/\tau_\varphi$ is the sum of the decoherence rates attributed to each process. In the following, we derive the expression of dephasing rates for electron-electron Coulomb interaction, electron-phonon interaction and electron-magnetic impurity interaction.

2.2.1 Coulomb interaction

Let us first consider only the dephasing by Coulomb interaction between electrons. We will not enter into great details here, but instead outline the main steps of the calculation of the Coulomb dephasing. For further references, see [2, 36, 41, 61].

Charge term

First, we will consider the spin independent part of the interaction between electrons, which we denote by "charge" term. It can be calculated in a mean

---

[8] As already stated in section 2.1.3, this is a good approximation of the actual non exponential behavior of the corrections to the Cooperon.

field approach, by considering that the phase of an electron is affected by the fluctuating electric potential $V(t, \mathbf{r})$ due to all the other electrons. As a consequence, terms $\mathcal{A}_{\circlearrowleft}\mathcal{A}^*_{\circlearrowright}$ in the Cooperon are modified by a phase factor $\mathrm{e}^{i\Phi_{\circlearrowleft}}$ where

$$\Phi_{\circlearrowleft} = \frac{e}{\hbar}\int_{\circlearrowleft} \mathrm{d}\tau V[\tau, \mathbf{r}_{\circlearrowleft}(\tau)] - \frac{e}{\hbar}\int_{\circlearrowright} \mathrm{d}\tau V[\tau, \mathbf{r}_{\circlearrowright}(\tau)] \tag{2.22}$$

The time averaged[9] dephasing factor for the particular path $\circlearrowleft$ is $\overline{\mathrm{e}^{i\Phi_{\circlearrowleft}}} = \mathrm{e}^{-\overline{\Phi^2_{\circlearrowleft}}/2}$. This quantity can be calculated from the time and space correlator $\langle V(t, \mathbf{r})V(t', \mathbf{r}')\rangle$, which can be related to the dielectric constant through the fluctuation-dissipation theorem. In a diffusive wire (quasi-one dimensional) of length L at temperature T, one gets

$$\overline{\Phi^2_{\circlearrowleft}} = \frac{4\pi k_B T}{\hbar}\frac{R}{R_K}\int_0^t \mathrm{d}\tau \frac{|\mathbf{r}_{\circlearrowleft}(\tau) - \mathbf{r}_{\circlearrowright}(\tau)|}{L} \tag{2.23}$$

In the end, one needs to average this dephasing factor $\mathrm{e}^{-\overline{\Phi^2_{\circlearrowleft}}/2}$ over all possible paths $\circlearrowleft$ in order to calculate the total dephasing. This can be done through a path integral approach [2], and one finds[10]

$$Z_c(t) \leftarrowtail Z_c(t)\langle\overline{\mathrm{e}^{i\Phi_{\circlearrowleft}}}\rangle_{\circlearrowleft} \approx Z_c(t)\mathrm{e}^{-t/\tau_\varphi^{(\mathrm{ee,charge})}} \tag{2.24}$$

with a phase coherence time

$$\tau_\varphi^{(\mathrm{ee,charge})} = \hbar\left(\frac{4\nu_F L S_e}{\pi k_B^2}\frac{R_K}{R}\right)^{1/3} T^{-2/3} \equiv A^{-1}T^{-2/3} \tag{2.25}$$

with ν_F the density of states at the Fermi level (both spin directions), S_e the wire cross-section, and R its resistance [1, 61].

As this dephasing process does not change the spins of the two interacting electrons, the charge term contributes both to the singlet and triplet part of the total dephasing rate due to electron-electron interactions.

---

[9] Up to a very good approximation, the modes of the electromagnetic field are quadratic, hence having gaussian fluctuations.

[10] Actually, this result is only a good approximation to the real phase relaxation, which is not exponentially decreasing. In fact, $\Phi^2_{\circlearrowleft}$ is proportional to the integral over time t of the fluctuations of the electric potential V on the length explored during t. Therefore $\Phi^2_{\circlearrowleft} \propto \int_0^t \mathrm{d}t' \langle \delta V^2\rangle_{R_{t'}}$ where R_t is the resistance of the explored part of the wire in a time t. As this distance grows like $\sqrt{t}$ in the diffusive case, and as the fluctuation-dissipation theorem states that $\langle \delta V^2\rangle_R \propto 4k_B T R$, one obtains $\Phi^2_{\circlearrowleft} \propto k_B T t^{3/2}$. More precisely, it is shown in [61] that in the general case, $\langle\overline{\mathrm{e}^{i\Phi_{\circlearrowleft}}}\rangle_{\circlearrowleft} \sim \mathrm{e}^{-\sqrt{\pi/2}(t/\tau_\varphi^{(\mathrm{ee,charge})})^{3/2}}$.

Spin term

The screened interaction between two electrons contains actually two terms. The first one, the charge term was analyzed in the previous section, and corresponds to a spin-independent interaction. The second one is proportional to the scalar product of the spin matrices of the two interacting electrons [28]. This does not mean that the Coulomb interaction is spin-dependent, but that the summation of the perturbation theory depends on the spin [69]. In the Landau theory of Fermi liquids, this interaction is characterized at first order by a real parameter F_0^σ. In particular the spin susceptibility is modified by this interaction so that, in metals with almost spherical Fermi surface[11], the Landé g-factor becomes

$$g = \frac{2}{1+F_0^\sigma}. \tag{2.26}$$

In the limit where F_0^σ goes to -1, which corresponds to the ferromagnetic (Stoner) instability, the Fermi liquid theory does not apply anymore. The Fermi liquid constant F_0^σ can be accessed by conduction electron spin resonance in noble metals, and was found to be in the range $F_0^\sigma \in [-0.21, 0.05]$ in silver [70]. In aluminum, assuming that the relation (2.26) holds (although the Fermi surface is not spherical), it was reported that $F_0^\sigma \approx +0.1$ [71]. As this interaction is spin-dependent it has different effects on the singlet and triplet dephasing rates. Its contribution to $\tau_\varphi^{(\mathrm{ee,T})}$ has never been calculated in a proper way to our knowledge. Still, it is expected that the total triplet

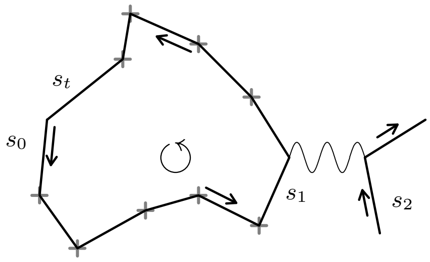

Fig. 2.10. Many spins enter in the calculation of the dephasing time $\tau_\varphi^{(\mathrm{ee})}$. In this work, the indices S or T refer to the singlet or triplet states of the spins s_0 and s_t. The interaction between the two electrons of spin s_1 and s_2 may depend on these spins, and one distinguishes the case where they form a singlet and the case where they form a triplet state. In this work, we denote the whole spin dependent part (s_1 and s_2) of the interaction as the *spin term*, and triplet or singlet always refer to the spins s_0 and s_t.

---

[11] This is the case for Ag, Au and Cu (see Table. A.3 in the appendix).

dephasing time $\tau_\varphi^{(\mathrm{ee,T})}$ is of the same order of magnitude as the total singlet dephasing time $\tau_\varphi^{(\mathrm{ee,S})}$. In our experiments, this time will be shown to be much larger than τ_{so} at all relevant temperatures, and therefore its contribution to the effective length $\Lambda^{(\mathrm{T})}(B)$ of Eq. (2.18) is negligible. In the following, we focus on the singlet dephasing time, which has a direct effect on the magnetoresistance.

Negligible spin-orbit interaction

Let us first present an expression of $\tau_\varphi^{(\mathrm{ee,S,spin-term})}$ in the approximation of negligible spin-orbit interaction. It turns out that $\tau_\varphi^{(\mathrm{ee,S,spin-term})}$ reads exactly as the charge dephasing time Eq. (2.25) except for a global prefactor λ_d, which depends on dimensionality d. Therefore, in case of negligible spin-orbit coupling (which is not the case in our experiments), the singlet term reads

$$\tau_\varphi^{(\mathrm{ee,S,spin-term})} = \lambda_1 \tau_\varphi^{(\mathrm{ee,S})} = \lambda_1 A^{-1} T^{-2/3} \tag{2.27}$$

The prefactor λ_1 depends only on the Fermi liquid constant F_0^σ. Aleiner *et al.* have developed a formalism to derive it, and in the one-dimensional case [72]:[12]

$$\lambda_1 = \frac{3(F_0^\sigma)^2}{1 + F_0^\sigma + \sqrt{1 + F_0^\sigma}}. \tag{2.29}$$

General case

In the general case where the spin-orbit scattering is dominant ($\hbar/\tau_{\mathrm{so}} \gg k_B T$), one can calculate $\tau_\varphi^{(\mathrm{ee,S,spin-term})}$ using the semiclassical theory (see section 3.4.1). As proven[13] in section 3.4.1,

$$\tau_\varphi^{(\mathrm{ee,S,spin-term})} = \frac{\pi^{2/3}}{2} \int_{\hbar/\tau_\varphi^{(\mathrm{ee,T})}}^{k_B T} \mathrm{d}\varepsilon \mathcal{K}_{\mathrm{Hartree}}(\varepsilon) k_B T \tag{2.30}$$

where $\mathcal{K}_{\mathrm{Hartree}}(\varepsilon)$ is the Hartree term of the kernel of Coulomb interaction and is given by Eq. (3.51). In the end,

$$\tau_\varphi^{(\mathrm{ee,S,spin-term})} = \frac{\pi^{1/3}\hbar}{\lambda_1 k_B (A\tau_{\mathrm{so}})^{3/2}} T^{-2}. \tag{2.31}$$

---

[12] The only published result is for the bi-dimensional case [69, 73]:

$$\lambda_2 = \frac{3(F_0^\sigma)^2}{(1 + F_0^\sigma)(2 + F_0^\sigma)}. \tag{2.28}$$

[13] The prefactor of this expression comes from the fact that τ_φ and $\tau_E^{\mathrm{ee}}(E = 0, T)$ are distinct. The prefactor allows one to find the actual value for τ_φ using Eqs. (3.61, 3.62).

Therefore, the final expression for $\tau_\varphi^{(\mathrm{ee,S})}$ is just

$$\tau_\varphi^{(\mathrm{ee})} = \left(\left(\tau_\varphi^{(\mathrm{ee,charge})}\right)^{-1} + \left(\tau_\varphi^{(\mathrm{ee,S,spin-term})}\right)^{-1}\right)^{-1} \approx A^{-1}T^{-2/3} \qquad (2.32)$$

In our experiment, the spin-dependent dephasing rate is negligible compared to the charge rate by 4 orders of magnitude (at 20 mK, $\tau_\varphi^{(\mathrm{ee,charge})} \approx 10$ ns whereas $\tau_\varphi^{(\mathrm{ee,spin-term})} \approx 0.3$ ms). Therefore, in practice the spin-dependent term has no effect on weak localization, and cannot be detected.

2.2.2 Electron-phonon coupling

Another type of dephasing occurs because of crystal vibrations. Indeed, collective modes of vibration of the ion lattice can both be excited by electrons or can excite electrons by transferring a wave vector $\mathbf{q}$. As electrons get kicked by phonons, they lose phase coherence and thus, the more often this exchange occurs, the smaller τ_φ gets. The typical wave vector of phonons at temperature T is of the order of $q_T = \frac{k_B T}{\hbar s}$ where s is the sound velocity in the metal (≈ 2.7 km.s^{-1} in silver). In 1955, Pippard showed [74] that for small enough q_T, the change in momentum is so small that electrons do not lose phase coherence. More precisely, a phonon can affect an electron only if the latter stays in the same momentum state over a distance larger than one phonon wavelength, which means that $l_e \gg 1/q_T$. Thus, for $l_e \approx 40$ nm as in our experiments, dephasing at temperatures below 0.5 K is much less effective than what is predicted for clean metals. Besides, one should distinguish between longitudinal and transversal phonons as they have different contributions to dephasing. However, applying results of Reizer *et al.* [75] to noble metals, one shows that, above 0.5 K, the effect of longitudinal phonons is larger than that of transversal ones.

Therefore, using the general results of [76, 77, 78] in the limit of $q_T l_e \gg 1$ and no transversal phonons, the dephasing rate due to phonons is[14]

$$\frac{1}{\tau_\varphi^{(\mathrm{e-ph})}} = \frac{7\pi\zeta(3)}{9}\frac{E_F^2 \nu_F k_B^3}{\hbar^3 \rho s^4 k_F^2} T^3 \equiv \mathcal{B}T^3 \qquad (2.33)$$

where ρ is the mass density (10.5×10^3 kg.m^{-3} for silver), E_F the Fermi energy (5.6 eV for silver) and $\zeta(z) = \sum_k k^{-z}$ is the zeta function ($\zeta(3) \approx 1.2$). For silver one finds $\mathcal{B}^{\mathrm{thy}} \approx 2 \times 10^6$ K^{-3}s^{-1}. As temperature is lowered, the clean metal approximation $q_T l_e \gg 1$ does not apply any longer and one has to consider the full formula for $\tau_\varphi^{(\mathrm{e-ph})}$ given in [76, 77, 78]. In this formula, depending on T, the temperature dependence is between T^2 and T^4 instead of T^3. The fit value for $\mathcal{B}$ in our experiments are larger than the theoretical value of $\mathcal{B}$ from Eq. (2.33) by one order of magnitude, which could be a sign that the experiments take place in such a cross-over regime rather than in the pure $\mathcal{B}T^3$ regime.

---

[14] as it is independent on spin, no triplet or singlet index is used

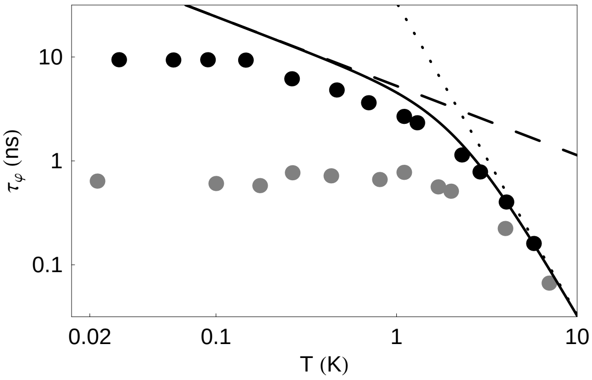

Fig. 2.11. Theoretical phase coherence times due to Coulomb interaction between electrons (dashed line) Eq. (2.25) and electron-phonon coupling (dotted line) Eq. (2.33). Coulomb term is set to its theoretical value $A = 0.19\ \mathrm{ns}^{-1}K^{-2/3}$ from Eq. (2.25), while $\mathcal{B} = 3. \times 10^{-2}\ \mathrm{ns}^{-1}\mathrm{K}^{-3}$ is a fit parameter. The resulting dephasing time Eq. (2.48) is represented as a thick line. Dots (light for implanted wire and dark for bare wire) represent the experimental data of Fig. 2.9.

At this point, we can try to interpret the measurements of $\tau_\varphi(T)$. As shown in Fig. 2.11, even for the bare wire, the effects of Coulomb interaction between electrons and electron-phonon coupling are not sufficient. We will see that the presence of a very small amount of magnetic impurities contributes drastically to decrease τ_φ, as expected from the data (see Fig. 2.9). The sensitivity of τ_φ to magnetic impurities can already be inferred from the comparison of $\tau_\varphi(T)$ on both wires which differ only by the presence of 0.65 ppm of Mn atoms.

2.2.3 Magnetic impurities

In a metal, some foreign atoms or molecules such as Cr, Mn, Fe, Co, Ni or CuO$_2$, can present magnetic properties. An electron can interact with such local moments by flipping its spin with the one of the magnetic impurity. This interaction is described in the Hamiltonian by a term $J\boldsymbol{S}.\boldsymbol{s}$ where J is a coupling constant, $\boldsymbol{S}$ is the impurity spin and $\boldsymbol{s}$ is the local spin density of itinerant electrons[15]. Such a scattering contributes to lowering the diffusion constant as more defects are present. But in contrast with static defects, local moments modify the electron spin and thus destroy interferences in the Cooperon channel. Therefore, this interaction contributes to dephasing. In order to calculate the corresponding dephasing rate, a first approach would use Fermi's golden rule, so that $1/\tau_\varphi^{(\mathrm{e}-\updownarrow)} = \pi\nu_F c_{\mathrm{MI}} J^2 S(S+1)/\hbar$ with c_{MI} the concentration of magnetic impurities in the metal (the number of impurities

---

[15] In second quantification formalism, $\boldsymbol{s} = \sum_{\mathbf{k},\mathbf{k}',\sigma,\sigma'} c^\dagger_{\mathbf{k}\sigma} \boldsymbol{\sigma}_{\sigma\sigma'} c_{\mathbf{k}'\sigma'}$

per unit volume). Yet, two complex effects can change drastically this simple result: the Kondo effect and the interaction between magnetic impurities.

Kondo effect

If one considers the interaction between a local spin $\boldsymbol{S}$ and a single electron with spin $\boldsymbol{s_1}$, the ground state of $J\delta(\mathbf{r})\boldsymbol{S}.\boldsymbol{s_1}$ is a singlet written $|\uparrow\downarrow\rangle - |\downarrow\uparrow\rangle$ in the basis $(\boldsymbol{S}, \boldsymbol{s_1})$. The first excited state is a triplet whose energy lies J above the singlet.

The interaction of a local spin $\boldsymbol{S}$ with the sea of electrons is more complicated. Counter-intuitively, even if conduction electrons move freely, a weak exchange constant J is enough to form a singlet between a cloud of electrons and the local spin. However, the characteristic energy of this singlet is not J, but the so-called Kondo temperature T_K times k_B given by

$$k_B T_K \approx \mathcal{D} \mathrm{e}^{-1/\nu_F J} \tag{2.34}$$

where $\mathcal{D} \approx E_F$ is a cutoff at large energies[16]. Electrons participate in this singlet differently depending on their energy. Kondo showed in particular that scattering of an electron by a local moment is logarithmically divergent for energies near $k_B T_K$, thus Fermi's golden rule is a very bad approximation in this regime [38]. Kondo effect is a cross-over phenomenon from $T \ll T_K$ where the electron cloud participating in the Kondo singlet screens the magnetic impurity spin efficiently, hence preventing spin-flip processes, to $T \gg T_K$ where most electrons contributing to electrical transport are too energetic to stay in the Kondo singlet, hence strongly suppressing spin-flip. Both limits $T \ll T_K$ and $T \gg T_K$ have been investigated decades ago [42, 80, 81, 82, 83] and the spin flip rate for the electrons $1/\tau_{\mathrm{sf}}$ was calculated. Very recently, the full dependence of the spin-flip rate on T was derived using numerical renormalization group (NRG) theory [84, 79]. These calculations confirm the high temperature behavior but predict a different result at low T, therefore we give the NRG results and corresponding references when available for each limit:

$$\frac{1}{\tau_{\mathrm{sf}}} = \frac{c_{\mathrm{MI}}}{\pi\hbar\nu_F} \times \begin{cases} \alpha_{\mathrm{lowT}} \dfrac{\pi^4}{6}\left(\dfrac{T}{T_K}\right)^2 & \text{if } T \ll T_K \text{ and } S = 1/2 \text{ [79]} \\ 16\pi^2 \dfrac{S^2 - 1/4}{\ln^2(T/T_K)} & \text{if } T \ll T_K \text{ and } S \geqslant 1 \quad \text{[82]} \\ \alpha_{\mathrm{highT}} \dfrac{\pi^2 S(S+1)}{\pi^2 S(S+1) + \ln^2(T/T_K)} & \text{if } T \gtrsim T_K \quad \text{[79]} \end{cases} \tag{2.35}$$

---

[16] The Kondo temperature is also related to the zero temperature susceptibility by $\chi = (g\mu_B)^2/4T_K$. At $T = 0.94T_K$, the resistance of a diffusive wire has half of its maximal value due to Kondo effect [79].

where $\alpha_{\mathrm{highT}} \approx 0.92$ has been deduced from Fig. 3 in Ref. [79] and $\alpha_{\mathrm{lowT}} \approx 0.927$ is explicitly given in the same reference. Notice that this is only valid if interactions between magnetic impurities can be neglected. We will now investigate when this assumption holds.

Interactions between magnetic impurities

The leading interaction between magnetic impurities in a metal is due to their coupling to the Fermi sea. The interaction between electrons and magnetic impurities tends to deplete the local density of electrons whose spin is aligned with the impurity spin. Therefore, if the distance between magnetic impurities is shorter than the extent of this local ordering of electron spins, an effective interaction takes place between them. This process, called the RKKY interaction, was named after its discoverers [85, 86, 87]. It can lead to a spin-glass transition for the ensemble of magnetic impurities, at a temperature T_{sg} that was calculated in Ref. [83]:

$$T_{\mathrm{sg}} = \frac{4c_{\mathrm{MI}}}{\pi k_B \nu_F \ln^2(v_F c_{\mathrm{MI}}^{1/3}/k_B T_K)} \tag{2.36}$$

In silver, 1 part per million (ppm) of magnetic impurities with a Kondo temperature $T_K \approx 40$ mK gives $T_{\mathrm{sg}} \approx 0.6$ mK. As pointed out in Ref. [83], as long as the probed temperatures are much above T_{sg}, RKKY interaction between impurities is negligible and Eq. (2.35) is valid. Our experiments, in which the lowest temperature was 20 mK and $c_{\mathrm{MI}} < 1$ ppm, were therefore not sensitive to interactions between magnetic impurities. An experiment probing the interplay of RKKY interactions and phase coherence was recently performed [88].

Phase decoherence rate

The spin-flip rate τ_{sf}^{-1} of an electron with magnetic impurities does not enter directly in the expression of τ_φ through a Matthiessen rule because the change in phase on reciprocal paths in the Cooperon can be correlated, depending on the spin configuration. In the beginning of this chapter (section 2.1.1), it is shown that decoherence corresponds to the suppression of interferences between the time-reversal symmetric paths $\circlearrowleft$ and $\circlearrowright$ of the Cooperon. If an electron undergoes a spin-flip on path $\circlearrowleft$, it might also do it on path $\circlearrowright$. But those two events are separated in time, and interferences between both paths depend if the impurity spins have changed between those two events or not. Changes of the spin of impurities occur through spin-flip scattering with all the electrons having an energy within $k_B T$ of the Fermi energy. Consequently, an impurity spin fluctuates with a characteristic time [89], called the Korringa time, which reads[17] $\tau_{\mathrm{Kor}} = \frac{1}{\pi S(S+1)}(J\nu_F)^{-2}\hbar/k_B T$. Depending on the ratio

---

[17] This is just a Fermi's golden rule,

between the Korringa time and the spin-flip time, the related weak localization correction changes.

Fast impurity dynamics ($\tau_{\mathrm{Kor}} \ll \tau_{\mathrm{sf}}$)

The magnetic field created by the magnetic impurities on conjugated paths of the Cooperon is random. Therefore, there is no correlation between the final spins of electrons in each path. Hence, in this case, the spin-flip rate is exactly the dephasing rate $\tau_\varphi^{(\mathrm{e}-\updownarrow)}$:

$$\tau_\varphi^{(\mathrm{e}-\updownarrow,\mathrm{S})} = \tau_\varphi^{(\mathrm{e}-\updownarrow,\mathrm{T})} = \tau_{\mathrm{sf}} \tag{2.38}$$

Slow impurity dynamics ($\tau_{\mathrm{Kor}} \gg \tau_{\mathrm{sf}}$)

The magnetic field created by the magnetic impurities on conjugated paths of the Cooperon is the same on both paths. In the singlet channel, it turns out that, as both electrons participating in the Cooperon travel the field $B(\boldsymbol{r})$ in opposite directions, the rate of destruction of the interferences is doubled compared to the case where the magnetic field is random. In the triplet channel, the contribution turns our to be three times larger [89, 61]:

$$\tau_\varphi^{(\mathrm{e}-\updownarrow,\mathrm{S})} = \tau_{\mathrm{sf}}/2 \tag{2.39}$$

$$\tau_\varphi^{(\mathrm{e}-\updownarrow,\mathrm{T})} = 3\tau_{\mathrm{sf}}/2 \tag{2.40}$$

Intermediate regime

For the same reason as with Coulomb interaction, the triplet term in the dephasing time cannot affect the magnetoresistance since $\tau_{\mathrm{so}} \ll \tau_\varphi^{(\mathrm{e}-\updownarrow,\mathrm{T})}$ for all relevant temperatures. Therefore, we focus on the singlet term only in the following analysis.

As both τ_{sf} and τ_{Kor} depend on temperature, we need to investigate not only the two limiting regimes above, but also the whole dependence of this factor $\eta = \tau_{\mathrm{sf}}/\tau_\varphi^{(\mathrm{e}-\updownarrow,\mathrm{S})}$ on the ratio[18]

$$\tau_{\mathrm{Kor}}/\tau_{\mathrm{sf}} = \frac{c_{\mathrm{MI}}\alpha_{\mathrm{lowT}}}{\nu_F k_B T}. \tag{2.41}$$

$$2\hbar\tau_{\mathrm{Kor}}^{-1} = 2\pi \int \mathrm{d}E J^2 \nu_F^2 S(S+1) f(E)(1-f(E)) \tag{2.37}$$

where $f(E)$ is the Fermi function at temperature T [90, 91]. Taking into account the Kondo effect, one can renormalize the coupling constant J in this expression.

[18] The Kondo effect renormalizes the divergence of the ratio $\tau_{\mathrm{Kor}}/\tau_{\mathrm{sf}}$ at low temperatures. At temperatures $T \lesssim T_K$ [92],

$$\tau_{\mathrm{Kor}}/\tau_{\mathrm{sf}} = \frac{c_{\mathrm{MI}}\alpha_{\mathrm{highT}}}{\nu_F k_B T_K}.$$

In Ref. [89], it is assumed that the magnetic field created by the magnetic impurities has a correlation time τ_{Kor}:

$$\langle B(\boldsymbol{r}, t=0) B(\boldsymbol{r}, t)\rangle \propto \mathrm{e}^{-|t|/\tau_{\mathrm{Kor}}}. \tag{2.42}$$

Replacing $1/\tau_{\mathrm{sf}}$ by $(1+\mathrm{e}^{-|t|/\tau_{\mathrm{Kor}}})/\tau_{\mathrm{sf}}$ in the diffusive equation for the Cooperon, one gets that the Cooperon has just to be replaced by [89]

$$Z_c(t) \leftarrowtail Z_c(t) \exp\left(-\frac{t}{\tau_{\mathrm{sf}}} - \frac{2\tau_{\mathrm{Kor}}}{\tau_{\mathrm{sf}}}\left(1-\mathrm{e}^{-|t|/2\tau_{\mathrm{Kor}}}\right)\right). \tag{2.43}$$

Plugging this formula in Eq. (2.7), one gets[19] a universal behavior for the weak localization correction depending on $\tau_{\mathrm{Kor}}/\tau_{\mathrm{sf}}$. This behavior can be related to an equivalent formulation of the dephasing associated with magnetic impurities by a simple phase decoherence rate $\tau_\varphi^{(\mathrm{e}-\updownarrow,\mathrm{S})}$ given by

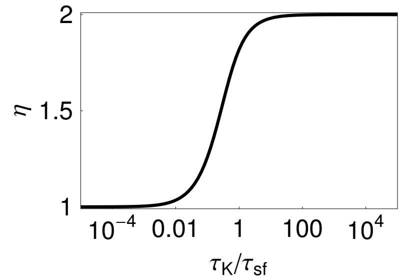

Fig. 2.12. Calculation of the ratio $\eta = \tau_{\mathrm{sf}}/\tau_\varphi^{(\mathrm{e}-\updownarrow,\mathrm{S})}$ depending on the ratio $\tau_{\mathrm{Kor}}/\tau_{\mathrm{sf}}$.

$$\tau_\varphi^{(\mathrm{e}-\updownarrow,\mathrm{S})} = \tau_{\mathrm{sf}}/\eta. \tag{2.44}$$

The dependence of η on the ratio $\tau_{\mathrm{Kor}}/\tau_{\mathrm{sf}}$ is plotted on Fig. 2.12. Numerically, this dependence is well approximated by

$$\eta \approx 1 + \left(1 + 0.22\left(\frac{\tau_{\mathrm{sf}}}{\tau_{\mathrm{Kor}}}\right)^{1.1}\right)^{-1}. \tag{2.45}$$

It can be checked on Fig. 2.12 that both limits described above ($\eta = 1$ and $\eta = 2$) are recovered. Interestingly, the cross-over is not sharp: it extends on nearly two decades of $\tau_{\mathrm{Kor}}/\tau_{\mathrm{sf}}$.

In our experiments, as shown on Fig. 2.13, one has to use the full expression for η as none of the limit regimes applies. Notice that this conclusion contradicts the statements of Refs. [41, 43, 65].

---

[19] Only in the limit where τ_e is much smaller than τ_{sf} and τ_{Kor}. In our experiment, $\tau_e \approx 0.1$ ps, whereas $\tau_{\mathrm{sf}} > 1$ ns, and $\tau_{\mathrm{Kor}} \approx 0.4$ ns at the highest probed temperatures.

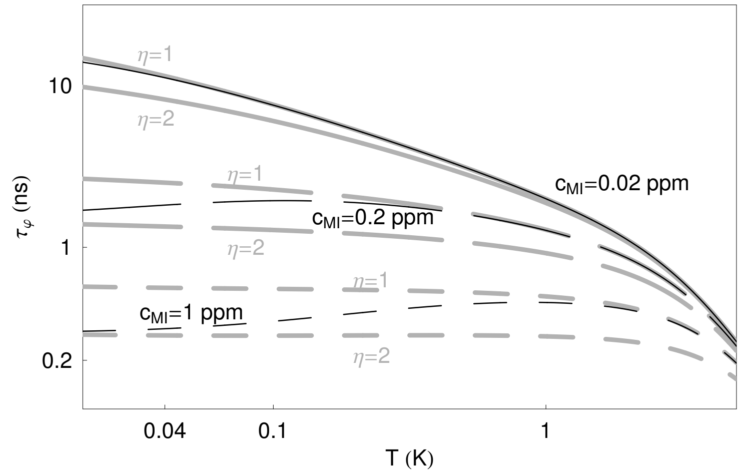

Fig. 2.13. Graph showing the crossover in temperature between the regimes where $\eta = \tau_{\mathrm{sf}}/\tau_\varphi^{(\mathrm{e}-\updownarrow,\mathrm{S})}$ is equal to 1 or 2. The phase coherence times are calculated using Eq. (2.48) with an electron-electron interaction term $A = 0.45\ \mathrm{ns}^{-1}\mathrm{K}^{-2/3}$ and a phonon-electron term $\mathcal{B} = 0.02\ \mathrm{ns}^{-1}\mathrm{K}^{-3}$, similar to the situation in our experiments. The dephasing time $\tau_\varphi^{(\mathrm{e}-\updownarrow,\mathrm{S})}$ represented as a thin black line is calculated using the numerical approximation Eq. (2.45) together with the high temperature limit of Eq. (2.35) for magnetic impurities concentrations $c_{\mathrm{MI}} = 0.02$, 0.2 and 1 ppm (whose properties are those of Mn in Ag, see later for details). For each value of c, two thick grey curves corresponding to $\eta = 1$ of $\eta = 2$ are also plotted.

2.2.4 Summary of the results on phase coherence used in the interpretation of our experiments

Phase coherence manifests itself through a change in resistance around zero magnetic field given by Eq. (2.17)

$$\frac{\Delta R}{R} \equiv \frac{R(B) - R(B=\infty)}{R(B=\infty)} = \frac{R}{R_K}\left(3\xi\left(\Lambda^{(\mathrm{T})}(B)\right) - \xi\left(\Lambda^{(\mathrm{S})}(B)\right)\right) \tag{2.46}$$

with $\xi(x) = x\coth(1/x) - x^2$, $\Lambda^{(\mathrm{T})}$ and $\Lambda^{(\mathrm{S})}$ the triplet and singlet normalized length describing weak localization given by

$$\begin{aligned} \Lambda^{(\mathrm{T})}(B) &= \frac{1}{L}\left(\frac{1}{L_\varphi^2} + \frac{4}{3L_{\mathrm{so}}^2} + \frac{S_e}{3L_B^4}\right)^{-1/2} \\ \Lambda^{(\mathrm{S})}(B) &= \frac{1}{L}\left(\frac{1}{L_\varphi^2} + \frac{S_e}{3L_B^4}\right)^{-1/2} \end{aligned} \tag{2.47}$$

where $L_\varphi = \sqrt{D\tau_\varphi}$, and τ_φ is determined by three different processes Eq. (2.21)

$$\frac{1}{\tau_\varphi} = \frac{1}{\tau_\varphi^{(\mathrm{ee})}} + \frac{1}{\tau_\varphi^{(\mathrm{e-ph})}} + \frac{1}{\tau_\varphi^{(\mathrm{e-}\updownarrow)}} \tag{2.48}$$

with

$$\begin{aligned} 1/\tau_\varphi^{(\mathrm{ee})} &= \frac{1}{\hbar}\left(\frac{\pi k_B^2}{4\nu_F L S_e}\frac{R}{R_K}\right)^{1/3} T^{2/3} \equiv A T^{2/3} \\ 1/\tau_\varphi^{(\mathrm{e-ph})} &= \mathcal{B} T^3 \\ 1/\tau_\varphi^{(\mathrm{e-}\updownarrow)} &= \frac{\eta c_{\mathrm{MI}} \alpha_{\mathrm{highT}}}{\pi \hbar \nu_F} \frac{\pi^2 S(S+1)}{\pi^2 S(S+1) + \ln^2(T/T_K)} \end{aligned} \tag{2.49}$$

where

$$\eta \approx 1 + \left(1 + 0.22\left(\frac{\nu_F k_B T}{c_{\mathrm{MI}}}\right)^{1.1}\right)^{-1},$$

and $\alpha_{\mathrm{highT}} \approx 0.92$ was estimated using NRG theory [79]. The prefactor η takes into account the dynamics of impurity spins, and was omitted in Refs. [41, 43, 65] (see above).

2.3 Experimental results and open questions

2.3.1 Quantitative analysis of the magnetic impurity concentration

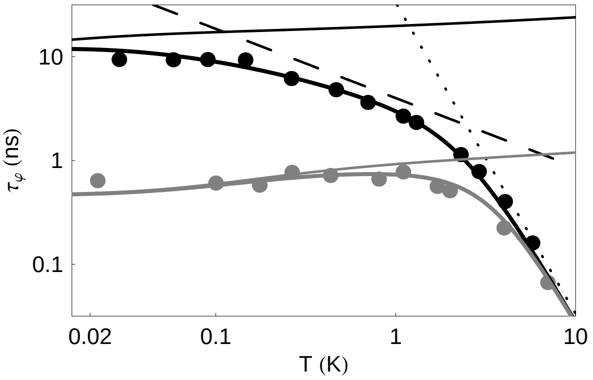

Fig. 2.14. Theoretical phase coherence times due to Coulomb interaction between electrons (dashed line) Eq. (2.25), electron-phonon coupling (dotted line) Eq. (2.33) and spin-flip processes with magnetic impurities (thin line) Eq. (2.49). Dark lines correspond to the bare wire and are fit with a concentration $c_{\mathrm{MI}} = 0.03$ ppm of Mn atoms and light lines correspond to the implanted wire and are fit with $c_{\mathrm{MI}} = 0.65$ ppm. Coulomb term $A = 0.25\ \mathrm{ns}^{-1}K^{-2/3}$ was adjusted to fit with the bare wire $\tau_\varphi(T)$ measurement and is 30% larger than the theoretical expectation from Eq. (2.25). Phonon term $\mathcal{B} = 3.5 \times 10^{-2}\ \mathrm{ns}^{-1}\mathrm{K}^{-3}$ was fit with the part above 1 K for both wires. Besides, the magnetic impurities are assumed to have a Kondo temperature $T_K = 40$ mK and spin $S = 5/2$. Total dephasing time Eq. (2.48) is represented as a thick line.

Using the measured phase coherence times $\tau_\varphi(T)$ on both wires bare and implanted (Fig. 2.9), we find a good overall agreement with the preceding description, as shown on Fig. 2.14.

The Coulomb term A was adjusted to fit with the experimental $\tau_\varphi(T)$ curve corresponding to the bare wire. The fit value, $A = 0.25\ \mathrm{ns}^{-1}K^{-2/3}$, is 30% larger than the theoretical expectation from Eq. (2.25). This disagreement is analyzed in great details in section 3.4.3.

We also can draw a conclusion on the role of magnetic impurities on dephasing. Not only have we analyzed the data of the bare and implanted wires of Fig. 2.9, but we have also reanalyzed on the same footing all the experiments by the collaboration between the Birge group and the Quantronics group that address the effect of magnetic impurities on dephasing (two implanted wires called Ag(5N)c$_{\mathrm{Mn0.3}}$ and Ag(5N)d$_{\mathrm{Mn1}}$, see Table. 2.3) [43, 36, 41]. First, we have better evaluated the concentration of magnetic impurities expected from the implantation procedure (as explained in section 8.4.2). Second, we have again fitted the experimental data taking into account the effect of the Korringa dynamics for the magnetic impurities (see section 2.2.3). The quantitative conclusions are shown on Table 2.3.

Wire name	Ref	$c_{\mathrm{MI}}^{(\mathrm{imp})}$ (ppm)	$c_{\mathrm{MI}}^{(\mathrm{fit})}$ (ppm)
Ag(5N)b	[43]	0	0.13
Ag(5N)$c_{\mathrm{Mn0.3}}$	[43]	0.14	0.25 ± 0.01
Ag(5N)d_{Mn1}	[43]	0.46	0.54 ± 0.03
bare	[65]	0	0.03
implanted	[65]	0.65	0.65 ± 0.07

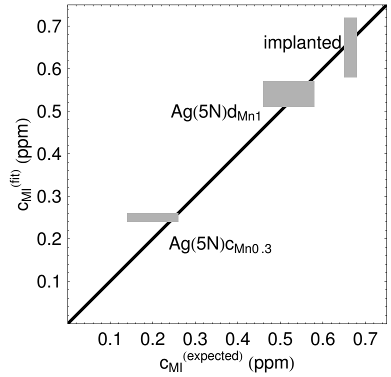

Table 2.3. For each wire, this table shows the fit value of the concentration $c^{(\mathrm{fit})}$ of Mn atoms and the concentration of implanted Mn atoms $c_{\mathrm{MI}}^{(\mathrm{imp})}$. Adding the fit value on the non implanted metals to the implanted concentration, one gets an uncertainty on the expected concentration $c_{\mathrm{MI}}^{(\mathrm{expected})}$ in Mn atoms which is reported on the graph as the width of the corresponding box in the horizontal direction. Uncertainties on the fit values for c_{MI} are reported as the height of the rectangles.

As seen from this table, the theoretical framework described in this chapter accounts quantitatively for the influence of dilute magnetic impurities on the phase coherence. The experiment on the bare and implanted wires alone has a much larger uncertainty on the fitted concentration of magnetic impurities than for the wires discussed in Ref. [43] As explained in section 2.1.6, this is due to the fact that the wires were not very long compared to the phase coherence length.

2.3.2 Which value for the spin S does enter in the spin-flip rate ?

Manganese has a spin $S = 5/2$ in vacuum. However, once located within a bulk metal, its magnetic moment is modified. In silver, the energy levels of the Mn atom lie within the 5s band, and electrons participating in the moment of the impurity are delocalized [93]. The Anderson model gives a first order estimate of the number of electrons effectively contributing to the magnetic moment [94]. Recently, this problem has been revisited in presence of spin-orbit interaction, finite size of the sample and disorder [95].

On the experimental side, the Landé g-factor has been measured for Mn in Ag by electron-paramagnetic-resonance [96], and it was found that $g = 2.010 \pm 0.005$. Using this value, measurements of the susceptibility as a function

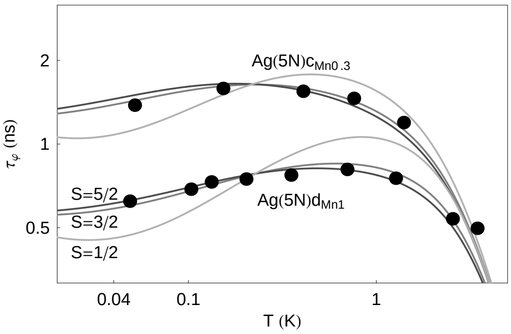

Spin	Ag(5N)c$_{\mathrm{Mn0.3}}$ (ppm)	Ag(5N)d$_{\mathrm{Mn1}}$ (ppm)
1/2	0.33	0.71
3/2	0.26	0.57
5/2	0.25	0.54

Fig. 2.15. Dots: phase coherence time extracted from magnetoresistance measurements on two silver wires implanted with a known amount of Mn impurities (0.14 ppm for Ag(5N)c$_{\mathrm{Mn0.3}}$ and 0.46 ppm for Ag(5N)d$_{\mathrm{Mn1}}$). Lines: the continuous lines are calculated using Eq. (2.48) for two samples and 3 possible values of the spin S with the best fitting parameters reproduced in the table on the right. Notice that in the wire Ag(5N)d$_{\mathrm{Mn1}}$, the phase coherence time decreases when temperature decreases between 1 and 20 mK. Of course, if the Kondo temperature were not so low (40 mK) this decreasing would occur at higher temperatures and would be hidden by Coulomb processes between electrons.

of the temperature in bulk samples of Ag hosting Mn impurities gave, using a fit with a Curie-Weiss law, an estimate of the magnetic moment of those impurities: $S = 2.02$ in Ref. [97] and $S = 2.4$ in Ref. [93].

In our experiments, one may wonder which value of S entering in the theoretical expression for $\tau_\varphi^{(\mathrm{e}-\updownarrow)}$ best accounts for our results[20]. Fits using $S = 3/2$ are actually slightly better than those using $S = 5/2$ as shown on Fig. 2.15. In contrast, $S = 1/2$ is clearly not acceptable. We therefore had no strong indication that another spin value would be more adequate, and kept $S = 5/2$ for the final fits of Fig. 2.14.

2.3.3 Conclusions

We have shown that the standard framework of Al'tshuler, Aronov [1, 2] for the phase coherence time describes quantitatively how the coupling between electrons and dynamic degrees of freedom limits phase coherence. In particular, the role of magnetic impurities with low Kondo temperature is quantitatively understood, as already demonstrated in Ref. [43]. Given the small amount of magnetic impurities needed for getting sizeable effects on phase coherence

---

[20] In the two samples Ag(5N)c$_{\mathrm{Mn0.3}}$ and Ag(5N)d$_{\mathrm{Mn1}}$, theoretical predictions for $\tau_\varphi(T)$ using different values for the spin S are more easily discriminated by the experiment than for the *implanted* wire. Here, we use those data rather than the ones for bare and implanted wires, where the error bars on the phase coherence time are bigger, due to the short length of the wires.

(no commercial metal is guaranteed with so few impurities), it is in practice extremely difficult to emancipate a τ_φ measurement from the possibility that the observed dephasing is due to such impurities.

The main results of this chapter are the following

- Successful measurement of $\tau_\varphi(T)$ on metallic wires as short as 40 μm, despite the difficulties discussed in 2.1.6.
- Quantitative support to the theory of dephasing by Kondo impurities Eq. (2.49), see Fig. 2.14 and Table. 2.3.
- A formalism taking into account the dynamics of the magnetic impurity spins in the calculation of τ_φ (see Fig. 2.13).
- Support to the expression of Ref. [66, 67] for the atomic number dependence of the spin-orbit time (2.15) as shown in Table. 2.1.

Questions remain on the dephasing rate by magnetic impurities at temperatures lower than T_K. It would be interesting to probe a metal in which a small concentration (no spin glass) of magnetic impurities with a higher Kondo temperature are present[21]. In particular, it would be interesting to see how the dephasing time increases at lower temperatures. More is to be done also on the interplay between RKKY interactions between magnetic impurities and dephasing.

In the next chapter, we probe the interactions between electrons and their environment in a different way. In particular, the interactions are probed at much higher energies than in the phase coherence time measurements.

---

[21] Such an experiment is currently being performed by two groups: Birge *et al.* and Saminadayar *et al.* [98, 99]

Chapter 3

Energy relaxation experiments

Contents

We have seen in the last section how the interactions between electrons and dynamic degrees of freedom (other electrons, phonons or magnetic impurities) limit the phase coherence time τ_φ. We now tackle the problem of interactions between electrons from another point of view, by introducing the lifetime of a quasiparticle[1] state τ_E, which is the average decay time of a state at

---

[1] In the following, Laudau quasi-particles are just called electrons as explained in section 1.1

energy E, all other quasi-particles being at equilibrium [2, 100]. Of course, creating a situation with only one excited electron is impossible, and one has to find an indirect way of accessing the information described by τ_E. In 1997, the Quantronics group developed a tunneling spectroscopy method to access the processes allowing the exchange of energy between electrons in diffusive metallic wires [34]. Using this method, one can identify quantitatively the contributions to the lifetime τ_E of each particular interaction between electrons and their environment. In this chapter, we present this tunneling spectroscopy technique and show quantitative measurements of the energy exchange between electrons through three kinds of interaction.

3.1 Semiclassical approach to transport

The phase coherence time τ_φ characterizes a deeply quantum mechanical property of electrons dynamics. By contrast, the electronic lifetime τ_E can be described in a semi-classical way through the Boltzmann equation [101, 1, 9, 102]. Using this picture with a diffusive wire, the population of electrons at energy E and at position x is characterized by the occupation function $f_x(E)$, which results from the balance of three processes. The first one is space diffusion and is described by a standard diffusion term. The second one decreases $f_x(E)$ and corresponds to the decay of an electron at energy E to any other energy state with a rate γ_e. The third one increases $f_x(E)$ and corresponds to the decay of a hole at energy E to any other energy state, with a rate γ_h. For a diffusive wire of length L, and in the reduced length unit x (normalized to L, see Fig 3.1)

$$\frac{\partial f}{\partial t} = \frac{1}{\tau_D}\frac{\partial^2 f}{\partial x^2} - f\gamma_\mathrm{e} + (1-f)\gamma_\mathrm{h} \tag{3.1}$$

where $\tau_D = L^2/D$ is the diffusion time, as defined in section 2.1.1.Explicit dependence on energy E, position x and function f has not been specified in Eq. (3.1) for clarity.

The rates γ_e and γ_h are determined by all the inelastic processes involving electrons. The Boltzmann equation (3.1) can be related to the lifetime τ_E of an electron at energy E. Indeed, assuming that $f(E)$ is a permanent solution of the Boltzmann equation, let us add a single electron at energy E above the Fermi sea. Therefore, $f(E)$ is modified by a small peak function $f(E) \leftarrowtail f(E) + p\delta(E)$. Plugging this into Eq. (3.1), one gets

$$\frac{\partial p}{\partial t} = -p\gamma_\mathrm{e} - p\gamma_\mathrm{h} \tag{3.2}$$

This relates the lifetime τ_E to the rates γ_e and γ_h

$$\tau_E = (\gamma_\mathrm{e} + \gamma_\mathrm{h})^{-1} \tag{3.3}$$

3.2 Link between the distribution function and interactions between electrons

To reveal the rates γ entering the lifetime τ_E, a constant voltage U is applied across a metallic wire in order to drive the electrons out of equilibrium. In this case, f is not trivial, and the Boltzmann equation (3.1) allows to relate f to the rates γ. Besides, f can be measured by tunneling spectroscopy, as described in the next section.

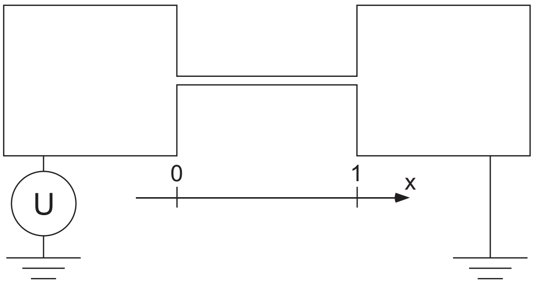

Fig. 3.1. Scheme of a biased metallic diffusive wire.

Since a bias voltage U is applied across the pads, the distribution functions at the edges of the wire are Fermi functions shifted by an energy eU:

$$f_{x=0}(E) = (1 + \mathrm{e}^{(E-eU)/k_BT})\ ;\ f_{x=1}(E) = (1 + \mathrm{e}^{E/k_BT}) \tag{3.4}$$

In case the voltage U is constant, we consider the stationary solution of the Boltzmann equation ($\partial f/\partial t = 0$).

$$\boxed{\frac{1}{\tau_D}\frac{\partial^2 f}{\partial x^2} = f\gamma_{\mathrm{e}} - (1-f)\gamma_{\mathrm{h}}} \tag{3.5}$$

We now solve the Boltzmann equation with the boundary conditions (3.4) in two opposite limits, depending on the ratio τ_E/τ_D.

3.2.1 Weak interaction regime

In the case where $\tau_E \gg \tau_D$, the right term of Eq. (3.5) is negligible and f reads

$$f_x(E) = xf_1(E) + (1-x)f_0(E) \tag{3.6}$$

This can be interpreted in the following way. If $\tau_E \gg \tau_D$, electrons do not change energy during their traversal of the wire, and $f_x(E)$ is given by the average of the Fermi distributions of the two populations of electrons coming

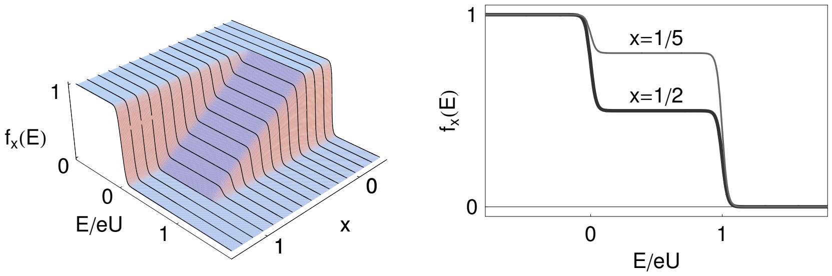

Fig. 3.2. Distribution function $f_x(E)$ without inelastic processes between electrons ("cold electrons" limit) for $eU = 50k_BT$.

from the left or right pad weighted by the probability to find an electron from each population[2]. Hence,

$$f_x(E) = \frac{x}{1 + \mathrm{e}^{E/k_BT}} + \frac{1 - x}{1 + \mathrm{e}^{(E-eU)/k_BT}} \tag{3.7}$$

3.2.2 Strong interaction regime

In the case where $\tau_E \ll \tau_D$, the electrons spend so much time in the wire, that they are involved in multiple inelastic collisions. Therefore, at any position x, a local equilibrium is reached and f_x obeys the statistics of Fermions. This

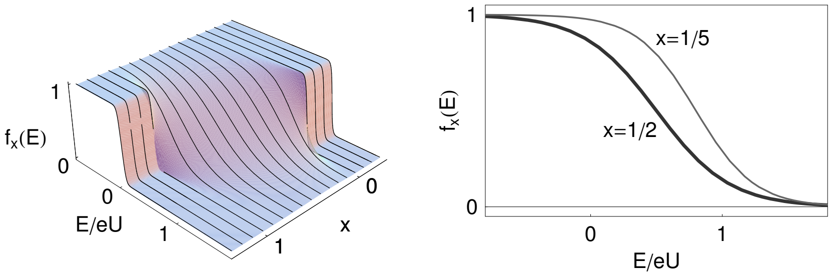

Fig. 3.3. Distribution function $f_x(E)$ with very frequent inelastic processes between electrons ("hot electrons" limit) for $eU = 50k_BT$.

can be found rigorously from the Boltzmann equation, when the rates γ tend

---

[2] Just as does the temperature profile of a metallic rod whose edges are at fixed temperatures.

to infinity, the distribution function f converges to a given function f_{hot}. Therefore, the left side of Eq. (3.5) tends to $\frac{1}{\tau_D}\frac{\partial^2 f_{\mathrm{hot}}}{\partial x^2}$ while the second term has a prefactor which diverges with γ. The only possibility for this is that the right hand side gets close to zero for strong interactions. Besides, a trivial zero of this term at any position x is[3] a Fermi function, whatever the value of γ. Therefore, f_{hot} is close to a Fermi function. As expected from Ohm's law, the electrochemical potential decreases linearly with position from $\mu = eU$ at $x = 0$ to $\mu = 0$ at $x = 1$. The temperature profile $T_{\mathrm{eff}}(x)$ can be found using energy conservation [103]: for each position x, the total exchanged energy $\int [f\gamma_{\mathrm{e}} - (1-f)\gamma_{\mathrm{h}}] E \mathrm{d}E$ is zero, hence $\int (E\partial^2 f_x(E)/\partial x^2)\mathrm{d}E = 0$. Replacing f with a Fermi function whose electrochemical potential is $\mu(x)$ leads to (see B.1.1 in the appendix)

$$\frac{\mathrm{d}^2}{\mathrm{d}x^2}\left(\frac{\pi^2}{6}k_B^2 T_{\mathrm{eff}}(x)^2 + \frac{(1-x)^2}{2}e^2U^2\right) = 0 \tag{3.8}$$

which, associated with the boundary conditions (3.4), gives

$$T_{\mathrm{eff}}(x) = \left[T^2 + (U^2/\mathcal{L})x(1-x)\right]^{1/2} \tag{3.9}$$

where $\mathcal{L} = \frac{1}{3}\left(\frac{\pi k_B}{e}\right)^2 \approx 2.4 \times 10^{-8}$ V^2.K^{-2} is the Lorentz number.

3.2.3 Intermediate regime

In order to probe the rates γ quantitatively, the geometry of the wire must be chosen so that $\tau_D \sim \tau_E$. Only then does the distribution function $f_x(E)$ depend on the inelastic processes between electrons in a non trivial way. We will see in the following how to calculate the rates of the various kinds of interaction between electrons and their environment. But first, we present the numerical tool developed to solve the Boltzmann equation (3.5).

Calculation of the distribution function

We have used and further developed a C++ code written by F. Pierre [36] to solve the Boltzmann equation iteratively, using the steepest descent method. At each step, a trial function $f_x(E)$ is used to calculate the rate

$$\dot{f}_x \equiv \frac{1}{\tau_D}\frac{\partial^2 f_x}{\partial x^2} - f_x\gamma_{\mathrm{e}} + (1-f_x)\gamma_{\mathrm{h}}. \tag{3.10}$$

Using this rate, the trial function $f_x(E)$ is modified using Eq. (3.1)

$$f_x \hookleftarrow f_x + \Delta\tau\dot{f}_x \tag{3.11}$$

---

[3] The right hand side of Eq. (3.5) is exactly zero at equilibrium when $U = 0$, because, in this case, the left term is zero.

where $\Delta\tau$ is a tunable time step. The process starts with the solution for cold electrons (3.7) and ends when f_x does not evolve noticeably from step to step at any position x. This code has been improved, in order to include the many effects described in what follows. Lately, we embedded it into a fit algorithm using the simplex method [104] in order to fit experimental data.

3.3 Measurement of the distribution function by tunneling spectroscopy

In order to probe the distribution function, a tunnel junction is fabricated at a position x of the wire, in series with an aluminum wire (called the *probe* in the following) of impedance $Z(\omega)$ in its non-superconducting state. In the following, we show that the probe has a singular tunneling density of states both in the superconducting regime (due to superconducting gap) and in the normal regime (due to the dynamical Coulomb blockade of tunneling). The sharpness of this singularity sets the resolution of the spectroscopy on $f(E)$.

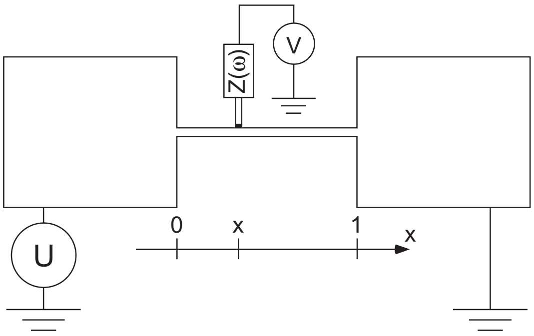

Fig. 3.4. Scheme of the biased metallic wire. A tunnel junction in series with an impedance $Z(\omega)$ sits at position x of the wire. See Fig. 9.4 to see an SEM picture of such a device.

3.3.1 Tunneling rate in case of a superconducting probe

The tunneling rate can be calculated through the Fermi's golden rule, assuming that the tunneling matrix elements are nearly constant on all energy states that matter for conductance measurement[4].

---

[4] The tunneling matrix elements vary on the same energy scale as the band structure at the interface between the electrode and the dielectric, therefore at the scale of the work function W. However, states participating to transport have an energy centered on E_F and sit in a bandwidth $\max(k_BT, eV)$ where V is the

In case the probe is superconducting, tunneling is elastic[5] because no energy can be dissipated in the electromagnetic environment. The total tunneling rate from the wire (x) to the probe (p) at energy[6] E, calculated by a golden rule, then reads

$$\Gamma_{x\to \mathrm{p}}(E) = \frac{1}{e^2 R_t} n_x(E) f_x(E) n_\mathrm{p}(E+eV)(1-f_\mathrm{p}(E+eV)) \tag{3.12}$$

where n_i is the density of states of the electrode i normalized to its bulk metallic value, and R_t ends up to just be the tunnel resistance. Similarly,

$$\Gamma_{\mathrm{p}\to x}(E) = \frac{1}{e^2 R_t} n_\mathrm{p}(E+eV) f_\mathrm{p}(E+eV) n_x(E)(1-f_x(E)) \tag{3.13}$$

Therefore, the total current across the tunnel junction reads

$$\begin{aligned} I(V) &= e\int (\Gamma_{x\to \mathrm{p}}(E) - \Gamma_{\mathrm{p}\to x}(E))\mathrm{d}E \\ &= \frac{1}{eR_t}\int n_x(E) n_\mathrm{p}(E+eV)(f_x(E) - f_\mathrm{p}(E+eV))\mathrm{d}E \end{aligned} \tag{3.14}$$

If f is a Fermi function, and if electrodes have constant density of states, one recovers the definition of the tunnel resistance R_t as stated above: $I(V) = V/R_t$.

Simplifying the current-voltage expression using the BCS density of states $n_\mathrm{BCS}(E) = \mathrm{Re}\left(\frac{|E|}{\sqrt{E^2-\Delta^2}}\right)$ with Δ the superconductor's gap, the tunneling current reads

$$I(V) = \frac{1}{eR_t}\int n_\mathrm{BCS}(E+eV)(f_x(E) - f_\mathrm{p}(E+eV))\mathrm{d}E. \tag{3.15}$$

Changing of variables $E \leftarrow E - eV$ and derivating $I(V)$ with respect to V, the conductance reads[7]

$$\frac{\mathrm{d}I}{\mathrm{d}V} = -\frac{1}{R_t}\int n_\mathrm{BCS}(E) f_x'(E-eV)\mathrm{d}E \tag{3.16}$$

and using both integration by part and the fact that n_BCS is even,

$$R_t \frac{\mathrm{d}I}{\mathrm{d}V} = 1 - \int n_\mathrm{BCS}'(eV-E) f_x(E)\mathrm{d}E \equiv 1 - n_\mathrm{BCS}' * f_x(eV) \tag{3.17}$$

where $*$ denotes the convolution product. We thus use the following procedure (see Figs. 3.5, 3.6) to measure $f_x(E)$:

---

voltage across the tunnel junction. As $\max(k_B T, eV) \ll W \approx E_F$, the coupling between electrodes on those states is nearly constant.

[5] Elastic tunneling means tunneling at constant energy

[6] The origin of energies being the Fermi energy in the wire at position 0

[7] In practice, f_p depends sometimes on the voltage V, and this simplification is not valid. Thus, this assumption has to be checked for each particular case. On the experiment discussed later in this chapter, this assumption is wrong, and it is more difficult to extract $f_x(E)$ from the tunneling conductance measurements.

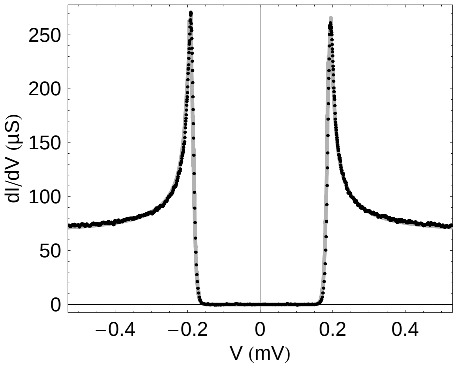

Fig. 3.5. Dots: differential conductance of a tunnel junction located at position $x = 0.25$ of the wire denoted by AgXII40 at a bias voltage $U = 0$ (see details of fabrication on page 87). Line: theoretical prediction for the same quantity using Eq. (3.17) with a gap $\Delta = 188$ μeV , a tunnel conductance $G_t = 1/R_t = 66.7$ μS and a temperature $T = 45$ mK (the energy was multiplied by a factor $(1+i\gamma)$ where $\gamma = 5 \times 10^{-5}$ to have the calculation converge). The line is well approximated by the exact BCS density of states times G_t.

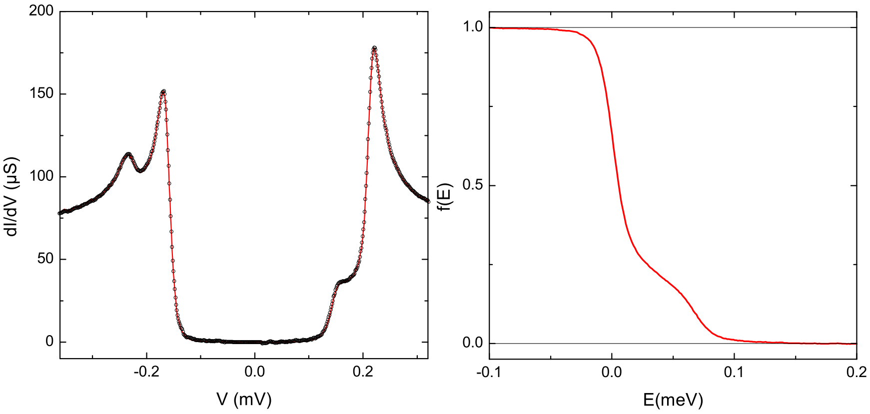

Fig. 3.6. Left panel–dots: differential conductance of the same tunnel junction as in Fig. 3.5, with a bias voltage $U = 71$ μV applied to the wire. Left panel–line: best fit using Eq. (3.17) where the BCS density of states n_{BCS} and the tunnel conductance G_t are deduced from the fit of Fig. 3.5. The corresponding distribution function in the wire $f_{x=0.25}(E)$ is plotted on the right panel.

- applying zero bias voltage $U = 0$ across the wire, we know that for all position x, f_x is a Fermi function at temperature T. Therefore, we can fit the gap Δ, the tunneling resistance R_t and the electron temperature T using Eq. (3.17).
- applying a finite voltage U across the wire, we can use the previous fit of Δ and R_t to calculate the function $f_x(E)$ through a numerical deconvolution of the conductance (3.17).

3.3.2 Tunneling rate in case of a resistive probe

Dynamical Coulomb blockade of tunneling

When a magnetic field larger than the critical field of the superconductor is applied, the impedance $Z(\omega)$ of the probe becomes non zero even at low energy, and inelastic electron tunneling cannot be neglected. In a semiclassical picture, after the tunneling of an electron, a positive charge is left behind on the starting electrode and a negative charge is created on the ending electrode. These charges disturb the electrons in the leads, and induce charge propagation. Dynamics of the propagation is controlled by the electromagnetic impedance $Z(\omega)$. The standard theory of dynamical Coulomb blockade [105, 106] deals with this problem. Within this picture, a tunneling electron can loose an energy $\hbar\omega$ when tunneling by emitting a photon which is absorbed by the impedance $Z(\omega)$. The frequency dependence of the impedance determines the selection in energy of the emitted photons. The corresponding

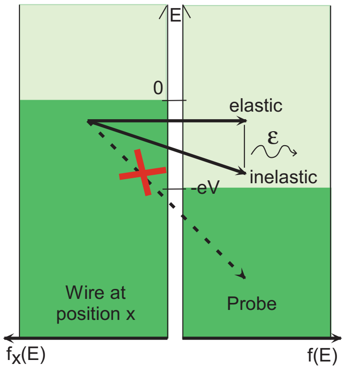

Fig. 3.7. Tunneling in semiconductor representation. The dark areas represent the occupied electron states. Depending on the energy ε dissipated in the impedance $Z(\omega)$, electrons tunneling from the wire with energy E end in the probe in a state of energy $E-\varepsilon$. The tunneling events are blocked by Pauli principle if the energy ε is too big (dashed line).

modification of the tunneling current is then entirely described by the probability $P(\varepsilon)$ for the environment to absorb a photon at energy ε. The tunneling current at energy E is then given, in case of non-superconducting electrodes, by

$$\begin{aligned} I_E(V) = \frac{1}{eR_t} \int & \mathrm{d}\varepsilon P(\varepsilon) \\ & \times \left[f_x(E)(1 - f_{\mathrm{p}}(E + eV - \varepsilon)) - (1 - f_x(E)) f_{\mathrm{p}}(E + eV + \varepsilon)\right] \end{aligned} \tag{3.18}$$

and the derivative of the total current reads[8]

$$\frac{\mathrm{d}I}{\mathrm{d}V}(V) = \frac{1}{R_t} + \frac{1}{R_t} \int \mathrm{d}E \int \mathrm{d}\varepsilon P(\varepsilon) f_x(E) \left[f'_{\mathrm{p}}(E + eV + \varepsilon) - f'_{\mathrm{p}}(E + eV - \varepsilon)\right]. \tag{3.19}$$

Hence,

$$\boxed{R_t \frac{\mathrm{d}I}{\mathrm{d}V}(V) = 1 - \int f_x(E) q_T(-eV - E) \mathrm{d}E = 1 - q_T * f_x(-eV)} \tag{3.20}$$

with $q_T(E)$ a function depending on the environment at temperature T

$$q_T(E) = \int \mathrm{d}\varepsilon P(\varepsilon) \left[f'_{\mathrm{p}}(-\varepsilon - E) - f'_{\mathrm{p}}(\varepsilon - E)\right]. \tag{3.21}$$

Derivation of $P(\varepsilon)$: a perturbative approach

In the simple case of zero temperature, we present here a perturbative derivation of $P(\varepsilon)$. Tunneling events are delta-correlated in time and thus, the current is approximately

$$I(t) = e \sum_i \delta(t - t_i) \tag{3.22}$$

and the energy dissipated in the impedance $E = \int \mathrm{d}t V(t) I(t)$ when one electron tunnels at time $t = 0$ (the corresponding current being $I(t) = e\delta(t)$) is just

$$E = eV(t = 0) = \int \mathrm{d}\omega \frac{e}{2\pi} \tilde{V}(\omega) \tag{3.23}$$

Using the Ohm's law $U(\omega) = Z(\omega) I(\omega)$ and the fact that $\tilde{I}(\omega) = e$,

$$E = \frac{e^2}{\pi} \int_0^{+\infty} \mathrm{d}\omega \mathrm{Re}[Z(\omega)] \tag{3.24}$$

By identification of terms at identical energies $\varepsilon = \hbar\omega$ with the expression

$$E = \int_0^{+\infty} P(\varepsilon) \varepsilon \mathrm{d}\varepsilon, \tag{3.25}$$

the probability $P(\varepsilon) = \delta E / \varepsilon$ to emit a photon of energy ε is just

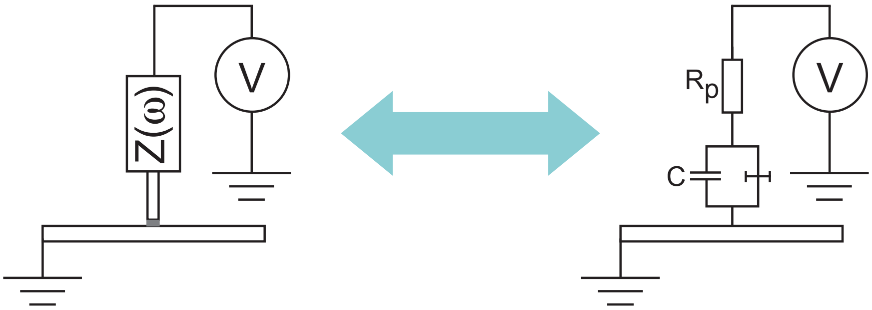

Fig. 3.8. Model for the environment of the tunnel junction in the experiment. The equivalent impedance is $Z(\omega) = R_p/(1 + iR_pC\omega)$, neglecting the wire resistance compared to R_p.

$$P(\varepsilon) = \frac{2}{\varepsilon} \frac{\mathrm{Re}[Z(\omega = \varepsilon/\hbar)]}{R_K} \tag{3.26}$$

In order to apply this theory to our experiment, the environment of the junction is modeled by an R-C circuit as schemed on Fig. 3.8. We neglect the contribution of the wire resistance compared to R_p since $R_p \approx 1$ kΩ and $R \approx 55$ Ω. Approximately,

$$P(\varepsilon) = \begin{cases} 2R_p/\varepsilon R_K & \text{if } \varepsilon < \hbar/R_pC \\ 0 & \text{if } \varepsilon > \hbar/R_pC \end{cases} \tag{3.27}$$

Using Eq. (3.19) in the case where the distribution functions f_x and f_p are Fermi functions shifted by the voltage bias eV at zero temperature, one gets the following expression for the conductance:

$$R_t \frac{\mathrm{d}I}{\mathrm{d}V}(V) = 1 - \int_{eV}^{+\infty} P(\varepsilon)\mathrm{d}\varepsilon \approx 1 + 2R_p/R_K \ln\left(V/V_0\right) \tag{3.28}$$

where $V_0 = \hbar(eR_pC)^{-1}$.

Full calculation of $P(\varepsilon)$

The non-perturbative calculation of $P(\varepsilon)$ at finite temperature T is given in Ref. [107] and reads

$$P(\varepsilon) = \int \frac{\mathrm{d}t}{h} \mathrm{e}^{J(t)+i\varepsilon t/\hbar} \tag{3.29}$$

where

$$J(t) = \int \frac{\mathrm{d}\omega}{\omega} \frac{2\mathrm{Re}[Z(\omega)]}{R_K} \frac{\mathrm{e}^{-i\omega t} - 1}{1 - \mathrm{e}^{-\hbar\omega/k_BT}} \tag{3.30}$$

---

[8] using $\int f'(E)\mathrm{d}E = -1$ and $\int P(\varepsilon)\mathrm{d}\varepsilon = 1$

In the R-C model depicted above and assuming $R_p \ll R_K$, the non-perturbative result reads

$$R_t \frac{\mathrm{d}I}{\mathrm{d}V}(V) \propto V^{2R_p/R_K} \tag{3.31}$$

for $k_B T < eV < \hbar/R_p C$ (for more details, see Ref. [41]). In our experiment, this behavior is found when $U = 0$. Fig. 3.9 is a plot of the tunnel conductance for the sample *bare wire*, compared to the theoretical prediction using Eq. (3.20) with $C = 4.4$ fF, $R_p = 0.96$ kΩ and $T = 50$ mK.

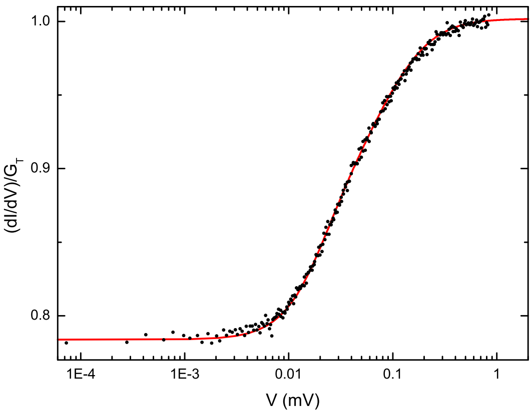

Fig. 3.9. Dots: dynamical conductance of the NIN junction formed between the bare wire and the probe in the normal state. Using Eq. (3.19, 3.29), the best parameters for the junction and its environment are a tunnel resistance $R_t = 16.45$ kΩ, a probe resistance $R_p = 0.96$ kΩ, a capacitance $C = 4.4$ fF and a temperature $T = 50$ mK. The corresponding theoretical curve is plotted as a line.

Application to the spectroscopy of $f(E)$

Fig. 3.10 shows the dynamical conductance measured with a finite bias voltage U. One might want to deconvolve this curve using Eq. (3.20) to access the distribution function $f(E)$ just as in the superconducting case. In practice, this procedure is hard to implement here as the conductance peak is far less sharp than the BCS anomalies at the gap. Moreover, the conductance of the tunnel junction in case of a resistive probe depends on more parameters than in the superconducting case (where only the gap and the tunneling resistance were free). In particular, the electrons in the probe can heat up. Therefore, we use the following strategy, in order to analyze the conductance at any bias U:

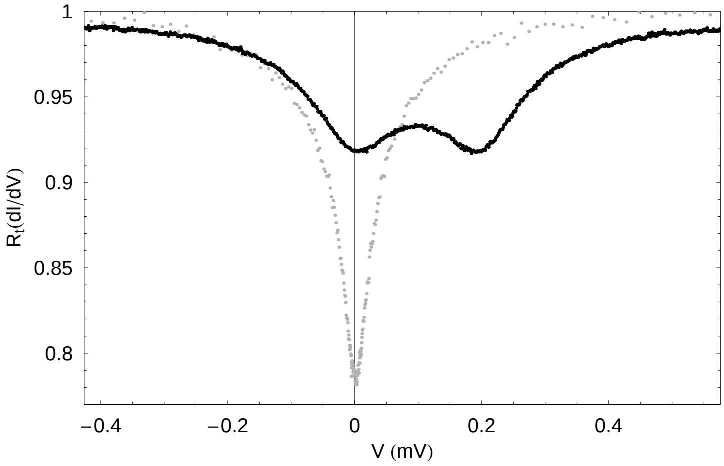

Fig. 3.10. Dynamical conductance of the NIN junction formed between the bare wire and the probe in the normal state at $U = 0$ (gray dots) and at $U = 200$ μV (black dots) for a magnetic field $B = 0.9$ T.

- At $U = 0$, the distribution function in the wire is a Fermi function $f_x(E) = (1 + \mathrm{e}^{E/k_BT_0})^{-1}$. Using Eq. (3.20), one deduces the function $q_{T_p}(E)$ from the measurement of the conductance at $T_p = T_0$, with a slight smearing on the scale of k_BT_0:

$$q_{T_0}(eV) \approx \frac{R_T}{e}\frac{\mathrm{d}^2I}{\mathrm{d}V^2}(V) \tag{3.32}$$

- In order to analyze the conductance $\mathrm{d}I/\mathrm{d}V$ measured at $U \neq 0$, the previously determined function $q_{T_0}(eV)$ is used in Eq. (3.20). Comparison between theory and experiment are made directly on the conductance curves.

Some important deviations to this simple picture must also be taken into account, and are listed in the following sections.

Parasitic effects

Heating of the pads

When a finite bias voltage U is applied across the wire, some energetic electrons flow through the pads and heat them. The boundary condition of the Boltzmann equation are thus modified. Besides, the thinner the pads, the more efficient this heating. In our experiments, the pads are as thin as the wire, and this effect is important. In a simple model, the pads are assumed to be infinite semi-planes. When applying a bias voltage U across the wire, a power U^2/R is dissipated in the pads. The excited electrons spread on a given distance R_M from the wire, which is given by the cooling process due to phonons or by incoming cold electrons from the bonding wires. Solving the heat equation in the pads, in a radial geometry, one finds the temperature profile [36]

$$T_e(r) = \sqrt{T_0^2 + (\alpha U)^2 \ln(R_M/r)} \tag{3.33}$$

where $\alpha = \frac{R_\square}{R}\frac{3e^2}{\pi^3 k_B^2}$ is a coupling constant, with $R_\square$ the resistance per square of the pads (typically around 0.5 Ω), and r the distance measured from the end of the wire. The temperature entering in the boundary conditions for the Boltzmann equation in the wire can be obtained by setting r to the width w of the wire. In practice, $\alpha^2 \ln(R_M/w)$ is determined experimentally as a fit parameter, as neither R_M nor $R_\square$ are actually measured [13].

Heating of the probe

When the wire or the probe are biased, the electrons of the probe are driven out of equilibrium. In this case, the function q_T entering in the calculation of the conductance is not the function q_{T_0} measured at equilibrium. The non-perturbative calculation of $P(\varepsilon)$ at finite temperature presented above can be used to determine a more appropriate q function. However, this calculation is so cumbersome that we used a numerical approximation. It turns out that, in our range of temperatures, the function q_{T_p} is well approximated by

$$q_{T_p}(E) \approx -\int q_{T_0}(E+\varepsilon) f'_{T_p}(\varepsilon)\mathrm{d}\varepsilon \tag{3.34}$$

where $f_{T_p}(\varepsilon) = (1 + \mathrm{e}^{\varepsilon/k_B T_p})^{-1}$ is the Fermi function of temperature T_p.

The temperature T_p still needs to be calculated for each bias voltages U and V. Actually there is no reason why the electrons in the probe should have a Fermi distribution function, since hot electrons are injected directly from the wire to the probe. However, an effective temperature T_p can still be defined out of equilibrium. Considering a distribution function $f_p(E)$ for the electrons at the probe/tunnel junction interface, T_p is defined by the temperature of the Fermi function for which the total electronic energy is the same:

$$(\pi k_B T_p)^2/6 = \int_{eV}^{\infty} (E - eV) f_p(E)\mathrm{d}E + \int_{-\infty}^{eV} (eV - E)(1 - f_p(E))\mathrm{d}E.$$

Besides $f_p(E)$ can be deduced from the conservation of the current density $i(E)$ at energy E. Across the tunnel junction,

$$i(E) = (f_p(E) - f(E))/eR_T$$

and across the whole aluminum probe resistor,

$$i(E) = \{(1 + \exp[(E - eV)/k_B T_0])^{-1} - f_p(E)\}/eR_N.$$

Those two quantities are identical so $f_p(E)$ is directly linked to $f(E)$ in the middle of the wire[9].

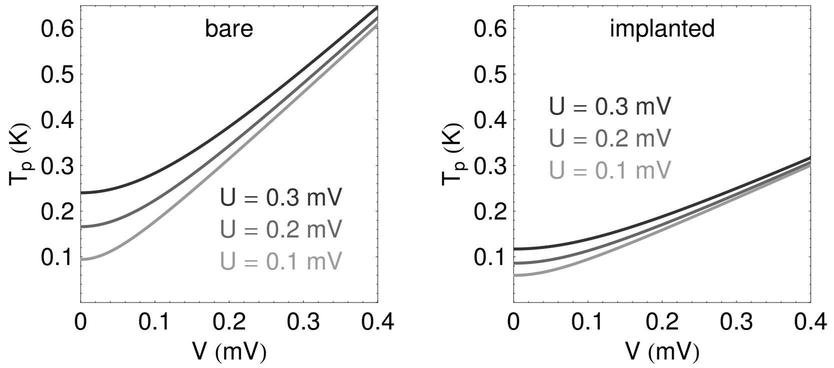

Fig. 3.11. Calculated probe temperature T_p as a function of V for both wires and various bias voltages U. Whereas both wires were fabricated altogether, the probe wire and junction were different because obtained in a separate step (see section 3.4.6) leading to different values of T_p for both wires.

We have compared the value of T_p obtained for the two limiting cases:

- assuming that there are no interaction between electrons in the wire (Fig. 3.2), the distribution function in the wire reads
$$f_{x=1/2}(E) = f_{T_0}(E - eU/2)/2 + f_{T_0}(E + eU/2)/2.$$
- assuming that the hot electron regime takes place (Fig. 3.3),
$$f(E) = f_{T_{\rm eff}}(E)$$
where $T_{\rm eff}^2 = T_0^2 + \frac{3}{4\pi^2}(eU/k_B)^2$.

For each value of the bias voltage U and for all V, the calculation in both limits leads to values of T_p differing by less than 1 mK. Therefore, the final value of T_p does not depend on the precise shape of the function $f(E)$ in the wire. The results of this calculation are reported on Fig 3.11 for the bare and implanted wires.

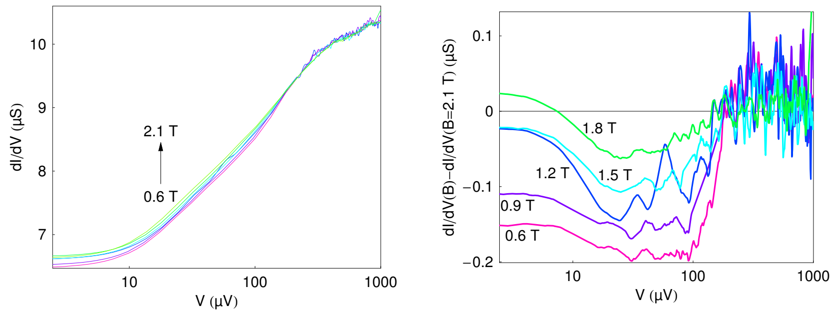

Fig. 3.12. Left panel: Dynamical conductance of the tunnel junction in the implanted wire sample as a function of the bias voltage V, for various magnetic fields B. Right panel: difference between the curves on the left panel and the conductance at $B = 2.1$ T.

Unexpected dependence on magnetic field of the equilibrium tunnel conductance

In the implanted wire, an unexpected effect was observed: at voltages V below 200 μV, the conductance at equilibrium ($U = 0$) increases with magnetic field. On Fig. 3.12, the conductance is shown for several values of magnetic field.

We did not find any satisfactory explanation for this behavior, in particular, none of the possible explanations account for the magnetic field constant threshold in voltage at 0.2 mV.

3.4 Inelastic processes limiting the lifetime of electrons

In this section, we present the theoretical framework used to derive the rates of all identified inelastic processes between electrons and their environment.

3.4.1 Coulomb interaction between electrons

Screened interaction

As already stated in section 1.1.1, electrons rearrange dynamically in metals so that the Coulomb interaction is partially screened. Therefore, one can change from the basis of Bloch states to a basis of weakly interacting quasi-particles.

---

[9] The last equation is valid when electron-electron interactions are negligible in the probe, which might not be the case. Yet, the final answer depends on the total heat flux only, and thus any assumption on the precise distribution of the currents $i(E)$ leads to the same result.

If this rearrangement is assumed instantaneous, the Coulomb interaction between quasi-particles can be evaluated using the approximation of Thomas-Fermi [29] leading to a potential $U(\boldsymbol{r}-\boldsymbol{r'}) = \frac{e^2}{4\pi\epsilon_0|\boldsymbol{r}-\boldsymbol{r'}|}\mathrm{e}^{-\kappa_s|\boldsymbol{r}-\boldsymbol{r'}|}$ where the inverse screening length κ_s is given by $\kappa_s^2 = e^2\nu_F/\epsilon_0$, and whose spatial Fourier transform reads $U(\boldsymbol{q}) = \frac{e^2}{4\pi\epsilon_0(q^2+\kappa_s^2)}$. In a diffusive metal, the response of electrons to a change in potential is not instantaneous so that the Coulomb potential becomes time dependent and reads $U(\boldsymbol{q},\hbar\omega) = \frac{e^2}{4\pi\epsilon_0 q^2}\frac{-i\omega+Dq^2}{-i\omega+Dq^2+D\kappa_s^2}$ which simplifies, for $ql_e \ll 1$, into [1, 61]

$$U(\boldsymbol{q},\hbar\omega) \approx \frac{1}{\nu_F}\frac{-i\omega+Dq^2}{Dq^2}. \tag{3.35}$$

Notice that this is the dynamic potential that was used in Eq. (2.22) in order to calculate the dephasing time due to Coulomb interaction between electrons.

Kernel of Coulomb interaction

The rates $\gamma_{\mathrm{e}}^{(\mathrm{ee})}(E)$ and $\gamma_{\mathrm{h}}^{(\mathrm{ee})}(E)$ associated with Coulomb interaction between electrons are obtained at first order using Fermi's golden rule:

$$\gamma_{\mathrm{e}}^{(\mathrm{ee})}(E) = 2\frac{2\pi}{\hbar\Omega\nu_F}\overline{\sum_{\alpha}\delta(E_\alpha - E)\sum_{\beta\gamma\rho}|\langle\alpha\beta|U|\gamma\rho\rangle|^2\delta(E_\alpha + E_\beta - E_\gamma - E_\rho)} \tag{3.36}$$

where α, β cover all the occupied electronic states, and γ, ρ cover all the unoccupied electronic states, Ω is the volume of the metal and $\overline{x}$ represents the average value of a quantity x on all disorder configurations (see section 2.1.1). A factor 2 accounts for spin degeneracy so that we omit spin indices in the following. Using the distribution function of the occupied electronic states $f(E)$, the rate simplifies into

$$\begin{aligned}\gamma_{\mathrm{e}}^{(\mathrm{ee})}(E) = {} & \tfrac{4\pi}{\hbar\Omega\nu_F}\overline{\textstyle\sum_\alpha \delta(E_\alpha - E)\times} \\ & \overline{\textstyle\sum_{\beta\gamma\rho} f(E_\beta)(1-f(E_\gamma))(1-f(E_\rho))|\langle\alpha\beta|U|\gamma\rho\rangle|^2\delta(E_\alpha + E_\beta - E_\gamma - E_\rho)}\end{aligned} \tag{3.37}$$

where, from now on, the sums extend on all states, occupied or not. Using the fact that $f(E_\mu) = \int \mathrm{d}E' f(E')\delta(E' - E_\mu)$ for all energy E_μ and function f,

$$\boxed{\begin{aligned}\gamma_{\mathrm{e}}^{(\mathrm{ee})}(E) = \textstyle\int_{-\infty}^{+\infty} & \mathrm{d}E' \textstyle\int_{-\infty}^{+\infty} \mathrm{d}\varepsilon K_{\mathrm{tot}}(\varepsilon, E, E') \\ & \times\ f(E')(1-f(E-\varepsilon))(1-f(E'+\varepsilon))\end{aligned}} \tag{3.38}$$

where $K_{\mathrm{tot}}(\varepsilon, E, E')$ is the interaction Kernel and is given by

$$\begin{aligned}K_{\mathrm{tot}}(\varepsilon, E, E') = {} & \tfrac{4\pi}{\hbar\Omega\nu_F} \\ & \times\overline{\textstyle\sum_{\alpha\beta\gamma\rho}\delta(E_\alpha - E)\delta(E_\beta - E')\delta(E_\gamma - E + \varepsilon)\delta(E_\rho - E' - \varepsilon)|\langle\alpha\beta|U|\gamma\rho\rangle|^2}\end{aligned} \tag{3.39}$$

Similarly for hole particles,

$$\gamma_{\mathrm{h}}^{(\mathrm{ee})}(E) = \int_{-\infty}^{+\infty} \mathrm{d}E' \int_{-\infty}^{+\infty} \mathrm{d}\varepsilon f(E') f(E+\varepsilon)(1-f(E'+\varepsilon)) K_{\mathrm{tot}}(\varepsilon, E, E') \tag{3.40}$$

Calculation of the kernel of Coulomb interaction between electrons

Taking into account the selection on energy of the states α, β, γ and ρ, and introducing the basis of position states $|\boldsymbol{r}\rangle$ in $\langle\alpha\beta|U|\gamma\rho\rangle$, one gets two terms

$$\langle\alpha\beta|U|\gamma\rho\rangle = \int \mathrm{d}\boldsymbol{r}\mathrm{d}\boldsymbol{r'}\langle\alpha|\boldsymbol{r}\rangle\langle\beta|\boldsymbol{r'}\rangle U(\boldsymbol{r}-\boldsymbol{r'},\varepsilon)\langle\boldsymbol{r}|\gamma\rangle\langle\boldsymbol{r'}|\rho\rangle \tag{3.41}$$

At this point, it is convenient to introduce the non-local density of states $\rho_{\boldsymbol{r_1},\boldsymbol{r_2}}(E) = \sum_\alpha \langle\alpha|\boldsymbol{r_1}\rangle\langle\boldsymbol{r_2}|\alpha\rangle\delta(E-E_\alpha)$ to simplify the kernel into [61]

$$\begin{aligned} K_{\mathrm{tot}}(\varepsilon, E, E') = \tfrac{4\pi}{\hbar\Omega\nu_F} \textstyle\int \mathrm{d}\boldsymbol{r_1}\, \mathrm{d}\boldsymbol{r'_1}\mathrm{d}\boldsymbol{r_2}\mathrm{d}\boldsymbol{r'_2} U(\boldsymbol{r_1}-\boldsymbol{r'_1},\varepsilon)U(\boldsymbol{r'_2}-\boldsymbol{r_2},\varepsilon) \\ \times\overline{\rho_{\boldsymbol{r_1},\boldsymbol{r_2}}(E)\rho_{\boldsymbol{r'_1},\boldsymbol{r'_2}}(E')\rho_{\boldsymbol{r_2},\boldsymbol{r_1}}(E-\varepsilon)\rho_{\boldsymbol{r'_2},\boldsymbol{r'_1}}(E'+\varepsilon)} \end{aligned} \tag{3.42}$$

And expanding the correlator by the Wick theorem,

$$K_{\mathrm{tot}}(\varepsilon, E, E') = \mathcal{K}_{\mathrm{Fock}}^{\mathrm{charge}}(\varepsilon, E, E') + \mathcal{K}_{\mathrm{Hartree}}^{\mathrm{charge}}(\varepsilon, E, E') \tag{3.43}$$

where

$$\begin{aligned} \mathcal{K}_{\mathrm{Fock}}^{\mathrm{charge}}(\varepsilon, E, E') &= \tfrac{4\pi}{\hbar\Omega\nu_F} \textstyle\int \mathrm{d}\boldsymbol{r_1}\mathrm{d}\boldsymbol{r'_1}\mathrm{d}\boldsymbol{r_2}\mathrm{d}\boldsymbol{r'_2}\overline{\rho_{\boldsymbol{r_1},\boldsymbol{r_2}}(E)\rho_{\boldsymbol{r_2},\boldsymbol{r_1}}(E-\varepsilon)} \\ &\times U(\boldsymbol{r_1}-\boldsymbol{r'_1},\varepsilon)U(\boldsymbol{r'_2}-\boldsymbol{r_2},\varepsilon)\overline{\rho_{\boldsymbol{r'_1},\boldsymbol{r'_2}}(E')\rho_{\boldsymbol{r'_2},\boldsymbol{r'_1}}(E'+\varepsilon)} \\ \mathcal{K}_{\mathrm{Hartree}}^{\mathrm{charge}}(\varepsilon, E, E') &= \tfrac{4\pi}{\hbar\Omega\nu_F} \textstyle\int \mathrm{d}\boldsymbol{r_1}\mathrm{d}\boldsymbol{r'_1}\mathrm{d}\boldsymbol{r_2}\mathrm{d}\boldsymbol{r'_2}\overline{\rho_{\boldsymbol{r_1},\boldsymbol{r_2}}(E)\rho_{\boldsymbol{r'_2},\boldsymbol{r'_1}}(E'+\varepsilon)} \\ &\times U(\boldsymbol{r_1}-\boldsymbol{r'_1},\varepsilon)U(\boldsymbol{r'_2}-\boldsymbol{r_2},\varepsilon)\overline{\rho_{\boldsymbol{r'_1},\boldsymbol{r'_2}}(E')\rho_{\boldsymbol{r_2},\boldsymbol{r_1}}(E-\varepsilon)} \end{aligned} \tag{3.44}$$

Fock term

The correlator $\overline{\rho_{\boldsymbol{r_a},\boldsymbol{r_b}}(E)\rho_{\boldsymbol{r_b},\boldsymbol{r_a}}(E')}$ can be expressed for $|\boldsymbol{r_a}-\boldsymbol{r_b}| \gg l_e$ in the diffusion approximation as [61]

$$\overline{\rho_{\boldsymbol{r_a},\boldsymbol{r_b}}(E)\rho_{\boldsymbol{r_b},\boldsymbol{r_a}}(E')} = \frac{\nu_F}{h}\int \frac{\mathrm{d}\boldsymbol{q}}{(2\pi)^3}\mathrm{e}^{i\boldsymbol{q}.(\boldsymbol{r_a}-\boldsymbol{r_b})}\frac{\hbar^2 D\boldsymbol{q}^2}{(E'-E)^2+\hbar^2D^2\boldsymbol{q}^4} \tag{3.45}$$

Fourier transforming Eq. (3.44),

$$\mathcal{K}_{\mathrm{Fock}}^{\mathrm{charge}}(\varepsilon, E, E') = K(\varepsilon) \tag{3.46}$$

with

$$K(\varepsilon) = \frac{2\nu_F}{\pi\hbar^3\Omega}\sum_{\boldsymbol{q}\neq 0}|U(\boldsymbol{q},\varepsilon)|^2\left(\frac{\hbar^2D\boldsymbol{q}^2}{\varepsilon^2+\hbar^2D^2\boldsymbol{q}^4}\right)^2 \tag{3.47}$$

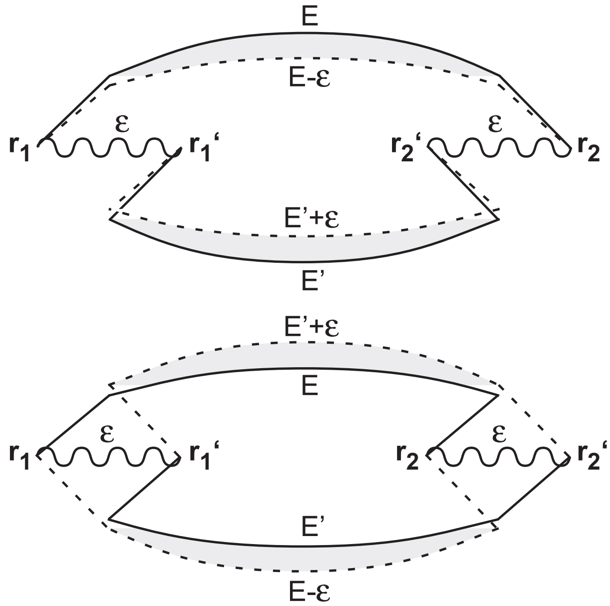

Fig. 3.13. Feynman diagrams for the Fock term (top) and Hartree term (bottom) in Eq. (3.44). Each wiggle represents a Coulomb factor $U(r, r', \varepsilon)$ and each couple of lines represent a product of density correlators. The grey areas represent coupling of the trajectories by disorder. With this representation [61], we see easily that the Fock term is short range and the Hartree term is long range. Indeed, only in the second, the lines of the correlators get spatially separated.

where the sum extends on all vectors $\boldsymbol{q}$ whose coordinates are $q_i = \pi n_i / L_i$ in the L_i-long direction i, with n_i an integer. Replacing $U(\boldsymbol{q}, \varepsilon)$ with its expression (3.35), one obtains

$$K(\varepsilon) = \frac{2}{\pi \hbar^3 \nu_F \Omega} \sum_{\boldsymbol{q} \neq 0} \frac{1}{(\varepsilon/\hbar)^2 + D^2 \boldsymbol{q}^4} \tag{3.48}$$

Hartree term

In the Fock term of Eq. (3.44) derived in the last section, the product of the density correlators is such that even long range terms $U(r, \varepsilon)$, where $r \gg l_e$, contribute. This is not the same for the Hartree term, in which the density correlators go to zero for long range interaction terms. Therefore, the Hartree term of Eq. (3.44) is negligible compared to the Fock term ([61]).

Kernel of interactions between electrons including spin

Up to now, the spin of the quasi-particles was only taken into account by a factor 2. However, similarly to the dephasing time calculation 2.2.1, a spin-dependent term exists. The Fock term has only contributions from interacting particles with identical spin, therefore, it is not modified when the spin is taken into account. However, the correction to the Hartree term is non zero.

$$\begin{aligned} K_{\mathrm{tot}} &= \mathcal{K}_{\mathrm{Fock}} + \mathcal{K}_{\mathrm{Hartree}} \\ \mathcal{K}_{\mathrm{Fock}} &= \mathcal{K}_{\mathrm{Fock}}^{\mathrm{charge}} \\ \mathcal{K}_{\mathrm{Hartree}} &= \underbrace{\mathcal{K}_{\mathrm{Hartree}}^{\mathrm{charge}}}_{\approx 0} + \mathcal{K}_{\mathrm{Hartree}}^{\mathrm{spin}} \end{aligned} \tag{3.49}$$

Neglecting the effect of magnetic impurities and spin-orbit scattering, the Hartree term can be approximated by the Fock charge term reduced by the prefactor λ_1 of Eq. (2.29) [72, 1, 108, 69]:

$$\mathcal{K}_{\mathrm{Hartree}}^{\mathrm{spin}}(\varepsilon) \approx \lambda_1 K(\varepsilon) \tag{3.50}$$

In case of strong spin-orbit interaction, like in our experiments (where $\tau_{\mathrm{so}} \approx 10$ ps, see Fig. 2.6), this Hartree term gets modified. Indeed, if the spin of an electron has enough time to change during the interaction (meaning during $\hbar/\varepsilon$) the Hartree term goes to zero. This introduces a cutoff at small energies in $\mathcal{K}_{\mathrm{Hartree}}^{\mathrm{spin}}(\varepsilon)$ which can be dealt with by replacing ε by $\left(\varepsilon^2 + \hbar^2/\tau_{\mathrm{so}}^2\right)^{1/2}$ [72]

$$\mathcal{K}_{\mathrm{Hartree}}^{\mathrm{spin}}(\varepsilon) \approx \lambda_1 K\left(\sqrt{\varepsilon^2 + \hbar^2/\tau_{\mathrm{so}}^2}\right). \tag{3.51}$$

The final expression for the Kernel reads then

$$K_{\mathrm{tot}}(\varepsilon) = K(\varepsilon) + \frac{3(F_0^\sigma)^2}{1 + F_0^\sigma + \sqrt{1 + F_0^\sigma}} K\left(\sqrt{\varepsilon^2 + \hbar^2/\tau_{\mathrm{so}}^2}\right). \tag{3.52}$$

In all what follows, we first neglect the Hartree term, and assume

$$K_{\mathrm{tot}}(\varepsilon) \approx K(\varepsilon).$$

Effective dimensionality

The last expression Eq. (3.48) for the kernel of Coulomb interaction between electrons allows to be more specific than in note 3 of section 2 about the effective dimensionality d of a diffusive metal. Depending on the energy probed ε, some terms in the sum become negligible. As soon as $\varepsilon \ll \hbar D\pi^2/L_i^2$, all terms of $q_i \neq 0$ are negligible for each direction i. In our experiments on metallic wires, the probed energies ε are such that only one direction of length L matters[10], and we can talk of quasi-one dimensional metals (see Fig. 3.19). In this particular case,

---

[10] The transversal lengths of the wire, typically of $w \approx 100$ nm correspond to energies $\hbar D\pi^2/w^2 \approx 10$ meV.

$$K(\varepsilon) = \frac{2}{\pi\hbar\nu_F L S_e} \sum_{n=1}^{+\infty} \frac{1}{\varepsilon^2 + (\pi^2\hbar D/L^2)^2 n^4} \tag{3.53}$$

with S_e the section of the wire. This can be calculated exactly[11]

$$K(\varepsilon \equiv \alpha\hbar D/2L^2) = \frac{2L^3}{\pi\hbar^3 D^2 \nu_F S_e} \left(\frac{\sinh(\sqrt{\alpha}) + \sin(\sqrt{\alpha})}{\cosh(\sqrt{\alpha}) - \cos(\sqrt{\alpha})} - 2\alpha^{-1/2} \right) \alpha^{-3/2} \tag{3.54}$$

At very low energies ε, the Kernel goes to $K(0) = \left(45\pi(\hbar D/L^2)^2 \hbar\nu_F S_e L\right)^{-1}$

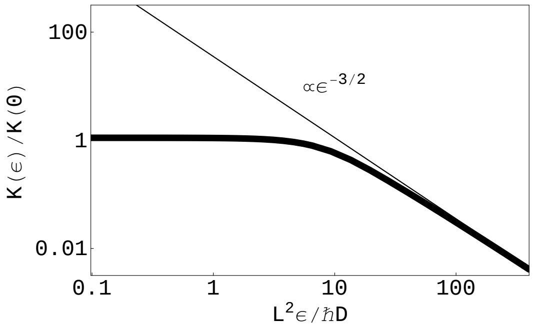

Fig. 3.14. Transition of the Coulomb interaction kernel from zero to one dimension. The thin line represents the $d = 1$ approximation Eq. (3.55).

and at intermediate energies $\hbar D/L^2 \ll \varepsilon \ll \hbar D/S_e$, the kernel scales like

$$\boxed{K(\varepsilon) = \kappa_{\mathrm{ee}} \varepsilon^{-3/2}} \tag{3.55}$$

with[12]

$$\kappa_{\mathrm{ee}} = \left(\pi\sqrt{2D}\hbar^{3/2}\nu_F S_e\right)^{-1}. \tag{3.56}$$

In the experiment, the probed energies are always in the range where this last expression is valid. Therefore, this is the equation we will use in practice in all further calculations. It is noteworthy that the Coulomb interaction between electrons in a diffusive wire is entirely described by one single real parameter κ_{ee}. The experiments we present here are able to quantify this parameter.

---

[11] Using the decomposition $\frac{1}{\alpha^2+n^4} = \frac{i}{2\alpha}\left(\frac{1}{i\alpha+n^2} - \frac{1}{-i\alpha+n^2}\right)$ and the identity $\sum_{n\geq 1} \frac{1}{n^2-\alpha} = \frac{1-\pi\sqrt{\alpha}\coth(\pi\sqrt{\alpha})}{2\alpha}$

[12] This prefactor has been confirmed by another derivation using fluctuation-dissipation theorem in [41].

Life time limitation due to Coulomb interaction between electrons

Using the definition of the lifetime

$$\tau_E = (\gamma_\mathrm{e} + \gamma_\mathrm{h})^{-1} \tag{3.57}$$

we get in the diffusive wire case,

$$\begin{aligned} \frac{1}{\tau_E^{(\mathrm{ee})}(E)} = & \int_{-\infty}^{+\infty} \mathrm{d}E' \int_{-\infty}^{+\infty} \mathrm{d}\varepsilon f(E')(1 - f(E-\varepsilon))(1 - f(E'+\varepsilon))K(\varepsilon) \\ & + \int_{-\infty}^{+\infty} \mathrm{d}E' \int_{-\infty}^{+\infty} \mathrm{d}\varepsilon f(E') f(E+\varepsilon)(1 - f(E'+\varepsilon))K(\varepsilon) \end{aligned} \tag{3.58}$$

Link between the lifetime and the phase coherence time

During a magnetoresistance measurement, f is just a Fermi function $f(E) = \left(1 + \mathrm{e}^{E/k_B T}\right)^{-1}$, as at every position, the electrons are at equilibrium. In this case, the lifetime at energy $E = 0$ simplifies into (see Eq. (A.5) in the appendix)

$$\frac{1}{\tau_E^{(\mathrm{ee})}(E=0,T)} = \int_0^{+\infty} \mathrm{d}\varepsilon K(\varepsilon) \frac{2\varepsilon}{\sinh(\varepsilon/k_B T)}. \tag{3.59}$$

This integral diverges at $\varepsilon = 0$ in the quasi-one dimensional case. This divergence comes from the fact that we considered arbitrarily small energy transfer ε, whereas the Heisenberg inequality prevents us from considering $\varepsilon < \hbar/\tau_E^{(\mathrm{ee})}$ in the integral[13]. We thus introduce a cut-off at small energies at $\hbar/\tau_E^{(\mathrm{ee})}$, and as most of the integral is dominated by the divergence at $\varepsilon = 0$, $\sinh(\varepsilon/k_B T)$ can be replaced by $\varepsilon/k_B T$, hence

$$\frac{1}{\tau_E^{(\mathrm{ee})}(E=0,T)} = 2k_B T \int_{\hbar/\tau_E^{(\mathrm{ee})}(E=0,T)}^{+\infty} \mathrm{d}\varepsilon K(\varepsilon) \tag{3.60}$$

Now, using Eq. (3.55), this self-consistent equation leads to

$$\tau_E^{(\mathrm{ee})}(E=0,T) = \left(\frac{4\kappa_\mathrm{ee} k_B}{\sqrt{\hbar}}\right)^{-2/3} T^{-2/3} \tag{3.61}$$

The phase coherence time τ_φ associated with Coulomb interaction between electrons, which we have defined through the weak localization effect, is the average rate at which electrons interact [61]. Therefore, it is proportional to $\tau_E^{(\mathrm{ee})}(E=0,T)$, and the prefactor can be identified from Eqs. (3.56, 2.25):

$$\tau_\varphi^{(\mathrm{ee})} = \left(\frac{\pi \kappa_\mathrm{ee} k_B}{2\sqrt{\hbar}}\right)^{-2/3} T^{-2/3} \tag{3.62}$$

---

[13] This cut-off at small energies has been derived in a more complete scheme in Ref. [109]. In particular, the self-consistent equation on $\tau_E^{(\mathrm{ee})}(E=0,T)$ is in fact obtained by approximating the decay of the electrons as exponential in time.

3.4.2 Electron-phonon interaction

As seen in section 2.2.2, longitudinal phonons can exchange energy with electrons. Neglecting edge effects, the rates $\gamma_{\mathrm{e}}^{(\mathrm{e-ph})}(E)$ and $\gamma_{\mathrm{h}}^{(\mathrm{e-ph})}(E)$ can be calculated in the Keldysh formalism [110]. A good approximation consists in replacing the electron occupation terms depending on E' in Eqs. (3.38, 3.40), and $K(\varepsilon)$ by an appropriate function of ε. Processes where the exchanged energy ε is negative (respectively positive) correspond to the annihilation (resp. creation) of a phonon in the mode ε, and as phonons are bosons, the occupation factor reads $n_{-\varepsilon} = (\mathrm{e}^{-\varepsilon/k_B T} - 1)^{-1}$ (resp. $1 + n_\varepsilon$), where T is the temperature of the phonons. Hence, using the fact that the phonon occupation factor reads $-\mathrm{sign}(\varepsilon) n_{-\varepsilon}$,

$$\gamma_{\mathrm{e}}^{(\mathrm{e-ph})}(E) = -\int_{-\infty}^{+\infty} \mathrm{d}\varepsilon (1 - f(E-\varepsilon)) \mathrm{sign}(\varepsilon) n_{-\varepsilon} K^{(\mathrm{ph})}(\varepsilon) \tag{3.63}$$

and

$$\gamma_{\mathrm{h}}^{(\mathrm{e-ph})}(E) = -\int_{-\infty}^{+\infty} \mathrm{d}\varepsilon f(E+\varepsilon) \mathrm{sign}(\varepsilon) n_{-\varepsilon} K^{(\mathrm{ph})}(\varepsilon) \tag{3.64}$$

We then can calculate the lifetime $\tau_E^{(\mathrm{e-ph})}(E,T)$ using Eq. (3.57),

$$\frac{1}{\tau_E^{(\mathrm{e-ph})}(E,T)} = 2\int_0^{+\infty} \mathrm{d}\varepsilon \frac{\cosh(E/2k_BT)^2 \coth(\varepsilon/2k_BT)}{\cosh(E/k_BT) + \cosh(\varepsilon/k_BT)} K^{(\mathrm{ph})}(\varepsilon) \tag{3.65}$$

The phase coherence time limitation due to electron-phonon interaction can then be evaluated from the $E = 0$ value of the lifetime,

$$\frac{1}{\tau_\varphi^{(\mathrm{e-ph})}} = \int_0^{+\infty} \mathrm{d}\varepsilon \frac{2}{\sinh(\varepsilon/k_BT)} K^{(\mathrm{ph})}(\varepsilon) \tag{3.66}$$

Making now the big assumption that $K^{(\mathrm{ph})}(\varepsilon)$ can be approximated by $\kappa_{\text{e-ph}}\varepsilon^p$ where p is a real number, which is justified in Ref. [111, 102, 36], we get if $p > 0$ (if not, it diverges),

$$\frac{1}{\tau_\varphi^{(\mathrm{e-ph})}} = \kappa_{\text{e-ph}}(4 - 2^{1-p})\Gamma(1+p)\zeta(1+p)(k_BT)^{p+1} \tag{3.67}$$

Therefore, if we want to recover the result Eq. (2.33), and in particular the temperature dependence $\tau_\varphi^{(\mathrm{e-ph})} \propto T^{-3}$, we must have

$$K^{(\mathrm{ph})}(\varepsilon) = \kappa_{\text{e-ph}}\varepsilon^2 \tag{3.68}$$

with

$$\kappa_{\text{e-ph}} = \frac{14\pi}{5 \times 3^3} \frac{E_F^2 \nu_F}{\hbar^3 \rho s^4 k_F^2} \tag{3.69}$$

However, as explained in section 2.2.2, this theory does not agree quantitatively with experiments. And in practice, $\kappa_{\text{e-ph}}$ is a free parameter related to the prefactor $\mathcal{B}$ of section 2.2.2. The good news comes from the fact that at low enough energies, such as those at which our experiments were performed, the electron-phonon interactions have a weak effect on the distribution functions.

3.4.3 Paper on the Intensity of Coulomb interaction between quasiparticles in diffusive metallic wires

We reproduce here our article Ref. [112] published in Solid State Communications in 2004. The main result of this paper is that Coulomb electron-electron interaction in diffusive wires is in good agreement with the picture dressed in section 3.4.1, but its intensity is underestimated at high energies. This paper shows that this is neither due to a change in effective dimensionality while energies get higher (see section 3.4.1), nor to the fact that distribution function measurement are performed out of thermodynamic equilibrium, nor to extrinsic processes.

Intensity of Coulomb interaction between quasiparticles in diffusive metallic wires

B. Huard, A. Anthore, F. Pierre, H. Pothier, Norman O. Birge, D. Esteve

Published in Solid State Communications, **131**, 599 (2004)

Abstract

The energy dependence and intensity of Coulomb interaction between quasiparticles in metallic wires is obtained from two different methods : determination of the temperature dependence of the phase coherence time from the magnetoresistance, and measurements of the energy distribution function in out-of-equilibrium situations. In both types of experiment, the energy dependence of the Coulomb interaction is found to be in excellent agreement with theoretical predictions. In contrast, the intensity of the interaction agrees closely with theory only with the first method, whereas an important discrepancy is found using the second one. Different explanations are proposed, and results of a test experiment are presented.

Introduction

The description of electrical transport in metals is based on the existence of long-lived quasiparticles. The finite quasiparticle lifetime appears in mesoscopic physics as a limitation of their phase coherence time, which determines the amplitude of quantum interference effects. The three kinds of processes that limit the quasiparticle lifetime in metals are electron-phonon scattering, electron-electron scattering, and spin-flip scattering of electrons from magnetic impurities[14]. At temperatures below about 1 K, the rate of electron-phonon scattering is weak, and in metallic samples without magnetic impurities the dominant inelastic scattering process should be the Coulomb interaction between electrons [1].

In this paper, we focus on experiments performed on very clean (99.9999%) silver wires, in which the effect of magnetic impurities is expected to be small [43, 40]. We review the results obtained from weak localization measurements, in which the phase coherence time $\tau_\varphi(T)$ is extracted, and from energy relaxation experiments, in which the energy exchange rate between quasiparticles

---

[14] Electrons lose phase coherence in the presence of magnetic impurities *via* a first-order scattering process [113]. They also exchange energy in the presence of magnetic impurities *via* a second-order process [37].

is derived from their energy distribution function $f(E)$. In the former experiments, we find that both the temperature dependence and overall magnitude of $\tau_\varphi(T)$ agree with the theoretical predictions. In the latter experiments, the energy dependence of the inelastic rate agrees with theoretical predictions, but the overall magnitude fluctuates significantly from sample to sample.

Two experiments for measuring Coulomb interaction between QPs

In metallic thin films, quasiparticles (QPs) experience frequent elastic scattering from grain boundaries, film edges and impurities. In this diffusive regime, characterized by a diffusion constant D, the screening of the Coulomb interaction is retarded, and the corresponding (squared) matrix element between two QPs, derived by Altshuler and Aronov in the early 80s [1], depends on the energy ε exchanged during the interaction process: $|M(\varepsilon)|^2 \propto \varepsilon^{-3/2}$ in quasi-one-dimensional wires. This energy dependence results in a temperature dependence of the phase coherence time $\tau_\varphi(T) \propto T^{-2/3}$ [2], which has been observed in silver wires by Wind *et al.* [32] down to 1K, and by Echternach *et al.* [114] in gold wires down to 100mK. The most convenient method to access τ_φ is the measurement of the magnetoresistance of wires with a length L long compared to the phase coherence length $L_\varphi = \sqrt{D\tau_\varphi}$, which exhibits a small peak or dip at zero magnetic field due to weak localization [115, 116]. When the rate of spin precession due to spin-orbit coupling exceeds the dephasing rate, as is usually the case at low temperature, the relative amplitude of the zero-field dip in the resistance gives direct access to L_φ :

$$\frac{\delta R}{R} \approx -\frac{R}{R_K}\frac{L_\varphi}{L}$$

with $R_K = h/e^2 \approx 26$ kΩ the resistance quantum. The width in field of this dip corresponds to a flux quantum in the area $L_\varphi w$, with w the wire width. In practice, magnetoresistance curves measured at different temperatures are fit with a theoretical expression for $\frac{\delta R}{R}(B)$ in which the only fit parameters are the phase coherence length L_φ, the spin-orbit length L_{so}, and the width of the wire w. The two last parameters, L_{so} and w are fixed at a constant value independent of temperature for each sample[15]. Then, τ_φ is obtained as L_φ^2/D, with D obtained from the resistance $R = \frac{1}{\nu_F e^2 D}\frac{L}{wt}$ where ν_F is the density of states at the Fermi energy (2 spin directions) and t the wire thickness. In order to compare with theory, the resulting curve $\tau_\varphi(T)$ is fit with

$$\tau_\varphi(T) = (AT^{2/3} + BT^3)^{-1}. \tag{3.70}$$

---

[15] The widths w of Ag wires determined from the best fits of magnetoresistance data to weak localization theory are often 10-15% smaller than the widths determined from electron microscope pictures. This is probably due to the granularity of the Ag wires.

where $AT^{2/3}$ is the Coulomb interaction rate and BT^3 the approximate electron-phonon scattering rate[16].

In theory, the exchange part of the Coulomb interaction leads to [117]

$$A = \frac{1}{\hbar}\left(\frac{\pi k_B^2}{4\nu_F Lwt}\frac{R}{R_K}\right)^{1/3} . \tag{3.71}$$

The contribution due to the Hartree term has not been evaluated for wires[17].

Another experimental method to access the interaction processes consists in driving the QPs out-of-equilibrium by a finite voltage U between two contacts at the ends of the wire [34]. At energies between 0 and eU, the diffusion of QPs from the occupied states at one end to empty states at the other end results, in absence of inelastic processes, in a two-step distribution function $f_x(E)$ inside the wire as pictured in Fig. 3.15. (The shorthand $f_x(E)$ stands for $f(x, E)$, where we measure distance in units of the wire length L, so that $0 < x < 1$.) This distribution function can be understood as a linear interpolation between the distribution functions at the boundaries of the wire. Electron-electron interactions lead to a redistribution of energy between QPs at each position, hence to a rounding of $f_x(E)$. In experiments, $f_x(E)$ at a given position in the wire is deduced from the differential conductance

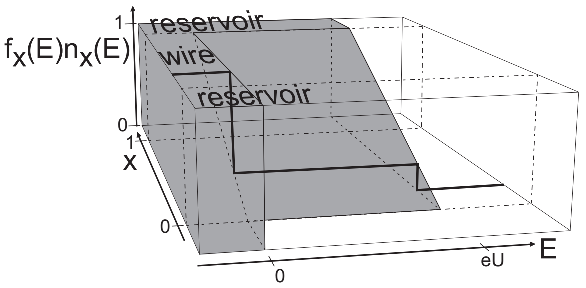

Fig. 3.15. Schematic diagram showing the spatial and energy dependences of the distribution function $f_x(E)$ of QPs driven out-of-equilibrium by the voltage U using the geometry of Fig. 3.20 with the switch in position 1. The surrounding box shows the uniform density of states in the metal and the gray volume shows the occupied states whose normalized density is $f_x(E)n_x(E)$. The thick line shows a typical double step distribution function at $x = 1/4$ as in Fig. 3.21.

---

[16] The purported T^3 power law for the electron-phonon scattering rate is not expected to be obeyed in disordered metals over any appreciable temperature range. Its observation over a limited range may be due to a crossover between T^4 and T^2 behaviors, or even between two T^2 regimes with different prefactors [76].

[17] In 2D films, both the singlet and triplet contributions to τ_φ have been calculated [73].

$dI/dV(V)$ of a tunnel junction between a superconducting probe electrode and the wire. In order to relate $f_x(E)$ to the matrix element of the interaction, the data are fit with the solution of the stationary Boltzmann equation in the diffusive regime [9, 118]:

$$\frac{1}{\tau_D}\frac{\partial^2 f_x(E)}{\partial x^2} + \mathcal{I}^{\text{in}}_{\text{coll}}(x, E, \{f\}) - \mathcal{I}^{\text{out}}_{\text{coll}}(x, E, \{f\}) = 0 \tag{3.72}$$

where $\mathcal{I}^{\text{in}}_{\text{coll}}(x, E, \{f\})$ and $\mathcal{I}^{\text{out}}_{\text{coll}}(x, E, \{f\})$ are the rates at which quasiparticles are scattered in and out of a state at energy E by inelastic processes. The diffusion time $\tau_D = L^2/D$ is the typical time spent by a QP in the wire. Assuming that the dominant inelastic process is Coulomb interaction between QPs and phonon emission or absorption, the inelastic scattering integrals read

$$\mathcal{I}^{\text{out}}_{\text{coll}}(x, E, \{f\}) = \int \mathrm{d}\varepsilon\ f_x(E)\,(1 - f_x(E-\varepsilon))\,W(\varepsilon) \tag{3.73}$$

$$\mathcal{I}^{\text{in}}_{\text{coll}}(x, E, \{f\}) = \int \mathrm{d}\varepsilon\ f_x(E+\varepsilon)\,(1 - f_x(E))\,W(\varepsilon) \tag{3.74}$$

with

$$W(\varepsilon) = W_{e-e}(\varepsilon) + W_{e-ph}(\varepsilon) \tag{3.75}$$

$$W_{e-e}(\varepsilon) = K(\varepsilon)\int \mathrm{d}E' f_x(E')\left(1 - f_x(E' + \varepsilon)\right) \tag{3.76}$$

$$W_{e-ph}(\varepsilon) = \kappa_{ph}\varepsilon^2(n_{ph}(|\varepsilon|) + \theta(\varepsilon)). \tag{3.77}$$

The kernel function $K(\varepsilon) = \kappa_{ee}\varepsilon^{-3/2}$ is proportional to the averaged squared interaction matrix element $|M(\varepsilon)|^2$ between two quasiparticles exchanging an energy ε [1]. Its intensity κ_{ee}, which can be derived either from the expression of the microscopic interaction potential [61, 41], or from the fluctuation-dissipation theorem [41], is[18]

$$\kappa_{ee} = \left(\sqrt{2D}\pi\hbar^{3/2}\nu_F w t\right)^{-1}. \tag{3.78}$$

This derivation takes into account the exchange term only. The Hartree contribution to $K(\varepsilon)$ is expected to be smaller [1, 61]. The electron-phonon coupling has an intensity κ_{ph} and is proportional to the sum of the Bose energy distribution of phonons $n_{ph}(|\varepsilon|)$ representing stimulated absorption or emission of phonons and the Heaviside function $\theta(\varepsilon)$ representing spontaneous emission. A more accurate description of electron-phonon coupling was developed in [76]. However, we restrict here to the simplistic form for W_{e-ph} because the effect of phonons is very small. Thus, for all the fits to the experiments, we fix the value of κ_{ph} at 4 $\text{ns}^{-1}\text{meV}^{-3}$, which is compatible with the weak localization measurements[19].

---

[18] This expression for κ_{ee} is half as large as the one used in refs. [41, 43, 40, 36, 35].

[19] In previous publications, we used $\kappa_{\text{ph}} = 8\ \text{ns}^{-1}\text{meV}^{-3}$ due to a factor of 2 error in extracting B in Eq. (3.70) from the Boltzmann equation (Eq. (3.72)).

The boundary conditions for Eq. (3.72) are Fermi-Dirac distributions at the ends of the wire, with a temperature higher than the cryostat temperature due to electron heating in the reservoirs[20] [119, 36].

The link between the two parameters determining the effect of Coulomb interaction, A and κ_{ee}, can be made explicit by noting that the dephasing rate is the average of the inverse of the lifetime of QPs at energies within $k_B T$ of the Fermi energy [120] :

$$\frac{1}{\tau_\varphi} \approx 2 \int_{\hbar/\tau_\varphi}^{k_B T} \mathrm{d}\varepsilon \frac{\kappa_{ee}}{\varepsilon^{3/2}} k_B T \tag{3.79}$$

$$\approx \frac{4\kappa_{ee}}{\sqrt{\hbar/\tau_\varphi}} k_B T \tag{3.80}$$

so that

$$\frac{1}{\tau_\varphi} \approx \left(\frac{4\kappa_{ee} k_B}{\sqrt{\hbar}} \right)^{2/3} T^{2/3}. \tag{3.81}$$

While this derivation reproduces the correct dependence on sample parameters of the more rigorous theory [2, 117], the prefactor depends on the exact value of the cutoff, whose order of magnitude is $\hbar/\tau_\varphi$. The choice of the cutoff can be made so that our derivation stays consistent with the expressions Eq. (3.71),(3.78) of A and κ_{ee}. Thus it is possible to express A as an intensity κ_A for Coulomb interaction, using

$$A \equiv \left(\frac{\pi \kappa_A k_B}{2\sqrt{\hbar}} \right)^{2/3}. \tag{3.82}$$

Comparison between experimental and theoretical results for both methods

We present here data taken on wires deposited from 6N-purity (99.9999%) silver sources. The fabrication procedure for weak localization type (WL) samples is described in Ref. [43]. The sample parameters are given in Table 3.1 (weak localization measurements) and Table 3.3 (energy relaxation measurements). The names of the samples used in energy relaxation (Relax) experiments contain Roman numerals, which indicate the index of the experiment, and a number, which is the (approximate) wire length in microns. Most Relax samples were obtained in a single step, using two-angle evaporations through a suspended mask [36]. Samples AgII5 and AgII10, on the one hand, and AgIV20α and AgIV20β, on the other hand, were fabricated at the same time, on the same chip. Samples AgXI10, AgXII40 and AgXIII40 were fabricated in two steps of e-beam lithography: in a first step, the wire pattern

---

[20] Surprisingly, the values of the reservoir heating parameters that produce the best fits to the data are somewhat smaller than the values calculated from the reservoir heating model discussed in [119].

was defined, then silver was evaporated and followed by a lift-off, and a new deposition of resist. In a second step, the pattern for the aluminum electrodes was exposed to the electron beam. In the vacuum chamber of the deposition machine, the silver layer was cleaned by argon ion milling. A thin (3 nm) layer of aluminum was then deposited, followed by an oxidation in 1.3 mbar of oxygen-argon (20%-80%) during 8 minutes, in order to form the tunnel barrier. Finally, a layer of aluminum was deposited.

Sample	L	w	t	R	τ_D	D
•	(μm)	(nm)	(nm)	(kΩ)	(μs)	(cm^2/s)
Ag(6N)a	136	65	47	1.44	1.58	117
Ag(6N)b	271	100	45	3.30	10.6	69.2
Ag(6N)c	400	105	53.5	1.44	8.54	187
Ag(6N)d	285	90	36	2.00	4.86	167

Table 3.1. Geometrical and electrical characteristics of samples for weak localization measurements. The diffusion coefficient D is obtained using Einstein's relation $1/\rho = \nu_F e^2 D$ with the density of states in silver $\nu_F = 1.03 \times 10^{47}$ J^{-1}m^{-3}, and the resistivity ρ extracted from the resistance R, thickness t, length L and width w of the wire.

Sample	A^{thy}	A	B
•		(ns^{-1}K$^{-2/3}$)	(ns^{-1}K^{-3})
Ag(6N)a	0.55	0.73	0.045
Ag(6N)b	0.51	0.59	0.05
Ag(6N)c	0.31	0.37	0.047
Ag(6N)d	0.47	0.56	0.044

Table 3.2. Theoretical predictions of EQ. (3.71) (A^{thy}) and fit parameters (A and B) for $\tau_\varphi(T)$ in the silver samples using the functional form given by EQ. (3.70). Comparison of A^{thy} and A is shown graphically in FIG. 3.18.

In FIG. 3.16, we present $\tau_\varphi(T)$ for the first three WL samples (the data points of the last one, which are presented in Ref. [43], are so close to those of the third one that they confuse the figure), as well as the best fits with EQ. (3.70). The fit parameters are given in TABLE 3.2. The fit value of A is very close to the theoretical value for the exchange contribution of the Coulomb interaction, as can be seen in FIG. 3.18 where the X-coordinate of the solid squares is the theoretical value of κ_A using EQS. (3.71) and (3.82), and the Y-coordinate is the value from experiment.

The situation is quite different in energy relaxation experiments. We show in FIG. 3.17 distribution functions $f(E)$ measured in the middle of sample

Sample ○	L (μm)	w (nm)	t (nm)	R (Ω)	τ_D (ns)	D (cm^2/s)
AgI5	5.05	90	43	41	2.1	121
AgII5	5.2	66	39	44	1.6	173
AgII10	10.3	65	39	81	5.6	191
AgIII20	19.6	160	43	45	16	241
AgIV20α	19.7	95	44	86	19	208
AgIV20β	19.9	100	44	91	21	188
AgX20	21.7	100	48	80	22	214
AgXI10	9.55	124	45	31	43	211
AgXII40	38	180	45	108(^{21})	87	165
AgXV40	38	145	45	134	87	165

Table 3.3. Geometrical and electrical characteristics of samples for energy relaxation measurements.

Sample ○	$\kappa_{ee}^{\mathrm{thy}}$ (ns^{-1}meV$^{-1/2}$)	κ_{ee}
AgI5	0.060	0.95
AgII5	0.076	0.5
AgII10	0.073	0.54
AgIII20	0.024	0.5
AgIV20α	0.043	0.40
AgIV20β	0.043	0.37
AgX20	0.037	0.11
AgXI10	0.032	< 0.18
AgXII40	0.025	0.18
AgXV40	0.031	0.32

Table 3.4. Theoretical predictions of EQ. (3.78) ($\kappa_{ee}^{\mathrm{thy}}$) and fit parameters ($\kappa_{ee}$) for $f_x(E)$ in the silver samples using the solution of the Boltzmann equation EQ. (3.72). The distribution functions measured on sample AgXI10 were so close to the noninteracting regime that it was only possible to give an upper bound to the value of κ_{ee}. Comparison of $\kappa_{ee}^{\mathrm{thy}}$ and κ_{ee} is shown graphically in FIG. 3.18.

AgIV20α, for U ranging from 0.1 to 0.5 mV, plotted as a function of the reduced energy E/eU. Solid lines are fits resulting from the numerical solution of the Boltzmann equation, obtained with $\kappa_{ee} = 0.40$ ns^{-1}meV$^{-1/2}$. The increase in slope of the middle step of $f(E)$ when U increases, characteristic of the effect of Coulomb interaction, is well reproduced. However, the fit value for κ_{ee} is nearly an order of magnitude larger than the value given by EQ. (3.78). Similar discrepancies exist for the other Relax samples. It could be argued that the numerical prefactor in EQ. (3.78) is incorrect. FIG. 3.18 seems to rule out this explanation: the circles corresponding to the theoretical and fit values,

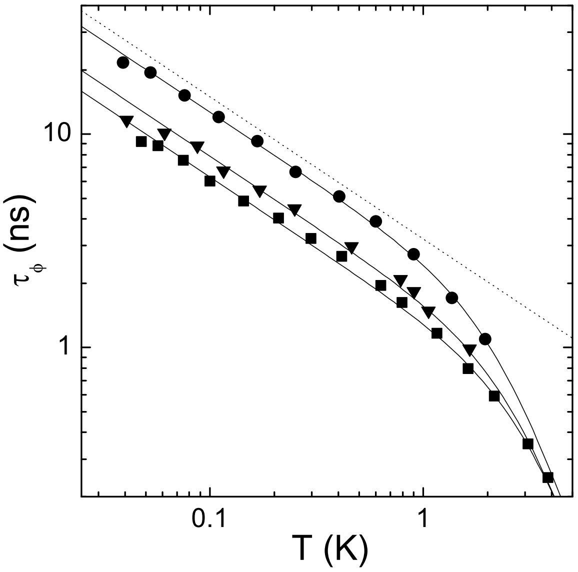

Fig. 3.16. Phase coherence time vs temperature in samples Ag(6N)a (■), Ag(6N)b (▼), and Ag(6N)c (●), all made of 6N sources. Continuous lines are fits of the data to Eq. (3.70). The quantitative prediction of Eq. (3.71) for electron-electron interactions in sample Ag(6N)c is shown as a dashed line.

given also in Table 3.4, present a large scatter, and so the ratio between experiment and theory does not appear to be constant.

Discussion of the discrepancy between the two experiments

Figure 3.18 reveals a very puzzling difference between weak localization (WL) and energy relaxation (Relax) experiments. Whereas the results of both types of experiments are precisely accounted for by the theory of Coulomb interactions in disordered wires as far as the energy dependence is concerned, the prefactor is well understood for the first, but not at all for the second. In order to resolve this puzzle, we now list the differences between the two types of experiments:

Possibility of extrinsic energy exchange processes in Relax samples

WL experiments are extremely sensitive to very small quantities of magnetic impurities. It was shown in [43] that even in our cleanest Ag(6N) wires, there was evidence for magnetic impurities at concentrations of about 0.01 ppm, i.e. 1 impurity atom for every 10^8 Ag atoms. Their contribution to τ_φ was visible only at the lowest experimental temperatures. In Fig. 3.18, we have indicated with the vertical dashed lines how far the fit values of κ_A can be

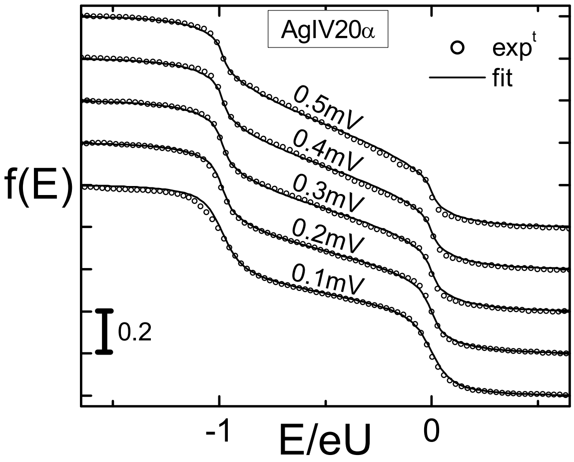

Fig. 3.17. Experimental measurements (○) and fits (solid curves) of the quasiparticle energy distribution function $f_{\frac{1}{2}}(E)$ for five different values of the applied voltage across the wire AgIV20α. The data have been shifted vertically for clarity.

reduced if one includes a small concentration of magnetic impurities as an extra fit parameter.

It is known that magnetic impurities also mediate energy exchange between electrons[22]. Could the presence of magnetic impurities explain the anomalously large values of κ_{ee} observed in many Relax experiments? Since most of the Ag samples used in the WL experiments were fabricated in the same deposition system used for the Relax samples, we expect that Relax samples should be equally clean. This hypothesis must be checked, however. The presence of magnetic impurities in Relax samples can be detected directly by performing the experiment as a function of magnetic field [40]. In samples AgX20 and AgXI10, the magnetic field dependence of the measurements set an upper bound to the concentrations of magnetic impurities at 0.1 and 0.6 ppm respectively. For sample AgX20, if we include the effect of 0.1 ppm of magnetic impurities into the analysis of the Relax data, the value of κ_{ee} is reduced by only 15%. In sample AgXI10, the distribution functions were so close to the noninteracting regime that it was only possible to place an upper bound on κ_{ee}, hence this sample does not appear in Fig. 3.18.

For the Ag Relax samples that were not measured in a magnetic field, we have estimated the systematic uncertainty in κ_{ee} by the following analysis. Assume that another process, other than electron-electron interactions, contributes to energy exchange in the Relax experiments. In particular, for the

---

[22] Electrons lose phase coherence in the presence of magnetic impurities *via* a first-order scattering process [113]. They also exchange energy in the presence of magnetic impurities *via* a second-order process [37].

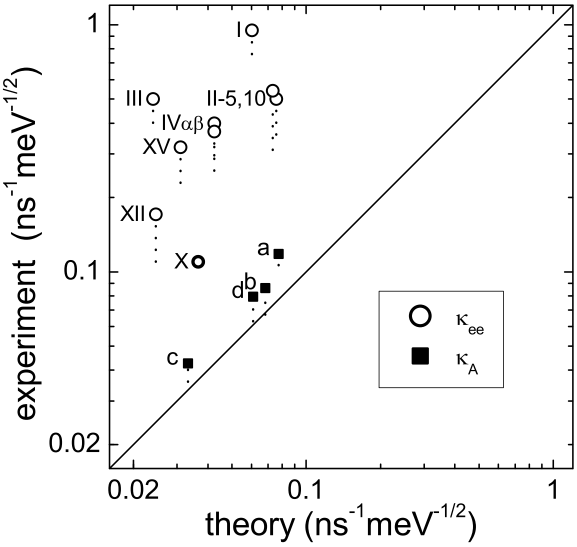

Fig. 3.18. Comparison of the experimental prefactor with the theoretical prediction, for weak localization experiments (■) and energy relaxation experiments (○). If we assume a small amount of magnetic impurities to be present in the WL samples, the fit values of κ_A can be reduced down to the bottom of the dashed lines below the squares. Similarly for the Relax experiments, if we assume an extrinsic process of the type $K(\varepsilon) \propto \varepsilon^{-2}$ in addition to the Coulomb interaction, we obtain a range of values of κ_{ee} compatible with the data, represented as a dashed line below the ○. The behavior of sample AgX20 was measured in a magnetic field, allowing us to place an upper bound on the concentration of magnetic impurities, and hence to rule out the possibility of reducing the value of κ_{ee} more than 15%. Thus, this data point is represented as a bold circle without any dashed line.

case of electron-electron interactions mediated by magnetic impurities, the interaction kernel is approximately of the form $K(\varepsilon) = \kappa_2 \varepsilon^{-2}$. If we fit the data using the value of κ_2 as an additional fit parameter, we can ask how small the value of κ_{ee} can become before the fits become clearly incompatible with the data. The results are shown by the dashed lines descending below the points for the Relax samples in FIG. 3.18. As can be seen, for some samples the fits are somewhat insensitive to the relative weights of κ_{ee} and κ_2, and the discrepancy between theory and experiment gets smaller. Nevertheless, the discrepancy still remains. We conclude for the time being that extrinsic energy exchange processes with $K(\varepsilon) \propto \varepsilon^{-2}$ are unlikely to explain completely the discrepancy between experiment and theory. This issue will be discussed further in section 3.4.3.

Sample dimensionality

In order to reduce the amplitude of conductance fluctuations, which spoil the analysis of the magnetoresistance in terms of the WL theory, we fabricate WL samples with lengths $L \gg L_\varphi\,(T_{\rm min})$, where $T_{\rm min}$ is the lowest experimental temperature. Typically, in the WL experiments, L_φ varies between 1 μm to 20 μm and the wire remains in the one-dimensional regime given by $w, t \ll L_\varphi \ll L$. In Relax experiments, on the other hand, the distribution function $f(E)$ only contains information on the interaction process if it is far from a Fermi function and far from a perfect double-step, *i.e.* if $L \approx$ few $L_\varphi\,(eU_{\rm max}/k_B)$. Thus the wire length is smaller than for the WL experiments. The dimensionality criterion for Relax is illustrated in FIG. 3.19, where we plot the function $K(\varepsilon)$ calculated using the discrete sum over the longitudinal and transverse wave vectors [61, 121]

$$K(\varepsilon) \propto \sum_{\substack{q_x \neq 0 \\ q_y, q_z}} \frac{1}{D^2 \boldsymbol{q}^4 + (\varepsilon/\hbar)^2} \tag{3.83}$$

where $q_x = \frac{\pi n_x}{L}$, $q_y = \frac{\pi n_y}{w}$ and $q_z = \frac{\pi n_z}{t}$ are the wave vector components with $n_x \in \mathbb{N}^*$ and $n_y, n_z \in \mathbb{N}$.

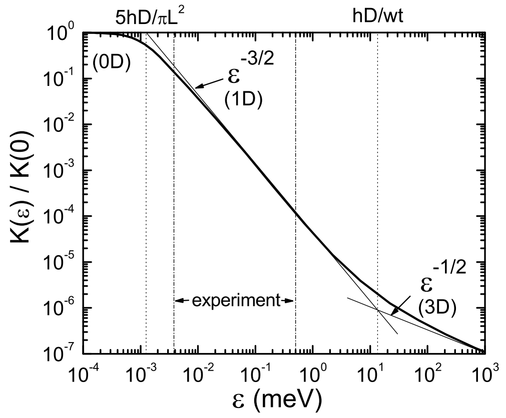

Fig. 3.19. Energy dependence of the kernel $K(\varepsilon)$ of Coulomb interaction in a wire with $L = 10\ \mu{\rm m}, w = 130\ {\rm nm}, t = 45\ {\rm nm}$ and $D = 200\ {\rm cm}^2/{\rm s}$. The asymptotic zero-, one- and three-dimensional regimes (0D, 1D, 3D) are characterized by $K(\varepsilon) = K(0)$, $K(\varepsilon) \propto \varepsilon^{-3/2}$ and $K(\varepsilon) \propto \varepsilon^{-1/2}$, respectively (straight lines). The two-dimensional regime is not clearly visible because $w \approx t$. The range of relevant ε's for the Relax experiments is determined by $k_B T_{\rm min}$ and $eU_{\rm max}$. The normalization factor on the y-axis is $K(0) = \left(45\pi(\hbar D/L^2)^2 \hbar \nu_F w t L\right)^{-1}$

Typical sample dimensions were chosen: $L = 10\ \mu\text{m}, w = 130\ \text{nm}, t = 45\ \text{nm}$ and $D = 200\ \text{cm}^2/\text{s}$. The figure 3.19 shows that for all relevant energies in the experiments, $K(\varepsilon)$ is far from the 1D-3D transition. For small energies near $k_B T_{min}$, the behavior of $K(\varepsilon)$ differs slightly from the $\varepsilon^{-3/2}$ power law, but this deviation goes in the wrong direction to explain the discrepancy between theory and experiment.

Diffusive approximation in narrow wires

The energy scales probed by WL and Relax experiments are rather different. In wires, the value of τ_φ is essentially determined by the low energy cut-off of the interaction, at $\hbar/\tau_\varphi$. In the samples presented here, τ_φ ranges (in the relevant temperature range: 1 K down to 40 mK) from 1 to 20 ns, corresponding to energies $\hbar/\tau_\varphi$ between 0.03 and 0.6 μeV. In the Relax experiments, the shape of $f(E)$ is entirely determined by energy exchanges of an amount between $k_B T$ and eU, in practice between 4 and 500 μeV. According to Eq. (3.83), the characteristic lengthscale $1/q = \sqrt{\hbar D/\varepsilon}$ for the interaction is therefore a few micrometers for WL, several hundreds of nanometers for Relax. The discrepancy between the results of the two types of experiment could point out a failure of the diffusive model, in which the QP dynamics is described by a single diffusion constant D. This argument is reinforced by the fact that the elastic mean free path deduced from D is of the order of the wire thickness t, indicating that surface and grain boundary scattering dominate the elastic processes. If surface scattering alone were dominant, the elastic mean free path of QPs with an instantaneous wavevector along the axis of the wire would be very different from that of QPs travelling in a perpendicular direction, and the diffusive approximation would break down. To our knowledge, Coulomb interaction has never been investigated in this regime. However it is not clear why this situation could be described by the same energy dependence and why the intensity could be larger.

Departure from equilibrium

WL experiments are performed very close to equilibrium. In Relax experiments, a voltage $U \gg k_B T/e$ is applied to the wires in order to establish an out-of-equilibrium situation. Near the Fermi level, the distribution function is very different from a Fermi function, and it could be argued that the derivation leading to the expression (3.78) of the prefactor κ_{ee} is no longer valid. In order to test this hypothesis, we have performed a complementary experiment, described below, in which the effect of the distance to equilibrium is investigated.

A new Relax experiment close to equilibrium

Fig. 3.20 shows a schematic of sample AgXII40, which was designed to investigate the effect of the deviation of $f(E)$ from an equilibrium Fermi distribution.

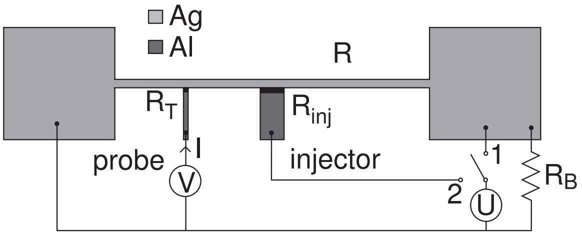

Fig. 3.20. Schematic diagram of an experiment to measure $f_x(E)$ in a wire close to equilibrium. Quasiparticles are injected into the wire from a superconducting wire (labelled *injector*) through a tunnel junction biased at potential U (switch position 2). The distribution function $f_x(E)$ at position $x = 0.25$ is then determined from the $\mathrm{d}I/\mathrm{d}V$ characteristic of the probe junction. Alternatively, the wire can be driven far from equilibrium by applying the voltage bias U across the wire (switch position 1). The resistance R_B is chosen so that the potential of the right reservoir remains close to zero when the switch is in position 2.

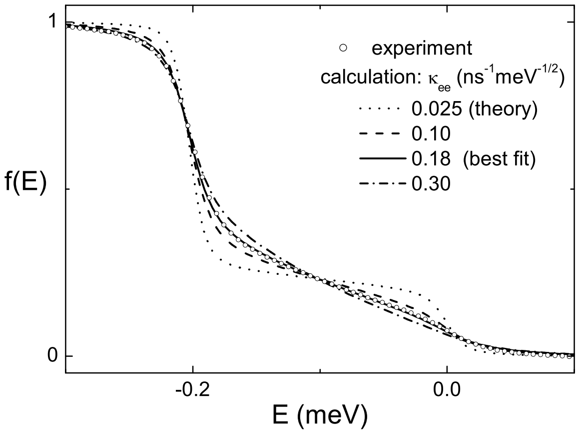

Fig. 3.21. Measured (○) distribution function $f_{\frac{1}{4}}(E)$ in the "conventional" Relax experiment using sample AgXII40 with the switch of Fig. 3.20 in position 1, and for $U = 0.2$ mV. The solid line is a numerical solution to the Boltzmann equation using the prefactor $\kappa_{ee} = 0.18$ ns^{-1}meV$^{-1/2}$ for the Coulomb interaction between electrons. As shown by the three dot-dashed lines, other values of κ_{ee} produce markedly worse fits to the data. In particular, the theoretical value $\kappa_{ee} = 0.025$ ns^{-1}meV$^{-1/2}$ does not come close to reproducing the experimental results.

As in other Relax experiments, a wire (38 μm long, 180 nm wide, 45 nm thick) is placed between large contact pads. A superconducting probe electrode is placed at $x = 1/4$, with a tunnel resistance to the wire of 15 $k\Omega$. The size of the tunnel junction was 0.18×0.23 μm^2. When the switch on FIG. 3.20 is placed in position 1, the "conventional" Relax experiment can be performed. A measured distribution function is shown in FIG. 3.21. The intensity of the Coulomb interaction deduced from the fits of $f(E)$ is $\kappa_{ee} = 0.18$ ns^{-1}meV$^{-1/2}$, as indicated in TABLE 3.4. EQ. (3.78) has been used [23] to calculate the theoretical value $\kappa_{ee}^{\text{thy}} = 0.025$ ns^{-1}meV$^{-1/2}$. This discrepancy is of the same type as the one observed in the other samples of TABLE 3.4. A second superconducting electrode, denoted *injector* in FIG. 3.20, forms a tunnel junction with the wire around its center, but with a much larger area than the probe junction: 0.57×0.8 μm^2. The junction was obtained at the overlap between the $w_{\text{inj}} = 0.8$ μm-wide superconducting electrode and the wire, which presents an intentional at this position. The corresponding tunnel resistance was $R_{\text{inj}} = 1.1$ kΩ. When the switch of FIG. 3.20 is placed in position 2, quasiparticles are injected through the tunnel junction into the wire when $U > \Delta/e$, with Δ the gap in the QP density of states of the injector. On the normal side of the tunnel junction, the QP distribution function is therefore expected to display a step, the shape of which reflects the BCS density of states $n_S(E) = \text{Re}\left(|E|/\sqrt{E^2 - \Delta^2}\right)$. The height of the step away from the BCS peak is given by the ratio of the injection rate of QPs to the diffusion rate towards the two normal reservoirs: $f_{\frac{1}{2}}(E) \sim \left(\frac{R}{4}\right)/R_{\text{inj}} \equiv r$ (the factor 1/4 results from the parallel combination of the two halves of the normal wire as will be shown below). A quantitative description follows from the introduction of new boundary conditions in the Boltzmann EQ. (3.72): $f_x(E)$ is a Fermi function with a zero electrochemical potential at $x = 0$ and eU_r at $x = 1$, whereas at $x = \frac{1}{2}$ current conservation at each energy implies

$$\nu_F wteD \left(\frac{\partial f_x(E)}{L\partial x}|_{x=\frac{1}{2}^+} - \frac{\partial f_x(E)}{L\partial x}|_{x=\frac{1}{2}^-} \right) = i_{\text{inj}}(E)$$

with

$$i_{\text{inj}}(E) = \frac{1}{eR_{\text{inj}}} n_S(E + eU) \left(f_S(E + eU) - f_{\frac{1}{2}}(E) \right)$$

where $f_S(E)$ is the distribution function in the superconducting injector. We neglect here the slight modification of the DOS in the wire due to proximity effect, because of the small transparency of the tunnel barrier. Finally,

---

[23] The resistivity of the wire could not be accessed in this experiment. It has thus been estimated from the measured parameters of AgXIII40 in order to calculate κ_{ee}^{thy}. Indeed, this sample AgXII40 and the sample AgXIII40 have been fabricated together.

$$\begin{aligned}&\frac{\partial f_x(E)}{\partial x}\Big|_{x=\frac{1}{2}^+}-\frac{\partial f_x(E)}{\partial x}\Big|_{x=\frac{1}{2}^-}\\&=\frac{R}{R_{\mathrm{inj}}}n_S(E+eU)\left(f_S(E+eU)-f_{\frac{1}{2}}(E)\right).\end{aligned}\tag{3.84}$$

The electrochemical potential eU_r in the right reservoir, which is connected to ground by a bias resistance $R_B = 12\ \Omega$, is given by $U_r = \frac{1}{2}\frac{RR_B}{R+R_B}\int i_{\mathrm{inj}}(E)\mathrm{d}E < \frac{R_B}{2R_{\mathrm{inj}}}U$. Since $\frac{R_B}{2R_{\mathrm{inj}}} \simeq 0.005$, we make the approximation $U_r = 0$, so that the situation is symmetric: $f_x(E) = f_{1-x}(E)$ and EQ. (3.84) becomes

$$\begin{aligned}&\frac{\partial f_x(E)}{\partial x}\Big|_{x=\frac{1}{2}^+}=-\frac{\partial f_x(E)}{\partial x}\Big|_{x=\frac{1}{2}^-}\\&=2rn_S(E+eU)\left(f_S(E+eU)-f_{\frac{1}{2}}(E)\right).\end{aligned}\tag{3.85}$$

In the absence of interactions, at $T = 0$, one obtains directly for $x < \frac{1}{2}$:

$$f_x(E)=\begin{cases}1 & \text{for } E<0\\ 2xf_{\frac{1}{2}}(E) & \text{for } E\in[0,eU-\Delta]\\ 0 & \text{for } E>eU-\Delta\end{cases}$$

and

$$f_{\frac{1}{2}}(E)=\frac{r\ n_S\,(E-eU)}{1+rn_S\,(E-eU)}.\tag{3.86}$$

The spatial dependence of $f_x(E)$ is plotted in FIG. 3.22 for $x < \frac{1}{2}$, assuming $r = 0.1$ for visibility. It is seen that $f_x(E)$ is much closer to a Fermi function than when the voltage is applied across the wire.

An experimental curve, obtained for $U = 0.29$ mV, is shown in FIG. 3.23. As predicted, it presents a very small step extending from $E = 0$ to $E = eU - \Delta$, with $\Delta = 0.18$ mV the gap for the injector deduced from its I-V characteristic, measured separately. The blow-up (×10, right scale) shows a small peak near $E = eU - \Delta$. We also show $f(E)$ calculated using the same parameters as those deduced from the "conventional" measurement, using EQ. (3.72) and (3.85). Except for a slight rounding of the small peak, the agreement is within experimental accuracy for all the values of U for which data were taken (0.22 to 0.31 mV). We show in particular that other values of κ_{ee} would produce curves which significantly differ from the measured one. Hence the value of κ_{ee} deduced from energy exchange experiments does not seem to depend on whether the distribution is far from equilibrium, as in the original experiment (FIG. 3.21), or close to equilibrium, as in the newer experiment described here. Our conclusion is that Coulomb interaction is not modified by the fact that $f(E)$ is not exactly a Fermi function.

Conclusions

Section 3.4.3, we discussed the possibility that the anomalously high rates of energy exchange observed in many Relax experiments could be caused by

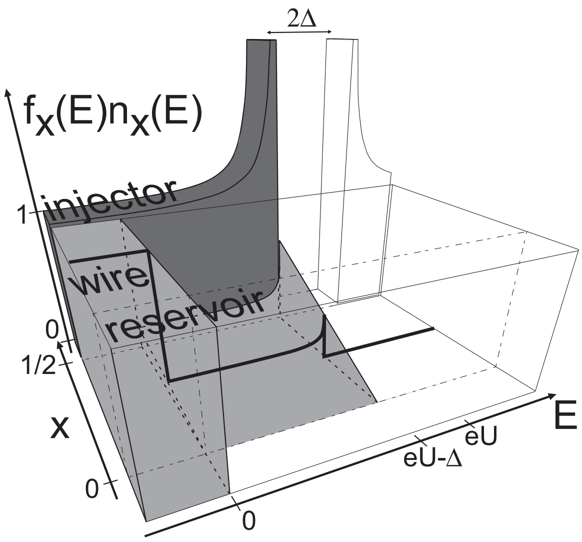

Fig. 3.22. Schematic diagram showing the spatial and energy dependences of the distribution function $f_{\frac{1}{4}}(E)$ of QPs driven out-of-equilibrium by the voltage U using the geometry with the switch of Fig. 3.20 in position 2. The surrounding box shows the density of states along the circuit and the gray volume shows the occupied states whose normalized density is $f_x(E)n_x(E)$. The inelastic processes involving QPs are assumed to be very weak for clarity. The thick line shows the distribution function at $x = 1/4$.

extrinsic sources, such as magnetic impurities. Two arguments against this hypothesis were: 1) it seems implausible that all samples used in Relax experiments contain impurities that are not present in any sample used for localization experiments, since both kinds of samples were fabricated in the same apparatus; and 2) we checked whether adding a term of the form $K(\varepsilon) \propto \varepsilon^{-2}$ to the interaction kernel could significantly decrease the value of κ_{ee} obtained from fitting the data to the solution of Eq. (3.72). But those two arguments do not rule out another possibility, namely that both kinds of samples contain magnetic impurities with integer spin and with a magnetic anisotropy of the form $\mathcal{K}S_z^2$ in the impurity Hamiltonian [122]. Such a term is predicted in the presence of spin-orbit scattering, for magnetic impurities located close to the sample surface [95]. If the characteristic energy $\mathcal{K}$ satisfies $k_BT \ll \mathcal{K} < eU$, then such impurities would contribute to energy exchange but not to dephasing. The contribution to $K(\varepsilon)$ from such impurities depends on both $\mathcal{K}$ and B, but is not expected to be of the form $K(\varepsilon) \propto \varepsilon^{-2}$. In principle, the presence of such impurities should be detectable in experiments in the presence of a magnetic field. Indeed once $g\mu B \gg eU$, their contribution vanishes. And

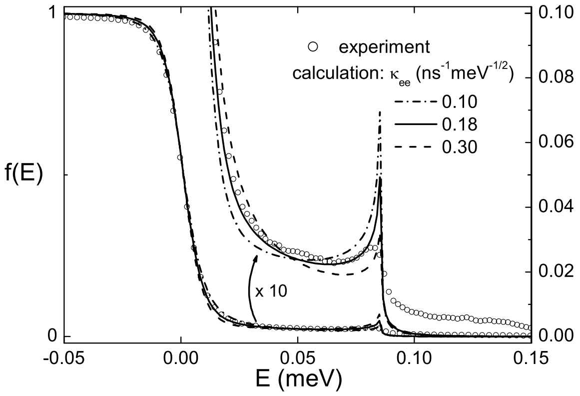

Fig. 3.23. Measured (○) distribution function $f_{\frac{1}{4}}(E)$ in the new Relax experiment using sample AgXII40 of Fig. 3.20 with the switch in position 2, and for $U = 0.27$ mV. The data for positive E are also shown magnified by a factor 10. The solid line is a numerical solution to the Boltzmann equation with boundary condition given by Eq. (3.86), using as prefactor for the Coulomb interaction the value $\kappa_{ee} = 0.18\mathrm{ns}^{-1}\mathrm{meV}^{-1/2}$. The two dot-dashed lines show that other values of κ_{ee} produce markedly worse fits to the data.

as the samples that were measured in presence of magnetic field showed no visible dependence on B, this possibility seems unlikely.

In conclusion, the energy dependence of Coulomb interaction in disordered wires is well explained by theory. The intensity of the interaction, as deduced from phase coherence time measurements, is quantitatively in agreement with theory, whereas for energy relaxation, an unexplained discrepancy remains. A new version of the Relax experiment has demonstrated that this discrepancy is not due to the out-of-equilibrium situation.

We gratefully acknowledge the contributions to this work by A. Gougam, and helpful discussions with H. Grabert, G. Goeppert, I. Aleiner, G. Montambaux. Work at Saclay was supported in part by the EU Network DIENOW. Work at Michigan State University was supported in part by the National Science Foundation under grant DMR-0104178, and by the Keck Microfabrication Facility supported by NSF DMR-9809688.

3.4.4 Comments on the paper

Another possible explanation

In this article, it is mentioned that the Hartree term of the kernel of the interaction between electrons is much smaller than the Fock term. This might in fact be a wrong statement. Indeed, if the charge Hartree term is indeed negligible, the spin term may not be so small (see Eq. (3.51)). What actually remains to be solved is the value of the factor F_0^σ in silver wires.

In the paper above, we have shown that a big discrepancy between theory and experiment exists on the rate of Coulomb interaction between electrons for the Relax experiment, although there is an agreement for the WL experiments (Fig. 3.18). One might wonder wether the neglected Hartree term could explain this.

The WL experiments probe the dephasing time, and, as proven in 2.2.1, the Hartree contribution to τ_φ is negligible, since the probed energies are much smaller than the spin-orbit characteristic energy $\hbar/\tau_{\mathrm{so}}$. This could be the reason why a prediction which neglects the Hartree term correctly describes the Coulomb interaction contribution to $\tau_\varphi(T)$ measurements. On the opposite, the Relax experiments probe energy exchange between electrons which are larger than $\hbar/\tau_{\mathrm{so}}$. In this case, the Hartree term might be not negligible.

However, in order to explain a factor 3 between the fitted $\kappa_{\mathrm{ee}}^{\mathrm{Fock}}$ from the experiment and the theoretical prediction $\kappa_{\mathrm{ee}}^{\mathrm{thy}}$ using the Fock term, it seems that one needs extremely low values for $1+F_0^\sigma$. An estimate for the experiments on the *bare* wire (see 3.4.7) gives $F_0^\sigma \approx -0.9$. Still, it contradicts conduction electron spin resonance measurements where $F_0^\sigma \in [-0.21, 0.05]$ in silver [70], therefore this explanation for the discrepancy discussed in the last paper is most certainly insufficient.

3.4.5 Interactions mediated by magnetic impurities

In section 3.4.3, we have seen the great achievements of the semi-classical approach to describe the dynamics of electrons in presence of Coulomb interaction between electrons and electron-phonon interactions. However, it turns out that this theory alone is not able to properly describe the transport in the big majority of metallic wires. In Ref. [36, 41], it has been demonstrated experimentally that as soon as the purity of a metal is not extremely high (the best available purity, called 6N, meaning less than 1 ppm of foreign atoms are not always enough), electrons exchange much more energy than predicted[24] [36]. At first sight, imputing this strong energy exchange to magnetic impu-

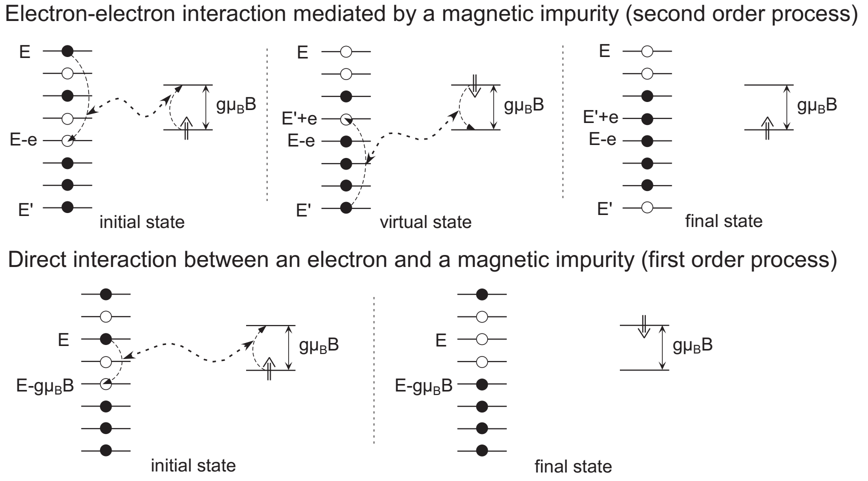

Fig. 3.24. Scheme of the processes involving magnetic impurities and allowing exchange of energy between electrons [37]. On each panel, the left ladder represents the electronic states and the right part schemes the two states of the magnetic impurity lifted by the Zeeman energy. In case the field is zero, both states are degenerate and only the second order process (top) can lead to energy exchange between electrons (figure taken from Ref. [41]).

---

[24] The mean free path l_e^{alien} before encountering an impurity can be estimated by saying that the volume Ω^{alien} associated to a single impurity is just the volume covered by an electron on a distance l_e^{alien}:

$$\lambda_F^2 l_e^{\mathrm{alien}} = \Omega^{\mathrm{alien}} = 1/c_{\mathrm{MI}} \tag{3.87}$$

In the case of silver, the density is 59 nm^{-3} (see Table A.2), therefore, for 1 ppm of impurities, we get $l_e^{\mathrm{alien}} \approx 3$ mm. It is clear that at this level, a modification in the metal purity does not affect the total mean free path l_e which is of the order of 40 nm in our thin films.

rities seemed wrong. Indeed, when an electron undergoes a spin-flip process with a magnetic impurity, it cannot exchange energy with it, as the magnetic impurity does not have any dynamical degree of freedom to stock this energy. In 2001, Kaminski and Glazman showed that this exchange is made possible through higher order processes [37]. Indeed, if two electrons undergo a spin-flip process with a magnetic impurity, they can exchange an energy ε with each other, because quantum mechanics states that energy conservation can be violated by an energy ε for a time $\Delta t = \hbar/\varepsilon$. Still, one might argue that such correlated spin-flip events are so rare that this exchange process is far less efficient than electron-electron interactions. Kaminski and Glazman realized that the Kondo effect (see section 2.2.3) increases dramatically the rate of those correlated events so that, for energies ε near the Kondo energy $k_B T_K$ and magnetic impurity concentrations high enough, electrons exchange more energy through Kondo impurities than through the Coulomb interaction. In this section, we present the formalism developed in Ref. [39] to take into account this new interaction as rates $\gamma_{\mathrm{e}}^{(\mathrm{e}-\updownarrow-\mathrm{e})}$ and $\gamma_{\mathrm{h}}^{(\mathrm{e}-\updownarrow-\mathrm{e})}$ in the Boltzmann equation (3.5) with a finite magnetic field.

Zero magnetic field

At zero magnetic field, as already mentioned, only processes involving at least two electrons contribute to the rates. Therefore, the amplitude of probability entering in the rate is in J^2 where J is the coupling constant between electrons and magnetic impurities (see 2.2.3). Hence, the rate is in J^4. In Ref. [37], the rates are derived in the case where the interactions between magnetic impurities is negligible ($T_{\mathrm{sg}} \ll T_K$, where T_{sg} is defined by (2.36)). In this regime,

$$\begin{aligned}\gamma_{\mathrm{e}}^{(\mathrm{e}-\updownarrow-\mathrm{e})}(E) = \int_{-\infty}^{+\infty} \mathrm{d}E' \int_{-\infty}^{+\infty} \mathrm{d}\varepsilon f(E')(1-f(E-\varepsilon))(1-f(E'+\varepsilon)) \\ \times K^{(\mathrm{e}-\updownarrow-\mathrm{e})}(\varepsilon, E, E', f)\end{aligned} \tag{3.88}$$

for electron-like quasi-particles and

$$\begin{aligned}\gamma_{\mathrm{h}}^{(\mathrm{e}-\updownarrow-\mathrm{e})}(E) = \int_{-\infty}^{+\infty} \mathrm{d}E' \int_{-\infty}^{+\infty} \mathrm{d}\varepsilon f(E')f(E+\varepsilon)(1-f(E'+\varepsilon)) \\ \times K^{(\mathrm{e}-\updownarrow-\mathrm{e})}(\varepsilon, E, E', f)\end{aligned} \tag{3.89}$$

for hole-like quasi-particles, where $K^{(\mathrm{e}-\updownarrow-\mathrm{e})}(\varepsilon, E, E', f)$ is the interaction Kernel for the electron-electron interaction mediated by Kondo impurities. For impurities of spin $S = 1/2$, the kernel reads

$$K^{(\mathrm{e}-\updownarrow-\mathrm{e})}(\varepsilon, E, E', f) \approx \varepsilon^{-2} \frac{3\pi^2}{4h} c_{\mathrm{MI}} \nu_F^3 J^4 \tag{3.90}$$

This expression gets modified by Kondo effect and, when $E, E' \gg \varepsilon \gg k_B T_K$, the coupling constant J has to be replaced by

$$\frac{8^{\frac{1}{4}}}{\nu_F}[\ln(E/k_BT_K)+\ln([E-\varepsilon]/k_BT_K)]^{-2}[\ln(E'/k_BT_K)+\ln([E'+\varepsilon]/k_BT_K)]^{-1/2} \tag{3.91}$$

Note that the case of strong interactions between magnetic impurities has also been derived in Ref. [83].

Finite magnetic field

In order to investigate quantitatively this second order process, one may apply an external magnetic field $B\boldsymbol{e_z}$ (with $\boldsymbol{e_z}$ a unitary vector) in order to lift the degeneracy between the impurity spin states in a controlled way.

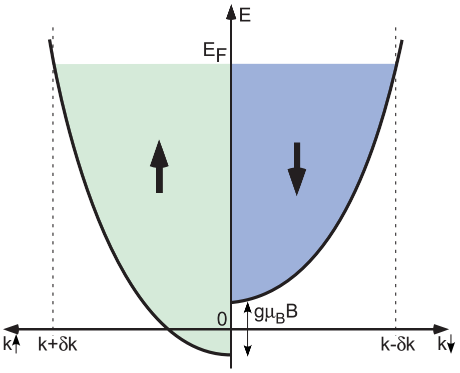

Fig. 3.25. Density of occupied electronic states in a metal under a magnetic field. Depending on the spin of the electrons, the densities of states differ (see Fig. 3 p. 842 from Ref. [123]).

If the electrons were independent, the effect of a magnetic field would only be to shift the densities of states of the electrons depending on their spin. Hence, the density of occupied states of the electrons whose spin is aligned with the magnetic field is $n(E)f(E)_\uparrow = \frac{1}{2}n(E - g\mu_B B/2)f(E)$ and for the opposite spins, $n(E)f(E)_\downarrow = \frac{1}{2}n(E + g\mu_B B/2)f(E)$, where $n(E)$ is just the metal density of states (see Fig. 3.25).

Interactions do not alter this global change in the populations of electrons, but the interaction rates $\gamma^{(\mathrm{e}-\updownarrow-\mathrm{e})}(E)$ get more difficult to work out. In Ref. [39], this calculation was performed in a regime where the electrons are excited well above k_BT_K ($eU \gg k_BT_K$), and for concentrations of spin 1/2 magnetic impurities c_{MI} low enough so that RKKY interactions are negligible (as defined by Eq. (2.36), $T \ll T_{\mathrm{sg}}$). Details of the calculation may be found also in Ref. [41]. Below, we will only present the main steps of the self-consistent calculation of the rates.

- One starts from a trial function $f_x(E)$. In the following, explicit reference to the position index x will not be specified.
- The populations of impurity spin $\uparrow$ or $\downarrow$ are calculated from the distribution function $f(E)$ and the magnetic field B.
- Using the single magnetic impurity spin operator basis $S^z, S^{\pm}$, and the two z electron spin states $|\uparrow\rangle$ and $|\downarrow\rangle$ one calculates the four renormalized coupling constants $J_{\updownarrow}^{z,\pm}(E)$ entering in the Hamiltonian

  $$\begin{aligned} H &= H_0 + H_c \\ H_0 &= \textstyle\sum_{k,\updownarrow} E_{k\updownarrow} c_{k\updownarrow}^{\dagger} c_{k\updownarrow} - g\mu_B B S^z \\ H_c &= \textstyle\sum_{k,k'} (J_{\uparrow}^{z} c_{k\uparrow}^{\dagger} c_{k'\uparrow} - J_{\downarrow}^{z} c_{k\downarrow}^{\dagger} c_{k'\downarrow}) S^z + J^{+} c_{k\downarrow}^{\dagger} c_{k'\uparrow} S^{+} + J^{-} c_{k\uparrow}^{\dagger} c_{k'\downarrow} S^{-} \end{aligned} \tag{3.92}$$

  where $c_{k\uparrow}^{\dagger}$ denotes the creation operator of an electron with wavevector k and spin $\uparrow$. The renormalization factor depends on the function $f(E)$ for each spin population.
- Using the renormalized coupling constants and the populations of electronic spin states, one can calculate the impurity spin correlator

  $$C(t) = [\,\underbrace{\overline{S^{+}(t)S^{-}(0)}}_{C_{+}(t)} + \underbrace{\overline{S^{-}(t)S^{+}(0)}}_{C_{-}(t)}\,]/2 + \underbrace{\overline{S^{z}(t)S^{z}(0)}}_{C_{z}(t)} \tag{3.93}$$

  whose Fourier transform is denoted by $\tilde{C}(\omega)$, and where $\bar{\cdot}$ denotes the average value on the occupied electron spin states.
- A new trial function $f(E)$ can be calculated using the Boltzmann equation and the following rates

  $$\begin{aligned} \gamma_{\mathrm{e}}^{(\mathrm{e}-\updownarrow-\mathrm{e})}(E) = \frac{c_{\mathrm{MI}}\nu_F}{8\hbar} \int_{-\infty}^{+\infty} & \mathrm{d}\varepsilon (1 - f(E-\varepsilon))[J^{-}(E)J^{+}(E-\varepsilon)\tilde{C}_{+}(\varepsilon/\hbar) \\ & + J^{+}(E)J^{-}(E-\varepsilon)\tilde{C}_{-}(\varepsilon/\hbar) \\ & + (J_{\uparrow}^{z}(E)J_{\uparrow}^{z}(E-\varepsilon) + J_{\downarrow}^{z}(E)J_{\downarrow}^{z}(E-\varepsilon))\tilde{C}_{z}(\varepsilon/\hbar)] \end{aligned} \tag{3.94}$$

  and

  $$\begin{aligned} \gamma_{\mathrm{h}}^{(\mathrm{e}-\updownarrow-\mathrm{e})}(E) = \frac{c_{\mathrm{MI}}\nu_F}{8\hbar} \int_{-\infty}^{+\infty} & \mathrm{d}\varepsilon f(E+\varepsilon)[J^{-}(E)J^{+}(E-\varepsilon)\tilde{C}_{+}(\varepsilon/\hbar) \\ & + J^{+}(E)J^{-}(E-\varepsilon)\tilde{C}_{-}(\varepsilon/\hbar) \\ & + (J_{\uparrow}^{z}(E)J_{\uparrow}^{z}(E-\varepsilon) + J_{\downarrow}^{z}(E)J_{\downarrow}^{z}(E-\varepsilon))\tilde{C}_{z}(\varepsilon/\hbar)] \end{aligned} \tag{3.95}$$

Recently, Glazman *et al.* have extended this calculation to all temperatures and energy regimes [124].

3.4.6 Paper on the Effect of magnetic impurities on energy exchange between electrons

We reproduce here our article published in Ref. [65]. The main result of this paper is a detailed quantitative comparison of measurement of energy relaxation in presence of a well controlled amount of magnetic impurities, with the theory of Ref. [39].

Effect of magnetic impurities on energy exchange between electrons

B. Huard, A. Anthore, Norman O. Birge, H. Pothier, D. Esteve

Published in Physical Review Letters, **95**, 036802 (2005)

Abstract

In order to probe quantitatively the effect of Kondo impurities on energy exchange between electrons in metals, we have compared measurements on two silver wires, with dilute magnetic impurities (manganese) introduced in one of them. The measurement of the temperature dependence of the electron phase coherence time on the wires provides an independent determination of the impurity concentration. Quantitative agreement on the energy exchange rate is found with a theory by Göppert *et al.* that accounts for Kondo scattering of electrons on spin-1/2 impurities.

Core of the paper

In diffusive metals, it is expected that the dominant inelastic electron scattering process at low temperature is the Coulomb interaction [2, 61], leading to a power law increase of the electron phase coherence time τ_φ with decreasing temperature T. However, in the presence of a small concentration of magnetic impurities with low Kondo temperature, τ_φ can be limited by spin-flip scattering, resulting in a nearly temperature independent phase coherence time over a broad temperature range [43]. As shown in Ref. [43], this mechanism could explain the apparent low-temperature saturation of τ_φ observed in many experiments, which caused a controversy in recent years [33, 78]. It was recently proposed that magnetic impurities also affect the energy exchange rate between electrons [37], which could explain the anomalous interaction rate observed in a series of experiments [34, 35]. A first hint that this proposal is relevant was the observation of a magnetic field dependence of the rate [40, 41], in a manner consistent with a theory taking into account the Kondo effect [39]. In those experiments, however, the nature and amount of magnetic impurities were not controlled. Assuming that the impurities were Mn, the concentrations needed to explain energy exchange experiments in silver wires were up to two orders of magnitude larger than the concentrations deduced from τ_φ measurements on similar samples [40, 41]. It was proposed that the samples for energy exchange rate measurements could have been contaminated during fabrication [40, 41]. Another hypothesis is that impurities other than Mn, which affect energy exchange rates more drastically then phase coherence, were present [125, 95]. Comparison of these proposals with existing experimental results is difficult because it requires dealing with more involved theories (large spin, surface anisotropy, large Kondo temperature), and pointless because it requires uncontrolled extra parameters. In order to overcome these difficulties and investigate quantitatively the mechanism proposed by Ref. [37], we have performed a comparative experiment described in this Letter, in which we probe the specific effect of the addition of 0.7 ppm (parts per million) of Mn atoms on energy exchange rate between electrons. We measured the temperature dependence of τ_φ on the same samples, accessing interactions in a complementary manner.

The scattering of electrons by magnetic impurities in metals is a many-body problem known as the Kondo effect: electrons tend to screen the spin of the impurity, leading to a renormalization of the scattering rate. The characteristic energy scale for this process is the Kondo temperature T_K. At $T \gtrsim T_K$, screening is incomplete, and spin-flip scattering takes place, whereas, at $T \ll T_K$, the impurity and the electrons form a singlet state, leading to potential scattering only. As far as electron dephasing is concerned, Kondo effect results in a maximal dephasing rate at T_K [84]. Kondo effect also provides a channel for efficient energy exchange between electrons scattering from the same magnetic impurity [37, 126, 127]. The rate of such a process depends on the energy of the states of the magnetic impurity, and is therefore sensitive to magnetic field because of the Zeeman effect [39]. The spin states of the magnetic impurities can furthermore be split in presence of spin-orbit scattering near an interface [128], which also modifies the rate. Further complication arises when the concentration of magnetic impurities is so high that the RKKY interaction between magnetic impurities constrains the spin dynamics [83, 88].

In order to test quantitatively the impact of magnetic impurities on energy exchange between electrons, we have compared the energy exchange rate and $\tau_\varphi(T)$ in two wires that differ only by the intentional addition of manganese impurities in one of them, with concentration low enough so that interactions between Mn impurities can be neglected [83]. To observe specifically the influence of the Mn impurities, the two samples were fabricated simultaneously on the same wafer. In a first step, a set of wires and their contact pads were patterned by e-beam lithography and evaporation of silver from a nominally 6N-purity source (99.9999% Ag from Alfa Aesar®). Mn^+ ions were implanted at 70 kV in half of them, using the ion implanter IRMA at CSNSM Orsay. The neutralization current from the sample holder to ground was monitored during the implantation, leading to a direct measurement of the number of implanted atoms. Monte Carlo simulations[25] yield the concentration of Mn atoms that stop inside the silver wire $c = 0.7 \pm 0.1$ ppm. In order to measure the energy exchange between electrons [34], a long and thin electrode forming a tunnel junction with the middle of the wire is used as a probe. This electrode

---

[25] Due to the finite thickness and width of the wire, out of four Mn ions impinging on the wire, only three stop inside it [129].

was patterned on individual chips in a second lithography step followed by evaporation of 3.5 nm of aluminum, oxidation, and evaporation of 16 nm of aluminum. We focus here on the results obtained on two wires, one without manganese added (labeled "bare" in the following), one with manganese added ("implanted"). For both samples, the wire length and cross-section area are $L = 40$ μm and $\mathcal{S}_e = 230$ nm $\times$ 42 nm. The samples were measured in a dilution refrigerator with base temperature of 20 mK. The low temperature wire resistance ($R = 55$ Ω) was identical for both wires, which yields the diffusion constant of electrons $D = 0.029$ m^2/s.

For each wire, we have first measured the magnetoresistance at temperatures ranging from 20 mK to 7 K. Following Ref. [117, 43], magnetoresistance curves are fit using the theory of weak localization, resulting in evaluations of the phase coherence time τ_φ. In the bare wire, it was important to take into account finite length corrections because τ_φ is comparable to the diffusion time $\tau_D = L^2/D \approx 56$ ns below 1 K [130], leading to a reduction of the predicted magnetoresistance by $\approx 30\%$ below 1 K. Reproducible conductance fluctuations were visible, so that the uncertainty in the determination of τ_φ becomes large below 60 mK in the bare sample. The spin-orbit time $\tau_{\mathrm{so}} \approx 8$ ps was extracted from the data above 1 K. The temperature dependence of τ_φ is shown in Fig. 3.26 for both wires. Below 1 K, τ_φ is smaller by nearly one order of magnitude in the implanted wire than in the bare one. In none of the samples does τ_φ increase as $T^{-2/3}$ when temperature is lowered, as would be expected if the electron-electron interaction was the dominant dephasing process (solid line labeled "pure" in Fig. 3.26). The apparent saturation of τ_φ is attributed to the presence of magnetic impurities [43]. This effect is quantified by a fit of the data with a sum of three terms:

$$\frac{1}{\tau_\varphi} = \mathcal{A}T^{2/3} + \mathcal{B}T^3 + \gamma_{\mathrm{sf}}(T), \tag{3.96}$$

with $\mathcal{A} = \frac{1}{\hbar}\left(\frac{\pi k_B^2}{4\nu_F L \mathcal{S}_e}\frac{R}{R_K}\right)^{1/3}$ describing Coulomb interaction [117], $\mathcal{B}$ electron-phonon interaction [78] and

$$\gamma_{\mathrm{sf}}(T) = \frac{c}{\pi\hbar\nu_F}\frac{\pi^2 S(S+1)}{\pi^2 S(S+1) + \ln(T/T_K)^2} \tag{3.97}$$

the spin-flip scattering rate, according to Nagaoka-Suhl formula[26] [43]. The density of states in silver is $\nu_F \approx 1.03 \times 10^{47}$ J^{-1}m^{-3} (2 spin states), the resistance quantum $R_K = h/e^2$, and the spin of the magnetic impurities S. Assuming that the only magnetic impurities present are Mn atoms, with $S = 5/2$ and $T_K = 40$ mK [131, 81] and that $\mathcal{A}$ is fixed at its theoretical value $\mathcal{A} = 0.19$ ns$^{-1}K^{-2/3}$, the best fits are obtained for $c_b = 0.10 \pm 0.01$ ppm and $\mathcal{B}_b \approx 3.7 \times 10^{-2}$ ns^{-1}K^{-3} for the bare wire, and $c_i = 0.95 \pm 0.1$ ppm,

---

[26] The width of the weak localization dip in the magnetoresistance, ≈ 10 mT, was small enough to neglect the variation of the spin-flip rate with magnetic field.

$\mathcal{B}_i \approx 5.5 \times 10^{-2}$ ns^{-1}K^{-3} for the implanted one [27]. The difference between the implanted and bare samples, $c_i - c_b = 0.85 \pm 0.1$ ppm, is in reasonable agreement with the estimated amount of implanted ions. The value of c_b is significantly larger than found in previous experiments [43], indicating a lesser quality of the source material or a slight contamination during fabrication.

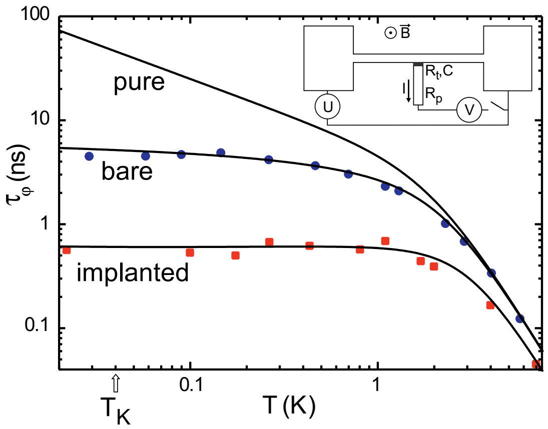

Fig. 3.26. (Color online) Symbols: measured phase coherence time in the two wires. Solid lines: best fits with Eq. (3.96), obtained with $c_b = 0.10 \pm 0.01$ ppm (bare wire) and $c_i = 0.95 \pm 0.1$ ppm (implanted wire). The upper line is the prediction without spin-flip scattering ($c = 0$). Inset: layout of the circuit. The switch is open for magnetoresistance measurements, closed for energy exchange measurements.

We have then measured the energy exchange rate between electrons and its dependence on magnetic field B on the same two wires. The principle of the experiment is to drive electrons out-of-equilibrium with a bias voltage $U \gg k_B T/e$. The distribution function $f(E)$ of the electrons in the middle of the wire depends crucially on energy exchange between electrons [34]. The differential conductance $\mathrm{d}I/\mathrm{d}V(V)$ of the tunnel junction between the wire and the probe electrode (inset of Fig. 3.26, switch closed; see also Ref. [40]) is a convolution product of $f(E)$ with a function $q(E)$ describing inelastic tunneling [40]:

$$R_t \frac{\mathrm{d}I}{\mathrm{d}V}(V) = 1 - \int f(E) q(eV - E) \mathrm{d}E \tag{3.98}$$

where R_t is the resistance of the tunnel junction. The information on $f(E)$ is therefore contained in $\mathrm{d}I/\mathrm{d}V(V)$ *via* the q function. The experiment is

---

[27] The difference between the $\mathcal{B}$ parameters is not understood, but it only affects the dependence of $\tau_\varphi(T)$ above 2 K, whereas the impurity concentrations c_i and c_b are determined by low-T behavior.

performed at $B \geq 0.3\ T$, and the aluminum probe electrode is in its normal state. The q function is obtained from $\mathrm{d}I/\mathrm{d}V(V)$ at $U = 0$, where $f(E)$ is a Fermi function. In this situation, $\mathrm{d}I/\mathrm{d}V(V)$ displays a sharp minimum at zero voltage (sometimes called "zero bias anomaly"), due to dynamical Coulomb blockade of tunneling [105]. The environmental impedance responsible for Coulomb blockade is the resistance R_p of the probe electrode. The conductance is reduced at $V = 0$ by a factor 0.78 in the bare sample and 0.62 in the implanted one. A slight (3% at most), unexpected dependence on B of $\mathrm{d}I/\mathrm{d}V(V)$ was observed on the implanted sample. In practice, we therefore derived a q function at each value of B from $\mathrm{d}I/\mathrm{d}V(V)$ taken at $U = 0$. Fits of $\mathrm{d}I/\mathrm{d}V(V)$ [132, 133] give the resistance of the environment $R_p = 0.95\ \mathrm{k\Omega}$ (respectively, $1.3\ \mathrm{k\Omega}$), the capacitance of the tunnel junction $C = 4.4$ fF (≈ 0.7 fF), the tunnel resistance $R_t = 16.5\ \mathrm{k\Omega}$ ($96.9\ \mathrm{k\Omega}$) and the temperature $T_0 = 45$ mK for the bare (implanted) sample. The differences in those parameters are essentially due to geometry, and do not interfere with the measurement of energy exchange between electrons in the wires. When electrons are driven out-of equilibrium ($U \neq 0$), $f(E)$ is not a Fermi function any longer. In the absence of energy exchange, $f(E)$ presents two steps at $E = -eU$ and $E = 0$, resulting in a splitting of the dip in $\mathrm{d}I/\mathrm{d}V(V)$ into two dips. In the opposite limit of very high energy exchange rate, $f(E)$ approaches a Fermi function at a temperature $T \approx \frac{\sqrt{3}}{2\pi}\frac{eU}{k_B}$, and $\mathrm{d}I/\mathrm{d}V(V)$ presents a broad dip [40].

In Fig. 3.27, we show the measured $\mathrm{d}I/\mathrm{d}V(V)$ characteristics of the tunnel junctions on the bare and implanted wires, for $U = 0.1$, 0.2 and 0.3 mV, and for B ranging from 0.3 T to 2.1 T by steps of 0.3 T. At $B = 0.3$ T, the measurements on the bare sample show two clear dips at $V = 0$ and $V = U$, whereas the measurements on the implanted sample show a single, broad dip around $V = U/2$. The addition of 0.7 ppm of Mn has therefore significantly increased the energy exchange rate between electrons, resulting in a strong energy redistribution during the diffusion time $\tau_D = 56$ ns. At $B = 2.1$ T, the broad dip found in the implanted sample has split into two dips for $U = 0.1$ and 0.2 mV, indicating that the energy exchange rate due to the Mn impurities is now smaller than $1/\tau_D$.

The coupling between electrons and magnetic impurities can be described by an exchange Hamiltonian, characterized by a coupling constant J. At zero magnetic field, this description leads to energy exchange in second order perturbation theory, as described in Ref. [37]. At finite magnetic field, the spin states of the impurities are split by the Zeeman energy $E_Z = g\mu_B B$. The energy E_Z can then be exchanged at the lowest order in perturbation theory between electrons and impurities. This approach is sufficient to understand qualitatively the magnetic field behavior: the rate of interaction decays rapidly when $E_Z > eU$, because very few electrons can excite the impurities. The magnetic fields $eU/g\mu_B$ (using $g = 2$ for Mn) are 0.86, 1.7 and 2.6 T for $U = 0.1$, 0.2 and 0.3 mV, which correspond in the implanted wire to the fields at which the curvature of $\mathrm{d}I/\mathrm{d}V(V)$ near $V = U/2$ changes sign. In the bare

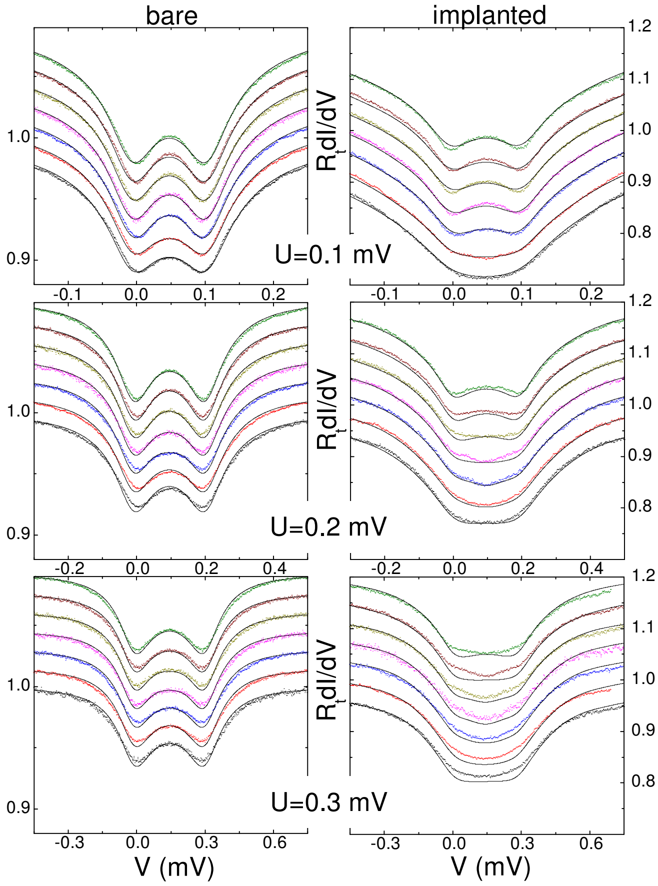

Fig. 3.27. (Color online) Differential conductance $\mathrm{d}I/\mathrm{d}V(V)$ of the tunnel junction (see inset of Fig. 3.26) for the bare (left) and implanted (right) wires, for $U = 0.1$ mV, 0.2 mV and 0.3 mV (top to bottom panels), and for $B = 0.3$ to 2.1 T by steps of 0.3 T (bottom to top in each panel). The curves were shifted vertically for clarity. Symbols: experiment. Solid lines: calculations using $c_b = 0.1$ ppm, $c_i = 0.95$ ppm and $\kappa_{ee} = 0.05\ \mathrm{ns}^{-1}\mathrm{meV}^{-1/2}$.

sample, the double dip also gets sharper when B is increased. This is an indication that, as inferred from $\tau_\varphi(T)$ measurements, this sample also contained some magnetic impurities. However, the corresponding energy exchange rate is always smaller than $1/\tau_D$, and $\mathrm{d}I/\mathrm{d}V(V)$ displays a double dip.

In order to compare quantitatively the measurements with theory, the renormalization of the coupling constant J by Kondo effect needs to be considered. Very roughly, this renormalization amounts to [37] $J_{\mathrm{eff}}/J \approx [\nu_F J \ln(eU/k_B T_K)]^{-1} \approx 3$. More precisely, J_{eff} depends on the distribution function $f(E)$, and only the full theory of Ref. [39] is able to quantify this effect and to treat the exchange Hamiltonian at all orders on the same footing. We have therefore solved the Boltzmann equation for $f(E)$ self-consistently, taking into account Coulomb interaction, electron-phonon interaction [36] and the effect of magnetic impurities in a magnetic field following the full theory of Ref. [39]. The concentration of magnetic impurities and the electron-phonon coupling were fixed at the values determined from the fit of $\tau_\varphi(T)$ [36]. We used $T_K = 40$ mK [131, 81] and $g = 2.0$ [134]. Note that theory assumes $S = 1/2$ whereas $S = 5/2$ for Mn atoms, but it is not expected that this difference has a large influence on energy exchange [125]. The intensity of Coulomb interaction alone could not be determined accurately from $\tau_\varphi(T)$, and since it was found that theory underestimates the intensity κ_{ee} of Coulomb interaction [112], κ_{ee} was used as a free parameter, common to both samples. A slight increase in temperature of the contact pads of the wire with U (0.76 K/mV) was taken into account [36]. We also included in the calculation a slight heating of the electrons in the probe electrode at the junction interface, due to the fact that R_p is not negligible compared to R_t. The corresponding temperature $T_p(U, V)$ of the electrons in the probe electrode is $T_p \approx 0.34$ K in the bare and 0.16 K in the implanted sample at the dips ($V = 0$ or U), at $U = 0.3$ mV where T_p is expected to be the largest. The differential conductance $\mathrm{d}I/\mathrm{d}V(V)$ was then computed using Eq. (3.98). The resulting curves are displayed as solid lines in Fig. 3.27. The best agreement between theory and all the data was found for $\kappa_{ee} = 0.05\ \mathrm{ns}^{-1}\mathrm{meV}^{-1/2}$. This value is larger than the prediction $\kappa_{ee}^{\mathrm{AAK}} = 0.016\ \mathrm{ns}^{-1}\mathrm{meV}^{-1/2}$ [2], as was repeatedly found in previous experiments [112]. A good overall agreement is found for both data sets, but some discrepancy appears for the implanted sample at $U = 0.3$ mV. We evaluated the sensitivity of the fits of the data on the implanted wire to the concentration c_i of the impurities, and found that the best agreement is obtained at $c_i = 0.9 \pm 0.3$ ppm, in good agreement with the value 0.95 ppm deduced from the data of Fig. 3.26.

In conclusion, in this comparative experiment, the observed effect of well-identified magnetic impurities on energy exchange is found to be in good quantitative agreement with the theory of Ref. [39], the concentration of impurities being fixed to the value deduced from the temperature dependence of the phase coherence time, which is also compatible with the expected value from implantation. This well-controlled experiment shows that the interaction mediated by dilute, low Kondo temperature magnetic impurities is well understood. However it remains that, in this experiment as in all previous ones, Coulomb interaction seems to be more efficient for energy exchange than predicted [112]. Open questions remain also on the contribution of Kondo effect to dephasing and energy exchange at energies below T_K [84], on the effect of the interactions between impurities at larger concentrations [83, 88] and on finite size effects [95].

This work was supported in part by EU Network DIENOW. We acknowledge the assistance of S. Gautrot, O. Kaitasov and J. Chaumont at the CSNSM in Orsay University, who performed the ion implantation. We gratefully acknowledge discussions with F. Pierre, H. Grabert, G. Göppert, A. Zawadowski and H. Bouchiat.

3.4.7 Comments on the paper

Since the writing of this paper, we have reconsidered the analysis of the weak localization measurements as summarized in Table 2.3. The calculations of the differential conductances of Fig. 3.27 with the newly determined concentrations of magnetic impurities are shown on Fig. 3.29. The agreement between theory and experiment does not change dramatically as compared to Fig. 3.27 where the concentrations which had been used were inconsistent with Table 2.3. In order to see the sensitivity of our measurement to the concentration in magnetic impurities c_{MI} in the implanted wire (which was found to be 0.65 ± 0.7 ppm in magnetoresistance measurements), the theoretical prediction for the conductance $\mathrm{d}I/\mathrm{d}V(V)$ at $B = 0.9$ T and $U = 0.2$ mV is plotted for various values of c_{MI} on Fig. 3.28. The sensitivity to the parameter κ_{ee} is investigated in the appendix (Figs. B.2,B.3). Finally, in order to emphasize the qualitative result of adding 0.65 ppm of Mn atoms to the bare wire, we show the raw experimental data taken at $U \approx 0.1$ mV for both wires at the extrema magnetic fields on Fig. 3.30. One surprising result is the slight modification in the conductance of the bare wire between low and high magnetic field. As shown on Fig. 3.31, this modification would have better been explained by the presence of a much larger amount of magnetic impurities than what was used on the actual comparison Fig. 3.29.

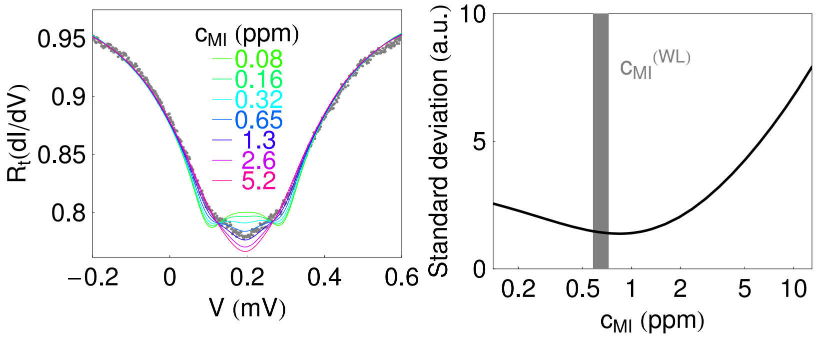

Fig. 3.28. Left panel–dots: differential conductance $\mathrm{d}I/\mathrm{d}V(V)$ of the tunnel junction for the implanted wire for $U = 0.2$ mV and $B = 0.9$ T. Left panel–lines: calculations using various values of c_{MI} and for $\kappa_{ee} = 0.05$ $\mathrm{ns}^{-1}\mathrm{meV}^{-1/2}$. Right panel: sum of all the standard deviations to the experimental curves corresponding to the implanted wire (gray dots of the right panels of Fig. 3.29) as a function of the used concentration c_{MI}. The result from weak localization experiments Table 2.3 is shown as a gray band.

In fact, this discrepancy between theory and experiment might be a signature of the decrease of the intensity of Coulomb interaction between electrons

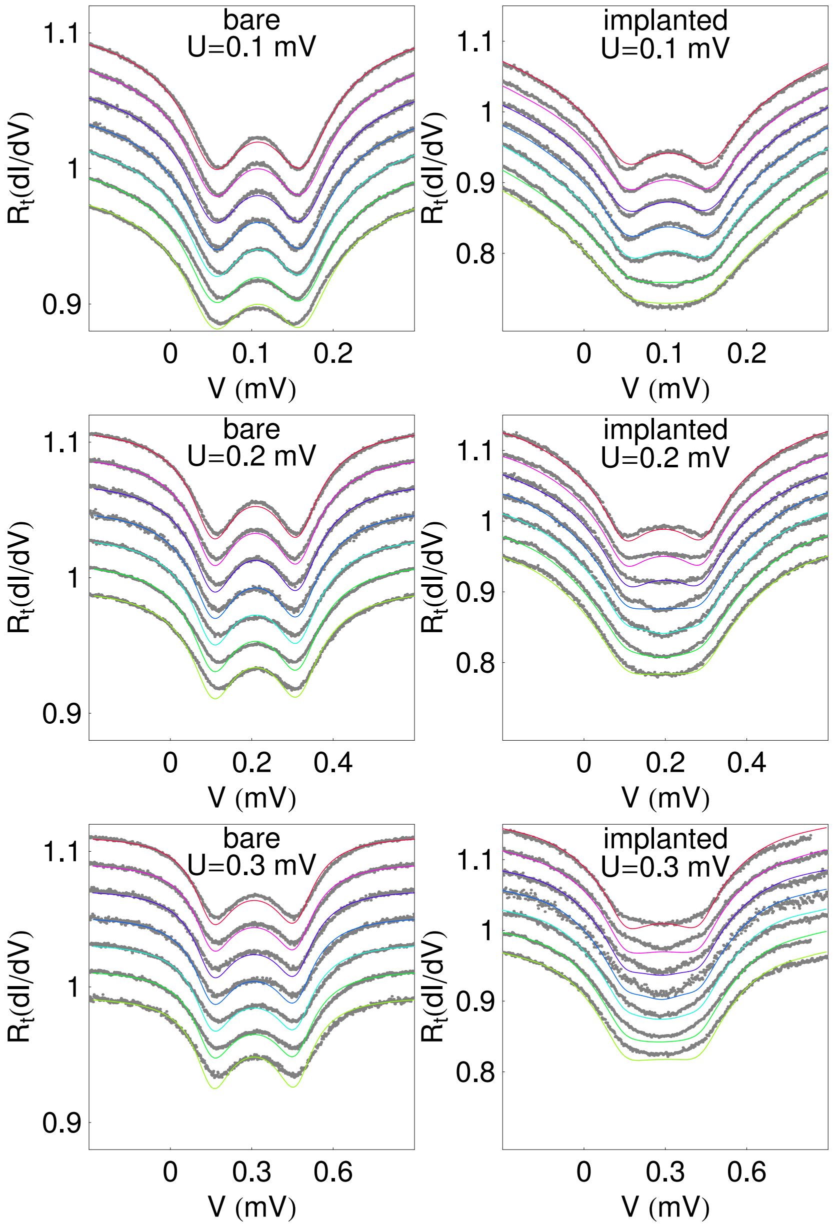

Fig. 3.29. Differential conductance $\mathrm{d}I/\mathrm{d}V(V)$ of the tunnel junction for the bare (left) and implanted (right) wires, for $U = 0.1$ mV, 0.2 mV and 0.3 mV (top to bottom panels), and for $B = 0.3$ to 2.1 T by steps of 0.3 T (bottom to top in each panel). The curves were shifted vertically for clarity. Symbols: experiment. Solid lines: calculations using $c_b = 0.02$ ppm, $c_i = 0.65$ ppm and $\kappa_{ee} = 0.05\ \mathrm{ns}^{-1}\mathrm{meV}^{-1/2}$.

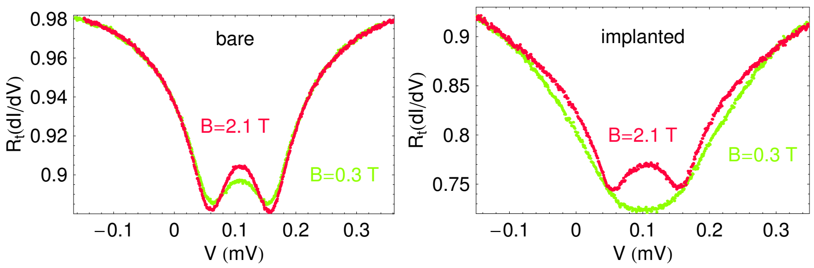

Fig. 3.30. Measured differential conductance $\mathrm{d}I/\mathrm{d}V(V)$ of the tunnel junction for $U = 0.1$ mV at extrema magnetic fields for both wires. The adding of 0.65 ppm Mn impurities leads to a dramatic change in the data at $B = 0.3$ T. By lifting the degeneracy between the spin states of the Mn impurities by a much larger amount than eU (which is the case for $B = 2.1$ T), the interactions between electrons come back to normal.

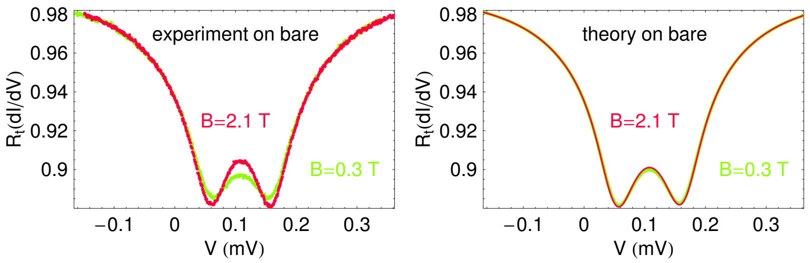

Fig. 3.31. Left panel: measured differential conductance $\mathrm{d}I/\mathrm{d}V(V)$ of the tunnel junction for $U = 0.1$ mV at extrema magnetic fields for the bare wire. Right panel: prediction for the same curves taken from Fig. 3.29. It is clear that a low concentration $c_{\mathrm{MI}} \approx 0.02$ ppm in the bare wire cannot explain the drastic change seen in the experiment between $B = 0.3$ T and $B = 2.1$ T.

when magnetic field increases. It is predicted that the Hartree term (3.51) diminishes when the magnetic field increases. The modification between the two curves of the left panel in Fig. 3.30 may thus be a measurement of the Hartree term. We calculated the prediction for the two experimental curves for the bare sample from Fig. 3.30 using the full kernel (3.52) for the interactions between electrons, using various values for F_0^σ. The result is shown on Fig. 3.32, and seems to indicate that, at the lowest magnetic field,

$$F_0^\sigma \approx -0.9. \tag{3.99}$$

If this is correct, that would mean that the silver is close to the ferromagnetic instability ($F_0^\sigma \approx -1$) which is in disagreement with previous measurements by conduction electron spin resonance leading to $F_0^\sigma \in [-0.21, 0.05]$ in silver [70].

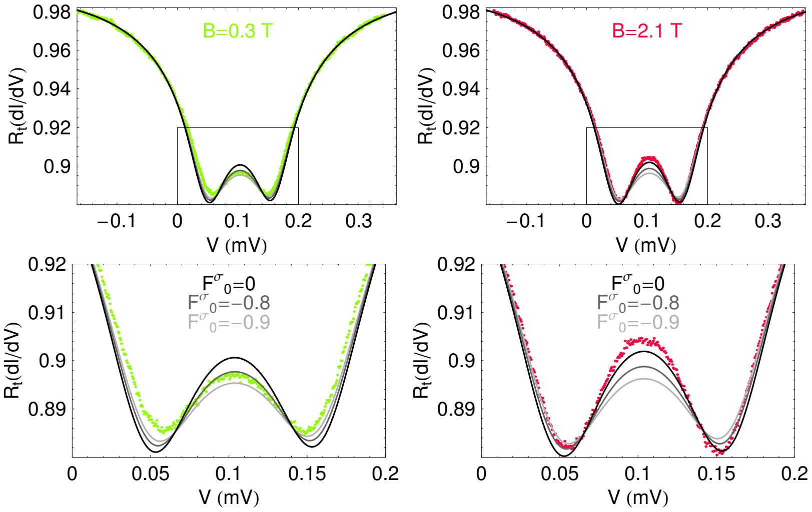

Fig. 3.32. Top panels–dots: experimental curves already shown on Figs. 3.31 for the bare wire at low and high magnetic fields. Top panels–lines: theoretical predictions for the differential conductance assuming that the Coulomb parameter is $\kappa_{ee} = 0.04\ \mathrm{ns}^{-1}\mathrm{meV}^{-1/2}$ for three values of F_0^σ. For these predictions, the full expression (3.52) for the rate of Coulomb interaction was used. Bottom panels: enlargement of the boxed region of the top panels.

3.5 Conclusions

We have performed a quantitative experiment probing the energy exchange rates between electrons in a metal. The process proposed by Kaminski and Glazman [37] for the exchange of energy between electrons mediated by magnetic impurities in the Kondo regime is quantitatively understood. A tiny concentration of magnetic impurities (less than 1 ppm) can lead to a dramatic decrease of the quasi-particle lifetime τ_E.

The main results of this chapter are the following:

- successful measurement of the distribution function of the electrons in a diffusive wire by tunneling spectroscopy using a superconductive or a normal probe electrode.
- the theory of Ref. [39] taking into account the role of magnetic impurities on the energy exchange between electrons as a function of the magnetic field has been quantitatively checked (see section 3.4.6).
- the intensity of the energy exchange between electrons is systematically higher than expected (Fig. 3.18). We have ruled out a possible explanation stating that the theory could not apply in out-of-equilibrium situa-

tions by performing a control experiment very close to equilibrium (see Fig. 3.20).

- observation of an unexplained dependence of the tunneling density of states at low voltages on the magnetic field (Fig. 3.12).
- the influence of the Hartree term to the energy exchange rate has been clarified (see section 3.4.1) and may be responsible for an observed effect Fig. 3.32.

In the future, the quantitative influence of the Hartree term on energy exchange could be investigated more thoroughly through the magnetic field dependence of inelastic processes involving electrons in a magnetic-impurity-free sample. Besides, it might be interesting to explore the role of the Hartree term on the zero bias anomaly in the tunneling.

Moreover, one misses an experiment probing the exchange of energies lower than $k_B T_K$ through the magnetic impurity mediated interaction between electrons. This could complete our picture on this interaction and test the results of Ref. [124].

Part II

Mesoscopic Josephson effects

Chapter 4

Landauer formalism

Contents

This chapter presents the Landauer formalism and applies it to various conductors.

4.1 Scattering approach

We follow here closely a discussion by Blanter and Büttiker ([52]) and refer the reader to this work for further information. Let us consider a fully phase-coherent conductor connected to two leads (left L and right R) only. Near the conductor, the transversal width of the leads is much smaller than the longitudinal one, so that quantization of electrons is mainly transverse. Electrons energy is still considered continuous as the longitudinal length is much longer than the Fermi wavelength. Thus, electrons of energy E are associated to fermionic operators[1] $\hat{a}_i^\dagger(E)$, with i varying from 1 to $M = \frac{k_F^2 S_e}{4\pi}$, where S_e is the section of the leads and k_F the Fermi wave vector. As the energy is the same for electrons moving in opposite directions at the same speed, two families of operators can be identified. By convention, $\hat{a}^\dagger$ creates electrons moving towards the conductor and $\hat{b}^\dagger$ outwards the conductor. Thus, in the leads near the conductor, electrons are described by the fermionic operators $\hat{a}_{i\alpha}^\dagger$ and $\hat{b}_{i\alpha}^\dagger$, where α is the lead index (L or R here). For convenience, we denote by $\mathbf{a}_\alpha^\dagger$ the vector $(\hat{a}_{1\alpha}^\dagger, \ldots, \hat{a}_{M\alpha}^\dagger)$ and the same for b.

---

[1] In all what follows, spin dependence is neglected, so that spin degeneracy just adds a factor 2 in the charge corresponding to each operator $\hat{a}_i^\dagger(E)$.

The conductor couples the incoming ($\hat{a}$) and outgoing ($\hat{b}$) operators by a unitary and symmetric[2] matrix **S** called the scattering matrix,

$$\begin{pmatrix} \mathbf{b}_{\mathrm{L}}^{\dagger}(E) \\ \mathbf{b}_{\mathrm{R}}^{\dagger}(E) \end{pmatrix} = \mathbf{S} \begin{pmatrix} \mathbf{a}_{\mathrm{L}}^{\dagger}(E) \\ \mathbf{a}_{\mathrm{R}}^{\dagger}(E) \end{pmatrix} ; \begin{pmatrix} \mathbf{b}_{\mathrm{L}}(E) \\ \mathbf{b}_{\mathrm{R}}(E) \end{pmatrix} = \mathbf{S}^{\dagger} \begin{pmatrix} \mathbf{a}_{\mathrm{L}}(E) \\ \mathbf{a}_{\mathrm{R}}(E) \end{pmatrix} . \tag{4.1}$$

The scattering matrix has a clearly interpretable block structure and reads $\begin{pmatrix} \mathbf{r(E)} & \mathbf{t(E)} \\ \mathbf{t(E)} & \mathbf{r(E)} \end{pmatrix}$. The diagonal matrix $\mathbf{r(E)}$ couples states of the same lead, thus it is called the reflection matrix, whereas $\mathbf{t(E)}$, coupling states of different leads, is called transmission matrix. As $\mathbf{t(E)}^{\dagger}\mathbf{t(E)}$ is hermitian, it can be diagonalized in a new basis of fermionic operators as a diagonal, real, and positive transmission matrix $\mathbf{T(E)}$. This new basis defines M independent "channels", each one being associated with a transmission coefficient τ_i, where $\mathbf{T(E)}_{ij} = \delta_{ij}\tau_i(E)$. This description is amazingly powerful, as all transport properties of the conductor depend on those M diagonal terms only. Moreover, the energy variation of the τ_i's is on the scale of E_F (a few thousands of Kelvins) which is always far bigger than other energy scales. Therefore, in the following, $\tau_i(E)$ will be denoted τ_i with no explicit reference to the energy E, and the set of transmission channels $\{\tau_i\}$ will be called the Personal Identification Number (PIN) of the conductor.

One of the most direct outcomes of this picture is the calculation of the average current from L to R. It is shown that

$$I = \frac{2e}{h} \int \mathrm{Tr}(\mathbf{T(E)})(f_L(E) - f_R(E))\mathrm{d}E \tag{4.2}$$

where $f_\alpha(E)$ is the occupation function of the states of energy E in the lead α and the factor 2 takes into account spin degeneracy. For big leads, $f_\alpha(E)$ is just a Fermi function, and one gets the conductance G of the coherent conductor,

$$G = 2G_K \sum_{i=1}^{M} \tau_i. \tag{4.3}$$

4.2 PIN of various conductors

In this section, we give the list of transmissions for various conductors. Some are the result of Random Matrix Theory (RMT) [135]. The principle of this calculation is to assume some probability distribution for the scattering matrices **S** of particular conductors from symmetry considerations, and to derive the probability distribution for the value of a transmission coefficient τ_i.

---

[2] The flux conservation in the scattering process implies that the matrix **S** is unitary.

Tunnel barrier

In a tunnel barrier, all channels see the same barrier width, and thus all the τ_i's are extremely small.

$$\forall i; \tau_i \ll 1 \tag{4.4}$$

For common tunnel junctions formed by oxidizing an aluminum thin film before being recovered by an aluminum counter electrode, τ_i is typically of the order of 10^{-6} as calculated from the typical values of the conductance of sub-micron junctions used in our experiments.

Diffusive wire

In the case of a fully phase-coherent diffusive wire of length L, the distribution[3] $P(\tau)$ of the channels transmissions can be calculated by RMT [136].

$$P(\tau) = \begin{cases} 0 & \text{if } \tau > 4\mathrm{e}^{-3L/2l_e} \\ \frac{2l_e}{3L} \frac{1}{\tau\sqrt{1-\tau}} & \text{otherwise} \end{cases} \tag{4.5}$$

where l_e is the mean free path of the electrons in the wire (see appendix Eq. (B.18) for the prefactor in the appendix). This distribution is named after Dorokhov [137].

Chaotic cavities

A chaotic cavity models situations where the conductor is a ballistic metal (very large mean free path) whose edges do not exhibit any particular symmetry. Quantum dots in 2 dimensional electron gas are such cavities. Such a conductor has a universal distribution of transmissions given by

$$P(\tau) = \frac{8}{\pi}\sqrt{\tau(1-\tau)} \tag{4.6}$$

Point and Atomic contacts

In the case where the conductor is realized as a constriction in a metal with transverse dimensions of the order of the Fermi wavelength, the number of channels is small. In bulk metals, atomic contacts can be fabricated, where the number of channels is the number of valence orbitals of the specific atom ([138]). Such systems are studied in chapter 5. In 2-dimensional metals, a constriction might be realized by varying a gate voltage and as few as one channel can describe such a Quantum Point Contact ([139, 140]).

---

[3] Recall that for transport to occur, L must be much smaller than the localization length (a coherent quasi 1-dimensional conductor of section S_e and length L is an Anderson insulator if L is smaller than the localization length $\xi = 4Ml_e/3$, where $M = \frac{k_F^2 S_e}{4\pi}$ is the number of channels), so the number of channel M is much larger than L/l_e and the distribution of the transmissions $P(\tau)$ is relevant.

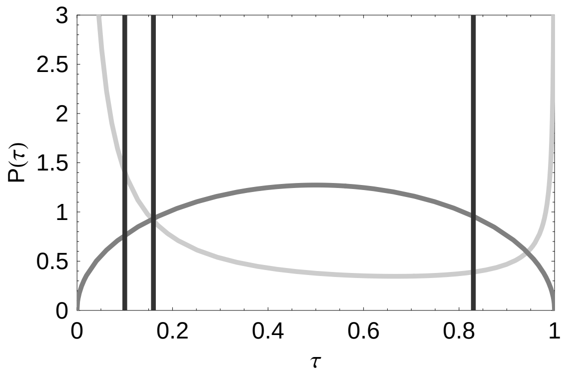

Fig. 4.1. Distribution of the transmissions τ_i for various conductors discussed in the text. Line ■ represents the diffusive wire case for $L = 5l_e$; line ■ represents the chaotic cavity case; line ■ represents the three channels of an Al atomic contact.

4.3 Limitations of Landauer formalism

The Landauer formalism requires two key assumptions to be valid.

First, the leads need to be “good”. Here “good” means that the operators $\hat{a}_L^\dagger(E)$ and $\hat{a}_R^\dagger(E)$ describing incoming left and right electrons need to be orthogonal. This is achieved if there is no link shorter than the phase coherence length L_φ between the left and right lead apart from the conductor. If there is one, this link can be included in the conductor to calculate the transport properties from left to right.

Second, the conductor must be phase coherent. That means that most of the electrons contributing to transport have to stay less than a time τ_φ in the conductor. This is the case for tunnel junctions or atomic point contacts. However, diffusive wires of length $L \ll L_\varphi$ might exhibit some deviation to the Landauer picture. For example, in the case of a normal (non-superconducting) wire between two superconducting leads, an electron can be reflected many times at the interfaces separating the wire and the leads. In this case, the actual time spent in the wire by this electron is much more than τ_φ and phase-coherence is broken.

This discussion shows the major role played by the phase coherence time τ_φ in understanding the limits of the Landauer formalism.

Chapter 5

Josephson effect through a coherent conductor

Contents

The word “coherence” is hazardous in physics as it covers a few parallel but distinct concepts. In particular, one distinguishes a fully coherent system, whose state can be described by one single complex order parameter $|\Delta|e^{i\varphi}$, from a (phase) coherent system, where each particle is in a different state, but remains phase coherent in the sense developed in chapter 2. At low temperatures, a large collection of bosons form a fully coherent system, as illustrated by the beautiful experiments on atomic Bose-Einstein condensates in the last decade. Superconductors and superfluids belong to the same class of fully coherent systems. In this part, we investigate the Josephson problem in which two fully coherent systems are connected by a small phase coherent link. In the kingdom of metals, this situation is obtained when one couples two superconductors of quantum phase φ_L and φ_R through a coherent conductor such as a tunnel junction.

The experiment we performed uses the smallest conductor: an atom between two leads. We focused in particular on the measurement of the current phase relation in these systems. This work was started in collaboration with Martin Chauvin, who did his PhD on this subject [21], and Maria Luisa Della Rocca, post-doc in the group.

5.1 Mesoscopic superconductivity

5.1.1 Bogoliubov-de Gennes theory for superconductivity

The adequate formalism to treat inhomogeneities in the phase φ of a superconductor is the so-called Bogoliubov-de Gennes theory of superconductivity. The Hamiltonian of this system contains a "normal" term

$$\mathcal{H}_\mathrm{N} = E_F \left(\frac{\hat{\boldsymbol{p}}^2}{\hbar^2 k_F^2} - 1 \right) + U(\hat{\boldsymbol{x}}),$$

where U is the static potential experienced by the electrons, and a superconducting term $\mathcal{H}_\mathrm{S}$ describing the attractive interaction between electrons leading to superconductivity. This last term is assumed to only couple counter-propagating electrons of opposite spin, with exactly opposite wavevectors. Choosing an arbitrary direction to quantize the spin, electrons with spin up are called *electron particles* and holes with spin down are called *hole particles.* The eigenvectors of the Hamiltonian are superpositions of electron and hole particles which can be denoted by

$$\begin{pmatrix} u_{\boldsymbol{k}} \\ v_{\boldsymbol{k}} \end{pmatrix} \Leftrightarrow \begin{array}{ll} \text{electron amplitude } \boldsymbol{k} \bullet \twoheadrightarrow & ; \text{spin} \uparrow \\ \text{hole amplitude } \boldsymbol{k} \quad\ \twoheadleftarrow \circ & ; \text{spin} \downarrow \end{array} \tag{5.1}$$

In this basis, $\mathcal{H}_\mathrm{S}$ couples electron and hole amplitudes. The coupling potential is nothing but the parameter order $|\Delta|\mathrm{e}^{i\varphi(\hat{\boldsymbol{x}})}$ of the superconductor. Therefore, the Schrödinger equation reads [141]

$$\begin{pmatrix} \mathcal{H}_\mathrm{N} & |\Delta|\mathrm{e}^{i\varphi(\hat{\boldsymbol{x}})} \\ |\Delta|\mathrm{e}^{-i\varphi(\hat{\boldsymbol{x}})} & -\mathcal{H}_\mathrm{N}^* \end{pmatrix} \begin{pmatrix} u_{\boldsymbol{k}} \\ v_{\boldsymbol{k}} \end{pmatrix} = E \begin{pmatrix} u_{\boldsymbol{k}} \\ v_{\boldsymbol{k}} \end{pmatrix} \tag{5.2}$$

and determines the electron and hole amplitudes $u_{\boldsymbol{k}}$ and $v_{\boldsymbol{k}}$ as a function of the energy E. In case the phase $\varphi(x)$ is constant and the potential $U(x) = 0$, this equation can be solved analytically. In the one-dimensional case, a basis of solutions is made of the vectors

$$\begin{pmatrix} u_k(x) \\ v_k(x) \end{pmatrix} = \begin{pmatrix} u_0 \\ v_0 \end{pmatrix} \mathrm{e}^{ikx} \tag{5.3}$$

where $|k|$ can take the two following values[1]

$$|k| = k_F \left(1 \pm \frac{|\Delta|}{E_F} \mathrm{sign}(E) \sqrt{|E/\Delta|^2 - 1}\right)^{1/2} \approx k_F. \tag{5.6}$$

where the square root of a negative number is by convention

$$\sqrt{-|\alpha|} \equiv i\sqrt{|\alpha|}.$$

The corresponding dispersion relation reads

$$E = \pm \sqrt{E_F^2 \left(\frac{k^2}{k_F^2} - 1\right)^2 + |\Delta|^2}. \tag{5.7}$$

The normalized associated eigenvectors verify then

$$\begin{cases} u_0^2 = \frac{\mathrm{e}^{2i\varphi}}{2} \left(1 \pm \mathrm{sign}(E)\sqrt{1 - |\Delta/E|^2}\right) \\ v_0^2 = \frac{1}{2} \left(1 \mp \mathrm{sign}(E)\sqrt{1 - |\Delta/E|^2}\right) \end{cases} \tag{5.8}$$

The normal state can be recovered by letting Δ go to zero. In this case, depending on the sign of $\pm$, the eigenvector is a pure electron ($\pm = 1 \Rightarrow v_0 = 0$) or a pure hole ($\pm = -1 \Rightarrow u_0 = 0$).

5.1.2 Andreev reflection

Wondering how heat could flow from a normal metal to a superconductor, Andreev realized that electrons incoming on the superconductor have a finite probability to be reflected as holes [142, 143]. The Bogoliubov-de Gennes formalism gives a simple way to calculate the amplitude of this event.

---

[1] Denoting $\Delta = |\Delta|\mathrm{e}^{i\varphi}$, one gets

$$\begin{cases} \Delta v = \left(E + E_F\left(1 + \frac{1}{k_F^2}\frac{\mathrm{d}^2}{\mathrm{d}x^2}\right)\right) u \\ \Delta^* u = \left(E - E_F\left(1 + \frac{1}{k_F^2}\frac{\mathrm{d}^2}{\mathrm{d}x^2}\right)\right) v \end{cases} \tag{5.4}$$

and looking for solutions of the type (5.3),

$$\begin{cases} \Delta v_0 = (E + E_F[1 - (k/k_F)^2]) u_0 \\ \Delta^* u_0 = \left(E - E_F[1 - (k/k_F)^2]\right) v_0 \end{cases} \tag{5.5}$$

Multiplying both equations, one finds two solutions for k^2 depending on energy, and dividing both equations, one finds an expression for u_0^2/v_0^2. The system being invariant by time reversal symmetry, wavevectors k and $-k$ are associated to the same energy E.

The NS interface can be modeled as a discontinuity in the parameter Δ from 0 in the normal metal ($x < 0$) to $\Delta \neq 0$ in the superconductor ($x > 0$). In the normal metal, the nullity of the gap leads to simple forms for the eigenstates of the Hamiltonian:

$$\text{electrons: } \begin{pmatrix} \mathrm{e}^{\pm i k_F x} \\ 0 \end{pmatrix} \text{ holes: } \begin{pmatrix} 0 \\ \mathrm{e}^{\mp i k_F x} \end{pmatrix} \tag{5.9}$$

where ± states for right going or left going particles. Let us denote a general state of energy E on the left side by

$$\begin{pmatrix} L^{(\mathrm{e})}_{\rightarrowtail} \mathrm{e}^{i k_F x} + L^{(\mathrm{e})}_{\leftarrowtail} \mathrm{e}^{-i k_F x} \\ L^{(\mathrm{h})}_{\leftarrowtail} \mathrm{e}^{i k_F x} + L^{(\mathrm{h})}_{\rightarrowtail} \mathrm{e}^{-i k_F x} \end{pmatrix} \tag{5.10}$$

with $L^{(\mathrm{e})}_{\rightarrowtail}, L^{(\mathrm{e})}_{\leftarrowtail}, L^{(\mathrm{h})}_{\leftarrowtail}, L^{(\mathrm{h})}_{\rightarrowtail}$ complex numbers. On the superconductor side (right), the states of energy E read

$$\begin{aligned} & R^{(\text{“e”})}_{\rightarrowtail} \begin{pmatrix} u_0^{(\mathrm{e})} \\ v_0^{(\mathrm{e})} \end{pmatrix} \mathrm{e}^{i k^{(\mathrm{e})} x} + R^{(\text{“e”})}_{\leftarrowtail} \begin{pmatrix} u_0^{(\mathrm{e})} \\ v_0^{(\mathrm{e})} \end{pmatrix} \mathrm{e}^{-i k^{(\mathrm{e})} x} \\ & \qquad + R^{(\text{“h”})}_{\leftarrowtail} \begin{pmatrix} u_0^{(\mathrm{h})} \\ v_0^{(\mathrm{h})} \end{pmatrix} \mathrm{e}^{i k^{(\mathrm{h})} x} + R^{(\text{“h”})}_{\rightarrowtail} \begin{pmatrix} u_0^{(\mathrm{h})} \\ v_0^{(\mathrm{h})} \end{pmatrix} \mathrm{e}^{-i k^{(\mathrm{h})} x} \end{aligned} \tag{5.11}$$

with $R^{(\text{“e”})}_{\rightarrowtail}, R^{(\text{“e”})}_{\leftarrowtail}, R^{(\text{“h”})}_{\rightarrowtail}, R^{(\text{“h}'')}_{\leftarrowtail}$ complex numbers.

The Andreev reflection of an electron is the process by which an electron-like particle is transferred into the superconductor. This condition reads formally $R^{(\text{“e”})}_{\leftarrowtail} = R^{(\text{“h”})}_{\rightarrowtail} = R^{(\text{“h”})}_{\leftarrowtail} = 0$, and sets strong constraints on the state in the normal metal. Indeed, the continuity of the wave function and of its first derivative at the NS interface provides[2] a single solution for the quasi-particle state in the normal electrode. The outgoing electronic part $L^{(\mathrm{e})}_{\leftarrowtail}$ and the incoming hole part $L^{(\mathrm{h})}_{\leftarrowtail}$ are negligible, and only two components remain: an

---

[2] We use the fact that amplitudes and their derivatives are equal at the interface $x = 0$, which gives four equations

$$\left\{ \begin{aligned} R^{(\text{“e”})}_{\rightarrowtail} u_0^{(\mathrm{e})} &= L^{(\mathrm{e})}_{\rightarrowtail} + L^{(\mathrm{e})}_{\leftarrowtail} \\ R^{(\text{“e”})}_{\rightarrowtail} k^{(\mathrm{e})} u_0^{(\mathrm{e})} &= k_F L^{(\mathrm{e})}_{\rightarrowtail} - k_F L^{(\mathrm{e})}_{\leftarrowtail} \\ R^{(\text{“e”})}_{\rightarrowtail} v_0^{(\mathrm{e})} &= L^{(\mathrm{h})}_{\rightarrowtail} + L^{(\mathrm{h})}_{\leftarrowtail} \\ R^{(\text{“e”})}_{\rightarrowtail} k^{(\mathrm{e})} v_0^{(\mathrm{e})} &= k_F L^{(\mathrm{h})}_{\rightarrowtail} - k_F L^{(\mathrm{h})}_{\leftarrowtail} \end{aligned} \right. \tag{5.12}$$

where the Andreev approximation $k^{(\mathrm{e})} \approx k^{(\mathrm{h})} \approx k_F$ has been used. Hence,

$$\left\{ \begin{aligned} L^{(\mathrm{e})}_{\leftarrowtail} / L^{(\mathrm{e})}_{\rightarrowtail} &= -\mathrm{sign}(E) \tfrac{|\Delta|}{4E_F} \sqrt{|E/\Delta|^2 - 1} \ll 1 \\ L^{(\mathrm{e})}_{\rightarrowtail} / R^{(\text{“e”})}_{\rightarrowtail} &\approx u_0^{(\mathrm{e})} \\ L^{(\mathrm{h})}_{\leftarrowtail} / L^{(\mathrm{h})}_{\rightarrowtail} &= -\mathrm{sign}(E) \tfrac{|\Delta|}{4E_F} \sqrt{|E/\Delta|^2 - 1} \ll 1 \\ L^{(\mathrm{h})}_{\rightarrowtail} / R^{(\text{“e”})}_{\rightarrowtail} &\approx v_0^{(\mathrm{e})} \end{aligned} \right. \tag{5.13}$$

incoming electron and an outgoing hole. The ratio between the hole and electron amplitude can be interpreted as a reflection coefficient: the probability amplitude for the Andreev reflection of an electron into a hole[3]:

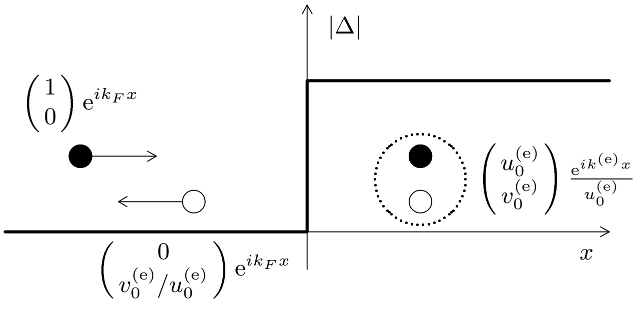

Fig. 5.1. Andreev reflection

$$a(E,\varphi)=\frac{v_0^{(\mathrm{e})}}{u_0^{(\mathrm{e})}}=\frac{1}{|\Delta|\mathrm{e}^{i\varphi}}\left(E-\operatorname{sign}(E)\sqrt{E^2-|\Delta|^2}\right) \tag{5.15}$$

In order to calculate the probability amplitude of reflection of a hole into an electron, one considers the case of an outgoing hole-like particle in the superconductor ($R_{\leftarrowtail}^{(\text{“e''})}=R_{\rightarrowtail}^{(\text{“e''})}=R_{\leftarrowtail}^{(\text{“h''})}=0$). The amplitude is then found to be $\frac{u_0^{(\mathrm{h})}}{v_0^{(\mathrm{h})}}=a(E,-\varphi)$.

5.1.3 Andreev bound states

Let us now consider two superconducting leads with a phase difference δ linked through a very short[4] coherent conductor. The conductor is fully characterized by the set of its transmission channels $\{\tau_1,\tau_2,\ldots\}$ (see chapter 4). The Landauer formalism allows to determine the properties of the conductor from the properties of a conductor with a single channel with transmission τ, which we propose to determine now.

---

[3] For energies E below the gap $|\Delta|$, the amplitude $a(E,\varphi)$ simplifies into

$$a(E,\varphi)=i\exp\left(-i[\varphi+\arcsin(E/|\Delta|)]\right) \tag{5.14}$$

[4] Smaller than the superconducting coherence length ξ, which provides a scale for the extension of Cooper pairs. In a diffusive link, $\xi=\sqrt{\hbar D/\Delta}$, and $\xi=\hbar v_F/\Delta$ in a ballistic one. For longer conductors, the decoupling of Andreev reflection and normal reflection parts that we will use is not valid.

The supercurrent through the conductor is carried by a discrete set of localized states called the *Andreev bound states.* In order to determine them, one uses the scattering matrix approach in the conductor and the Andreev reflections in the superconductor. Using the same notations for the coefficients as before, and assuming that $k \approx k_F$, whatever the state of the particle is, one can develop the Andreev bound states on the pure electron and hole states[5].

$$
\begin{array}{rc|cl}
|\psi_L\rangle = L^{(\mathrm{e})}_{\rightarrowtail} \mathrm{e}^{ik_F x}\begin{pmatrix}1\\0\end{pmatrix} & \rightarrow & \rightarrow & R^{(\mathrm{e})}_{\rightarrowtail} \mathrm{e}^{ik_F x}\begin{pmatrix}1\\0\end{pmatrix} = |\psi_R\rangle \\
+L^{(\mathrm{e})}_{\leftarrowtail} \mathrm{e}^{-ik_F x}\begin{pmatrix}1\\0\end{pmatrix} & \leftarrow & \leftarrow & +R^{(\mathrm{e})}_{\leftarrowtail} \mathrm{e}^{-ik_F x}\begin{pmatrix}1\\0\end{pmatrix} \\
+L^{(\mathrm{h})}_{\rightarrowtail} \mathrm{e}^{-ik_F x}\begin{pmatrix}0\\1\end{pmatrix} & \dashrightarrow & \dashrightarrow & +R^{(\mathrm{h})}_{\rightarrowtail} \mathrm{e}^{-ik_F x}\begin{pmatrix}0\\1\end{pmatrix} \\
+L^{(\mathrm{h})}_{\leftarrowtail} \mathrm{e}^{ik_F x}\begin{pmatrix}0\\1\end{pmatrix} & \dashleftarrow & \dashleftarrow & +R^{(\mathrm{h})}_{\leftarrowtail} \mathrm{e}^{ik_F x}\begin{pmatrix}0\\1\end{pmatrix}
\end{array}
\tag{5.16}
$$

The scattering matrix $\mathbf{S}$ of the conductor relates the pure electron parts and the pure hole parts of the left and right states in the following way[6]:

$$
\begin{pmatrix} L^{(\mathrm{e})}_{\leftarrowtail} \\ R^{(\mathrm{e})}_{\rightarrowtail} \end{pmatrix} = \mathbf{S} \begin{pmatrix} L^{(\mathrm{e})}_{\rightarrowtail} \\ R^{(\mathrm{e})}_{\leftarrowtail} \end{pmatrix} \quad \text{and} \quad \begin{pmatrix} L^{(\mathrm{h})}_{\leftarrowtail} \\ R^{(\mathrm{h})}_{\rightarrowtail} \end{pmatrix} = \mathbf{S}^\dagger \begin{pmatrix} L^{(\mathrm{h})}_{\rightarrowtail} \\ R^{(\mathrm{h})}_{\leftarrowtail} \end{pmatrix}
\tag{5.17}
$$

Besides, for the states to be localized at the interface, all the departing components of the states must be Andreev reflected back into arriving components. Hence,

$$
\begin{pmatrix} L^{(\mathrm{h})}_{\rightarrowtail} \\ R^{(\mathrm{h})}_{\leftarrowtail} \end{pmatrix} = \begin{pmatrix} a(E,\varphi_L) & 0 \\ 0 & a(E,\varphi_R) \end{pmatrix} \begin{pmatrix} L^{(\mathrm{e})}_{\leftarrowtail} \\ R^{(\mathrm{e})}_{\rightarrowtail} \end{pmatrix}
\tag{5.18}
$$

where φ_L and $\varphi_R = \delta + \varphi_L$ are the superconductor phases of the left and right leads respectively. And reciprocally,

$$
\begin{pmatrix} L^{(\mathrm{e})}_{\rightarrowtail} \\ R^{(\mathrm{e})}_{\leftarrowtail} \end{pmatrix} = \begin{pmatrix} a(E,-\varphi_L) & 0 \\ 0 & a(E,-\varphi_R) \end{pmatrix} \begin{pmatrix} L^{(\mathrm{h})}_{\leftarrowtail} \\ R^{(\mathrm{h})}_{\rightarrowtail} \end{pmatrix}
\tag{5.19}
$$

Combining all these equations, one finds a circular relation:

$$
\begin{pmatrix} L^{(\mathrm{h})}_{\rightarrowtail} \\ R^{(\mathrm{h})}_{\leftarrowtail} \end{pmatrix} = \begin{pmatrix} a(E,\varphi_L) & 0 \\ 0 & a(E,\varphi_R) \end{pmatrix} \mathbf{S} \begin{pmatrix} a(E,-\varphi_L) & 0 \\ 0 & a(E,-\varphi_R) \end{pmatrix} \mathbf{S}^\dagger \begin{pmatrix} L^{(\mathrm{h})}_{\rightarrowtail} \\ R^{(\mathrm{h})}_{\leftarrowtail} \end{pmatrix} .
\tag{5.20}
$$

Introducing the notation

---

[5] The pure electrons and holes are excited states of the superconductor. However, they form a basis for the particle states in the superconductor.

[6] Here, an essential assumption is that the length is small compared to ξ, so that one can neglect the Andreev processes within the channel.

$$\mathbf{M} = a(E,0)^2 \mathbf{S} \begin{pmatrix} 1 & 0 \\ 0 & \mathrm{e}^{-i\delta} \end{pmatrix} \mathbf{S}^\dagger \begin{pmatrix} 1 & 0 \\ 0 & \mathrm{e}^{i\delta} \end{pmatrix} \tag{5.21}$$

the later equation reads

$$\begin{pmatrix} L^{(\mathrm{h})}_{\rightarrowtail} \\ R^{(\mathrm{h})}_{\leftarrowtail} \end{pmatrix} = \mathbf{M}^{-1} \begin{pmatrix} L^{(\mathrm{h})}_{\rightarrowtail} \\ R^{(\mathrm{h})}_{\leftarrowtail} \end{pmatrix} . \tag{5.22}$$

Therefore, the Andreev bound states are entirely determined by the eigenvectors of $\mathbf{M}$ associated to an eigenvalue 1. Since $\mathbf{M}$ has 2 dimensions, at most two vectors are enough to generate all the Andreev bound states.

For a transmission τ, the scattering matrix reads $\mathbf{S} = \begin{pmatrix} -ir & t \\ t & -ir \end{pmatrix}$ with r and t real numbers such that $t^2 = \tau$ and $r^2 = 1 - \tau$. Hence,

$$\mathbf{M} = a(E,0)^2 \begin{pmatrix} r^2 + \mathrm{e}^{-i\delta} t^2 & irt(\mathrm{e}^{i\delta} - 1) \\ irt(\mathrm{e}^{-i\delta} - 1) & r^2 + \mathrm{e}^{i\delta} t^2 \end{pmatrix} . \tag{5.23}$$

From Eq. (5.22), for an Andreev bound state of energy E to be non-zero, 1 has to be an eigenvalue of $\mathbf{M}$. Therefore,

$$\det(\mathbf{M} - \mathbf{I}) = 0 \tag{5.24}$$

which leads to

$$1 - 2a(E,0)^2(1 - 2\tau \sin^2(\delta/2)) + a(E,0)^4 = 0 \tag{5.25}$$

Using Eq. (5.15), one gets only two possible values for the energy E:

$$\boxed{E_{|\tau_\pm\rangle} = \pm|\Delta|\sqrt{1 - \tau \sin^2(\delta/2)}} \tag{5.26}$$

The two orthonormal generating states of the set of Andreev bound states are associated with these energies and are denoted $|\tau_\pm\rangle$. The energy spectrum $E_{|\tau_\pm\rangle}(\delta)$ is shown on Fig. 5.2 for three values of τ. The spectrum of the Andreev states is the central prediction of the general theory of the Josephson effects in short conductors, from which all the transport properties can be derived [17, 18, 19, 20]. In the following, we discuss an experiment in which three transport properties are measured: the current-phase relation, the inductance-phase relation and the current-voltage characteristics.

5.1.4 Measurable quantities deduced from the Andreev spectrum

Current-phase relation

The phase difference δ between the two superconductive electrodes is the conjugated operator of the number $\hat{N}$ of Cooper pairs having passed through the coherent conductor:

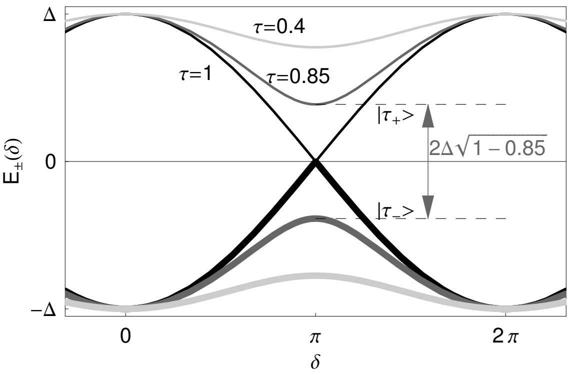

Fig. 5.2. Energy spectrum of the Andreev bound states for three values of the transmission τ of the single channel of the conductor. The minimum gap between Andreev bound states is obtained at $\delta = \pi$ and is given by $2\Delta\sqrt{1-\tau}$.

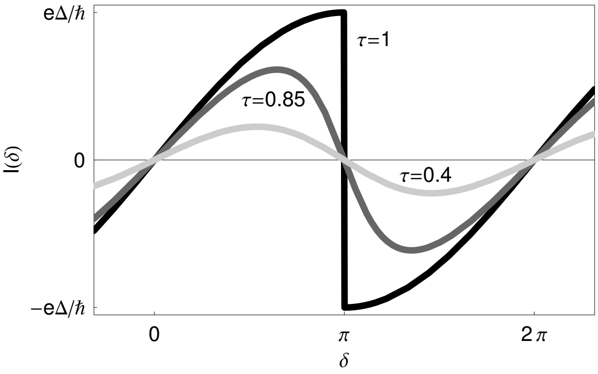

Fig. 5.3. Phase driven supercurrent through a single channel for three transmissions $\tau = 1, 0.85$ or 0.4.

$$[\delta, \hat{N}] = i. \tag{5.27}$$

As a consequence, each one of the two Andreev bound states of a channel carries a supercurrent given by

$$I_\tau(\delta) = \frac{1}{\varphi_0}\frac{\partial E_{|\tau\pm\rangle}}{\partial \delta} \tag{5.28}$$

where $\varphi_0 = \hbar/2e$, and I_τ and $E_{|\tau\rangle}$ are the quantum average of the current and energy. If the temperature is such that $k_B T \ll 2\Delta\sqrt{1-\tau}$ which is the splitting of the Andreev bound states (Fig. 5.2), the system is in the Andreev ground state $|\tau_-\rangle$ and the supercurrent reads (see Fig. 5.3)

$$\boxed{I_\tau(\delta) = \frac{e\Delta}{2\hbar}\frac{\tau\sin(\delta)}{\sqrt{1-\tau\sin^2(\delta/2)}}} \tag{5.29}$$

Case of a tunnel junction

The consistency of this result can be checked on the tunnel junction. According to Eq. (4.4), all channels are very weakly transmitted, so that the total current is approximated by

$$I(\delta) = \sum_i \frac{e\Delta}{2\hbar}\tau_i \sin(\delta) = \frac{R_K}{R_t}\frac{e\Delta}{4\hbar}\sin(\delta) \tag{5.30}$$

with R_t the resistance of the junction in the normal state (high enough temperature, voltage or magnetic field). Using Eq. (4.3), one gets the Josephson relation

$$I(\delta) = I_0 \sin(\delta) \tag{5.31}$$

where the critical current I_0 is given by

$$I_0 = \frac{\pi}{2}\frac{\Delta}{eR_t} \tag{5.32}$$

which is the Ambegaokar-Baratoff relation at zero temperature [144].

Diffusive conductor

If the length L of a diffusive constriction is much smaller than the phase coherent length L_φ the distribution of the transmissions is given by the Dorokhov distribution (4.5). If the length is also much smaller than the superconducting coherence length ξ, so that the Andreev reflections within the conductor can be neglected, the current-phase relation is:

$$I(\delta) = M\int_0^1 I_\tau(\delta)P(\tau)\mathrm{d}\tau = \frac{2Ml_e}{3L}\int_0^1 \frac{\mathrm{d}\tau}{\tau\sqrt{1-\tau}} I_\tau(\delta) \tag{5.33}$$

where M is the number of channels, and where the contribution of I_τ at phases $\delta < 4\mathrm{e}^{-3L/2l_e}$ has been neglected. Using Eq. (4.3), one can link M to the conductance in the wire, and find $M\frac{2l_e}{3L} = \frac{Gh}{4e^2}$. Hence,

$$I(\delta) = \frac{Gh}{4e^2}\frac{e\Delta}{2\hbar}\sin(\delta)\int_0^1 \frac{\mathrm{d}\tau}{\sqrt{1-\tau}\sqrt{1-\tau\sin^2(\delta/2)}} \tag{5.34}$$

which simplifies into

$$I(\delta) = \frac{\pi\Delta}{2e}Gf(\delta) \tag{5.35}$$

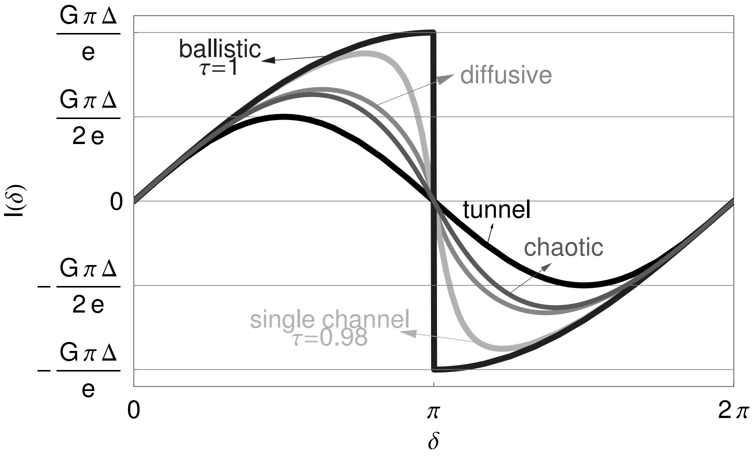

Fig. 5.4. Current-phase relation for various short conductors. As seen on this curve, the sine behavior for a tunnel junction is an exception. The result for diffusive (respectively chaotic) conductor can be approximated by the one of a single channel with transmission 0.8 (resp. 0.7).

where

$$f(\delta) = \frac{1}{2}\sin(\delta)\int_0^1 \frac{\mathrm{d}\tau}{\sqrt{1-\tau}\sqrt{1-\tau\sin^2(\delta/2)}}. \tag{5.36}$$

Using the same technique, one can predict the current-phase relation of any short coherent conductor (see Fig. 5.4).

Inductance-phase relation

Let us now consider the case where the phase δ is not fixed, but is oscillating with a small amplitude and frequency so that, again, only the ground state is occupied. The voltage is linked to the phase by definition:

$$V \equiv \varphi_0 \frac{\partial \delta}{\partial t}. \tag{5.37}$$

One can write

$$V = \varphi_0 \frac{1}{\partial I_\tau / \partial \delta} \frac{\partial I_\tau}{\partial t} = L_\tau(\delta)\frac{\partial I_\tau}{\partial t} \tag{5.38}$$

which shows that the conductor can be seen as an non-linear inductor of inductance (see Fig. 5.5)

$$L_\tau(\delta) = \varphi_0^2 \left(\frac{\partial^2 E_{|\tau_-\rangle}}{\partial \delta^2}\right)^{-1}. \tag{5.39}$$

Note that $L_\tau(\delta)$ is not always positive and diverges at the phase δ where $I_\tau(\delta)$ is extremal ($\delta_{\max}$ and $2\pi - \delta_{\max}$ with the notations of section B.4.1).

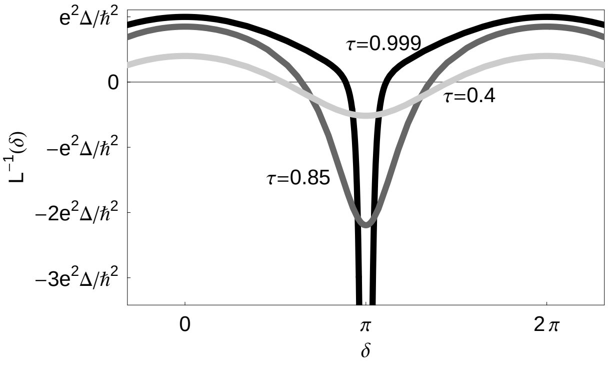

Fig. 5.5. *Inverse* of the non-linear Josephson inductance as a function of the phase difference δ of a single channel plotted for three values of the transmission $\tau = 0.999, 0.85$ and 0.4.

Tunnel junction

Similarly to the current phase relation, one can predict the inductance phase relation for a tunnel junction. In this case,

$$L_\tau(\delta) = \frac{\varphi_0}{I_0 \cos(\delta)}. \tag{5.40}$$

Current-voltage characteristic

When the conductor is biased at a constant voltage, the phase increases in average at a speed set by Eq. (5.37). As the phase evolves in the potentials $E_{|\tau\pm\rangle}(\delta)$, Landau-Zener transitions from the ground to the excited Andreev bound state can occur [18, 20]. The complex dynamics of the phase leads to an average current which can be calculated without actually solving the full phase dynamics. At voltages lower than twice the superconducting gap, only multiple charges can be transferred through the conductor through multiple Andreev reflections (MAR) processes. Conjugating MAR processes and standard scattering, one can derive the I-V characteristic of a single channel [145, 146, 18, 17, 20, 21]. We reproduce on Fig. 5.6 the (numerical) result for several values of the transmission. Non-linearities are observable at $eV = 2\Delta/n$ where n is an integer. Indeed, when the voltage exceeds $2\Delta/en$, a new charge carrying process becomes available: the MAR of order n. A MAR process of order n transfers n charge quanta from one lead to the other. At order n, the gap 2Δ can thus be crossed only if $ne|V| > 2\Delta$. Besides, the probability of charge transfers of order n is proportional to τ^n and thus rapidly decreases for increasing n.

The high non-linearity of the $I(V)$ curves allows to access the transmissions of a conductor with a few channels by fitting its $I(V)$ curve with the sum of the $I(V)$ curves of several channels. Current-voltage characteristics measured on atomic contacts by several groups were found to be in agreement with this theory (see Ref. [46] for a review). In particular, quantitative independent experiments (for example on the noise [14]) agree on the values of the transmissions measured by this technique.

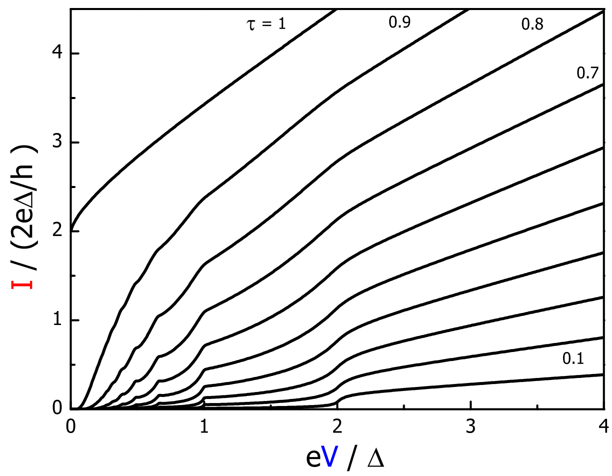

Fig. 5.6. Calculated normalized current-voltage characteristics of single channel conductors between two superconducting leads. Values of the transmission τ are plotted from 0.1 to 1.

5.2 Current-phase relation measurement

We have carried out experiments designed to probe the Josephson effect through short conductors with a few channels. As already mentioned, the conductors we used are aluminum atomic contacts whose transmissions can be modified *in situ* by changing the stress on the aluminum constriction (see section 9.1.3). It has been established that the number of channels in a one-atom contact corresponds to the number of valence orbitals of the atom [147]. Therefore, conductors with a few channels are genuinely fabricated using atomic contacts.

Measuring the current phase relation between two superconductors connected through a weak link has been the topic of a long standing research activity. The first measurement of Anderson and Rowell in 1963 demonstrated the current phase relation of a tunnel junction [16] and observed what Josephson had just predicted one year before [15]. More recently, the current-phase relation has been measured for a ferromagnetic weak link and a dephasing by

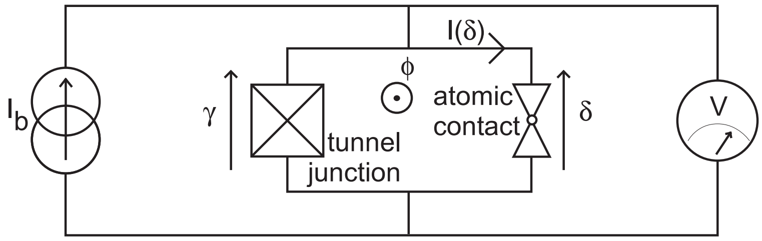

Fig. 5.7. Scheme of the atomic contact experiment. A superconducting loop encloses the atomic contact and a Josephson junction. The loop is biased by a current source I_b and the voltage V across the junction can be measured.

π of the relation for a normal tunnel junction was observed [148]. Measuring the current-phase relation in atomic contacts or quantum point contact has been performed by Koops *et al.* in 1996 [149]. In their experiment, they observed non-sinusoidal current-phase relation similar to what is predicted on Fig. 5.4. However, since they did not measure the I-V characteristics of the atomic contacts, they were not able to determine the PIN of the contacts, and thus to perform a quantitative test of the theory.

The aim of the experiments we have performed is to measure the current-phase relation in well characterized contacts, by measuring both the transmission of the channels from the current-voltage characteristics and the current-phase relation. The first measurement requires to voltage or current bias the atomic contact, whereas the second requires to phase bias the contact. Placing a big superconducting Josephson junction in parallel with the atomic contact, one can conjugate these apparently exclusive biasing schemes. In the setup of Fig. 5.7, a superconducting loop is formed by the parallel combination of the atomic contact and of a large[7] tunnel junction. Ideally, in the "zero-voltage state" of the junction, the atomic contact is phase biased by the flux threading the loop, whereas at finite voltage, when the junction is in its "voltage state" it is voltage biased.

In order to understand the phase biasing better, we first present the dynamics of Josephson junctions.

5.2.1 Josephson junction dynamics

The dynamics of Josephson junctions has been studied extensively both experimentally and theoretically in the last decades, and more recently in the context of superconducting q-bits [150, 151]. The only degree of freedom for

---

[7] Here, large means that the supercurrent I_0 of Eq. (5.32) is much larger than the current $I(\delta)$ through the atomic contact. We will see later how it simplifies the interpretation of the data.

the state of a junction is the phase difference γ across it[8]. We already calculated the supercurrent $I(\gamma)$ through a tunnel junction (5.31). Assuming that the junction is current biased by a current sI_0 where the critical current I_0 is given by (5.32), and $0 < s < 1$ is a real parameter, the energy U of the system made of the Josephson junction and the current source (see Fig. 5.8) reads

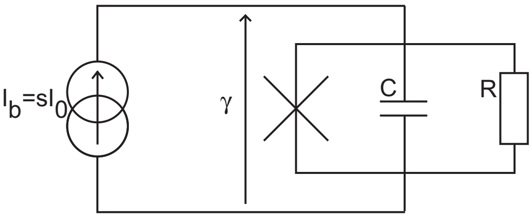

Fig. 5.8. Model for the Josephson junction alone in presence of an RC environment.

$$U(\gamma) = -\varphi_0 I_0 \cos(\gamma) - \varphi_0 I_0 s\gamma. \tag{5.41}$$

where $\varphi_0 I_0 s\gamma$ is the integrated work of the current source. Notice that derivating this expression with respect to γ leads to the Josephson relation Eq. (5.31). This potential is shown on Fig. 5.9.

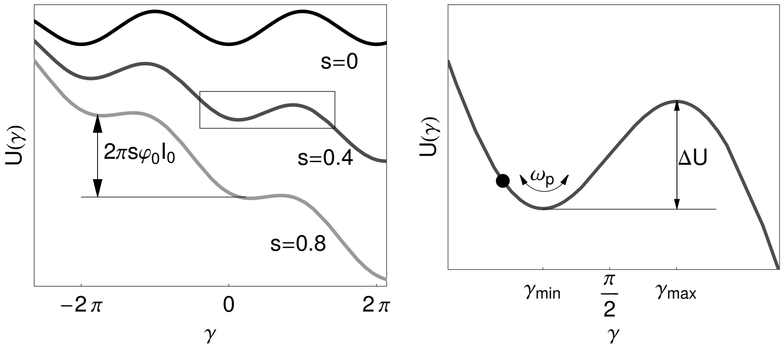

Fig. 5.9. Left panel: Energy potentials of a Josephson junction for three values of the bias current. Right panel: enlargement of the area enclosed by the box on the left plot. The phase oscillates at the plasma frequency ω_p around the minimum at $\gamma_{\min}$.

---

[8] This is true in the case where the charging energy $E_C = e^2/2C$ is much smaller than the Josephson energy $E_J = \varphi_0 I_0$. In our case, $E_C \approx 10^{-6} E_J$.

Classical analogy

In a classical picture, the phase can be mapped onto the position of a marble evolving on a one dimensional playground whose vertical profile is given by the potential $U(\gamma)$. When the marble gets trapped into a well (local minimum of the potential), it oscillates at a characteristic frequency called the plasma frequency ω_p. Friction tends to stop the marble in the bottom of the well. A real kid's marble indeed stops in the bottom of wells. This is due to the fact that the thermal fluctuations of the playground are several orders of magnitude smaller than what is needed to have the marble go over the barrier of the well. For the phase γ of the junction, the thermal energy $k_B T$ is not negligible compared to the barrier height ΔU so that the oscillations of the phase never stop.

Not only are the fluctuations in phase sizeable on the scale of the barrier height, but also is there a finite probability $P_t(s)$ for the marble to go over the barrier and escape the well in a time t. This probability is set by a rate $\mathit{\Gamma}(s)$ according to

$$P_t(s) = 1 - \mathrm{e}^{-\mathit{\Gamma}(s)t} \tag{5.42}$$

where the rate $\mathit{\Gamma}$ is given by an Arrhenius-like activation law [152]:

$$\mathit{\Gamma}(s) = \underbrace{\lambda(Q)\frac{\omega_p(s)}{2\pi}}_{A}\ \underbrace{\mathrm{e}^{-\Delta U(s)/k_B T_{\mathrm{esc}}}}_{\mathrm{e}^{-B}} \tag{5.43}$$

where $\lambda(Q)$ takes into account the friction and is given below and where T_{esc} is called the escape temperature. In the thermal regime, T_{esc} is the temperature of the electromagnetic environment of the Josephson junction. The barrier height is approximately[9]

$$\Delta U(s) = \frac{4\sqrt{2}}{3}\varphi_0 I_0 (1-s)^{3/2} + O\left((1-s)^{5/2}\right) \tag{5.45}$$

and the plasma frequency ω_p is given by the curvature of the potential at the bottom of the well:

$$\omega_p(s) = \omega_0 (1-s^2)^{1/4} \tag{5.46}$$

with $\omega_0 = \sqrt{\frac{I_0}{\varphi_0 C}}$, where C is the parallel capacitance (see Fig. 5.8).

After having escaped, the marble starts to fall off the well. Then, two dynamic regimes can occur. In absence of friction, like when the marble evolves

---

[9] The Taylor series of $\sqrt{2}\Delta U(s)(1-s)^{-1/2}$ in powers of $(1-s)$ is given by

$$\Delta U(s) = \frac{4\sqrt{2}}{3}(1-s)^{3/2} + \frac{\sqrt{2}}{15}(1-s)^{5/2} + O\left((1-s)^{7/2}\right) \tag{5.44}$$

in vacuum, the marble will gain enough kinetic energy to go over the next barrier, and will run away indefinitely. In the opposite limit, with strong friction, like when the marble evolves in water, the marble may lose enough kinetic energy by friction so that it cannot go over the next barrier, and it gets trapped in the next well. The transition between those two dynamic regimes is parameterized by a real parameter: the quality factor Q which, for the model of Fig. 5.8, is just $Q = RC\omega_p$. In this classical picture, the two regimes are:

- Underdamped regime ($Q \gg 1$): the marble runs away indefinitely as soon as it escapes a well. The junction is said to *switch*, since a permanent voltage suddenly develops according to Eq. (5.37).
- Overdamped regime ($Q \lesssim 1$): the marble can get trapped in a new minimum soon after having escaped from one well. In some cases, the phase can run away in a diffusive motion, stopping in wells for some time before starting to fall continuously.

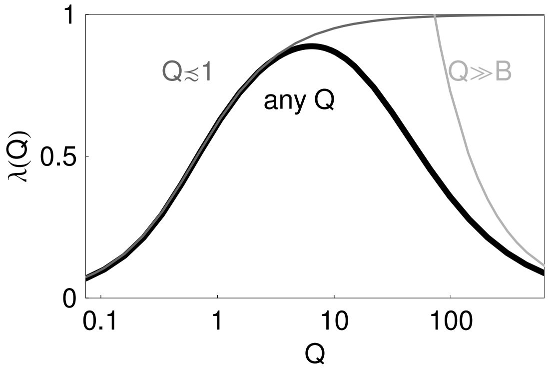

Fig. 5.10. Dark line: theoretical correction $\lambda(Q)$ to the prefactor A in the rate (5.43) using $B = \Delta U/k_B T_{\mathrm{esc}} = 10$. Gray lines: limit behaviors as derived by Kramers in 1940.

Friction introduces a correction in the prefactor of the rate, which was already derived by Kramers in 1940 in the limit regimes [153, 154]

$$\begin{aligned}\lambda(Q) &= \kappa(Q)\exp\left(\tfrac{1}{\pi}\textstyle\int_{-\infty}^{\infty}\tfrac{\mathrm{d}y}{1+y^2}\ln(1-\mathrm{e}^{-\Delta E(1+y^2)/4k_BT_{\mathrm{esc}}})\right)\\ &= \begin{cases}\kappa(Q) & \text{if } Q \lesssim 1\\ \frac{36}{5Q}\frac{\Delta U(s)}{k_BT_{\mathrm{esc}}} & \text{if } Q \gg \frac{\Delta U(s)}{k_BT_{\mathrm{esc}}}\end{cases}\end{aligned} \tag{5.47}$$

with

$$\kappa(Q) = \frac{1}{2Q}\left(\sqrt{1+4Q^2}-1\right) \tag{5.48}$$

where ΔE is the average reduction of energy due to friction during the trajectory of the particle starting from the barrier top, traversing the potential well once and returning in the vicinity of the barrier top[10].

Classical to quantum escape

We have described how thermal fluctuations can cause the junction to switch. Of course, quantum physics states that the phase might also tunnel across the potential barrier without going over it. The corresponding tunneling rate can be calculated for the particular potential $U(\gamma)$ and is well approximated, in the underdamped regime, by [155]

$$\Gamma_{\text{tunnel}}(s) = 6^{3/2}\pi^{-1/2}\omega_p(s)\left(\frac{\Delta U(s)}{\hbar\omega_p(s)}\right)^{1/2}\exp\left(-\frac{36}{5}\frac{\Delta U(s)}{\hbar\omega_p(s)}\right). \tag{5.50}$$

From Eqs. (5.43, 5.50), the cross-over temperature between thermal activation and quantum tunneling occurs at

$$T_{\text{co}} = \frac{1}{2\pi}\frac{\hbar\omega_p}{k_B}. \tag{5.51}$$

Switching regime in our experiments

As the environment of the junction plays an essential part in the junction dynamics, the biasing scheme must be clarified at this point. In the experiment, the junction is neither perfectly current or voltage biased. The biasing circuit was designed in order to control the environment parameters at best (Fig. 5.11).

In our experiments, the quality factor Q is set[11] by the environment[12] shown on Fig. 5.11. The electromagnetic parameters of the various samples

---

[10] A derivation of ΔE is proposed in [154]

$$\begin{aligned}\Delta E = {} & \tfrac{36}{5}\,\Delta U(s)\tfrac{\kappa}{Q}(1+\tfrac{1}{4Q^2})^2 \\ & \times\left(1+60\tfrac{1}{Q}\left[1+\tfrac{1}{4Q^2}\right]^{1/2}\kappa^{-8}\left[\psi_1(\kappa^{-2})-\kappa^2-\kappa^4/2-\kappa^6/6\right]\right)\end{aligned} \tag{5.49}$$

with ψ_1 the trigamma function.

[11] The calculation of Q is done by solving $Y(\omega) = 0$ where Y is the admittance of the circuit seen by the bias line. If ω is a solution, $Q = \frac{\text{Re}(\omega)}{2\text{Im}(\omega)}$. For our circuit, one finds

$$Q(s) = \frac{1}{2}\frac{\left(4-\left(Q_{R_b}^{-1}-Q_r^{-1}\right)^2\right)^{1/2}}{Q_{R_b}^{-1}+Q_r^{-1}} \tag{5.52}$$

where $Q_{R_b} = R_bC\omega_p(s)$ and $Q_r = (rC\omega_p(s))^{-1}$.

[12] In our experiments, the intrinsic capacitance of the junction (between 10 and 500 fF as estimated from the area of the junction and compared to the fit of Fig. 3.9) had always a negligible admittance as compared to the capacitance C in series with r.

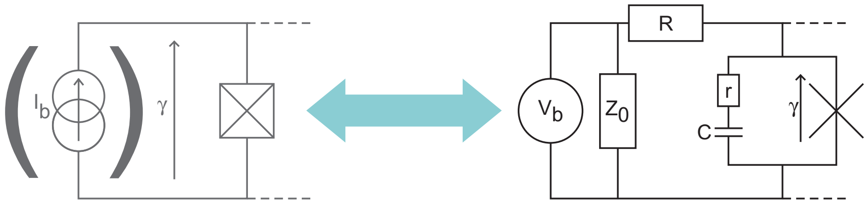

Fig. 5.11. Model of the circuit used to bias the superconducting loop of Fig. 5.7. The characteristic impedance of the transmission lines is $Z_0 = 50\ \Omega$. The capacitance C depends on the actual geometry and typically $C \approx 30$ pF. The resistance r is the sheet resistance of the electrodes that form the external capacitor $r \approx 0.1 - 1\ \Omega$.

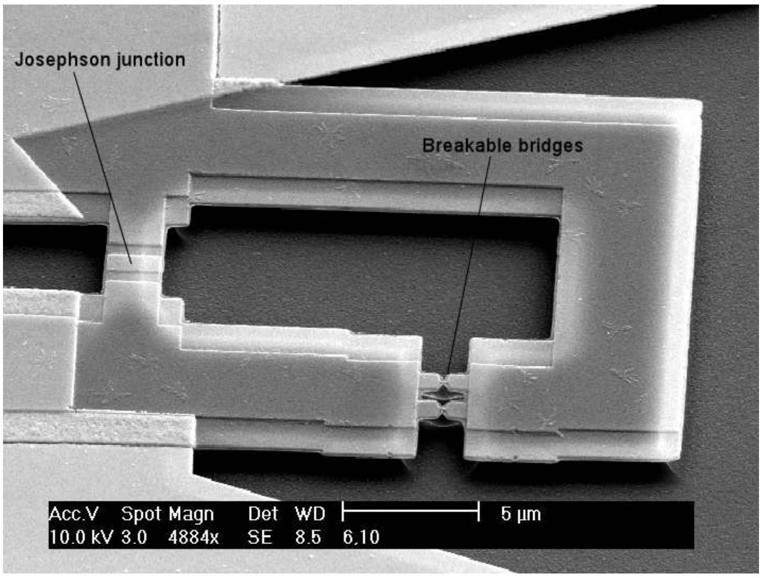

Fig. 5.12. Scanning Electron Microscope picture of the loop schemed on Fig. 5.7. The sample was covered with a thin layer of gold in order to improve the contrast. The picture is taken at an angle of 45° so that it is clear that the polyimide layer has been etched underneath the bridges. The fact that two bridges are present instead of one is a result of the double-angle evaporation technique used for fabricating the Josephson junction, and is of no importance as only one of them forms an atomic contact just before breakage.

measured are given in Table. 5.1. The cross-over temperature T_{co} is always much smaller than the minimal refrigerator temperature and the quality factor larger than 1. Therefore, the junction switches at a rate given by the thermal activation expression (5.43).

Sample	C (pF)	R (Ω)	r (Ω)	R_t (Ω)	I_0 (nA)	$\omega_p/2\pi$ (GHz)	Q	I_0/Area (μA.μm^{-2})
CP1 [21]	33.7 (fit)	50	0.57 (fit)	357	750 [785]	1.34 (μ-wave)	4.3	0.25
CP2	20	50	0.6	893	304 [306]	1.08	4.3	0.38
CP3	15	50	0.6	?	961 [?]	2.22	4.5	0.32
CP4	20	50	0	324	? [870]	1.83	15	0.48
CP5	20	50	0.6	628	448 [450]	1.31	4.4	0.28
CP6	21.2 (fit)	50	0.6	390	720 [730]	1.62 (μ-wave)	4.6	0.36
CP7	20	50	0.6	2160	? [130]	0.7	3.3	0.30

Table 5.1. Electrical characteristics of the measurement circuit for 6 samples denoted by CP1 to CP6 (as in "Current-Phase"). When a microwave measurement has been performed (CP1 and CP6), the capacitance is deduced from the measured value of ω_p and from I_0. If not, it is estimated from the geometry. The resistance r in series is either exactly 0 because the electrodes were superconductive or approximately 0.6 Ω (either from a fit of the microwave signal reflection or from geometrical considerations). The tunnel resistance R_t was measured in the normal state and I_0 was deduced from the fitting procedure used in Fig. 5.13. For each sample, we also give (in brackets) the prediction for I_0 using Eq. (5.32) and $\Delta = 180$ μeV. Finally, except for CP1 and CP6, the plasma frequency was calculated from the estimation of C and I_0, and the quality factor was calculated using Eq. (5.52). All measurements on the atomic contacts AC1, AC2 and AC3 presented in this work have been performed with the sample CP6.

Measurement of the electronic temperature

The escape rate $\Gamma(s)$ gives access to the electronic temperature of the components of the circuit responsible for dissipation. In the experiment, a current pulse is applied with an amplitude sI_0 during a time τ_p. If the junction switches, a DC voltage develops and is detected by a counter. The junction can then be "reset" by setting the bias current to zero (to trap the phase in a potential well). This experiment is repeated typically ten thousands times and the switching probability $P_{\tau_p}(s)$ is estimated by the number (which is acquired using a frequency counter) of times the voltage across the junction exceeds a small threshold[13] divided by 10000.

---

[13] In order to get rid of offsets in the current bias, associated with thermoelectric voltages, the DC current offset of the source is adjusted so that the same pulses with the opposite amplitude lead to the same switching probabilities.

Using Eqs. (5.45, 5.43), one may define the parameter b as

$$b \equiv \frac{k_B}{\varphi_0 I_0} \frac{3}{4\sqrt{2}} B \tag{5.53}$$

The escape temperature is then simply related to b by

$$b^{2/3} = (1-s) T_{\text{esc}}^{-2/3}. \tag{5.54}$$

Therefore, the quantity $b^{2/3}$ as a function of s is a straight line extrapolating to zero at $s = 1$. This property, which is valid at any temperature T_{esc} gives a unique determination of the critical current I_0. Besides, its slope $-T_{\text{esc}}^{-2/3}$ gives access to the escape temperature. The escape temperature may differ from the environment temperature, either because of current noise (see section 7.3.1), or because the quantum tunneling is not negligible (see Eq. (5.51)).

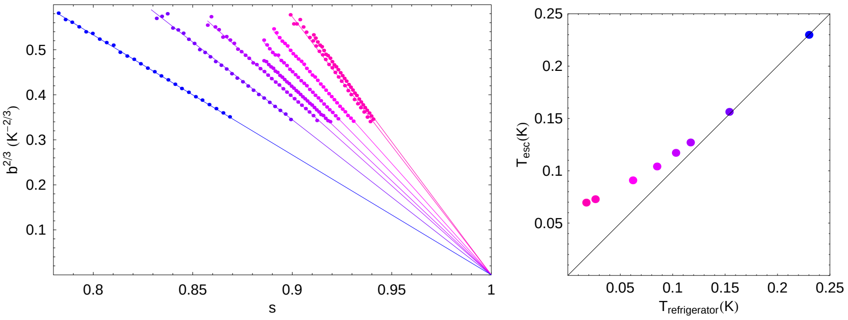

Fig. 5.13. Left panel–dots: Function $b^{2/3}$ plotted as a function of s for different temperatures from the measurements of the switching probability on sample CP3 (see Table. 5.1). The critical current $I_0 = 961$ nA was chosen so that all the curves extrapolate to 0 at $s = 1$. Left panel–lines: best straight lines passing through the experimental points and through 0 at $s = 1$. The slope of these curves gives the escape temperature T_{esc} through Eq. (5.54). Right panel: escape temperature T_{esc} extracted from the left plot as a function of the refrigerator temperature. The minimal escape temperature in this experiment was 70 mK at a base refrigerator temperature of 18 mK.

At the temperatures where Eq. (5.54) is valid, the escape temperature measured on the sample CP3 saturates to a minimum value of 70 mK. As the cross-over temperature T_{co} is much smaller[14], the saturation at low temperature is not the signature of a change from classical to quantum escape, but supplies a measurement of the electrical noise which prevents the electrons in the environment to cool down to the temperature $T_{\text{refrigerator}}$ of the refrigerator.

---

[14] For $2\pi\omega_p = 1$ GHz, the cross-over temperature is $T_{\text{co}} \approx 7$ mK.

Phase diffusion

For some combinations of the critical current I_0, and quality factor Q, the escape dynamics does not verify Eq. (5.54) at temperatures higher than a given threshold. In these situations, the phase escapes a well according to Eq. (5.54) but has a finite probability of being trapped in one of the following wells. For a voltage to develop, this trapping must be overcome, so that the phase runs down the potential without being stopped and a sizeable voltage develops [156]. As a result, the increase of the rate with the s parameter is much sharper than expected in the underdamped case (see Fig. 5.14).

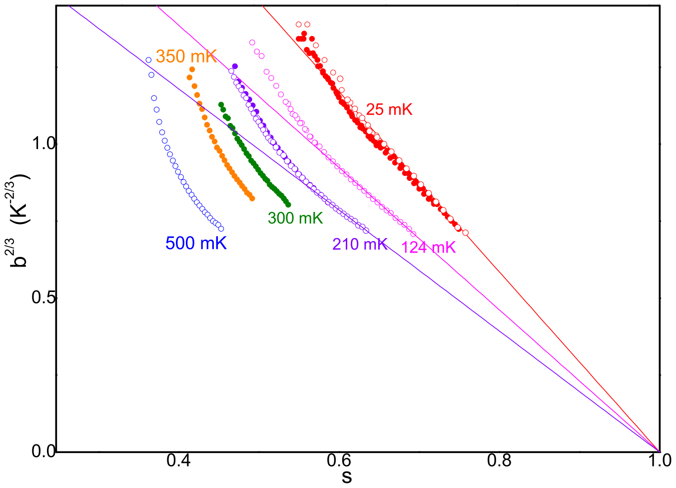

Fig. 5.14. Function $b^{2/3}$ plotted as a function of s for different temperatures from the measurements of the switching probability on sample CP2 (see Table. 5.1). The critical current $I_0 = 304$ nA was chosen so that the three lines cross at 0 for $s = 1$.

5.2.2 Current-phase relation measurement

The actual experiment consists in measuring the current-phase relation $I(\delta)$ of a one-atom contact placed in parallel with the tunnel junction. As in the case where the atomic contact is fully open (tunnel junction alone), a switching experiment can be performed. In this setup, the potential in which the phase γ evolves is not just given by (5.41) because the energy of the Andreev bound states also contributes:

$$U^{(-)}(\gamma) = -\varphi_0 I_0 \cos(\gamma) - \varphi_0 I_b \gamma - |\Delta| \sum_i \sqrt{1 - \tau_i \sin^2(\delta/2)} \qquad (5.55)$$

where I_b is the bias current. Here, $U^{(-)}(\gamma)$ denotes the potential corresponding to the case in which only the Andreev ground state $|\tau_-\rangle$ is occupied. Using the setup of Fig. 5.7, an external magnetic flux ϕ is applied through the superconducting loop enclosing the contact and the Josephson junction. The phase differences γ and δ are thus linked by the flux[15], and

$$\delta = \gamma + \phi/\varphi_0 \equiv \gamma + \varphi \tag{5.56}$$

where $\varphi \equiv \phi/\varphi_0$ is the reduced flux.

For a few channels, the contribution of the Andreev energy term to the total potential $U^{(-)}$ can be treated pertubatively if $|\Delta| \lesssim \varphi_0 I_0$. Using Eq. (5.32), this condition is equivalent to $R_t \lesssim R_K/8 \approx 3\ \mathrm{k}\Omega$, where R_t is the resistance of the Josephson junction in the normal state. In this case, switching occurs when the value of the phase γ at the minimum of the potential is nearly identical to the one γ_0 in case the tunnel junction is alone (see Appendix B.5). Therefore, the so-called *switching current* I_b^{Γ} for which switching occurs at a rate Γ is the current going through the parallel combination of the tunnel junction and the atomic contact when $\gamma = \gamma_0$. That is

$$I_b^{\Gamma}(\varphi) = I_0 \sin(\gamma_0) + \sum_i I_{|\tau_i -\rangle}(\gamma_0 + \varphi). \tag{5.57}$$

where $I_{|\tau_i -\rangle}$ is given by (5.29).

In the experiment described here, the resistance of the tunnel junction in the normal state was $R_t = 385\ \Omega$. Thus, $R_t \ll R_K/8$ and the atomic contact term in the potential can indeed be treated perturbatively. We present on Fig. 5.15 the measured switching current $I_b^{\Gamma_{\mathrm{exp}}}(\varphi)$ as a function of the flux φ in the loop, for a constant switching rate[16] $\Gamma_{\mathrm{exp}} = 23.3 \pm 0.6$ kHz for three atomic contacts.

5.2.3 I-V characteristics

In order to measure the transmissions of the atomic contact independently, we have measured the current-voltage characteristics of the parallel combination of the contact and the Josephson junction. Ideally, the Josephson junction

---

[15] The geometrical inductance of the loop is negligible (in the experiment, $L \approx 0.5\mu_0 \times \mathrm{length} \approx 10$ pH [157]), compared to the inductance of the tunnel junction ($\varphi_0/I_0 \approx 1$ nH) and of the atomic contact (≈ 10 nH).

[16] In the preliminary experiments presented in Ref. [21], the technique used was to ramp the bias current I_b and to record the average switching time as a function of the flux. However, the amplitude of the ramp was so large that many quasiparticles were created because the voltage after switching exceeded $2\Delta/e$ by far. This procedure heats the electrons noticeably and we present here data for which this heating effect was circumvented using a smaller bias resistance and pulses of current instead of ramps.

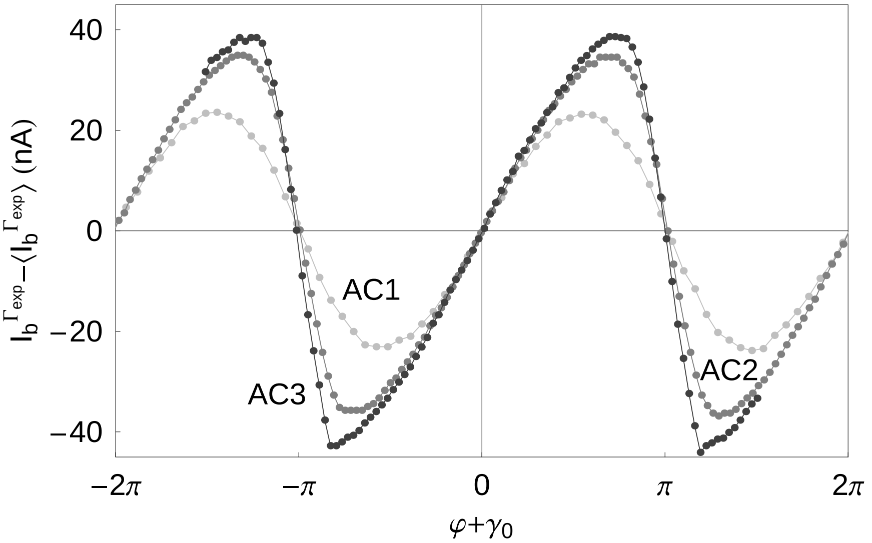

Fig. 5.15. Switching current $I_b^{\Gamma_{\rm exp}}(\varphi)$ at constant rate $\Gamma_{\rm exp} = 23.3 \pm 0.6$ kHz as a function of the reduced flux φ in the loop for three atomic contacts (AC). The data are shifted vertically so that the mean current is zero (the average value $\langle I_b^{\Gamma_{\rm exp}}(\varphi)\rangle$ of the current is of the order of $0.85 I_0$) and horizontally so that the origin is a point of symmetry. The highest the transmissions of the contact, the sharper the curve.

alone should act as an open circuit at voltages V smaller than $2\Delta/e$. The current measured below the gap should then be due to the atomic contact only. However, in the experiment, the junction alone did present some sub-gap current at the scale of 10 nA, which is of the order of the current flowing through a one-channel conductor ($e\Delta/\hbar \approx 44$ nA for aluminum). It was therefore necessary to perform a subtraction, as described below.

Current-voltage characteristics of the Josephson junction

The $I(V)$ curve of the Josephson junction alone in sample CP6 (when the atomic contact is fully open) is plotted on Fig. 5.16. A current is visible below the gap, at $|eV| < 2\Delta \approx 0.4$ meV. Besides, the current-voltage curve presents a back-bending at $eV \approx 2\Delta$. Both effects are unexpected for Josephson junctions.

Sub-gap currents are sometimes attributed to pin-holes in the tunnel junction. This is not the case here: such shorts could be described as channels with a transmission larger than the average one, and lead to MAR structures [158]. But what we observe cannot be only attributed to MAR processes, at least because the current has a non-monotonous dependence on voltage (Fig. 5.16).

Another possibility would be that the electromagnetic environment presents some resonances at frequencies which are of the order of $eV/\hbar$ where V is the

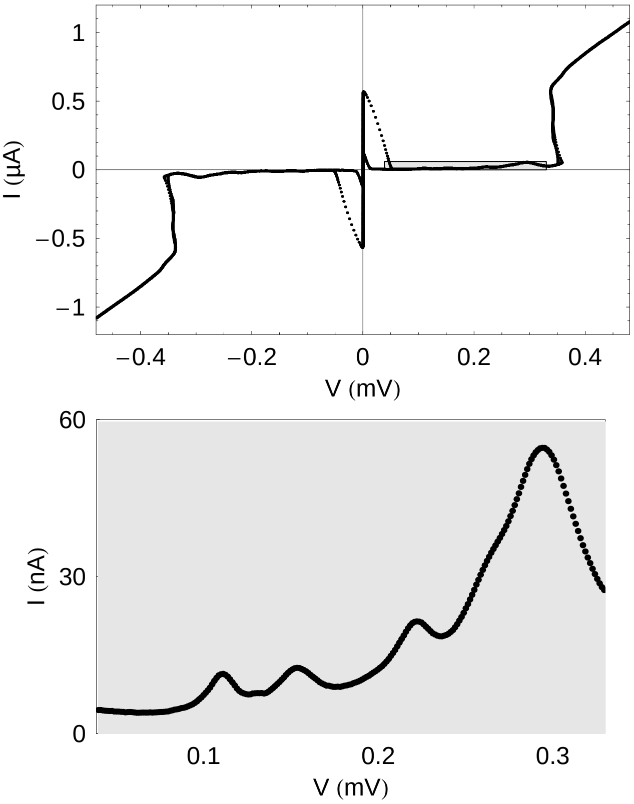

Fig. 5.16. Top: current-voltage characteristics of the Josephson junction of the sample CP6 on which all measurements on atomic contacts presented in this work were performed. Bottom: a close-up of the gray area of the plot of the top panel.

voltage at one of the peaks in the sub-gap structure. In that case, inelastic tunneling of Cooper pairs can produce a sizeable current [159] of the order of I_0^2.

The reentrant behavior at $eV \approx 2\Delta$ is more common for junctions of that size with critical current I_0 of the order of the μA. Qualitatively, it can be attributed to a heating effect of the electrodes when the current starts flowing, which leads to a reduction of Δ at the junction.

Similar sub-gap currents were observed in several samples of Table. 5.1 which had various environments and geometries (see Fig. 5.17). The sub-gap structure seems to rapidly decrease with the critical current of the junction regardless of the critical current density. In particular, on all the junctions we fabricated presenting a critical current below nearly 350 nA, the sub-gap

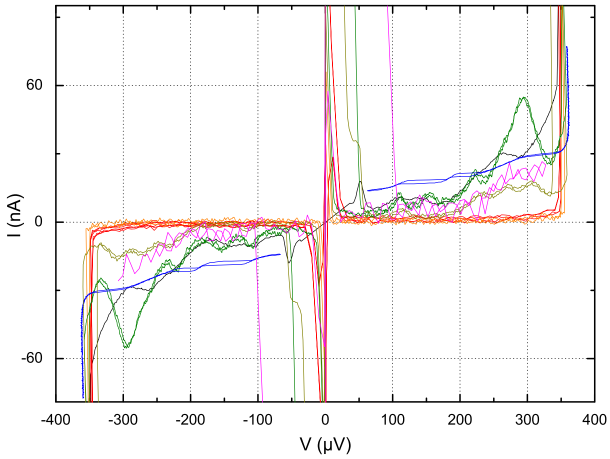

Sample	I_0 (nA)	I_0/Area (μA.μm^{-2})
CP3	961	0.32
CP4	[870]	0.48
CP1	750	0.25
CP6	720	0.36
CP5	448	0.28
CP2	304	0.38
CP7	[130]	0.30

Fig. 5.17. Sub-gap structure of the measured current-voltage characteristics $I_{\mathrm{JJ}}(V)$ for the Josephson junction of the seven samples CP1 to CP7. The table recalls some parameters shown in Table. 5.1 (Color online)

structure is greatly diminished. We have not found a satisfactory explanation for this behavior.

Current voltage characteristics of an atomic contact

In order to go further, we make the assumption that the total current I going through the circuit at a given voltage V is just the sum of the current in the tunnel junction alone and of the current in the atomic contact alone at the same voltage. In other words, we assume that the $I(V)$ curve of each junction is not affected by the presence of the other. In the experiment, we therefore subtracted from the $I_{\mathrm{tot}}(V)$ curve measured in presence of an atomic contact the $I_{\mathrm{JJ}}(V)$ curve measured with the contact open(see Fig. 5.18). The obtained curve $I(V)$ was fit with the MAR theory (see Fig. 5.19).

Technical difficulties in the $I-V$ measurement

The measurement of $I(V)$ presented some difficulties. The current above the gap (of the order of 1 μA) is much larger than the sub-gap current. We took two sets of measurements: one below the gap, with amplifiers adapted to the range of tens of nA, and one above the gap, in the range of a few μA (see Fig. 5.16). The resolution is thus barely good enough above the gap. The low-frequency cut-off of the lines used to measure the current caused retardation effects that led to uncertainties in the $I(V)$, in particular around $|eV| = 2\Delta$. Finally, the subtraction of the $I(V)$ curves is impossible at $eV \approx 2\Delta$ because of the reentrance effect discussed above, and at very low voltages because

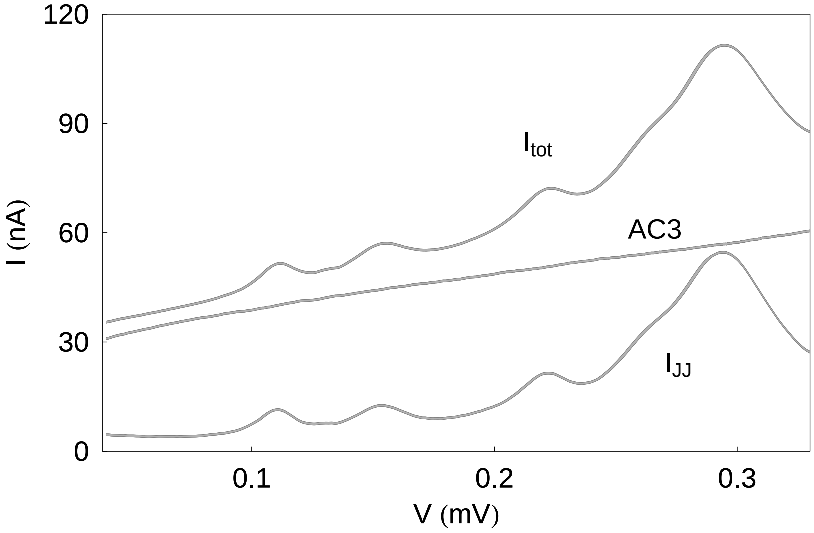

Fig. 5.18. Measured current-voltage characteristics $I_{\mathrm{tot}}(V)$ for the atomic contact AC3 and $I_{\mathrm{JJ}}(V)$ for the Josephson junction alone. The subtraction of those two curves gives the $I(V)$ curve of the atomic contact alone, labeled AC3. The uncertainty of this determination is the width of the line.

of the retrapping on the supercurrent branch. The plotted $I(V)$ curves were measured using the following procedure:

- a differential measurement was performed using homodyne detection at 136.49 Hz. The resulting $\mathrm{d}I/\mathrm{d}V(V)$ curve was integrated to get low noise current measurement. However, the absolute values of I and V are not known with this method. Besides, hysteretic parts of the $I(V)$ characteristics cannot be accessed.
- a set of one thousand $I(V)$ curves were acquired with a digital oscilloscope. In order to minimize errors due to the delays in the measurement lines, each curve took as long as 10 s to be measured. The drawback of this long-time measurement is that $1/f$ noise gives some uncertainty on the measurement of I and V. Each of the 1000 curves were first centered in voltage using the supercurrent branch, then the whole set of curves was averaged. The resulting curve was centered in current using the oddness of $I(V)$.
- this $I(V)$ was used as a reference to determine the absolute offsets in current and voltage for the curve obtained by integration of $\mathrm{d}I/\mathrm{d}V(V)$ at step 1.

In the end, an uncertainty of 0.9 μV in voltage and 0.3 nA in current remains below the gap. Only a few points were measured above the gap for the

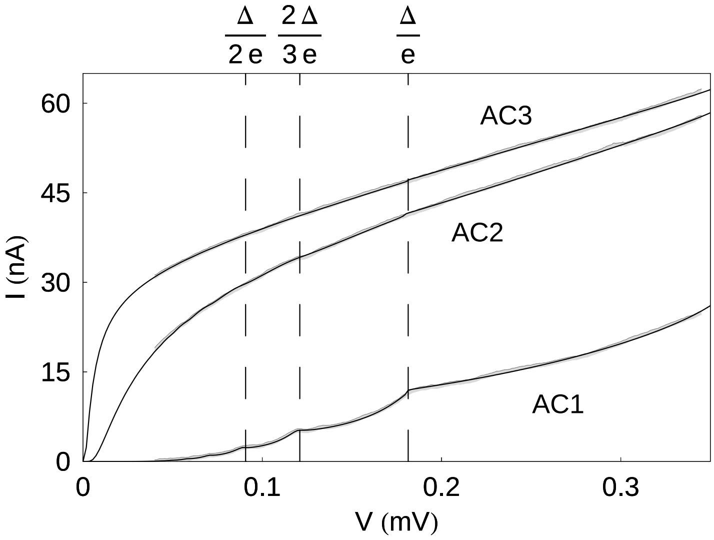

Fig. 5.19. Gray thick lines: $I(V)$ curves for atomic contacts AC1, AC2 and AC3 as deduced from the subtraction of the measured curves $I_{\mathrm{tot}}(V)$ and $I_{\mathrm{JJ}}(V)$. The thickness gives the uncertainty on the measurement. Black thin lines: best fit with the Multiple Andreev Reflection current (see Fig. 5.6) obtained for the PIN reported on Table 5.2.

Josephson junction alone with the homodyne detection. Therefore, the uncertainty on the slope of the $I(V)$ characteristics at $eV > 2\Delta$ was larger than the required precision for determining the conductance of the contact at high voltages[17].

On Fig.5.19, the $I(V)$ characteristics for three contacts are plotted with gray lines. The PIN $\{\tau_i\}$ of the atomic contact are fitted using the formalism of section 5.1.4. The corresponding theoretical curves are plotted on the same figure as black lines.

5.2.4 Current-phase relation, theory versus experiment

The zero temperature current-phase relation for AC1, AC2 and AC3, computed using (5.57), is compared on Fig. 5.20 with the measured $I_b^{\Gamma_{\mathrm{exp}}}(\varphi)$. The maximal and minimal values of the PIN given explicitly for each channel on Table 5.2 lead to a determination of the uncertainty on the prediction, which is represented by the width of the theoretical line. There is an overall good agreement between the experimental curve and the theoretical prediction, supporting the picture of the Andreev bound states in short conductors. Still, the

---

[17] The conductance of the atomic contact at high voltage is of the order of 4×10^{-5} S at best whereas the uncertainty on the $\mathrm{d}I/\mathrm{d}V$ curve was of the order of 10^{-4} S.

Atomic contact	PIN
AC1	$\{\mathbf{0.62}\pm0.01;\mathbf{0.12}\pm0.015;\mathbf{0.115}\pm0.01;\mathbf{0.11}\pm0.01;\mathbf{0.11}\pm0.01\}$
AC2	$\{\mathbf{0.957}\pm0.01;\mathbf{0.185}\pm0.05\}$
AC3	$\{\mathbf{0.992}\pm0.003;\mathbf{0.089}\pm0.06;\mathbf{0.088}\pm0.06\}$

Table 5.2. Transmissions of the channels for three atomic contacts. The measured values correspond to the best fit obtained using the theory of MAR (see § 5.1.4). The uncertainty on the transmissions is calculated from the uncertainty on the measured $I(V)$ curves.

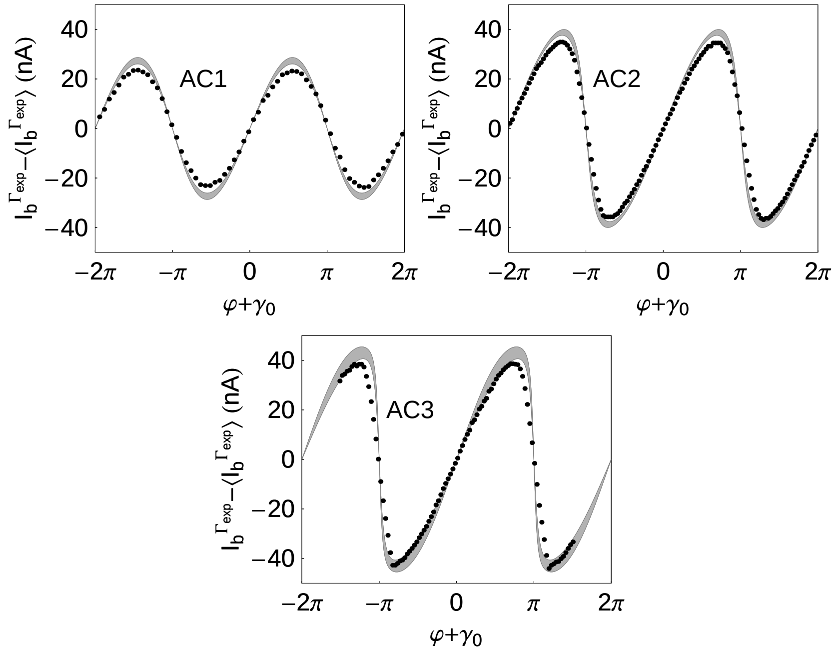

Fig. 5.20. Dots: measured switching current $I_b^{\Gamma_{\mathrm{exp}}}$ as a function of the reduced flux φ for the three atomic contacts described in Table 5.2. Grayed bands: theoretical current-phase relation at $T=0$ (5.57) using the PIN of Table 5.2. The width of the gray area corresponds to the uncertainty on the PIN.

amplitude of the experimental oscillations in $I_b^{\Gamma_{\rm exp}} - \langle I_b^{\Gamma_{\rm exp}} \rangle$ is always smaller than expected from the zero temperature theory (5.57). As a first correction to (5.57), the thermal excitations of the phase in the potential well $U^{(-)}$ can be included.

Effect of temperature on the switching current: a qualitative approach

At finite temperature, switching occurs before the current actually reaches the critical current I_0. As a consequence, the switching current is not only determined by the amount of current deviated to the atomic contact at the value γ_0 of the phase γ for which the large Josephson junction alone would switch, but by the total potential $U^{(-)}(\gamma)$. Using Eq. (5.55), the barrier height reads

$$\begin{aligned}\Delta U^{(-)} &= U(\gamma_{\rm max}) - U(\gamma_{\rm min}) \\ &\quad + \textstyle\sum_i \left[E_{|\tau_i -\rangle}(\delta = \gamma_{\rm max} + \varphi) - E_{|\tau_i -\rangle}(\delta = \gamma_{\rm min} + \varphi)\right] \\ &= U(\gamma_{\rm max}) - U(\gamma_{\rm min}) + \sum_i \int_{\gamma_{\rm min}}^{\gamma_{\rm max}} \frac{\partial E_{|\tau_i -\rangle}}{\partial \delta}(\delta = \gamma + \varphi) \mathrm{d}\gamma \\ &= U(\gamma_{\rm max}) - U(\gamma_{\rm min}) + \varphi_0 \sum_i \int_{\gamma_{\rm min}}^{\gamma_{\rm max}} I_{|\tau_i -\rangle}(\gamma + \varphi) \mathrm{d}\gamma\end{aligned} \tag{5.58}$$

where the phase $\gamma_{\rm min}$ ($\gamma_{\rm max}$ respectively) is the phase at which the potential presents a local minimum (maximum, see Fig. 5.9). Besides, if the potential $U^{(-)}$ is only slightly changed by the atomic contact ($R_t \lesssim R_K/8$), the phases $\gamma_{\rm min}$ and $\gamma_{\rm max}$ are nearly identical to those obtained for the Josephson junction alone, and

$$\begin{aligned}\gamma_{\rm min} &\approx \arcsin(I_b/I_0) = \arcsin(s) \\ \gamma_{\rm max} &\approx \pi - \arcsin(I_b/I_0) = \pi - \arcsin(s)\end{aligned} \tag{5.59}$$

In our experiment, the switching current $I_b^{\Gamma_{\rm exp}} = sI_0$ is measured at a constant rate Γ for various fluxes φ. Therefore, $\Delta U^{(-)}$ is kept nearly constant when the flux is varied. Let us introduce the averaged current function for the atomic contact

$$I_{\rm av}(\varphi, s) = \frac{1}{\pi - 2\arcsin(s)} \sum_i \int_{\arcsin(s)}^{\pi - \arcsin(s)} I_{|\tau_i -\rangle}(\gamma + \varphi) \mathrm{d}\gamma. \tag{5.60}$$

Then, the switching current $s(\varphi)$ is just a solution of

$$\Delta U^{(-)}(\varphi, s[\varphi]) = \Delta U^{(-)}(\varphi_\triangledown, s_\triangledown) \tag{5.61}$$

where $\varphi_\triangledown$ and $s_\triangledown$ are such that[18] $I_{\rm av}(\varphi_\triangledown, s_\triangledown = s[\varphi_\triangledown]) = 0$ (in practice, the flux $\varphi_\triangledown$ is the flux for which $I_b^{\Gamma_{\rm exp}}$ is at its average value). The later equation (5.61) can be developed as

---

[18] The flux $\varphi_\triangledown$ exists since the function $I(\delta)$ is continuous, periodic and has a zero average value.

$$\frac{4\sqrt{2}}{3}I_0\varphi_0(1-s)^{3/2}+\varphi_0(\pi-2\arcsin[s])I_{\mathrm{av}}(\varphi,s)=\frac{4\sqrt{2}}{3}I_0\varphi_0(1-s_\triangledown)^{3/2}. \tag{5.62}$$

Denoting $s=s_\triangledown+\varepsilon$, this equation can be expanded[19] in powers of ε:

$$\begin{aligned}\frac{4\sqrt{2}}{3}I_0(1-s_\triangledown)^{3/2}&\left(1-\left[1+\frac{\varepsilon}{1-s_\triangledown}\right]^{3/2}\right)+o(\varepsilon^2)\\&=\sum_i\int_{\arcsin(s_\triangledown+\varepsilon)}^{\pi-\arcsin(s_\triangledown+\varepsilon)}I_{|\tau_i-\rangle}(\gamma+\varphi)\mathrm{d}\gamma.\end{aligned}\tag{5.64}$$

hence,

$$\begin{aligned}2\sqrt{2}I_0\ (1-s_\triangledown)^{1/2}\varepsilon+o(\varepsilon^2)&=\sum_i\int_{\arcsin(s_\triangledown)+\varepsilon(1-s_\triangledown^2)^{-1/2}}^{\pi-\arcsin(s_\triangledown)-\varepsilon(1-s_\triangledown^2)^{-1/2}}I_{|\tau_i-\rangle}(\gamma+\varphi)\mathrm{d}\gamma\\=\sum_i\Bigg(&\int_{\arcsin(s_\triangledown)}^{\pi-\arcsin(s_\triangledown)}I_{|\tau_i-\rangle}(\gamma+\varphi)\mathrm{d}\gamma\\+&\frac{\varepsilon}{\sqrt{1-s_\triangledown^2}}\left[I_{|\tau_i-\rangle}(\pi-\arcsin(s_\triangledown)+\varphi)+I_{|\tau_i-\rangle}(\arcsin(s_\triangledown)+\varphi)\right]\Bigg)\end{aligned}\tag{5.65}$$

$$\varepsilon I_0\left[2\sqrt{2}(1-s_\triangledown)^{1/2}+o(1)\right]+o(\varepsilon^2)=\sum_i\int_{\arcsin(s_\triangledown)}^{\pi-\arcsin(s_\triangledown)}I_{|\tau_i-\rangle}(\gamma+\varphi)\mathrm{d}\gamma\tag{5.66}$$

The last equation comes from the fact that we assumed that the potential of the atomic contact is negligible compared to the potential of the Josephson junction: $\sum_i I_{|\tau_i-\rangle}\ll I_0$. We thus get an equation relating the switching current $I_b^{\Gamma_{\mathrm{exp}}}=(s_\triangledown+\varepsilon)I_0$ to the flux φ.

$$\boxed{I_b^{\Gamma_{\mathrm{exp}}}(\varphi)\approx s_\triangledown I_0+I_{\mathrm{av}}(\varphi,s_\triangledown)\alpha(s_\triangledown)}\tag{5.67}$$

where

$$\alpha(s_\triangledown)=\frac{\pi-2\arcsin(s_\triangledown)}{2\sqrt{2}(1-s_\triangledown)^{1/2}}.\tag{5.68}$$

As $\alpha(s_\triangledown)$ is of order 1 (see Fig. 5.21), the measured switching current $I_b^{\Gamma_{\mathrm{exp}}}(\varphi)$ is given by a constant $\langle I_b^{\Gamma_{\mathrm{exp}}}(\varphi)\rangle$ plus the averaged current-phase relation $I_{\mathrm{av}}(\varphi,s_\triangledown)$, weighted by $\alpha(s_\triangledown)$.

---

[19] The notation $f[x]=o(g[x])$ for any continuous functions f and g of the complex parameter x is defined by:

$$f[x]=o(g[x])\Leftrightarrow\lim_{x\to 0}\frac{f[x]}{g[x]}=0\tag{5.63}$$

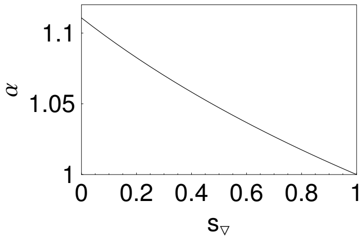

Fig. 5.21. Plot of the function $\alpha(s_\nabla)$.

Notice that, in this model, the effect of temperature enters only through the mean value of the switching current $\langle I_b^{\Gamma_{\text{exp}}}(\varphi)\rangle = s_\nabla I_0$. In the experiment, the constant rate at which the $I_b^{\Gamma_{\text{exp}}}(\varphi)$ curve was measured is $\Gamma_{\text{exp}} \approx 23.3$ kHz, which corresponds to $s_\nabla \approx 0.9$. Therefore, the experiment measures for each value of the flux the current-phase relation, averaged on $\gamma_{\text{max}} - \gamma_{\text{min}} \approx 1$ rad. Thus, in a first approximation, the effect of temperature on the phase dynamics consists in smoothing the zero temperature $I_b^{\Gamma_{\text{exp}}}(\varphi)$ curve on about 1 rad.

Using Eq. (5.43), one can estimate the temperature of the environment of the Josephson junction from the average value $s_\nabla I_0$ of $I_b^{\Gamma_{\text{exp}}}(\varphi)$. Indeed,

$$k_B T_{\text{env}} = \frac{4\sqrt{2}}{3}\varphi_0 I_0 (1 - s_\nabla)^{3/2} \left(\ln[\omega_p(s_\nabla)/(2\pi\Gamma_{\text{exp}})]\right)^{-1}. \tag{5.69}$$

The temperature for each $I_b^{\Gamma_{\text{exp}}}(\varphi)$ measurement is given on Table. 5.3. It is always of the order of 130 mK. This is quite a high temperature compared to the base refrigerator temperature $T_0 = 20$ mK and one could think that improving the filtering of the measurement lines would lead to a significant increase of the resolution of the measurement of $I(\delta)$. A quick estimate of this resolution is obtained using the approximative expression (5.45) for the barrier height. Indeed, if the noise was perfectly filtered in our experiment, so that

	$s_\nabla = \langle I_b^{\Gamma_{\text{exp}}}(\varphi)\rangle/I_0$	α	$T_{\text{env.}}$ (in mK)
AC1	0.872	1.01	137
AC2	0.883	1.01	120
AC3	0.876	1.01	131

Table 5.3. Environment temperature corresponding to each experimental curve of Fig. 5.15 as deduced from the average value of the switching current at $\Gamma_{\text{exp}} = 23.3$ kHz.

the escape temperature entering in (5.45) would be just T_0, an experiment performed at the same rate Γ_{exp} would verify

$$\frac{(1-s_{\nabla})^{3/2}}{T_0} \approx \frac{(1-0.9)^{3/2}}{135 \text{ mK}} \tag{5.70}$$

Thus, the bias current needed to switch at rate Γ would be $I_b^{\Gamma_{\mathrm{exp}}} \approx 0.97 I_0$.

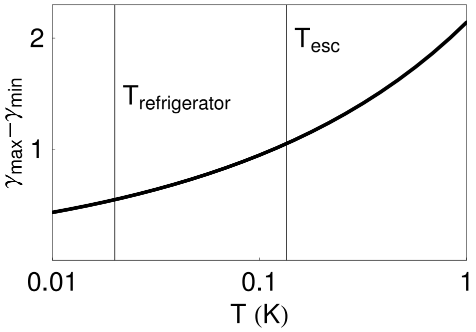

Fig. 5.22. Resolution of the measurement of the current phase relation in the switching experiment as a function of temperature. The base refrigerator temperature is $T_0 = 20$ mK and the actual environment temperature as measured in a switching experiment (see Table. 5.3) is $T_{\mathrm{esc}} \approx 135$ mK.

This value corresponds to a resolution on δ in the current phase relation of $\pi - 2\arcsin(0.97) \approx 0.5$ rad. We see that by lowering the noise temperature by a factor 6, the resolution only improves by a factor 2.

Effect of temperature on the switching current: a quantitative approach

With only the ground Andreev state occupied

In the previous section, we have seen how the temperature of the environment can smooth the measurement of the current-phase relation. In order to compare experiment and theory quantitatively, we have calculated numerically the barrier height $\Delta U^{(-)}$ as function of the flux ϕ using the measured PIN of the contact (see Table 5.2). Then, using the measured environment temperature T_{esc}, we calculated explicitly the switching current $I_b^{\Gamma_{\mathrm{exp}}}(\varphi)$ using Eqs. (5.43, 5.55). The results are plotted on Fig. 5.23. The comparison with Fig. 5.20 shows that a large fraction of the discrepancy between experiment and theory in Fig. 5.20 could be attributed to a first effect of temperature: switching is determined by the shape of the potential on a finite phase region so that the switching current behaves essentially as a sliding average on this

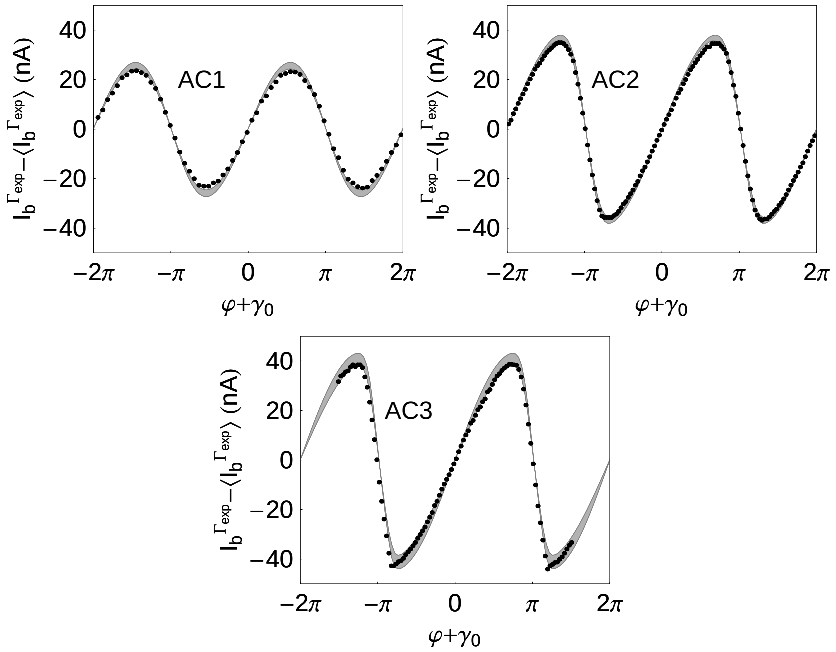

Fig. 5.23. Dots: measured switching current $I_b^{\Gamma_{\exp}}$ shifted by their average value as a function of the reduced flux φ for the three atomic contacts described in Table 5.2. Grayed bands: theoretical switching current taking into account the dynamics of the phase in an environment at finite temperature T_{esc} given on Table. 5.3. The width of the gray area corresponds to the uncertainty on the PIN.

region of the actual current phase relation. The results of this calculation for the three atomic contacts are reported on Fig. 5.23. This theory clearly better describes the experimental curves than the theory at zero temperature of Fig. 5.20. Yet, some discrepancy remains, and in fact, a finite temperature does not only have an effect on the phase dynamics in the potential $U^{(-)}$, but also possibly on the populations of the excited Andreev bound states. Since the splitting between the Andreev bound states is at least $2\Delta\sqrt{1-\tau}$, an effect is mostly expected for the contact AC3 for which this splitting is 0.4 K for the most transmitted channel at $\delta = \pi$. In the following, we explore this effect in order to find out whether it can explain the remaining discrepancy between experiment and theory in Fig. 5.23.

Populating the Andreev states

As each Andreev bound state can be either occupied or empty, four configurations are possible per channel. Thermal fluctuations of the phase can couple the Andreev states to photons[20] so that the four configurations are occupied with a probability obeying the Boltzmann distribution at the same temperature T_{esc}, the statistical occupation of the four configurations at a *fixed* phase δ are given on Table 5.4. We can calculate the switching current in two limits.

$\vert\tau_-\rangle$ $\vert\tau_+\rangle$	occupied (•−)	unoccupied (•0)
unoccupied (0•)	$P^{\tau}_{0-}(\delta) = \mathrm{e}^{E_{\vert\tau_+>}(\delta)/k_B T_{\mathrm{esc}}}/\Sigma$	$P^{\tau}_{00}(\delta) = 1/\Sigma$
occupied (+•)	$P^{\tau}_{+-}(\delta) = 1/\Sigma$	$P^{\tau}_{+0}(\delta) = \mathrm{e}^{-E_{\vert\tau_+>}(\delta)/k_B T_{\mathrm{esc}}}/\Sigma$

Table 5.4. Occupation probability of the four possible configurations of the Andreev states in a channel with transmission τ. Each probability is given by the Boltzmann distribution and $\Sigma = 4\cosh^2\left(E_{|\tau_->}(\delta)/2k_B T_{\mathrm{esc}}\right)$ is a normalization factor.

Fast excitation rates for the Andreev bound states

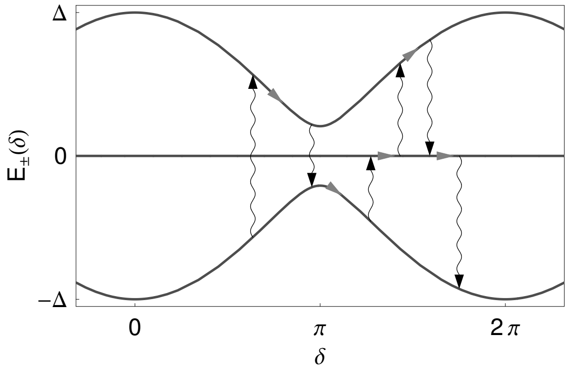

Fig. 5.24. Case of fast transitions between Andreev states. While the phase performs one oscillation in the potential well $U(\gamma)$, the system jumps many times between Andreev states.

In case the occupation of the states changes at a rate much larger than the escape attempt time ($\approx \omega_p^{-1} \approx 1$ ns in our experiment), the potential $U(\delta)$ in which the phase δ evolves changes many times before a switching event occurs.

---

[20] It has been shown that the coupling to acoustic phonons is very weak in this system due to the fermionic nature of the Andreev states [160].

Therefore, as a first approximation, at any phase δ, the mean occupation of the Andreev state configurations is set by the probabilities $P_j(\delta)$. We will see that this statement is invalid for slow dynamics of the states. The phase dynamics is the same as the one in the average potential $\bar{U}$:

$$\bar{U}(\delta) = \sum_{j_1 \in \{+0,+-,00,0-\}} \cdots \sum_{j_M \in \{+0,+-,00,0-\}} P_{j_1}^{\tau_1}(\delta) \cdots P_{j_M}^{\tau_1}(\delta) \sum_{i=1}^{M} U^{(\tau_i, j_i)}(\delta) \tag{5.71}$$

where M is the total number of channel. Now using the expression of the Andreev bound state energy (5.26), the average potential reads[21]

$$\boxed{\bar{U}(\delta) = U(\delta) + \sum_{i=1}^{M} \left[P_{0-}^{\tau_i}(\delta) - P_{+0}^{\tau_i}(\delta)\right] E_{|\tau_i -\rangle}(\delta)} \tag{5.74}$$

where the sums over j are always on all four configurations $\{+0, +-, 00, 0-\}$. On Fig. 5.25, the theoretical prediction for the switching current $I_b^{\Gamma_{\mathrm{exp}}}(\varphi)$ is plotted for a temperature T_{esc} given by Table. 5.3. The prediction for all contacts has been barely modified from the crude calculation of Fig. 5.23. In order to get the data inside of the theoretical band, it seems that the temperature should be higher than the measured escape temperature. It might be that a non thermal radiation excite the Andreev bound states, or that the assumption of fast excitation rates is wrong.

Slow excitation rates for the Andreev bound states.

During a switching attempt (an oscillation of the phase in the potential well), the phase explores a finite phase space which can be estimated by the width $\Delta\gamma$ of the potential well at its summit (see Fig. 5.26) for a bias current sI_0 such as $\Gamma(s) = \Gamma_{\mathrm{exp}}$. The assumption that the populations of the Andreev bound states change slower than the escape attempt time ($\approx \omega_p^{-1} \approx 1$ ns in our experiment) implies that each switching attempt is performed in a potential determined by one out of 4^M configurations $j_1, \cdots, j_M$ where

---

[21]

$$\begin{aligned} \bar{U}(\delta) &= U(\delta) + \textstyle\sum_{j_1} \cdots \sum_{j_M} P_{j_1}^{\tau_1}(\delta) \cdots P_{j_M}^{\tau_1}(\delta) \sum_{i=1}^{M} E_{|\tau_i, j_i\rangle}(\delta) \\ &= U(\delta) + \textstyle\sum_{i=1}^{M} E_{|\tau_i,+\rangle}(\delta) P_{+0}^{\tau_i}(\delta) \prod_{k\neq i} \left(\sum_{j_k} P_{j_k}^{\tau_k}(\delta)\right) \\ &\quad + \textstyle\sum_{i=1}^{M} E_{|\tau_i,-\rangle}(\delta) P_{-0}^{\tau_i}(\delta) \prod_{k\neq i} \left(\sum_{j_k} P_{j_k}^{\tau_k}(\delta)\right) \end{aligned} \tag{5.72}$$

and as, $\left(\sum_{j_k} P_{j_k}^{\tau_k}(\delta)\right) = 1$, one gets

$$\begin{aligned} \bar{U}(\delta) &= U(\delta) + \textstyle\sum_{i=1}^{M} E_{|\tau_i,+\rangle}(\delta) P_{+0}^{\tau_i}(\delta) \\ &\quad + \textstyle\sum_{i=1}^{M} E_{|\tau_i,-\rangle}(\delta) P_{-0}^{\tau_i}(\delta) \\ &= U(\delta) + \textstyle\sum_{i=1}^{M} (P_{0-}^{\tau_i}(\delta) - P_{+0}^{\tau_i}(\delta)) E_{|\tau_i -\rangle}(\delta) \end{aligned} \tag{5.73}$$

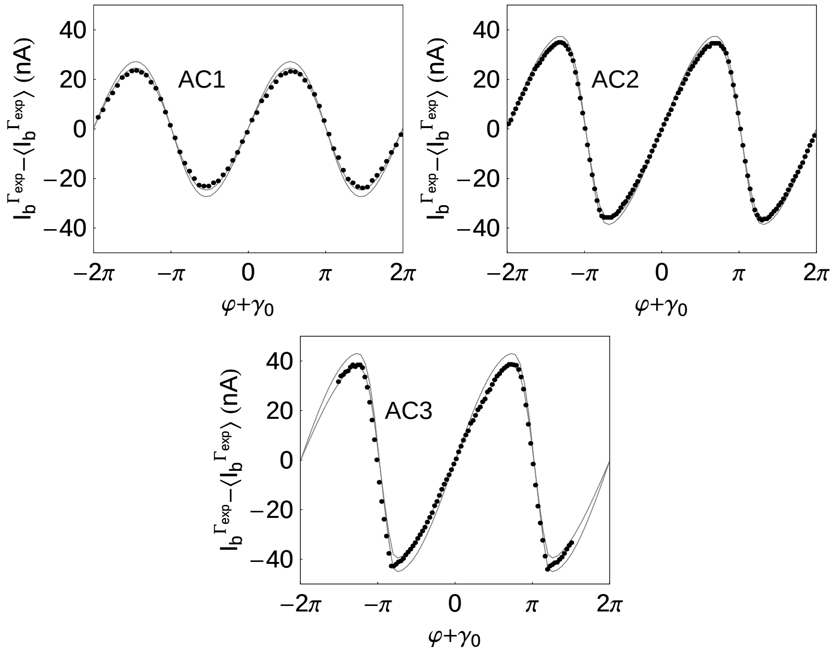

Fig. 5.25. Dots: measured switching current $I_b^{\Gamma_{\mathrm{exp}}}$ shifted by their average value as a function of the reduced flux φ for the three atomic contacts described in Table 5.2. Bands: theoretical switching current using the approximation of **fast excitation rates** and assuming a Boltzmann distribution for the configurations of the Andreev bound states with a temperature given in Table. 5.3. The width of the gray area corresponds to the uncertainty on the PIN given in Table. 5.2.

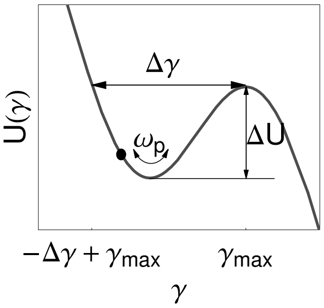

Fig. 5.26. Potential as a function of the phase γ. The width of the well opening is called $\Delta\gamma$.

$j_i \in \{+0, +-, 00, 0-\}$. Therefore, the average switching rate is the sum of the rates obtained for each configuration weighted by their respective probabilities $\prod_i \bar{\mathcal{P}}_{j_i}^{\tau_i}(\delta)$. Notice that these probabilities $\bar{\mathcal{P}}_j^{\tau}(\delta)$ are not the same as the ones used for the fast excitation rates assumption. In case of slow dynamics (Fig. 5.27), the phase oscillates many times before the Andreev state changes. Therefore, the probability $\bar{\mathcal{P}}_j^{\tau}(\delta)$ is the average value of $P_j^{\tau}(\delta)$ for δ varying between $\varphi + \gamma_{\max} - \Delta\gamma$ and $\varphi + \gamma_{\max}$ (see Fig. 5.26):

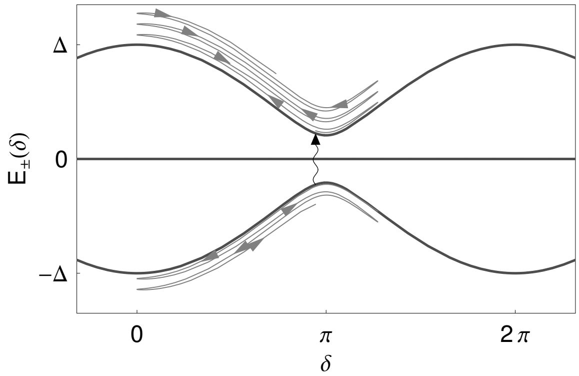

Fig. 5.27. Case of slow transitions between Andreev states. While the phase moves in the potential well $U(\gamma)$, the occupied Andreev states change slowly.

$$\bar{\mathcal{P}}_j^{\tau}(\delta) = \frac{1}{\Delta\gamma}\int_{\gamma_{\max}-\Delta\gamma}^{\gamma_{\max}} P_j^{\tau}(\varphi+\gamma)\mathrm{d}\gamma. \tag{5.75}$$

Given the exponential form of $P_j^{\tau}(\delta)$, and the fact that $\Delta\gamma$ is of order 1, $\bar{\mathcal{P}}_j^{\tau}(\delta)$ is approximately given by the standard probability $P_j^{\tau}(\delta_j^*)$ evaluated on a phase δ_j^* which maximizes $P_j^{\tau}(\delta)$ on the region where the phase varies (see Fig. 5.26). Then δ^* does not depend on j or τ, and:

$$\bar{\mathcal{P}}_j^{\tau}(\delta) \approx P_j^{\tau}(\delta^*) \equiv \max_{\gamma_{\max}-\Delta\gamma<\gamma<\gamma_{\max}} P_j^{\tau}(\varphi+\gamma). \tag{5.76}$$

The calculation of the switching current $I_b^{\Gamma_{\exp}}(\varphi)$ can thus be performed as follows. First one calculates the switching rate $\Gamma^{(j_1,\cdots,j_M)}(I_b^{\Gamma_{\exp}},\varphi)$ in each of the 4^M possible configurations for the Andreev states. Then one solves the following equation in $I_b^{\Gamma_{\exp}}(\varphi)$ for all values of φ.

$$\boxed{\sum_{j_1}\cdots\sum_{j_M} P_{j_1}^{\tau_1}(\delta^*)\cdots P_{j_M}^{\tau_M}(\delta^*)\Gamma^{(j_1,\cdots,j_M)}(I_b^{\Gamma_{\exp}}(\varphi),\varphi) = \Gamma_{\exp}} \tag{5.77}$$

The result of this calculation is shown on Fig. 5.28. Once again, the theoretical curves do not change dramatically for most contacts from the curves of

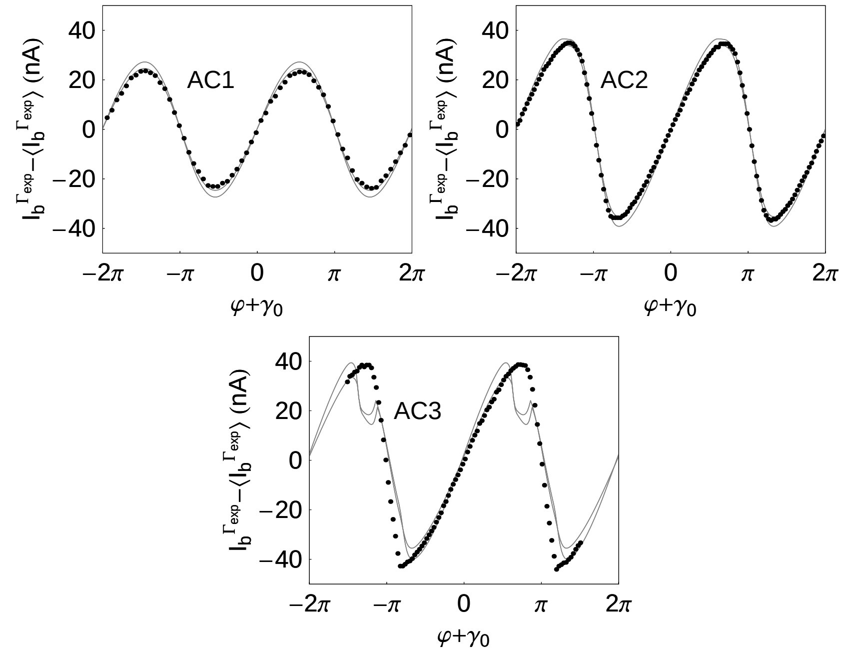

Fig. 5.28. Dots: measured switching current $I_b^{\Gamma_{\rm exp}}$ shifted by their average value as a function of the reduced flux φ for the three atomic contacts described in Table 5.2. Bands: theoretical switching current using the approximation of **slow excitation rates** and assuming a Boltzmann distribution for the configurations of the Andreev bound states with a temperature given in Table. 5.3. The width of the gray area corresponds to the uncertainty on the PIN given in Table. 5.2.

Fig. 5.23, supporting the idea that a non thermal radiation excite the Andreev bound states. Besides, this calculation gives an absurd result for the highest transmissions. Indeed, when the transmission is high, the gap between the ground and excited states is small and the assumption of slow excitation dynamics is wrong.

5.2.5 Origin of the asymmetry in $I_b^{\Gamma_{\rm exp}}(\varphi)$

On Fig. 5.15, a clear asymmetry appears for the contact AC3. The actual current-phase relation $I(\delta)$ is an odd function of δ, therefore, this asymmetry should be based on the measurement technique. In order to understand this phenomena better, the potentials of the system can be plotted when the Josephson junction and the Andreev bound states are in the ground state and when only the highly transmitting channel is in the excited state (see Fig. 5.29):

$$\begin{aligned} U^{(-)}(\gamma) = -\varphi_0 I_0 \cos(\gamma) & -\varphi_0 I_b \gamma - |\Delta|\sqrt{1-\tau_1\sin^2(\delta/2)} \\ & -|\Delta| \textstyle\sum_{i\geq 2}\sqrt{1-\tau_i\sin^2(\delta/2)} \\ U^{(+)}(\gamma) = -\varphi_0 I_0 \cos(\gamma) & -\varphi_0 I_b \gamma + |\Delta|\sqrt{1-\tau_1\sin^2(\delta/2)} \\ & -|\Delta| \textstyle\sum_{i\geq 2}\sqrt{1-\tau_i\sin^2(\delta/2)}. \end{aligned} \tag{5.78}$$

It appears clearly on this figure that the sharp feature in the curve $I_b^{\Gamma_{\mathrm{exp}}}$

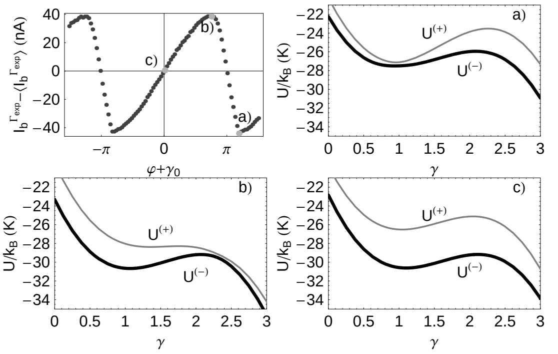

Fig. 5.29. Top-left panel: measured switching current $I_b^{\Gamma_{\mathrm{exp}}}$ shifted by their average value as a function of the reduced flux φ for the atomic contact AC3. Three points are denoted by a), b) and c) and correspond to one of the three other panels. a,b,c): On each panel are plotted both potentials $U^{(-)}$ and $U^{(+)}$ as a function of γ, using $\delta = \varphi + \gamma$ where φ is estimated from the phase of the first panel by $\varphi = (\varphi + \gamma_0) - \pi/2$, and using I_b from the first panel.

occurs at a flux φ such that the gap between $U^{(-)}$ and $U^{(+)}$ is minimum at the minimum of the potential $U^{(-)}$ (panel a). Therefore, we suspect transitions from the states (−) to (+) to occur and be responsible of the strong change in the current $I_b^{\Gamma_{\mathrm{exp}}}$, but were unable to find a satisfactory explanation. For some unknown reason, the situation where the minima of $U^{(-)}$ and $U^{(+)}$ coincide may be singular.

5.2.6 Another method to measure the current-phase relation

In the last sections, it was shown that the measurement of the switching current $I_b^{\Gamma_{\mathrm{exp}}}$ as a function of the flux is a way to access the current-phase relation. Yet, the dynamics of the phase of the measuring Josephson junction leads to the smoothing of the actual current-phase relation. Another possibility consists in measuring the switching current I_b^{Γ} for several values of Γ. This measurement allows to plot the parameter $\eta = [-\ln(2\pi\Gamma/\omega_0)]^{2/3}$ as a function of the current I in the Josephson junction. Eventually, this measurement

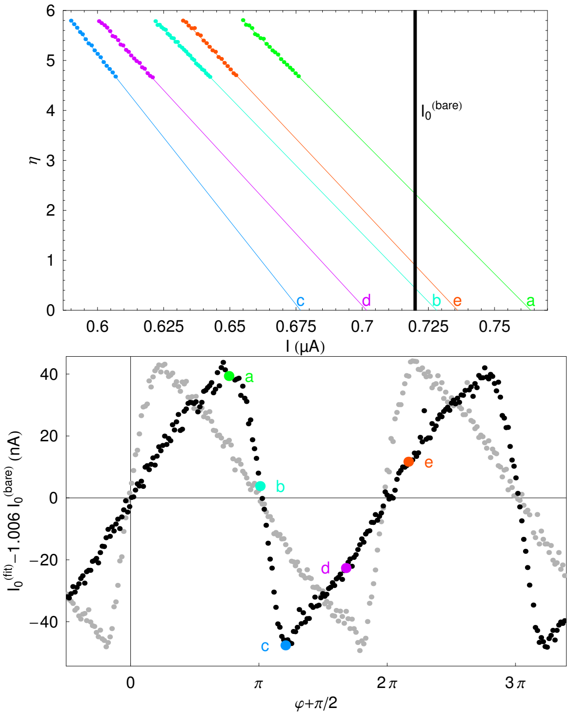

Fig. 5.30. Top panel–dots: measurement of the parameter η for several values of the current I in the Josephson junction and of the flux (identified by both a color and a letter). Top panel–lines: linear interpolation of the dots for each value of the flux. The current $I_0^{(\mathrm{fit})}$ is defined by the current at the crossing of the line and of the axes $b = 0$. Bottom panel–dots: each dot represents the value of $I_0^{(\mathrm{fit})}$ as a function of φ shifted vertically by $1.006 I_0$ where I_0 is the critical current of the Josephson junction (720 nA). The black dots are associated with one sign of the current in the Josephson junction and the gray dots to the opposite sign. The five dots which are colored and denoted by a letter correspond to the curves of the top panel.

gives access to the current $I_0^{(\mathrm{fit})}$ at which the extrapolated line going through the curve $\eta(I)$ crosses 0 (see top panel of Fig. 5.30).

We calculated the expected value of $I_0^{(\mathrm{fit})}$ as a function of φ in the case of the contact AC2 by determining the curve $\eta(I)$ using the rate formula (5.43) with the potential (5.55). It turns out, for the contact AC2, that this recipe leads to

$$I_0^{(\mathrm{fit})}(\varphi) \approx I(\varphi) + 1.006 I_0 \tag{5.79}$$

to a very good approximation (see Fig. 5.31). This shows that the above recipe gives a direct measurement of the current-phase relation of the contact AC2.

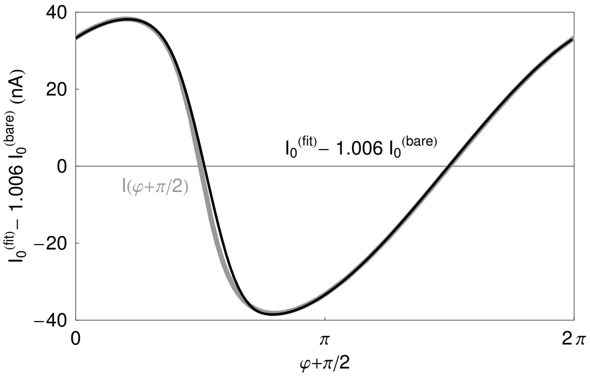

Fig. 5.31. Gray line: theoretical current-phase relation (5.29) as a function of $\delta = \varphi + \pi/2$ for the transmissions $\tau = \{0.957; 0.185\}$ of the contact AC2. Black line: theoretical calculation of $I_0^{(\mathrm{fit})} - 1.006 I_0$ as a function of $\varphi + \pi/2$ for the same transmissions(see text).

On Fig. 5.32 one can compare the theoretical current-phase relation to the experimental $I_0^{(\mathrm{fit})}$ as a function of the flux. The agreement between both curves is good except on its extrema around $\delta = \varphi + \pi/2 \approx \pi$. At this phase, the gap between the two Andreev bound states is the smallest (see Fig. 5.26) and Zener transitions or thermal excitation are more likely.

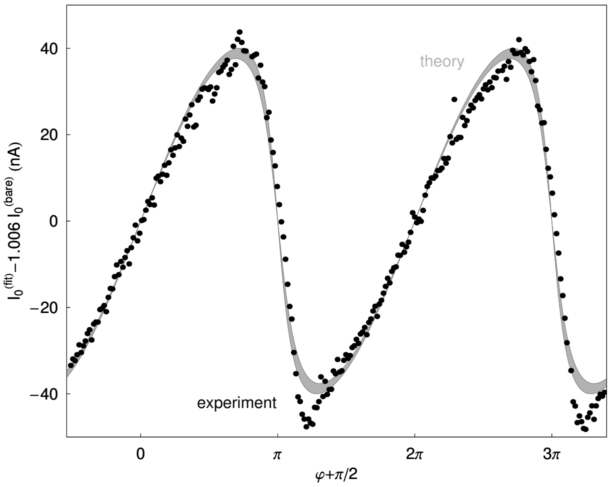

Fig. 5.32. Grayed bands: theoretical current-phase relation at $T = 0$ (5.57) using the PIN of Table 5.2 for the contact AC2 (same curve as on Fig. 5.20). The width of the gray area corresponds to the uncertainty on the PIN. Dots: experimental value of $I_0^{(\mathrm{fit})} - 1.006 I_0$ (same curve as on Fig. 5.30).

5.3 Measurement of the phase-inductance relation

We have shown that the spectrum of the Andreev bound states can be accessed experimentally through the measurement of its first derivative with respect to the phase difference δ: the current-phase relation. The second derivative can also be accessed experimentally, by measuring the effective inductance of an atomic contact (see Eq. (5.39)). In this section, we discuss measurements of this inductance performed on the very same contacts on which we measured the current-phase relation.

5.3.1 Principle of the measurement

The actual setup of the experiment was slightly more complex than what was shown on Figs. 5.7, 5.11: a transmission line was installed in parallel with the bias line in order to perform microwave measurements (see Figs. 5.33 and 9.5). The capacitance $C \approx 30$ pF represented on Fig. 5.11, and the parallel combination of the two Josephson inductances, form an L-C resonator. Therefore, neglecting the electrodes resistance r, the resonant frequency of the circuit is $\omega_{\mathrm{res}} = (L_{\parallel} C)^{-1/2}$, where $L_{\parallel}$ is the effective inductance of the parallel combination of the two non-linear Josephson inductors. Using Eq. (5.39), and assuming that both the Josephson junction and the atomic contact are on the superconducting branch[22]:

---

[22] Recall that the geometrical inductance of the loop is negligible (about 10 pH)

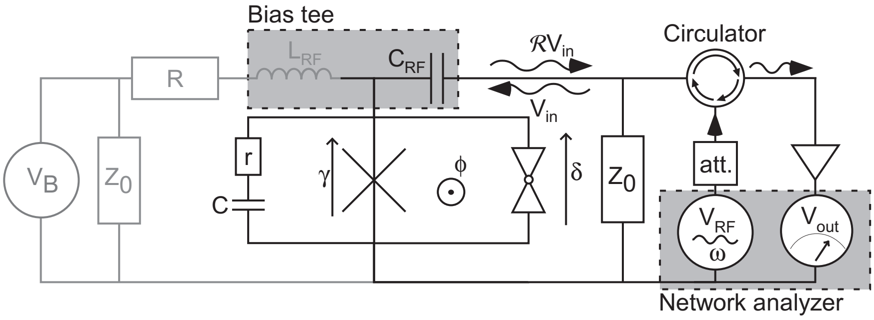

Fig. 5.33. Schematic of the electrical circuit involved in the measurement of the Josephson inductance. A bias tee made of a large capacitance C_{RF} and a large inductance L_{RF} decouples the DC from the AC signal. A network analyzer sends a radiofrequency (RF) signal V_{in} onto the superconducting loop which partially reflects it. The reflected signal $\mathcal{R}V_{\mathrm{in}}$ is forced into the return line by a circulator. The signal is amplified and then measured by the network analyzer. For further details, see Fig. 9.5.

$$L_{\|} = \left(L_{\mathrm{AC}}^{-1}(I_b,\varphi) + L_{\mathrm{JJ}}^{-1}(I_b,\varphi)\right)^{-1} \tag{5.80}$$

where, at zero temperature,

$$\begin{aligned} L_{\mathrm{AC}}(I_b,\varphi) &= \varphi_0^2 \left(\sum_i \frac{\partial^2 E_{|\tau_i -\rangle}}{\partial \delta^2} \left[\gamma(I_b,\varphi)+\varphi\right] \right)^{-1} \\ L_{\mathrm{JJ}}(I_b,\varphi) &= \frac{\varphi_0}{I_0 \cos(\gamma[I_b,\varphi])}. \end{aligned} \tag{5.81}$$

The phase $\gamma(I_b,\varphi)$ corresponds to the minimum of the total potential:

$$\frac{\partial U^{(-)}(I_b,\varphi,\gamma)}{\partial \gamma}(\gamma[I_b,\varphi]) = 0 \tag{5.82}$$

which is equivalent to

$$I_b = I_0 \sin(\gamma[I_b,\varphi]) + \sum_i I_{|\tau_i -\rangle}(\gamma[I_b,\varphi]+\varphi). \tag{5.83}$$

Reflectometry

In the experiment, a voltage V_{in} at microwave frequency $\omega/2\pi$ is sent through a transmission line terminated by the superconducting loop. Since the load impedance Z of the circuit differs from the impedance $Z_0 = 50\ \Omega$ of the line, the microwave signal is partly reflected and the complex amplitude of the reflected signal reads $\mathcal{R}V_{\mathrm{in}}$ where

$$\mathcal{R} = \frac{Z - Z_0}{Z + Z_0}. \tag{5.84}$$

The impedance Z has the following expression:

$$Z = \left(\frac{1}{iL_{\|}\omega} + \frac{iC\omega}{1 + irC\omega} \right)^{-1} \tag{5.85}$$

In the experiment, we measured both the modulus and the phase of $\mathcal{R}$. On Fig. 5.34 we show the measured $|\mathcal{R}(\omega)|$ as a function of the flux φ at $I_b = 0$. We call ω_{min} the frequency at which the modulus of the reflection coefficient is minimum. One can show (see Appendix Eq. (B.32)) that

$$\omega_{\text{min}} = \frac{1}{\sqrt{L_{\|}C}} \left(\sqrt{1 - \frac{L_{\|}}{2CZ_0^2} - \frac{r^2C}{2L_{\|}}} \right)^{-1} \tag{5.86}$$

To give an order of magnitude of the correction to the situation without dissipation, we estimate $L_{\text{JJ}}^{-1} \approx \varphi_0/I_0 \approx 2{\times}10^9\ \text{H}^{-1}$ and $L_{\text{AC}}^{-1}(I_b, \varphi) < 10^8\ \text{H}^{-1}$ so that the parallel inductance is just $L_{\|} \approx L_{\text{JJ}} \approx 0.4$ nH. The capacitance is $C \approx 21$ pF (from the measurement of the plasma frequency of the Josephson junction alone), and with $Z_0 = 50\ \Omega$ and $r \approx 0.5\ \Omega$:

$$\omega_{\text{min}} \approx \frac{1}{\sqrt{L_{\|}C}} + 0.5\% \tag{5.87}$$

Similarly, one can calculate the characteristic frequency ω_c at which the phase $\arg(\mathcal{R})$ transits (see Fig. 5.35):

$$\omega_c = \frac{1}{\sqrt{L_{\|}C}} \left(\sqrt{1 - \frac{r^2C}{L_{\|}}} \right)^{-1} \approx \frac{1}{\sqrt{L_{\|}C}} + 0.6\%. \tag{5.88}$$

These results show that the frequency at which the density plots Figs. 5.34, 5.35 exhibit a transition is very close to $\frac{1}{\sqrt{L_{\|}C}}$. Using the PIN of the atomic contact from Table. 5.2, one can calculate the value of $L_{\|}$ at $I_b = 0$. Then, one compares directly the resulting $\frac{1}{\sqrt{L_{\|}(\varphi)C}}$ curve with the position of the minimum of the measured reflection coefficient $|\mathcal{R}|$ or with the position of the abrupt phase change $\arg(\mathcal{R})$.

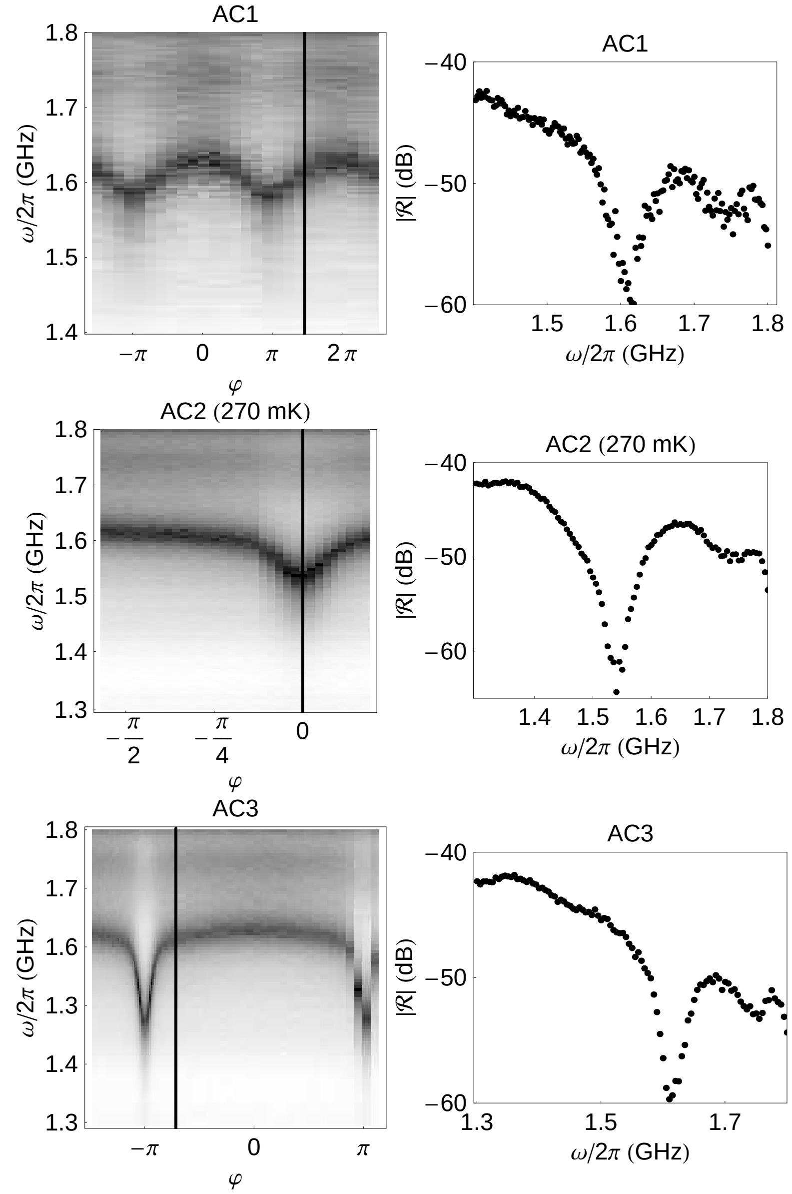

Fig. 5.34. Left panel: measured reflection coefficient amplitude $|\mathcal{R}|$ as a function of the excitation frequency $\omega/2\pi$ and reduced magnetic flux φ for the three atomic contacts AC1, AC2 and AC3. The darker the bin, the smaller the reflection amplitude. The profiles along the thick vertical line are plotted on the right panel. The actual level is lowered by approximately 40 dB due to the losses and amplifications in the measurement lines. All measurements were performed at the base refrigerator temperature (20 mK) except those corresponding to the contact AC2, which were taken at 270 mK. Two resonances (dark areas) can be observed as a function of the flux on the left panels near 1.6 and 1.75 GHz. The biggest one is due to the LC resonator to which the atomic contact belongs. The smallest one occurs at the same frequency for all values of the flux, and is attributed to the impedance of the circulators.

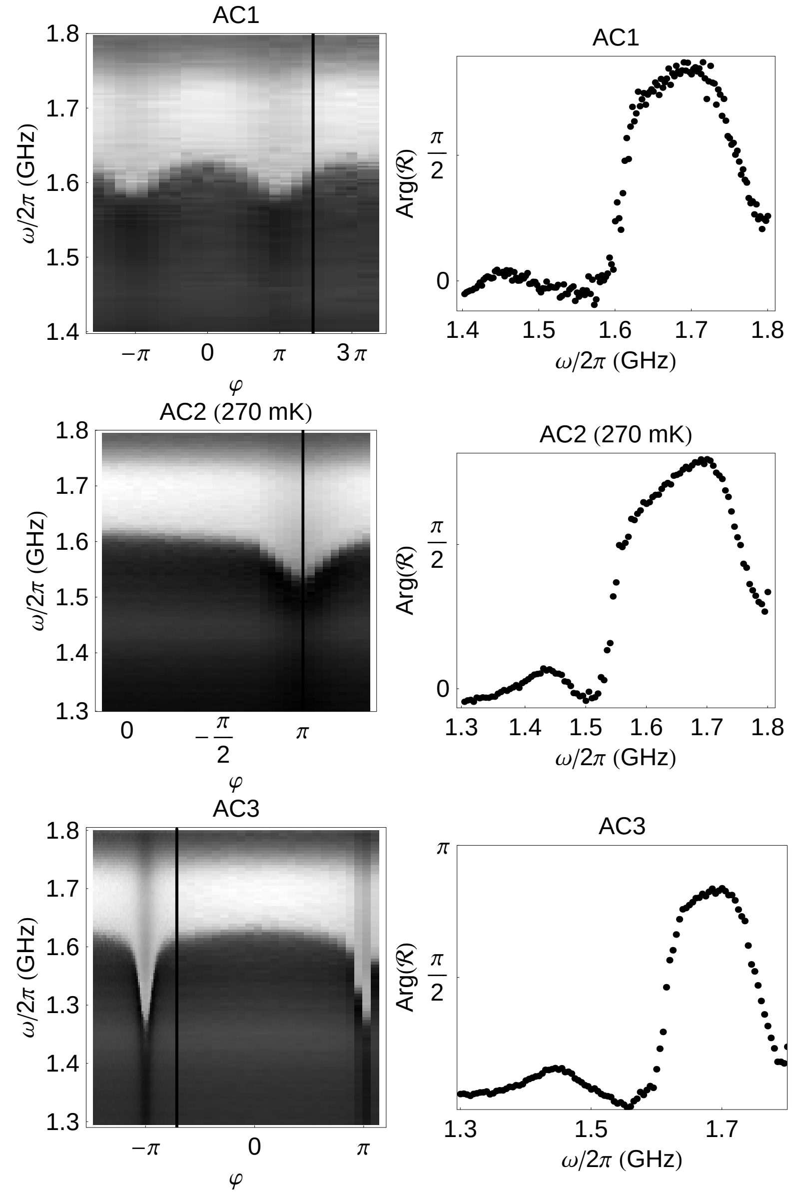

Fig. 5.35. Same plot as on Fig. 5.34 but for the phase of the reflection coefficient $\mathcal{R}$. The finite length of the transmission lines leads to a constant increase of $\arg(\mathcal{R})$ as a function of the frequency. Therefore, a linear background was subtracted from the raw data (on the plot, the zero of phase is arbitrary). The same parasitic resonance as on Fig. 5.34 occurs at a fixed frequency near 1.75 GHz. All measurements were performed at the base refrigerator temperature (20 mK) except those corresponding to the contact AC2, which were taken at 272 mK.

5.3.2 Comparison with theory at zero temperature

Using the expressions of the parallel inductance $L_{\|}$ at zero temperature Eqs. (5.80, 5.81), one easily calculate the zero temperature estimation of the transition frequencies $\omega_{\min}$ and ω_c. The comparison with this crude model is shown for $|\mathcal{R}|$ in Fig. 5.36. Similar curves are obtained for the phase $\arg(\mathcal{R})$. The comparison with the theory at zero temperature shows a qualitative agreement. Yet, some finite temperature calculation still have to be done in order to perform a quantitative comparison [21].

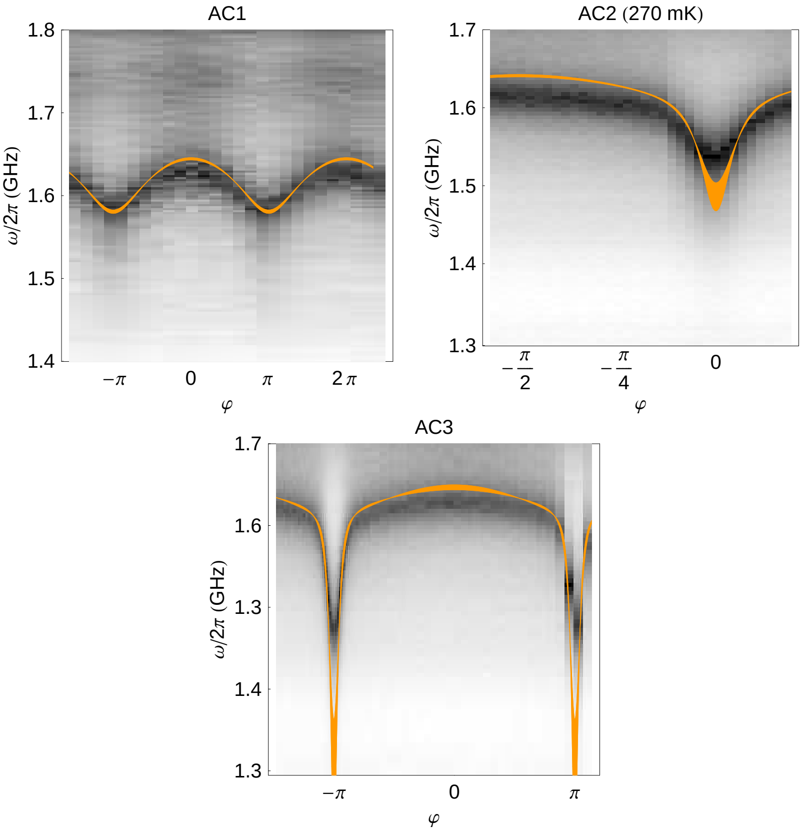

Fig. 5.36. Each density plot corresponds to a measurement of $|\mathcal{R}|$ as a function of the flux φ and the frequency ω, with the same colors as those used on Fig. 5.34. The lines correspond to the calculation of the frequency $\omega_{\text{res}} = (L_{\|}C)^{-1/2}$ as a function of the flux using Eqs. (5.80, 5.81) together with the PIN given on Table. 5.2 for each contact.

5.4 Conclusions

The experiments discussed in this chapter support strongly the theory that describes Josephson supercurrents as proceeding through Andreev bound states. In particular, we have shown that quantities closely related to the current-phase relation and the inductance-phase relation can be measured and are in close to a perfect agreement with the theoretical predictions. Further work needs to be done to carefully take into account the effect of the environment and of the noise on those quantities.

The main points of this chapter are the following

- the current-phase relationship of an atomic contact was successfully measured in a SQUID made of an atomic contact and a tunnel junction (Fig. 5.15)
- the inductance-phase relation was successfully measured in the same system (Figs. 5.34, 5.35)
- Josephson junctions may exhibit sub-gap structures whose amplitude seems to depend strongly on the value of the critical current I_0 (Fig. 5.17)
- the main influence of temperature on the switching current in the experiment comes from the dynamics of the phase of the Josephson junction in a fixed potential well. We have shown explicitly that the measured switching current as a function of the flux can be obtained by locally averaging the current-phase relation on a width increasing with temperature (see Eq. (5.67))
- the influence of the excitations of the Andreev bound states on the switching current was investigated in two limit behaviors: fast and slow excitation rates compared to the plasma frequency. At the temperatures used in our experiment, the effect of these processes was found to be negligible (see Figs. 5.25 and 5.28)
- the remaining discrepancy between experiment and theory could be due to non-thermal noise sources that excite the Andreev states

This experiment still remains to be improved in order to reduce the uncontrolled noise which leads to an excitation of the Andreev states. Furthermore, following a proposal by Shumeiko *et al.*, one may think of using Andreev bound states as the states of a q-bit [161]. An experiment trying to perform quantum manipulation of the state of atomic contacts could be performed in the near future. We already tried to shine microwave signals at frequencies of the order of the Andreev gap while looking at a possible change in the current-phase relationship, but were unsuccessfull in discriminating the respective roles of pure heating and of direct excitation by photonic absorbtion. At least measuring the life time of an Andreev state would be both challenging and rewarding, from a fundamental point of view.

Part III

Asymmetric current fluctuations

Chapter 6

Full Counting Statistics

Contents

Let us consider a conductor biased by a voltage source. The full counting statistics addresses the question of determining how many charge carriers have passed through an arbitrary cross-section of the conductor during a time t. To answer that question, we consider an ideal measurement device for the number $\hat{N}$ of charges having passed from one side (left) of the cross-section to the other (right). Quantum mechanics gives a probabilistic answer to that problem, $P(n,t)$ being the probability that n charges have passed during a time t

Calculating directly $P(n,t)$ is a difficult task and it turns out that working on its Fourier transform in the n domain is more convenient. This chapter is a short introduction to the field of full counting statistics with electrons, which was pioneered in the 1990's by Levitov *et al.* [162, 22]. In particular, we show the results of the full counting statistics theory on coherent conductors, which is entirely determined by its PIN (see § 4).

6.1 Generating function formalism

This section shows how the calculation of $P(n,t)$ can be reduced to a problem in the Keldysh formalism. Here, we follow closely the treatment of Kindermann [163]. It can be shown that, in the case of coherent conductors in the long time t limit, the only property of quantum mechanics needed to calculate $P(n,t)$ correctly is the Pauli exclusion principle. Interference effects between electrons and the phase of electrons does not modify the final results [164].

6.1.1 General definitions

For any operator $\hat{B}$, we use the time-dependent operator representation

$$\hat{B}(t) = \mathrm{e}^{i\hat{H}t/\hbar}\hat{B}\mathrm{e}^{-i\hat{H}t/\hbar} \tag{6.1}$$

where $\hat{H}$ is the Hamiltonian of the whole system. The moment generating function of $\hat{N}$ at time t and field ξ is defined as

$$\mathcal{F}_m(\xi,t) = \left\langle \exp(-i\xi\hat{N})(t) \right\rangle \tag{6.2}$$

where the average $\langle\cdots\rangle$ is taken over the initial density matrix ρ_0 of the electrons. This function is said generating because the moments of $\hat{N}$ are obtained by simply derivating it.

$$\left\langle \hat{N}(t)^k \right\rangle = i^k \frac{\partial^k \mathcal{F}_m(\xi=0,t)}{\partial \xi^k}. \tag{6.3}$$

Another quantity in probability theory is the cumulant $\left\langle\left\langle \hat{N}(t)^k \right\rangle\right\rangle$ of $\hat{N}(t)$. The cumulants[1] and their generating function $\mathcal{F}_c(\xi,t)$ are defined by

$$\mathcal{F}_c(\xi,t) \equiv \sum_{k=0}^{\infty} \left\langle\left\langle \hat{N}(t)^k \right\rangle\right\rangle \frac{(\xi/i)^k}{k!} \equiv \ln\left\langle \mathrm{e}^{-i\xi\hat{N}}(t) \right\rangle = \ln\left(\mathcal{F}_m(\xi,t)\right). \tag{6.4}$$

---

[1] A recipe allows one to link the cumulants to the moments [165]. Let p be a integer between 0 and $k-1$. Let us write down k times the character $\hat{N}$. Then let us divide this writing in $p+1$ subsets with brackets:

$$\left\langle \hat{N}\hat{N} \right\rangle \left\langle \hat{N} \right\rangle \cdots \left\langle \hat{N}\hat{N}\hat{N} \right\rangle.$$

Let us call C_p the sum of all those kind of terms. Then, the cumulant of order k is given by the sum

$$\left\langle\left\langle \hat{N}^k \right\rangle\right\rangle = \sum_{p=0}^{k-1} (-1)^p p! C_p.$$

Similarly to the function $\mathcal{F}_m(\xi,t)$, the cumulants are obtained by simple derivation of the function $\mathcal{F}_c(\xi,t)$. Finally, the probability $P(n,t)$ that n electrons are measured at time t, which is just $P(n,t) \equiv \langle |n\rangle\langle n|(t)\rangle$, is the Fourier transform of $\mathcal{F}_m(\xi,t)$:

$$\mathrm{e}^{\mathcal{F}_c(\xi,t)} = \left\langle \mathrm{e}^{-i\xi\hat{N}}(t)\right\rangle = \sum_{m=-\infty}^{+\infty} P(m,t)\mathrm{e}^{-i\xi m}.$$

which yields:

$$P(n,t) = \frac{1}{2\pi}\int_{-\pi}^{+\pi} \mathrm{e}^{\mathcal{F}_c(\xi,t)+in\xi}\mathrm{d}\xi. \tag{6.5}$$

The cumulants have no particular meaning. Two possibilities occur for the cumulants. Either only the two first cumulants are non-zero and Eq. (6.5) proves that $P(n,t)$ is a Gaussian, or one cumulant of order above 2 is non-zero and then an infinite number of cumulants are non-zero (otherwise, $P(n,t)$ would not be positive). This is the Marcienkiewicz theorem [166, 167].

6.1.2 Derivation of the generating function in the Keldysh formalism

We have seen that the calculation of $P(n,t)$ reduces to the calculation of the generating function $\mathcal{F}_c(\xi,t)$. In this section, we present the derivation of $\mathcal{F}_c(\xi,t)$ as done by Nazarov *et al.* [168, 163]. Using the definition of the generating function

$$\mathcal{F}_c(\xi,t) \equiv \ln\left\langle \mathrm{e}^{-i\xi\hat{N}}(t)\right\rangle \tag{6.6}$$

one may write

$$\begin{aligned}\mathcal{F}_c(\xi,t) &= \ln\left\langle \mathrm{e}^{i\hat{H}t/\hbar}\mathrm{e}^{-i\xi\hat{N}}\mathrm{e}^{-i\hat{H}t/\hbar}\right\rangle \\ &= \ln\left\langle \mathrm{e}^{-i\xi\hat{N}/2}\left[\mathrm{e}^{i\xi\hat{N}/2}\mathrm{e}^{i\hat{H}t/\hbar}\mathrm{e}^{-i\xi\hat{N}/2}\right]\left[\mathrm{e}^{-i\xi\hat{N}/2}\mathrm{e}^{-i\hat{H}t/\hbar}\mathrm{e}^{i\xi\hat{N}/2}\right]\mathrm{e}^{-i\xi\hat{N}/2}\right\rangle \\ &= \ln\left\langle \mathrm{e}^{-i\xi\hat{N}/2}\exp\left[\tfrac{it}{\hbar}\mathrm{e}^{i\xi\hat{N}/2}\hat{H}\mathrm{e}^{-i\xi\hat{N}/2}\right]\exp\left[-\tfrac{it}{\hbar}\mathrm{e}^{-i\xi\hat{N}/2}\hat{H}\mathrm{e}^{i\xi\hat{N}/2}\right]\mathrm{e}^{-i\xi\hat{N}/2}\right\rangle\end{aligned} \tag{6.7}$$

where we have used the fact that for any observable $\hat{B}$,

$$\mathrm{e}^{i\xi\hat{N}/2}\mathrm{e}^{\hat{B}}\mathrm{e}^{-i\xi\hat{N}/2} = \exp\left(\mathrm{e}^{i\xi\hat{N}/2}\hat{B}\mathrm{e}^{-i\xi\hat{N}/2}\right). \tag{6.8}$$

This last expression simplifies if one introduces the Hamiltonian $\hat{H}_\xi$ of the same system in presence of a (counting) vector potential $\hat{\mathbf{A}}(\xi) = \xi\varphi_0\delta(\hat{x})\mathbf{u_x}$ ($\mathbf{u_x}$ being a vector unit pointing towards the right lead)[2].

---

[2] This Hamiltonian $\hat{H}_\xi$ is obtained from $\hat{H}$ by replacing the momentum $\hat{\mathbf{p}}$ by

$$\hat{\mathbf{p}}_\xi = \mathrm{e}^{-i\xi\hat{N}/2}\hat{\mathbf{p}}\mathrm{e}^{i\xi\hat{N}/2} = \hat{\mathbf{p}} - e\hat{\mathbf{A}}(\xi). \tag{6.9}$$

$$\mathcal{F}_c(\xi,t) = \ln\left\langle \mathrm{e}^{-i\xi\hat{N}/2}\mathrm{e}^{i\hat{H}_{-\xi}t/\hbar}\mathrm{e}^{-i\hat{H}_{\xi}t/\hbar}\mathrm{e}^{-i\xi\hat{N}/2}\right\rangle . \tag{6.10}$$

Then, assuming also that at time $t = 0$ the number of electrons having passed is set to zero, the generating function reads

$$\mathcal{F}_c(\xi,t) = \ln\left\langle \mathrm{e}^{i\hat{H}_{-\xi}t/\hbar}\mathrm{e}^{-i\hat{H}_{\xi}t/\hbar}\right\rangle . \tag{6.11}$$

Furthermore, in the semiclassical approximation[3], one can replace $\hat{H}_\xi$ by its Taylor series at first order:

$$\mathcal{F}_c(\xi,t) = \ln\left\langle \mathrm{e}^{i(\hat{H}-\xi\varphi_0\hat{I})t/\hbar}\mathrm{e}^{-i(\hat{H}+\xi\varphi_0\hat{I})t/\hbar}\right\rangle . \tag{6.17}$$

The remaining of the calculation uses the identity

$$\mathrm{e}^{-i(\hat{H}+\xi\varphi_0\hat{I})t/\hbar} = \mathrm{e}^{-i\hat{H}t/\hbar}\overrightarrow{T}\mathrm{e}^{-i\xi\varphi_0\int_0^t \hat{I}(t)\mathrm{d}t} \tag{6.18}$$

where $\overrightarrow{T}$ denotes the normal time ordering. Finally,

$$\boxed{\mathcal{F}_c(\xi,t) = \ln\left\langle \overleftarrow{T}\mathrm{e}^{-i\xi/2e\int_0^t \hat{I}(\tau)\mathrm{d}\tau}\overrightarrow{T}\mathrm{e}^{-i\xi/2e\int_0^t \hat{I}(\tau)\mathrm{d}\tau}\right\rangle} \tag{6.19}$$

The Taylor series[4] of this expression makes clear the link between the moments of the number $\hat{N}(t)$ and the integrated current operators $\int_0^t \hat{I}(\tau)\mathrm{d}\tau$. The complex time-ordering in the current operators, which was badly taken

---

[3] If we assume that $\hat{H} = \sum_i \frac{\hat{\mathbf{p}}_\mathbf{i}{}^2}{2m} + V(\hat{\mathbf{r}}_\mathbf{i})$, then

$$\hat{H}_\xi = \sum \frac{\hat{\mathbf{p}}_\xi^2}{2m} + V(\hat{\mathbf{r}}) \tag{6.12}$$

and

$$\begin{aligned}\hat{\mathbf{p}}_\xi^2 &= \mathrm{e}^{-i\xi\hat{N}/2}\hat{\mathbf{p}}^2\mathrm{e}^{i\xi\hat{N}/2} &(6.13)\\ &= (1 - i\xi\hat{N}/2)\hat{\mathbf{p}}^2(1 + i\xi\hat{N}/2) + O(\xi^2) &(6.14)\\ &= \hat{\mathbf{p}}^2 + i\xi/2\left[\hat{\mathbf{p}}^2, \hat{N}\right] + O(\xi^2) &(6.15)\end{aligned}$$

and finally

$$\hat{H}_\xi = \hat{H} + i\xi/2\left[\hat{H}, \hat{N}\right] + O(\xi^2) = \hat{H} + \varphi_0\xi\hat{I} + O(\xi^2), \tag{6.16}$$

The expansion in power of ξ is valid as the generating function is used only near $\xi = 0$ in the calculation of the cumulants.

[4] The term of order n in ξ reads

$$\left\langle\left\langle \hat{N}(t)^n \right\rangle\right\rangle (-i\xi)^n = \frac{(-i\xi/2e)^n}{n!}\int_{\mathcal{C}_\mathcal{K}} \mathrm{d}t_1 \cdots \int_{\mathcal{C}_\mathcal{K}} \mathrm{d}t_n \langle T^{\mathcal{C}_\mathcal{K}} I(t_1)\cdots I(t_n)\rangle$$

where $\mathcal{C}_\mathcal{K}$ is the Keldysh contour [169].

into account in the first trials to derive high moments of electrical noise [162], appears in this formula in a compact way. In 1993, Levitov *et al.* calculated the generating function at first order in the development of the exponent for a tunnel junction, and found that $\hat{N}$ obeys a Poisson law similarly to what happens in vacuum diodes [22]. One may recognize in the expression (6.19) an integral on a Keldysh contour $\mathcal{C}_{\mathcal{K}}$ [169]. Nazarov and Belzig showed [168, 54] that using the standard Keldysh formalism with boundary conditions containing a term depending on the counting field ξ, one can calculate (6.19) directly. It is remarkable that the Full Counting Statistics of the number $\hat{N}$ can be calculated using the same mathematical apparatus as for the calculation of other transport properties.

In section 6.2, we will only give the results of this calculation for coherent conductors, as derived by Nazarov *et al.* Recently, two other formalisms have been developed to calculate the cumulants of $\hat{N}$, especially at finite times [170, 171]. Here, in the case of coherent conductors at long times, we focus on the Keldysh derivation only because it allows to calculate cumulants at any order from a single function.

6.1.3 Link with the spectral density of noise

Differentiating (6.19) twice with respect to $(-i\xi)$, one finds an expression for the second cumulant of the number $\hat{N}$ according to (6.4)

$$\left\langle\left\langle \hat{N}(t)^2 \right\rangle\right\rangle = \frac{1}{e^2}\int_0^t\int_0^t \mathrm{d}\tau\mathrm{d}\tau' \left\langle \delta\hat{I}(\tau)\delta\hat{I}(\tau')\right\rangle \tag{6.20}$$

where $\delta\hat{I}(t) = \hat{I}(t) - \left\langle \hat{I}(t)\right\rangle$. Assuming that the noise is invariant by time translation, and using the change of variable ($\eta = \tau - \tau'$ and $\alpha = (\tau+\tau')/2$) this equation reads

$$\left\langle\left\langle \hat{N}(t)^2 \right\rangle\right\rangle = \frac{1}{e^2}\int_0^t \mathrm{d}\alpha \int_{-\mu(\alpha)}^{\mu(\alpha)} \mathrm{d}\eta \left\langle \delta\hat{I}(\eta)\delta\hat{I}(0)\right\rangle . \tag{6.21}$$

where

$$\mu(\alpha) = \begin{cases} \alpha & \text{if } \alpha < t/2 \\ t-\alpha & \text{if } \alpha \geq t/2 \end{cases} .$$

We will assume[5] that the time correlation t_c of the current is much smaller than the time t. Hence,

---

[5] In fact, we can go further without this assumption. Indeed, the spectral density of states is just the Fourier transform of the current correlator

$$\left\langle \delta\hat{I}(\eta)\delta\hat{I}(0)\right\rangle = \frac{1}{4\pi}\int_{-\infty}^{+\infty} \mathrm{e}^{-i\omega\eta} S_I(\omega)\mathrm{d}\omega \tag{6.22}$$

and the second cumulant reads

$$\left\langle\left\langle \hat{N}(t)^2 \right\rangle\right\rangle \underset{t \gg t_c}{=} \frac{t}{e^2} \int_{-\infty}^{\infty} \left\langle \delta\hat{I}(\eta)\delta\hat{I}(0) \right\rangle \mathrm{d}\eta. \tag{6.24}$$

Introducing the current noise spectral density[6]

$$S_I(\omega) = 2 \int_{-\infty}^{+\infty} \mathrm{e}^{i\omega\tau} \left\langle \delta\hat{I}(\tau)\delta\hat{I}(0) \right\rangle \mathrm{d}\tau, \tag{6.25}$$

we see that the second cumulant of $\hat{N}$ has a very simple interpretation in terms of the zero frequency noise spectrum

$$\left\langle\left\langle \hat{N}(t)^2 \right\rangle\right\rangle \underset{t \gg t_c}{=} \frac{t}{2e^2} S_I(0). \tag{6.26}$$

Finally, using the fact that the first order cumulant of $\hat{N}$ is just given by the average current

$$\left\langle\left\langle \hat{N}(t) \right\rangle\right\rangle = \langle I \rangle\, t/e, \tag{6.27}$$

the link between the first and second cumulants of $\hat{N}$ is just:

$$\left\langle\left\langle \hat{N}(t)^2 \right\rangle\right\rangle = \frac{S_I(0)}{2e\,\langle I \rangle} \left\langle\left\langle \hat{N}(t) \right\rangle\right\rangle. \tag{6.28}$$

In the so-called shot-noise limit, where $S_I(0) = 2e\,\langle I \rangle$, we find the standard result that the width of the distribution $P(n,t)$ grows like $\sqrt{\left\langle\left\langle \hat{N}(t) \right\rangle\right\rangle}$.

6.2 Application of the Full Counting Statistics theory to coherent conductors

The cumulant generating function $\mathcal{F}_c(\xi,t)$ can be calculated at long time t compared to the correlation time t_c of the current correlator for a coherent conductor biased by a voltage V. Depending on the type of reservoirs, Belzig and Nazarov predicted different generating functions [172].

$$\left\langle\left\langle \hat{N}(t)^2 \right\rangle\right\rangle = \frac{1}{4\pi e^2} \int_0^t \mathrm{d}\alpha \int_{-\mu(\alpha)}^{\mu(\alpha)} \mathrm{d}\eta \int_{-\infty}^{+\infty} \mathrm{e}^{-i\omega\eta} S_I(\omega) \mathrm{d}\omega. \tag{6.23}$$

[6] This definition corresponds to the asymmetric current noise. Indeed, as current operators at different times do not commute, multiple definitions exist for the spectral density $S_I(\omega)$. In our definition, for positive (negative) frequency ω, the spectrum $S_I(\omega)$ is the absorption (emission) rate of photons of energy $|\hbar\omega|$ by the conductor. The classical definition of the noise spectral density is then $(S_I(\omega) + S_I(-\omega))/2$

6.2.1 General case

For long time $t \gg t_c$, $\mathcal{F}_c(\xi, t) = t\mathcal{F}_c(\xi)$ where $\mathcal{F}_c(\xi)$ does not depend on time. The biggest simplification in the calculation of $\mathcal{F}_c(\xi)$ for a coherent conductor is the fact that the contributions of each transmission channel just add up directly. For a coherent conductor whose PIN is $\{\tau_i\}$,

$$\mathcal{F}_c(\xi) = \sum_i \mathcal{F}_c^{\tau_i}(\xi). \tag{6.29}$$

Depending on the type of electrodes, different expressions for $\mathcal{F}_c^{\tau_i}(\xi)$ are obtained.

Normal electrodes (NXN)

Let us call f_L and f_R the energy distribution function of the electrons in the left and right electrodes. We will assume that they are Fermi functions with different chemical potentials: $f_L(E + eV) = f_R(E) = (\mathrm{e}^{E/k_BT} + 1)^{-1}$. The result of Nazarov *et al.* is:

$$\begin{aligned} \mathcal{F}_c^{\tau}(\xi) = \frac{1}{h}\int_{-\infty}^{+\infty} \mathrm{d}E \ln[1 + \tau f_L(E)(1 - f_R(E))(\mathrm{e}^{-i\xi} - 1) + \\ \tau f_R(E)(1 - f_L(E))(\mathrm{e}^{i\xi} - 1))] \end{aligned} \tag{6.30}$$

Zero temperature limit

For temperatures such that $k_BT \ll eV$, the expression Eq. (6.30) simplifies into

$$\mathcal{F}_c^{\tau}(\xi) = \frac{e|V|}{h} \ln[1 + \tau(\mathrm{e}^{-\mathrm{sgn}(V)i\xi} - 1)] \tag{6.31}$$

where sgn(V) is the sign of V. The corresponding probability distribution of the number $\hat{N}$ of electrons going through a single channel of transmission τ can be calculated using Eq. (6.5). It is binomial and reads for positive V

$$P(n, t) = \binom{\left\langle \hat{N}(t) \right\rangle / \tau}{n} \tau^n (1 - \tau)^{\left\langle \hat{N}(t) \right\rangle / \tau - n} \tag{6.32}$$

It is noteworthy that current fluctuations in coherent conductors do not obey to a pure Gaussian law in general.

Superconducting electrode on one side and normal electrode on the other (NXS)

If one electrode is normal while the other is superconducting, the general expression for the generating function reads

$$\mathcal{F}_c^{\tau}(\xi) = \frac{1}{h}\int_{-\infty}^{+\infty} \mathrm{d}E \ln\left[1 + \sum_{q=-2}^{2} A_{\tau,q}(E)(\mathrm{e}^{-iq\xi} - 1)\right] \tag{6.33}$$

where the coefficients $A_{\tau,q}(E)$ are related to the transfer of q charges in the channel of transmission τ and can be found in [173]. In particular, for one single channel of transmission τ, at zero temperature, and for voltages below Δ/e, the generating function reads[174]

$$\mathcal{F}_c^{\tau}(\xi) = \frac{e|V|}{h}\ln\left[1 + \frac{\tau^2}{(2-\tau)^2}(\mathrm{e}^{-2i\xi} - 1)\right] \tag{6.34}$$

Hence, for $eV < \Delta$, the probability distribution is zero for odd charges and binomial for even charges

$$\begin{aligned} &P(2n,t) = \tbinom{\langle \hat{N}(t)\rangle/\tau}{2n}\left(\tfrac{\tau}{2-\tau}\right)^{2n}\left(1 - \left(\tfrac{\tau}{2-\tau}\right)^{2}\right)^{\langle \hat{N}(t)\rangle/(2\tau)-n} \\ &P(2n+1,t) = 0 \end{aligned} \tag{6.35}$$

Finally, for $eV \gg \Delta$, single tunneling can occur and dominate the noise signal. Therefore, the generating function is the same as in the case of normal metal electrodes Eq. (6.30).

Superconducting electrodes on both sides (SXS)

In the case where superconducting electrodes are on each side of the conductor, like in our experiments (see section 5.1.4), the statistics if much more difficult to calculate. In fact, multiple charge transfers (Multiple Andreev Reflection processes) contribute to $\mathcal{F}_c^{\tau}(\xi)$ at all charge multiples. The zero temperature cumulant generating function has been calculated in Ref. [175] and reads

$$\mathcal{F}_c^{\tau}(\xi) = \frac{1}{h}\int_{0}^{eV} \mathrm{d}E \ln\left[1 + \sum_{n=-\infty}^{\infty} P_n(E,V)(\mathrm{e}^{-in\xi} - 1)\right] \tag{6.36}$$

We refer the reader to the work of Cuevas and Belzig for the calculation of the probability $P_n(E,V)$ that n charge quanta of energy E have passed through the contact [175].

6.2.2 Tunnel junction

Case of an NIN tunnel junction

In the case of a tunnel junction ($\forall i; \tau_i \ll 1$, see (4.4)), we have, using (A.5) (see Appendix),

$$\begin{aligned}\mathcal{F}_c(\xi,t) &\approx \frac{t}{h}\sum_i \tau_i \int_{-\infty}^{+\infty} \mathrm{d}E[f_L(E)(1-f_R(E))(\mathrm{e}^{-i\xi}-1) \\ &\quad + f_R(E)(1-f_L(E))(\mathrm{e}^{i\xi}-1)] \qquad (6.37)\\ &\approx \frac{eVt}{h}\frac{h}{e^2R}\left[\frac{1}{1-\mathrm{e}^{-\frac{eV}{k_BT}}}(\mathrm{e}^{-i\xi}-1)+\frac{1}{\mathrm{e}^{\frac{eV}{k_BT}}-1}(\mathrm{e}^{i\xi}-1)\right] \qquad (6.38)\\ &\approx -\frac{Vt}{eR}\left[2\coth\left(\frac{eV}{2k_BT}\right)\sin^2(\xi/2)+i\sin\xi\right] \qquad (6.39)\end{aligned}$$

which coincides with the expression derived, in a first order approach, by Levitov and coworkers [22]. Thus, using Eq. (6.4), the cumulants are given by

$$\left\langle\left\langle \hat{N}(t)^k \right\rangle\right\rangle = \begin{cases} \frac{tV}{eR}\coth\left(\frac{eV}{2k_BT}\right) & \text{if } k \text{ is even} \\ \frac{tV}{eR} & \text{if } k \text{ is odd}\end{cases} \qquad (6.40)$$

In order to check the consistency of this expression with existing theory of the noise spectral density, we use Eq. (6.26) for $k=2$ and get

$$S_I(0) = \frac{2e^2}{t}\left\langle\left\langle \hat{N}(t)^2 \right\rangle\right\rangle = 2eI\coth\left(\frac{eV}{2k_BT}\right) \qquad (6.41)$$

This is in agreement with the standard formula for the zero frequency noise [52].

At zero temperature, all cumulants are equal to the mean value $\left\langle \hat{N}(t)\right\rangle$ of $\hat{N}$. Therefore, $P(n,t)$ is a Poisson distribution:

$$P(n,t) \sim \frac{\left\langle \hat{N}(t)\right\rangle^n}{n!}\mathrm{e}^{-\left\langle \hat{N}(t)\right\rangle} \qquad (6.42)$$

At high temperatures, the even cumulants are all equal to $\frac{R_K}{R}\frac{2tk_BT}{h}$ which is proportional to the variance of a classical conductor as is proven below in Eq. (6.48).

Case of an NIS tunnel junction

If one of the electrodes is superconducting, at zero temperature and for voltages $V \geq \Delta/e$, the result of the calculation of the probability $P(n,t)$ using Eq. (6.33) is exactly the same as for an NIN junction Eq. (6.42). The only difference is the fact that $\left\langle \hat{N}(t)\right\rangle = tI/e \neq tV/eR$ (see Fig. 7.4).

6.3 Full counting statistics for incoherent conductors

When the charge carriers are not independent, the theory of Full Counting Statistics is much harder to deal with. Some works have investigated this regime, among them Refs. [176, 177, 178, 179, 180, 181, 182, 183]. First, we discuss the case of the most common type of incoherent conductors: classical ones.

6.3.1 Thermalized conductor

The current fluctuations through a thermalized conductor of resistance R are due to thermal noise only. Therefore, $P(n,t)$ is purely Gaussian and the generating function of the cumulants reads

$$\mathcal{F}_c(\xi,t) = 1 - i\xi \left\langle\left\langle \hat{N}(t) \right\rangle\right\rangle - \frac{\xi^2}{2} \left\langle\left\langle \hat{N}(t)^2 \right\rangle\right\rangle . \tag{6.43}$$

where $\left\langle\left\langle \hat{N}(t) \right\rangle\right\rangle = Vt/eR$. In order to calculate the second cumulant of $\hat{N}$, we use Eq. (6.21):

$$\left\langle\left\langle \hat{N}(t)^2 \right\rangle\right\rangle = \frac{1}{e^2} \int_0^t \mathrm{d}\alpha \int_{-\mu(\alpha)}^{\mu(\alpha)} \mathrm{d}\eta \left\langle \delta\hat{I}(\eta)\delta\hat{I}(0) \right\rangle . \tag{6.44}$$

Besides, the spectral density is then given by the Johnson-Nyquist formula

$$S_I(\omega) = \frac{4}{R} \frac{\hbar\omega}{1 - \mathrm{e}^{-\frac{\hbar\omega}{k_B T}}} \tag{6.45}$$

Hence, by Fourier transforming (according to (6.22)), we have[7],

$$\left\langle \delta\hat{I}(\eta)\delta\hat{I}(0) \right\rangle = \frac{\hbar}{\pi\eta^2 R} \left[1 - \left(\frac{\eta\omega_1/2}{\sinh(\eta\omega_1/2)} \right)^2 \right] \tag{6.47}$$

where $\omega_1 = 2\pi k_B T/\hbar$ is the first Matsubara frequency. Going through the calculation, we get[8]

---

[7] One can use the identity

$$2\int_0^{+\infty} \cos(x\eta) \frac{x}{1 - \mathrm{e}^{x\beta}} \mathrm{d}x = \eta^{-2} \left(\left(\frac{\pi\eta}{\beta} \right)^2 / \sinh^2 \left(\frac{\pi\eta}{\beta} \right) - 1 \right) . \tag{6.46}$$

[8] Notice that for long time $t \gg 1/\omega_1$, the cumulant $\left\langle\left\langle \hat{N}(t)^2 \right\rangle\right\rangle$ is just proportional to the time t:

$$\left\langle\left\langle \hat{N}^2 \right\rangle\right\rangle \sim \frac{R_K}{R} \frac{2k_B T}{h} t. \tag{6.48}$$

This is a direct consequence of the fact that for long times $\mathcal{F}_c(\xi,t) \propto t$.

$$\left\langle\left\langle \hat{N}^2 \right\rangle\right\rangle = \frac{4\hbar}{\pi e^2 R} \ln\left(\frac{\sinh(\omega_1 t/4)}{\omega_1 t/4}\right). \tag{6.49}$$

Finally, the probability $P(n,t)$ is a Gaussian

$$P(n,t) = \frac{e^{-(n-\bar{n}(t))^2/\sigma^2(t)}}{\sigma(t)\sqrt{\pi}} \tag{6.50}$$

centered on $\bar{n}(t) = Vt/eR$ and whose variance is given by

$$\sigma(t) = \sqrt{2\left\langle\left\langle \hat{N}(t)^2 \right\rangle\right\rangle}. \tag{6.51}$$

6.3.2 Diffusive wire

In a diffusive wire, one can calculate the statistics of the current by using the results on coherent conductors only if the length L of the wire is much smaller than the coherence length L_φ and if the time t at which the cumulant generating function $\mathcal{F}_c(\xi,t)$ is calculated is much longer than the diffusion time and $eV/\hbar$. See section B.9 for a full calculation of the generating function, and of the first cumulants.

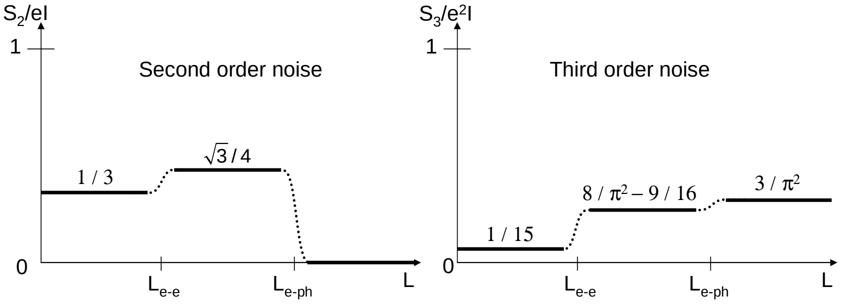

Fig. 6.1. Second and third noise densities at zero frequency as a function of the wire length in the limit of small temperatures (see text).

The general case with strong interactions has been also investigated in three different formalisms [184, 185]. On the experimental side, measuring the spectral density of the noise has proven to be an elegant way to measure the intensity of interactions between electrons in a wire [12, 13]. The second and third cumulants of the current fluctuations have been calculated in the zero frequency limit and their value is closely related to the length of the wire. At low temperatures, where $eV \gg k_B T$ and where $L_\varphi^{(\mathrm{ee})} \ll L_\varphi^{(\mathrm{e-ph})}$ (see section 2.2), the spectral density of the noise $S_I(\omega = 0)$ is multiplied by a factor

1.3 when the length increases above $L_\varphi^{(\mathrm{ee})}$ whereas the third order density[9] $S_I^{(3)}(0,0)$ is multiplied by a factor 3.7 (see Fig. 6.1) [186].

---

[9] The third order density of the current fluctuations is defined by

$$S_I^{(3)}(\omega_1,\omega_2)=\int_{-\infty}^{+\infty}\mathrm{d}\tau_1\mathrm{e}^{i\omega_1\tau_1}\int_{-\infty}^{+\infty}\mathrm{d}\tau_2\mathrm{e}^{i\omega_2(\tau_2-\tau_1)}T^{\mathcal{C}_\mathcal{K}}\left\langle\delta\hat{I}(\tau_2)\delta\hat{I}(\tau_1)\delta\hat{I}(0)\right\rangle. \tag{6.52}$$

Chapter 7

Josephson junction as a current noise detector

Contents

The previous chapter describes how the Full Counting Statistics theory can predict the probability $P(n,t)$ for n charges to pass through a conductor in a time t. In this chapter, we discuss a preliminary experiment using a Josephson junction as a threshold detector for the current, which probes properties of the charge transfer statistics.

7.1 Josephson junction in a noisy environment

7.1.1 Setup of the measurement device

In section 5.2.1, it was shown that Josephson junctions can go from a “zero voltage” state to a dissipative state if the current slightly increases from a value just below the so-called critical current I_0. Hence, Josephson junctions can be seen as current threshold detectors. In 2004, Tobiska and Nazarov proposed to use such threshold detectors to probe the Full Counting Statistics of charge transfer [27]. The idea is to bias a Josephson junction just below I_0 so that large enough, positive fluctuations of the current lead to a switching event. Ideally, the switching probabilities are then directly linked to the distribution of the current fluctuations. Yet, a realistic Josephson junction is not an ideal current threshold detector and a rough estimate [27] shows that an overdamped Josephson junction should not be sensitive to large enough current fluctuations to detect anything else than the few first cumulants of the current. Tobiska and Nazarov suggested to add in parallel with the Josephson junction a device with negative inductance, because it should be sensitive to much larger current fluctuations than the Josephson junction alone, thus theoretically allowing the access to cumulants of any order [27]. Our experiment was conceived as a preliminary test of the noise detecting skills of Josephson junctions. Therefore, we used a single junction only and tried to understand up to which order of the cumulants of current fluctuations it is sensitive. In the experiment, a mesoscopic device (an NIS tunnel junction) is biased at a constant voltage. The current going through it is the sum of a constant part and of a fluctuating part: $I_m(t) = \langle I_m \rangle + \delta I_m(t)$ (see Fig. 7.1). The constant part $\langle I_m \rangle$ of the current is forced to flow into an impedant return line while the fluctuating part flows directly through the Josephson junction. Meanwhile,

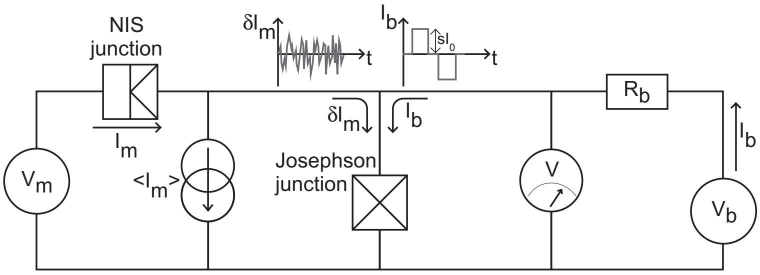

Fig. 7.1. Scheme of the experiment. The fluctuations δI_m of a mesoscopic conductor (an NIS tunnel junction in our experiment) are forced to pass through a Josephson junction. A bias line sends current pulses $I_b(t)$ on top of the fluctuations δI_m in the junction. The switching probability of the junction during one pulse can be related to the current fluctuations.

current pulses $I_b(t)$ are forced through the junction through a bias line similarly to the atomic contact experiment. The switching rate of the junction is then measured for various amplitudes of the current pulse.

7.1.2 Ideal case

In order to understand the principle of the experiment, let us first consider the ideal case of a perfect threshold detector instead of the Josephson junction. This means that the "Josephson junction" switches only when the current exceeds the critical current I_0 (see §5.2.1 in the zero temperature limit). Of course, there is no sense in speaking of instantaneous values of the current. We need to introduce a "counting time" τ_0 during which the junction measures the current before "deciding" to switch or not. In the picture of classical phase dynamics (see § 5.2.1), current fluctuations correspond to fluctuations in the tilt of the potential well. It is known that the resonant activation of a junction using an oscillating bias signal at a fixed frequency presents a sharp cut-off near the plasma frequency [187] (see Fig. 7.6), indicating that fluctuations of the tilt which last shorter than $(2\pi/\omega_p)$ do not contribute to the escape dynamics. However, tilting the potential during more than $2\pi/\omega_p$ affects the switching rate. The counting time of this detector can thus be defined as $\tau_0 = 2\pi/\omega_p$.

During a current pulse[1] of length τ_{pls} and of height sI_0, the probability P_{sw} for the junction to switch can be easily derived. The time window τ_{pls} can be cut into intervals of length τ_0, and P_{sw} is just the probability for the junction to switch in at least one of these intervals. Therefore, assuming the noise in the junction is correlated on a timescale[2] smaller than τ_0,

$$P_{\text{sw}} = 1 - [1 - P(n \geq N(s), \tau_0)]^{\tau_{\text{pls}}/\tau_0} \tag{7.1}$$

where $P(n \geq N(s), \tau_0)$ is the probability that the number n of charges having passed through the noisy mesoscopic conductor during τ_0 exceeds a threshold $N(s) = \frac{\tau_0 I_0}{e}(1-s)$.

$$P(n \geq N(s), \tau_0) = \sum_{n=N(s)}^{+\infty} P(n, \tau_0). \tag{7.2}$$

Thus, in an ideal experiment, the switching probability is linked to the counting probability $P(n,t)$ straightforwardly by a simple derivative. However, with a real Josephson junction at finite temperatures, the switching probability cannot be expressed in such a direct way in terms of the counting probability and one has to use a more elaborated theoretical approach to predict it.

---

[1] Meaning that $I_b(t)$ is always zero except during a time window τ_{pls} where it reads sI_0.

[2] In a perfect voltage bias situation, the correlation time between two tunneling events is of the order of $\hbar/eV$. In our experiment, $\tau_0 \approx 1$ ns and $\hbar/eV \approx 0.1-1$ ps.

7.1.3 Simple signature of non-Gaussian noise

We have seen in chapter 6 that the current passing through a voltage-biased coherent conductor has non-Gaussian statistics in general. In our experiment, the conductor is just a tunnel junction and the statistics of the charge transfers is a Poisson distribution. Therefore, large positive fluctuations (positive meaning in the same direction as the average current) are more likely than large negative fluctuations (see Fig. 7.2). This asymmetry can be tested directly within our experimental setup. Indeed, for the same pulse height sI_0, the switching probabilities in the case of a positive or a negative average current $\langle I_m \rangle$ should differ.

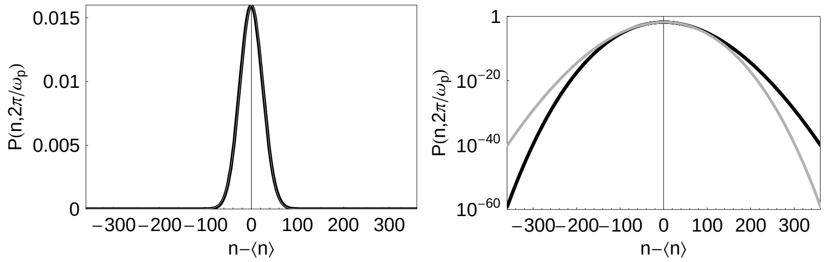

Fig. 7.2. Predicted distribution function $P(n, 2\pi/\omega_p)$ in case of a tunnel junction (Poisson distribution see Eq. (6.42)). The black curve corresponds to a positive average number of particles passing through the junction and the gray curve to the opposite situation. Here, the average current was set to 0.1 μA and $\omega_p/2\pi$ was set to 1 GHz. The right panel shows the same function as in the left panel in log scale. A clear asymmetry can be seen in log scale between the two directions of the current.

7.2 Characterization of the circuit

In this section, we describe more thoroughly the characteristics of the electrical circuit. The electrical properties of the discrete elements were measured and are given in appendix C.1.

7.2.1 NIS junction properties

The conductor which produces the noise under study is a tunnel junction between a copper electrode and an aluminum electrode in its superconductive state. The normal state resistance of the junction was $R_t \approx 1.57$ kΩ. A measurement of its current-voltage characteristics is shown on Fig. 7.4. The theoretical prediction for this curve can be calculated by integrating Eq. (3.17) in the zero temperature limit:

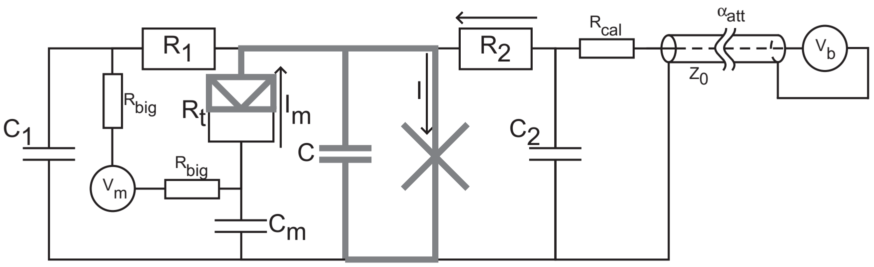

Fig. 7.3. Scheme of the electromagnetic environment of the Josephson junction. Apart from the elements denoted with tiny drawings and letters, all the circuit is fabricated on the silicon chip. Besides, all the thick gray parts are made of aluminum, which is a superconductor at the temperatures achieved in the experiment. The transmission line on the right has a characteristic impedance $Z_0 = 50\ \Omega$ and is interrupted by attenuators whose total attenuation is denoted by α_{att}. The measurement lines are reported on the technical scheme Fig. 9.7.

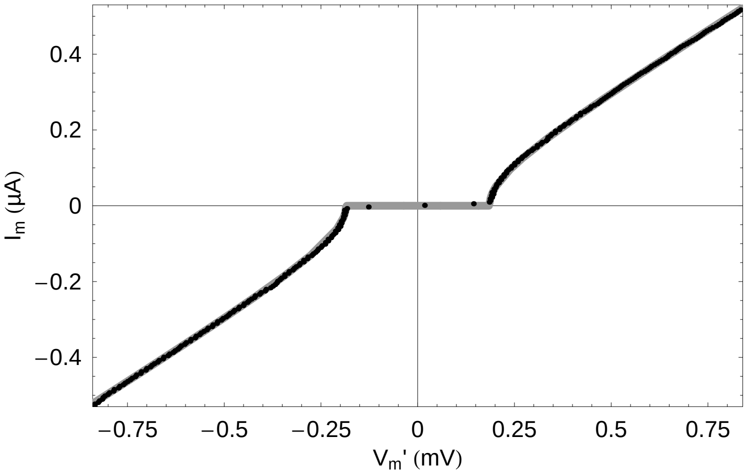

Fig. 7.4. Dots: Measured current-voltage characteristics of the NIS junction at a refrigerator temperature of $T_{\mathrm{refrigerator}} = 20$ mK. Line: Theoretical curve using Eq. (3.17) at zero temperature with a tunnel resistance of $R_t = 1.57$ kΩ and a superconducting gap $\Delta = 185.5\ \mu$eV.

$$I_m(V'_m) = \mathrm{sgn}(V'_m)\mathrm{Re}\left(\sqrt{V'^2_m - \Delta^2/e^2}\right)/R_t. \tag{7.3}$$

As for the current noise, the two following limits can be derived.

Low voltage $eV'_m < \Delta$:

At voltages below the gap, charges are transferred by units of $2e$ only (using the Andreev reflection § 5.1.2). In this case, the statistics of charge transfers is described by Eq. (6.35). This case was not accessed experimentally because the corresponding current and noise were very small[3].

High voltage $eV'_m \gg \Delta$:

For temperatures small compared to eV, $P(n,t)$ is a Poisson distribution and the cumulants of the number of transferred charges are given by Eq. (6.40):

$$\left\langle\left\langle \hat{N}(t)^k \right\rangle\right\rangle = \begin{cases} \frac{t\langle I_m\rangle}{e}\coth\left(\frac{eR_t\langle I_m\rangle}{2k_BT}\right) & \text{if } k \text{ is even} \\ \frac{t\langle I_m\rangle}{e} & \text{if } k \text{ is odd} \end{cases} \tag{7.4}$$

7.2.2 Josephson junction properties

Current-voltage characteristics

The current-voltage characteristics exhibits two unusual features shown on Fig. 7.5. First, the reentrant behavior at $eV \approx 2\Delta$ is very similar to what is observed on the Josephson junctions investigated in the experiments on atomic contacts in section 5.2.3. Second, a clear structure appears at about the third of the gap. Moreover, this structure seems insensitive to external noise as the gray and black dots do not differ on Fig. 7.5. This could be attributed to resonances in the electromagnetic environment of the Josephson junction (as in section 5.2.3), but no clear understanding of this feature was obtained.

Determination of the plasma frequency by resonant activation

Applying a high frequency AC bias voltage to the Josephson junction can modify the switching rate Γ. The corresponding increase in the switching rate depends strongly on the quality factor Q and the plasma frequency ω_p of the circuit. We performed such a resonant activation experiment of the switching on our circuit in order to determine these quantities experimentally. The NIS junction was biased with a constant and tiny voltage $V_m = 0.23$ mV

---

[3] The conductance of an NIS junction below the gap is given by $R(L_\varphi)/R_t^2$ where $R(L_\varphi)$ is the resistance of a part of length L_φ of the normal part [188]. A simple explanation for this behavior in $R(L_\varphi)$ is that the more an electron or a hole diffuses inside of the normal metal, the more attempts he will have to cross the tunnel barrier and be Andreev reflected into the superconducting side. The behavior in R_t^{-2} comes from the co-tunneling of an electron and its Andreev reflected hole (see section 5.1.2).

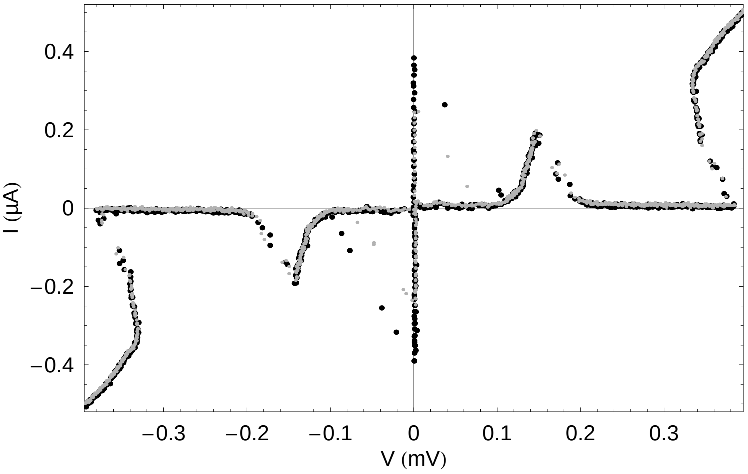

Fig. 7.5. Measured current-voltage characteristics of the Josephson junction at different values of the current I_m in the NIS junction and at a refrigerator temperature of $T_{\mathrm{refrigerator}} = 20$ mK. The black dots were measured with $\langle I_m \rangle = 5.3$ nA and the gray dots with $\langle I_m \rangle = 0.64$ μA.

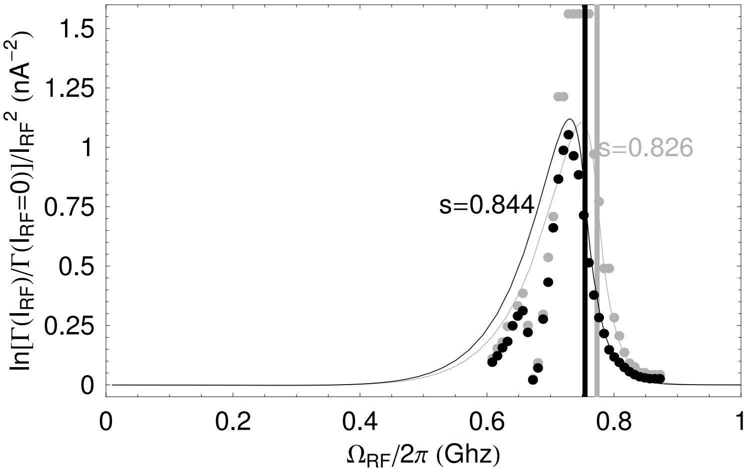

Fig. 7.6. Dots: resonant activation parameter $\ln\left[\frac{\Gamma(I_{\mathrm{RF}})}{\Gamma(0)}\right]$ calculated using the measured value of the RF power P_{RF} when $\Gamma(I_{\mathrm{RF}}) \approx 2\Gamma(0)$, for an escape temperature of 120 mK (as measured by the switching experiment). Each curve correspond to a different value of the pulse height sI_0. Thin lines: the best fits of the experiment obtained assuming a capacitance $C = 36$ pF and a global attenuation of the bias line of $\alpha_{\mathrm{att}} = 58.5$ dB. Thick lines: Position of the plasma frequency.

so that its dynamical resistance is fixed to 0.93 kΩ (see Fig. 7.4). The switching probability of the Josephson junction was measured with current pulses on the bias line. Their height is denoted by sI_0 and their length was always $\tau_{\text{pls}} = 49\ \mu$s. The switching rate Γ was measured for two values of the parameter s: $\Gamma \approx 1.3$ kHz for $s = 0.826$ and $\Gamma \approx 7.3$ kHz for $s = 0.844$. Then, in order to observe resonant activation of the switching, a tiny additional microwave signal was send through the bias line at a frequency Ω_{RF},

$$I_b(t) = I_{\text{pulse}}(t) + I_{\text{RF}} \cos(\Omega_{\text{RF}} t). \tag{7.5}$$

In the limit where the amplitude I_{RF} is small enough for the rate to double at most ($\Gamma(I_{\text{RF}}) < 2\Gamma(0)$), the rate increase is predicted by the theory developed in Ref. [187]:

$$\ln\left[\frac{\Gamma(I_{\text{RF}})}{\Gamma(0)}\right] = c_{\text{fit}} Q I_{\text{RF}}^2 \frac{\Delta U(s)}{C\omega_p(s)^2 (k_B T_{\text{esc}})^2} f(Q, \Omega_{\text{RF}}/\omega_p(s)) \tag{7.6}$$

where ΔU, ω_p , Q and T_{esc} are defined in section 5.2.1, $f(Q,x)$ is given in appendix Eq. (B.33)and c_{fit} is of order 5 and its dependence on Q is given explicitly in Fig. 19 of Ref. [187]. In the experiment, we measure the amplitude I_{RF} needed to double the switching rate as a function of the frequency Ω_{RF}. Both curves taken at $s = 0.826$ and $s = 0.844$ are then fit using Eq. (7.6) with the capacitance C and the attenuation of the bias line α_{att} left as free parameters. The best fit shown on Fig. 7.6 is obtained for $C = 36$ pF and for an attenuation of $\alpha_{\text{att}} = 58.5$ dB for the whole bias line (the measured attenuation at DC was 50.0 dB). Actually, the quantity measured in the experiment is the power of the RF microwave and not the current I_{RF}. The relation between those two quantities can be derived straightforwardly (see Eq. (B.38) in the appendix). Finally,

$$C \approx 36 \text{ pF} \ ; \ \omega_p(s=0) \approx 1.0 \text{ GHz} \ ; \ Q(s=0) \approx 22 \tag{7.7}$$

Switching dynamics

Quality of the pulse

In order to perform a sensitive switching experiment, one needs to control the current pulses at best. It would be naive to believe that the pulses propagate perfectly from the voltage source to the Josephson junction. Indeed, filters, attenuators and losses in the transmission line modify the pulse because their impedance varies slightly with frequency. And as these components vary with temperature, it is of no use to calibrate the pulse sequence at room temperature. Therefore, our experiment needed a control of the pulse shape using only the experimental measurement lines. We chose to use the information contained in the histogram of the switching events as a function of the time. If the bias current is low enough so that the switching rate Γ is much less

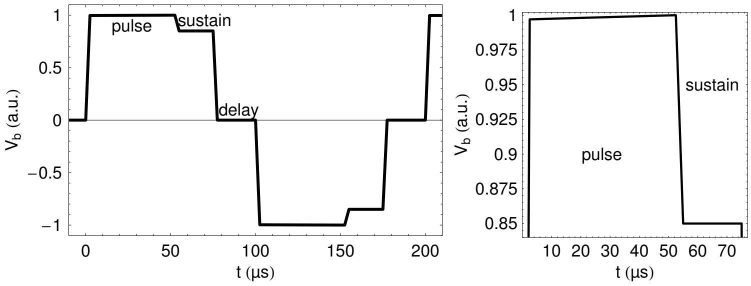

Fig. 7.7. Left panel: Shape of the pulses we used in order to optimize the histogram of Fig. 7.8. Positive and negative pulses with the same nominal shape were used in series. All the switching events occur during the part denoted as *pulse*. The *sustain* part is small enough ($\kappa = 85\%$ of the pulse height) not to lead to any switching and allows the voltage which develops after a switching event to hold for a longer time, therefore facilitating the measurement. On this pulse sequence, $t_{\mathrm{pulse}} = 50\ \mu s$, $t_{\mathrm{sustain}} = 22.5\ \mu s$ and $t_{\mathrm{delay}} = 27.5\ \mu s$. Right panel: zoom on the pulse and sustain regions of the left panel. The precise shape of the pulse sent by the source is chosen so that once it arrives on the Josephson junction, it looks as rectangular as possible.

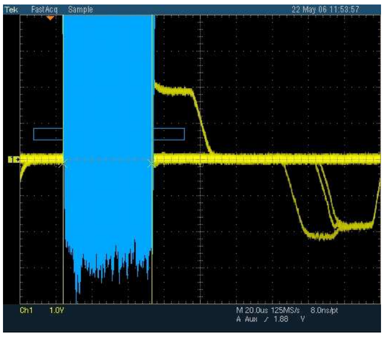

Fig. 7.8. Screen capture (color online) of an oscilloscope in histogram mode. The bias line is gone through by a series of current pulses as shown on Fig. 7.1 such that the switching probability is much less than 1 (here around 5%, which also means that $\Gamma\tau_{\mathrm{pls}} \approx 0.05$). Sometimes, when a switching occurs, a voltage (light line) develops across the Josephson junction. When the voltage crosses a given threshold shown by the bottom of empty rectangle, the bin corresponding to the time at which this crossing happens increases by one unit (notice that the histogram points down). The dark gray histogram shows the amplitude of the bins after 1.5×10^6 pulses. The effective width of the pulse seen by the Josephson junction is given by the width of the histogram: $\tau_{\mathrm{pls}} \approx 49.1\ \mu$s.

than τ_{pls}^{-1}, the probability to switch at a time $t < \tau_{\mathrm{pls}}$ is nearly constant. In this case, the switching histogram in time should be constant on the pulse length. By varying slightly the shape of the pulses, the histogram could be made reasonably flat (see Figs. 7.7 and 7.8).

Critical current

In a set of measurements, the tunnel junction was biased at a constant current[4] $\langle I_m \rangle \approx 0.22\ \mu\mathrm{A}$ while a standard switching experiment similar to the one presented on Fig. 5.13 is performed on the Josephson junction. On Fig. 7.9, the function $b^{2/3}$ of Eq. (5.54) is shown as a function of s for various refrigerator temperatures. The critical current $I_0 = 479$ nA was fit in order to get most extrapolating lines to cross 0 at $s = 1$. The escape temperature for each curve is plotted as a function of the refrigerator temperature on the same figure. The shot noise contribution to the temperature shifts all temperatures by about 90 mK.

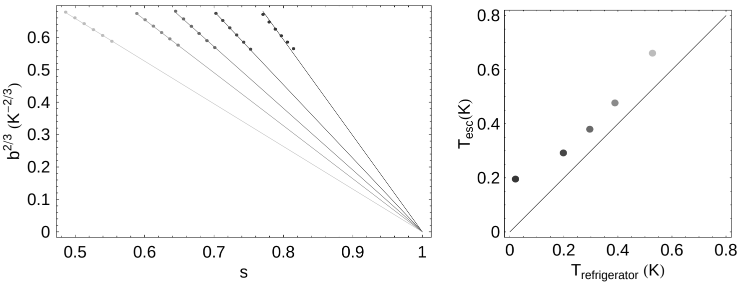

Fig. 7.9. Left panel–dots: Function $b^{2/3}$ plotted as a function of s for different temperatures from the measurements of the switching probability. The critical current used to get most curves to extrapolate to 0 at $s = 1$ is $I_0 = 479$ nA. The point color codes the refrigerator temperature and can be decoded using the right panel. Left panel–lines: best straight lines passing through the experimental points and through 0 at $s = 1$. The slope of these curves gives the escape temperature T_{esc} through Eq. (5.54). The points at the lowest temperature do not follow the line closely as a result of heating effects that are described in the following. Right panel: escape temperature T_{esc} extracted from the left panel as a function of the refrigerator temperature.

---

[4] As shown on Fig. 9.7, switching events are detected by the appearance of a finite voltage across the capacitor C_m. Once a finite voltage develops across the Josephson junction, it takes at least a characteristic time $R_m C_m$ to develop across C_m, where R_m is the differential resistance $\mathrm{d}V'm/\mathrm{d}I_m$ of the tunnel junction (see Fig. 7.4). When the voltage V_m is zero, R_m goes to infinity. Thus, it is preferable to set V_m at a finite value in order to avoid large time constants in the measurement of switching events.

7.2.3 Summary of the electrical quantities

Quantity	Value	Reference
C_1	0.13 nF	C.1
R_1	202 Ω (at DC)	C.1
R_{big}	10573 Ω	C.1
R_t	1.57 kΩ	Fig. 7.4
C_m	0.85 nF	C.1
C	36 pF	Fig. 7.6
I_0	479 μA	Fig. 7.9
C_2	0.13 nF	C.1
R_2	202.1 Ω (at DC)	C.1
R_{cal}	10.18 Ω	C.1
Z_0	50 Ω	C.1
α_{att}	50.0 dB (at DC)	C.1
α_{att}	58.5 dB (at 1 GHz)	Fig. 7.6

Table 7.1. Electrical properties of the circuit shown on Fig. 7.3.

7.3 Influence of the current noise in the tunnel junction on the switching dynamics

7.3.1 Gaussian noise

How to measure the spectral density of the noise ?

As described in section 5.2.1, the escape dynamics of a Josephson junction in the thermal regime[5] is approximately given by the escape rate

$$\Gamma(s) = \underbrace{\lambda(Q)\frac{\omega_p(s)}{2\pi}}_{A} \underbrace{\mathrm{e}^{-\Delta U(s)/k_B T_{\mathrm{esc}}}}_{\mathrm{e}^{-B}} \tag{7.8}$$

where T_{esc} reflects the current fluctuations through the Josephson junction. In order to be more concrete about the link between the current fluctuations and the escape temperature T_{esc}, we introduce the equation that describes the dynamics of the phase γ across the Josephson junction. Using the Kirchoff's laws for the circuit shown on Fig. 7.3 and Eq. (5.37),

$$\frac{\mathrm{d}^2\gamma}{\mathrm{d}t^2} + \frac{1}{R_{\mathrm{eq}}C}\frac{\mathrm{d}\gamma}{\mathrm{d}t} + \frac{I_0}{\varphi_0 C}\sin\gamma - \frac{sI_0}{\varphi_0 C} = \frac{1}{\varphi_0 C}\delta I(t) \tag{7.9}$$

---

[5] At $T > T_{\mathrm{co}}$, see Eq. (5.51).

where R_{eq} is the total resistance seen by the Josephson junction and $\delta I(t)$ is the difference between the instantaneous current and the average one in the Josephson junction. In our case, where the current noise is due to thermal fluctuations in the various resistors and to shot noise in a tunnel junction, and assuming that the Josephson junction is insensitive to high frequency components of the noise[6], the correlation time of the noise is negligible and one gets

$$\begin{aligned} \langle \delta I(t) \rangle &= 0 \\ \langle \delta I(t) \delta I(t') \rangle &= \frac{1}{2} S_I(\omega_p) \delta(t-t') \end{aligned} \tag{7.10}$$

where $S_I(\omega)$ is the spectral density of the noise, which is constant in this approximation. If noise would be due to thermal fluctuations in the resistor R_{eq} at temperature T_{env}, the spectral density of the noise would be given by the Johnson-Nyquist expression (6.45), and one would get

$$\langle \delta I(t) \delta I(t') \rangle = \frac{2 k_B T_{\text{env}}}{R_{\text{eq}}} \delta(t-t'). \tag{7.11}$$

The results of section 5.2.1 show that, in this case, the escape temperature would just be the real temperature $T_{\text{esc}} = T_{\text{env}}$. Therefore, in the general case, as long as noise is frequency independent, the escape temperature is the temperature of the environment that leads to the same spectral density in the thermal fluctuation regime alone. In case the spectral density of the noise is not flat, one has to be careful. Given the resonant activation measurements, the frequency at which the Josephson junction is the most sensitive is the plasma frequency. Therefore, at first order,

$$\boxed{T_{\text{esc}} \approx \frac{R_{\text{eq}}}{4 k_B} S_I(\omega_p)} \tag{7.12}$$

Application to our experiment

In our experiment, one can find the spectral density of the current produced by the environment of the Josephson junction by applying the following theorem of circuit theory [189].

Theorem: Let us consider a one port network made of branches of admittances $Y_j(\omega)$, and let us denote by $Y(\omega)$ the total admittance as seen from the port. Then, the spectral density of the current going through a short at the port is given by

$$S_I(\omega) = \sum_j \left| \frac{\partial Y}{\partial Y_j} \right| S_I^{(j)}(\omega) \tag{7.13}$$

---

[6] Here, *high* means higher than $k_B T/\hbar$. Indeed, the Johnson-Nyquist spectral density is flat for frequencies lower than this threshold as proven by Eq. (6.45). In the experiment, $T > 0.1$ K (see discussion about Fig. 7.12), so that the spectrum is flat up to 2 GHz which is way too high for exciting the Josephson junction as proven by resonant activation (Fig. 7.6).

where $S_I^{(j)}(\omega)$ *is the spectral density of the current in the branch* j.

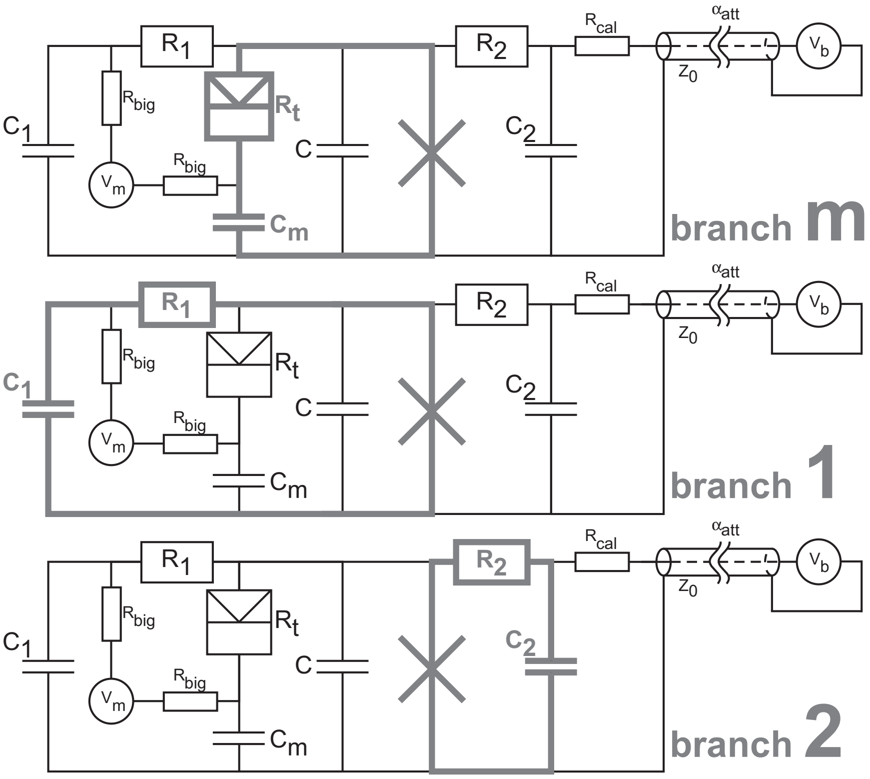

Fig. 7.10. Copies of the scheme of the circuit 7.3 where the thick parts show the various branches where the current fluctuations δI in the Josephson junction flow (see text).

In our setup, in the limit where $k_B T_j \gg \hbar\omega_p$, the three main dissipative elements in the Josephson junction environment are three parallel branches denoted by m for the branch passing by the mesoscopic noisy conductor (NIS tunnel junction), 1 and 2 for the biasing impedances (see Fig. 7.10). Their admittances and noise spectral densities are given by

$$\begin{aligned} Y_1(\omega) &= \left(R_1 + [iC_b\omega]^{-1}\right)^{-1} \quad ; \quad S_I^{(1)}(\omega_p) \approx 4k_BT_1/R_1 \\ Y_2(\omega) &= \left(R_2 + [iC_b\omega]^{-1}\right)^{-1} \quad ; \quad S_I^{(2)}(\omega_p) \approx 4k_BT_2/R_2 \\ Y_m(\omega) &= \left(R_t + [iC_m\omega]^{-1}\right)^{-1} \quad ; \quad S_I^{(m)}(\omega_p) \approx 2e\langle I_m\rangle \coth\left(\frac{eR_t\langle I_m\rangle}{2k_BT_m}\right) \end{aligned} \tag{7.14}$$

where the expression for the noise $S_I^{(m)}(\omega_p)$ comes from Eq. (6.41), and where T_j is the temperature of the dissipative element in the branch j. Since the three branches are in parallel, the theorem above applies easily to give the total spectral density of the current

$$S_I(\omega_p) = \frac{4k_B T_1}{R_1} + \frac{4k_B T_2}{R_2} + 2e\langle I_m\rangle \coth\left(\frac{eR_t\langle I_m\rangle}{2k_B T_m}\right) \tag{7.15}$$

and finally, using Eq. (7.12),

$$T_{\mathrm{esc}} = \left(\frac{1}{R_1} + \frac{1}{R_2} + \frac{1}{R_t}\right)^{-1} \left[\frac{T_1}{R_1} + \frac{T_2}{R_2} + \frac{e\langle I_m\rangle}{2k_B} \coth\left(\frac{eR_t\langle I_m\rangle}{2k_B T_m}\right)\right]. \tag{7.16}$$

Besides, the limit behavior when $eR_t\langle I_m\rangle \gg 2k_B T_m$ (which is valid in all our measurements but a few[7]) is given by

$$\boxed{T_{\mathrm{esc}} = \left(\frac{1}{R_1} + \frac{1}{R_2} + \frac{1}{R_t}\right)^{-1} \left[\frac{T_1}{R_1} + \frac{T_2}{R_2} + \frac{e\langle I_m\rangle}{2k_B}\right]} \tag{7.17}$$

Temperature of the bias resistors

In order to test experimentally the last equation (7.17), one needs to determine the values of the temperatures T_1, T_2 and T_m. The case of T_m can be treated easily because the electrons tunneling from the electrode with the higher electrochemical potential into the other do not stay in the vicinity of the tunnel barrier, but diffuse away rapidly. Therefore, the temperature of the electrons which tunnel through the insulating barrier is the one of the Fermi sea in the leads, which is cooled down by phonons at the temperature $T_{\mathrm{refrigerator}}$.

In the SMC resistors used in the branches 1 and 2, the value of the temperature is not so trivial. It turns out that Joule power can heat significantly the electrons in the resistors, and the values of T_1 and T_2 vary with the pulse shape and with the value of the current $\langle I_m\rangle$. We evaluate this effect in what follows.

Resistor R_1

The temperature T_1 depends on the current passing through the branch 1, and therefore, should only depend on the current in the tunnel junction $\langle I_m\rangle$. Assuming that Joule power is mostly dissipated by phonons[8], and using Eq. (B.6) from the appendix, one gets an upper estimate of the temperature as a function of the current $\langle I_m\rangle$:

---

[7] At worst, that is at $T_m = 530$ mK for our data, this approximation is valid as soon as $\langle I_m\rangle > 1\ \mu$A.

[8] Neglecting the role of cooling by electronic heat conduction compared to cooling by electron-phonons interaction leads at worst to an overestimate of the tem-

$$\Omega\Sigma(T_1^5 - T_{\text{refrigerator}}^5) = R_1 \langle I_m^2 \rangle \tag{7.19}$$

with Ω the volume of the metallic film and Σ is a material dependent factor. The constructor of the SMC, Vishay, does not communicate the exact dimensions of the resistive NiCr film used in their resistors. Yet, as the value of T_1 depends on the volume Ω at the power $1/5$, a rough estimate of the volume is sufficient. Vishay provided us with typical values for the length L, width w and thickness t of the thin films: $L \approx 0.9$ mm, $w \approx$ 0.6 mm and $t \approx$ 0.1 μm. Given the resistivity of a Cu/Ni alloy $\rho \approx 110$ $\mu\Omega$.cm, these dimensions correspond to a 20 Ω resistance. As in our case, the resistance was $R_1 \approx 200$ Ω, the thickness t or width w should be actually reduced by a factor 10. The total volume is then $\Omega \approx 5 \times 10^3$ μm^3. Besides, the value of the prefactor Σ of the order of a few 10^9 W.m^{-3}K^{-5} in metals [190], is not known for NiCr. Using $\Sigma = 10^9$ W.m^{-3}K^{-5}, we obtained the estimates of Fig. 7.11. The temperature

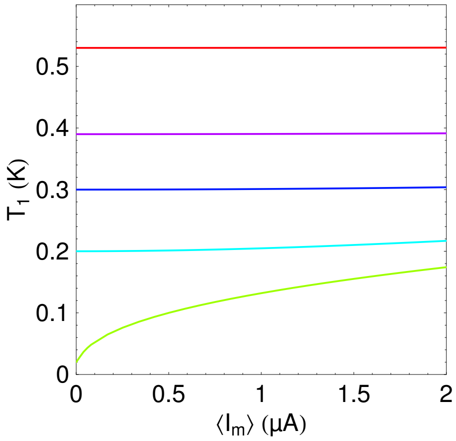

Fig. 7.11. Predicted temperatures of the SMC resistors R_1 as a function of the current in the tunnel junction $\langle I_m \rangle$, using Eq. (7.19) for five refrigerator temperatures (corresponding to the experiment, and given by the temperature of the lines at zero current on the left plot).

---

perature. Moreover, the SMC resistor is connected to a thin film (10 nm of Au topping 54 nm of Cu) on one side and to the same film in parallel with an aluminum wire on the other side. The aluminum being superconducting, no heat can flow through it, and the thin film is so thin that phonons thermalize it badly on short distances. In the end, the additional term in Eq. (7.19) that would describe conduction heat flow, is negligible:

$$\frac{wt}{\rho}\mathcal{L}T\nabla T \ll \Omega\Sigma(T_1^5 - T_{\text{refrigerator}}^5) \tag{7.18}$$

because ∇T is small.

of resistor R_1 is found to vary significantly with $\langle I_m \rangle$ only in the set of data taken at the lowest temperature (20 mK).

Resistor R_2

The case of resistor R_2 is more tricky than the case of R_1 because the current in R_2 is not constant. The Joule energy $\mathcal{E}_2$ dissipated in the resistor R_2 during one pulse sequence can be estimated by

$$\mathcal{E}_2 = \int_0^{t_{\text{pulse}}+t_{\text{sustain}}} R_2 I(t)^2 \mathrm{d}t \tag{7.20}$$

For a given switching rate Γ, the probability for the current I to keep a value sI_0 during a time $t < t_{\text{pulse}}$ is $\Gamma \mathrm{e}^{-\Gamma t}$. When the Josephson junction switches, the working point of the circuit follows the load line towards a point where $V \approx 0.1$ mV and $I \ll I_0$ (see Fig. 7.5). The current stays at this low value until the next pulse is applied. If the switching does not occur before t_{pulse}, the current is sustained for an additional time t_{sustain} at the value $sI_0\kappa$, where $\kappa = 0.85$ (see Fig. 7.7). Therefore, the average Joule energy is given by

$$\mathcal{E}_2 = \int_0^{t_{\text{pulse}}} [tR_2 s^2 I_0^2] \Gamma \mathrm{e}^{-\Gamma t} \mathrm{d}t + R_2 s^2 I_0^2 (t_{\text{pulse}} + t_{\text{sustain}}\kappa^2) \mathrm{e}^{-\Gamma t_{\text{pulse}}} \tag{7.21}$$

hence,

$$\mathcal{E}_2(s, \Gamma) = R_2 s^2 I_0^2 \left[\Gamma^{-1} \left(1 - \mathrm{e}^{-\Gamma t_{\text{pulse}}}\right) + t_{\text{sustain}} \kappa^2 \mathrm{e}^{-\Gamma t_{\text{pulse}}} \right]. \tag{7.22}$$

Assuming that this energy is mostly dissipated by phonons, one gets an upper estimate of the temperature T_2 as a function of the current $\langle I_m \rangle$ using a similar equation to Eq. (7.19)

$$\Omega \Sigma (T_2^5 - T_{\text{refrigerator}}^5)(t_{\text{pulse}} + t_{\text{sustain}} + t_{\text{delay}}) = \mathcal{E}_2. \tag{7.23}$$

One gets an estimate of T_2 as a function of s, Γ and t_{delay}. At the lowest temperature of Fig. 7.9, it seems that the experimental dots of the left panel do not follow the theoretical line as well as for higher temperatures. Our interpretation is that it is a signature of the heating of R_2 we have just discussed. In order to test this description more thoroughly, we measured the switching rates Γ for several values of s and of t_{delay} while the current in the tunnel junction $\langle I_m \rangle$ was zero. The corresponding escape temperatures, calculated using Eq. (7.8) for each value of s and t_{delay}, are reported on Fig. 7.12. The two top panels of this figure show that the escape temperature depends on s, and that it decreases when the delay between pulses increases. In order to compare the experiment with the predictions of Eq. (7.23), we use Eq. (7.16) with $T_1 = T_m = T_{\text{refrigerator}} = 20$ mK, and $R_t = +\infty$ (see Fig. 7.4 at $\langle I_m \rangle = 0$). The corresponding predictions for the escape temperature are reported on the bottom panel of Fig. 7.12. The qualitative agreement between the data and

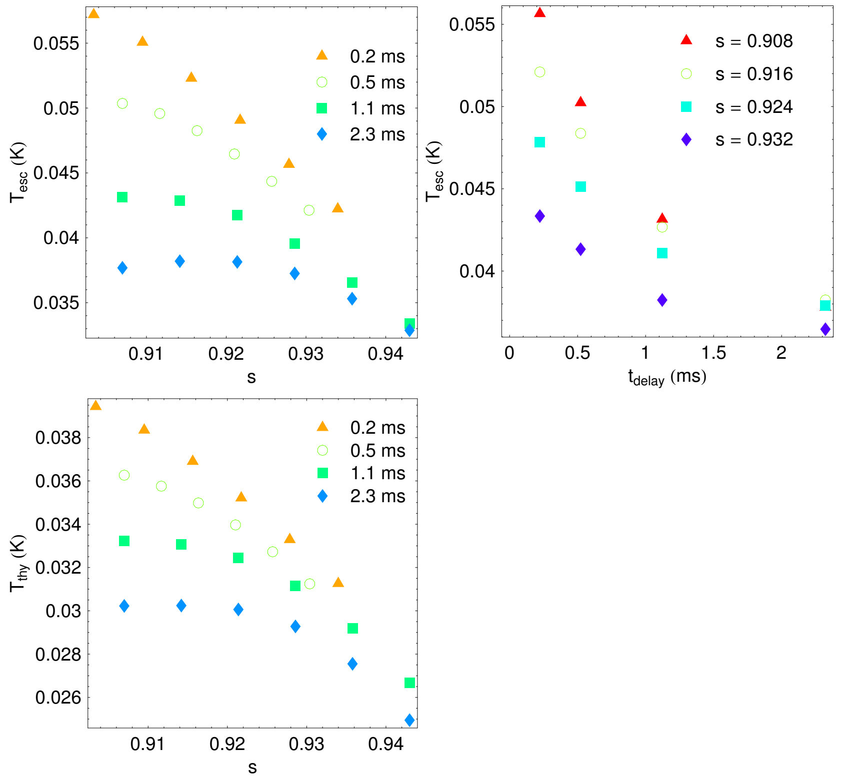

Fig. 7.12. Left-top panel: Escape temperature as a function of the bias pulse height sI_0 estimated from Eq. (7.8) using the switching rates measured for several delay times (see Fig. 7.7) at the base refrigerator temperature $T_{\text{refrigerator}} = 20$ mK. In the estimation, the critical current was fixed to $I_0 = 479$ nA according to Fig. 7.9. Right-top panel: same data plotted as a function of the delay time for several values of s. Left-bottom panel: Prediction for the escape temperature as a function of s and of the delay time t_{delay} using Eqs. (7.23,7.16) with the parameters given in the text.

the predictions are good up to a prefactor of order 1 which might be due to an error on the actual value of $\Omega\Sigma$, thus supporting our interpretation of the heating effects. This complicates the analysis of our experiment at low temperatures. Yet, as soon as the refrigerator temperature gets as high as 200 mK, this heating effect becomes negligible, as proven by the good fit of the $b^{2/3}$ plots on Fig. 7.9.

Measurement of the escape temperature

In the experiment, we performed switching rate measurements as a function of the pulse amplitude sI_0 for several values of the average current $\langle I_m \rangle$ through the tunnel junction and at several temperatures $T_{\text{refrigerator}}$ (see Fig. 7.1). For each measurement, we extracted the escape temperature using Eq. (7.8). On Fig. 7.13, the escape temperatures corresponding to several values of the current through the tunnel junction and of the refrigerator temperature are reported. These measurements were taken using the pulse sequence plotted on Fig. 7.7 whose delay time t_{delay} was short (see Fig. 7.12). In order to check the consistency of our derivation above (Eq. (7.17)), we have subtracted in Fig. 7.14 the expected contribution of Johnson-Nyquist noise

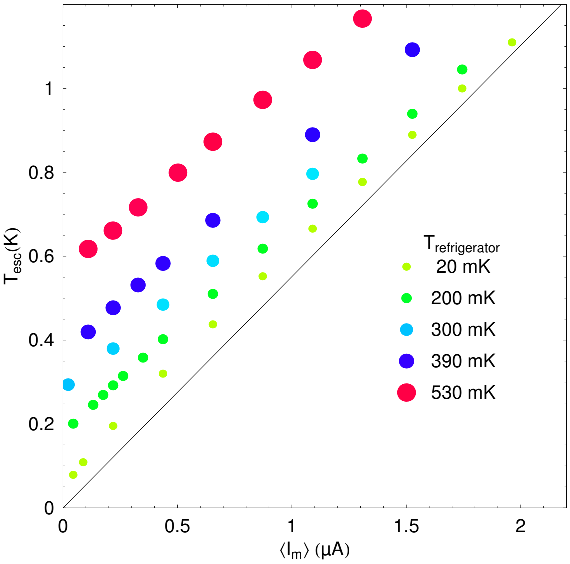

Fig. 7.13. Escape temperatures extracted from the measurement of the rate as a function of s using Eq. 7.8 for several values of the current in the tunnel junction I_m and of the refrigerator temperature $T_{\text{refrigerator}}$. The parameters used in the extraction are $I_0 = 479$ nA, $C = 36$ pF and $R_{\text{eq}} \equiv (R_1^{-1} + R_2^{-1} + R_t^{-1})^{-1} = 95\ \Omega$. The line shows the expected escape temperature at $T_{\text{refrigerator}} = 0$ using the same parameters and Eq. (7.12).

$$\left(\frac{1}{R_1} + \frac{1}{R_2} + \frac{1}{R_t}\right)^{-1} \left[\frac{T_1}{R_1} + \frac{T_2}{R_2}\right] \tag{7.24}$$

in resistors R_1 and R_2 from the escape temperature T_{esc}. We have used here $T_1 = T_2 = T_{\text{refrigerator}}$ which, according to the preceding section, should be valid at least for the data sets taken at $T_{\text{refrigerator}} \geq 200$ mK.

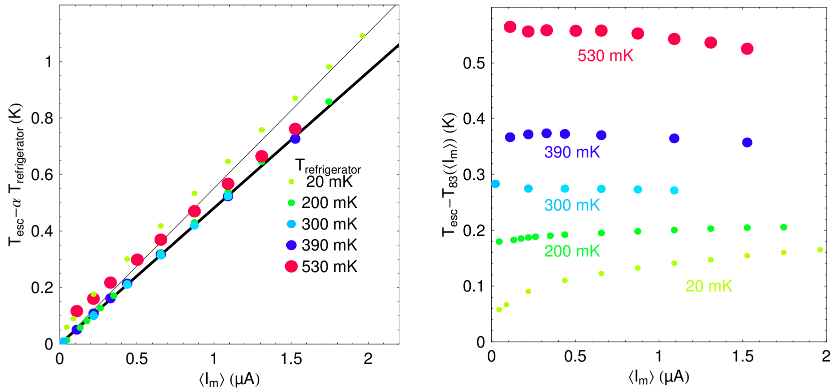

Fig. 7.14. Left panel: same escape temperatures as on Fig. 7.13 but shifted vertically by $\alpha T_{\text{refrigerator}}$ where $\alpha = \left(\frac{1}{R_1}+\frac{1}{R_2}+\frac{1}{R_t}\right)^{-1}\left[\frac{1}{R_1}+\frac{1}{R_2}\right] \approx 0.95$. The thin line shows the expected escape temperature at $T_{\text{refrigerator}}=0$ using Eq. (7.17) with $R_{\text{eq}} \equiv (R_1^{-1}+R_2^{-1}+R_t^{-1})^{-1} = 95\ \Omega$ as measured, whereas the thick line represents the prediction for $R_{\text{eq}} = 83\ \Omega$. Right panel: same escape temperatures as on Fig. 7.13 but shifted vertically by $T_{83} = 83\ \Omega \times e\langle I_m\rangle/2k_B$ (which is the thick line of the left panel). According to Eq. (7.17), this should be a measurement of $\left(\frac{1}{R_1}+\frac{1}{R_2}+\frac{1}{R_t}\right)^{-1}\left[\frac{T_1}{R_1}+\frac{T_2}{R_2}\right]$. Notice the resemblance with Fig. 7.11.

All curves, except the one at base temperature, nearly merge on a single line. Yet, this line is not exactly the line that could be predicted from Eq. (7.17) using the parameters $I_0 = 479$ nA, $C = 36$ pF and $R_{\text{eq}} = 95\ \Omega$. Since both $I_0 = 479$ nA and $C = 36$ pF have been measured using the phase dynamics near the plasma frequency[9], only R_{eq} is suspicious. Indeed, this value of R_{eq} comes from DC measurements of the resistivity of the three dissipative elements constituting the environment of the Josephson junction. It might well be that this value differs from the impedance seen at frequencies as high as the bare ($s = 0$) plasma frequency $\omega_{p0}/2\pi = 1$ GHz. On Fig. 7.14, it seems that $R_{\text{eq}} = 83\ \Omega$ accounts better for the data.

Discrepancy at $T = 20$ mK

From Fig. 7.14, it is clear that some heating occurs at the lowest refrigerator temperature. In order to understand the origin of this heating, we compare the data at 20 mK with the predictions on T_1 from Eq. (7.19), using $\Sigma = 10^9$ W.m^{-3}K^{-5} and $\Omega = 5 \times 10^3\ \mu$m^3. The good overall agreement supports our description.

---

[9] I_0 was measured from a switching experiment, and C was measured by resonant activation, which depends only slightly on R_{eq}.

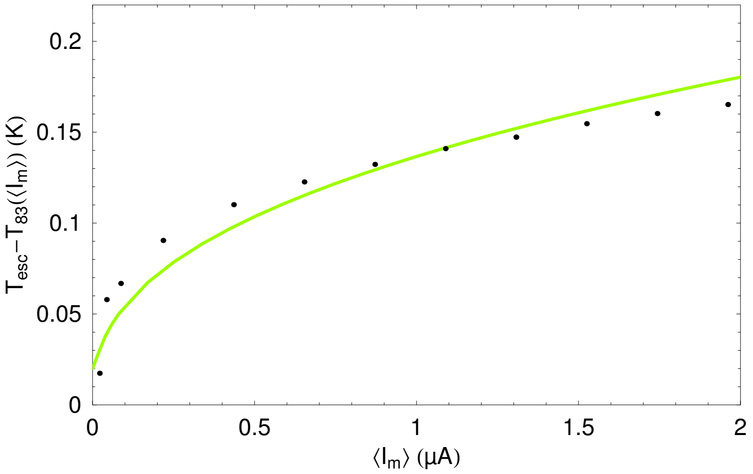

Fig. 7.15. Comparison between the experimental dots of the right panel of Fig. 7.14 and the expression (7.19) using $\Sigma = 10^9$ W.m^{-3}K^{-5} and $\Omega = 5 \times 10^3$ μm^3.

7.3.2 Beyond Gaussian noise

In this section, we are interested in possible signatures of the current noise on the switching, which are not entirely contained in the influence of the spectral density of the noise on the escape temperature. In particular, as explained in the beginning of this chapter, the switching rate should differ with the direction of the current through the tunnel junction. Several experimental effects could produce such an asymmetry, and one needs to be particularly careful with the way the bias is performed.

Complete description of the biasing circuit

Using the following voltage sources, we tried to minimize current leakage in parasitic lines.

Voltage source V_b

The voltage source V_b shown on Fig. 7.3 was actually realized with a series of three elements:

- an arbitrary signal generator (Agilent 33250A)
- a buffer which decoupled the ground of the bias line from the ground of the signal generator (voltage amplifier SR560 with gain 1 from Stanford Research Systems)
- a large series capacitor (220 μF) so that the average value of V_b is exactly zero (the average voltage is set by the attenuators of the transmission

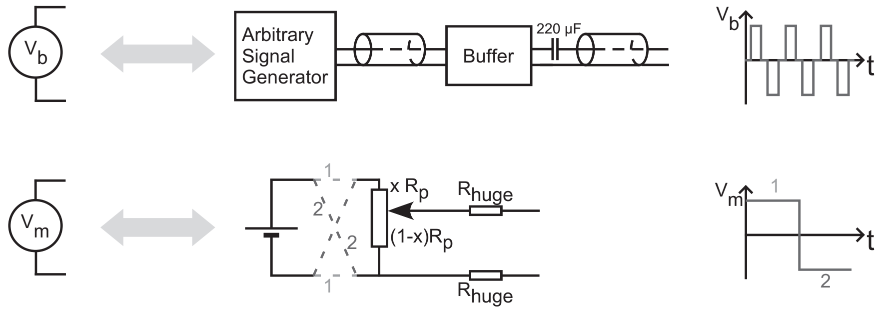

Fig. 7.16. Scheme of the two voltage sources involved in the biasing of the circuit Fig. 7.3. Concerning V_b, the arbitrary signal generator is the Agilent 33250A, the Buffer is a voltage amplifier SR560 with gain 1 from Stanford Research Systems. Concerning V_m, the real source are two 1.5 V AA batteries in series. A switch can be turned in position 1 or 2 depending on the current in a coil next to it so that the voltage V_m can be set to opposite values quickly and automatically. Finally, a potentiometer allows to adjust manually the output voltage V_m continuously. $R_\mathrm{p} \approx 50\ \mathrm{k}\Omega$ and $R_\mathrm{huge} \approx 475\ \mathrm{k}\Omega$.

line). This capacitor prevents unwanted offsets that would be introduced by thermoelectric voltages on the bias line between the circuitry at room temperature and the first 50 Ω attenuator in the dilution refrigerator at 1 K.

Voltage source V_m

The floating voltage source V_m shown on Fig. 7.3 was actually implemented in a way that maximizes the electrical insulation from the remaining of the circuit. The reason is that a leakage current to ground from either of the conductors would give rise to a current in the Josephson junction . The quality of this isolation is verified by the observation of the correct symmetry in the measured signals (see below). Besides, a controllable switch allows to rapidly and automatically change the sign of the voltage.

Measurement of the switching rate with opposite biasing voltages

The experimental procedure consists in repeating measurements of the switching probability for all four possible combinations of the signs of voltages V_m and V_b. The aim is to make sure that no uncontrolled offset current contributes to the measured asymmetry in the switching probabilities. In absence of any offset, one expects the following pairs of equivalent measurements.

$$\begin{array}{c} (V_m > 0; V_b > 0) \Longleftrightarrow (V_m < 0; V_b < 0) \\ (V_m > 0; V_b < 0) \Longleftrightarrow (V_m < 0; V_b > 0) \end{array} \tag{7.25}$$

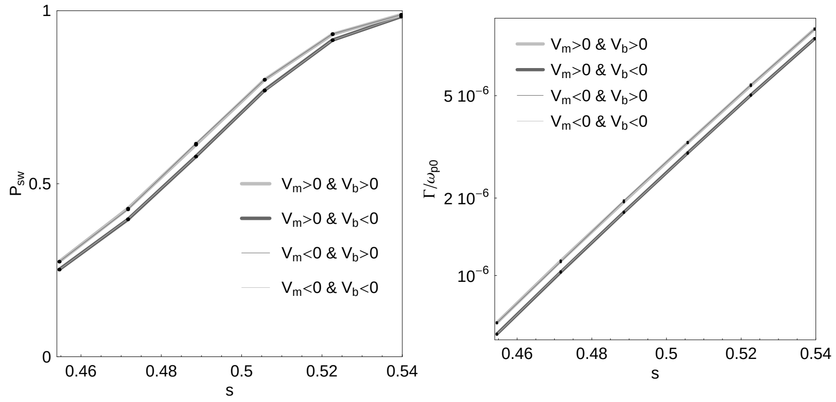

Fig. 7.17. Left panel–dots: switching probabilities P_{sw} measured using the technique discussed in the text as a function of the pulse height sI_0 for $V_m = \pm 25.00$ mV ($\langle I_m \rangle \approx 1.1\ \mu$A at a temperature $T_{\mathrm{refrigerator}} \approx 197$ mK. The probabilities are calculated by doing a statistics on 2×10^5 to 5×10^5 pulse sequences depending on the desired accuracy. Left panel–lines: straight lines through the dots. Four groups of dots and lines are shown depending on the signs of the bias voltages (the width codes the sign of V_m while the color codes the sign of V_b). The groups coincide almost perfectly and are therefore hardly distinguishable in agreement with Eq. (7.25). Right panel: switching rates corresponding to the probabilities shown on the left panel. The error bars on the rates are at most $5 \times 10^{-8} \omega_{p0}$ and are thus less than the size of the dots.

The measurement procedure goes as follows. The pulse sequence plotted on Fig. 7.7 is applied 10,000 times on V_b while a constant voltage V_m is applied on the tunnel junction bias line, then the switch of Fig. 7.16 is changed position so that $-V_m$ is applied and 10,000 other pulse sequences are applied on V_b. This procedure is repeated often enough so that a good precision on the switching rate is achieved[10]. In the end, the switching events are packed into four groups corresponding to the four combinations of the signs of V_m and V_b. An example

---

[10] For each pulse we recorded the answer to the question *Has the voltage across the Josephson junction crossed the threshold ?* (1 means yes and 0 means no). The answers are independent random variables X_i with binomial distribution, P being the expectation for $X_i = 1$. Therefore, the standard deviation of the average $N^{-1} \sum_{i=1}^{N} X_i$ is $\sqrt{P(1-P)/N}$. And using

$$P = 1 - \mathrm{e}^{-\Gamma \tau_{\mathrm{pls}}}, \tag{7.26}$$

one gets the standard deviation of the switching rate

$$\Delta\Gamma = \sqrt{\frac{P}{N(1-P)}} \tau_{\mathrm{pls}}^{-1} . \tag{7.27}$$

of the result is shown on Fig. 7.17, showing good consistency with Eq. (7.25). In order to verify these conditions, the current leakage between the wires

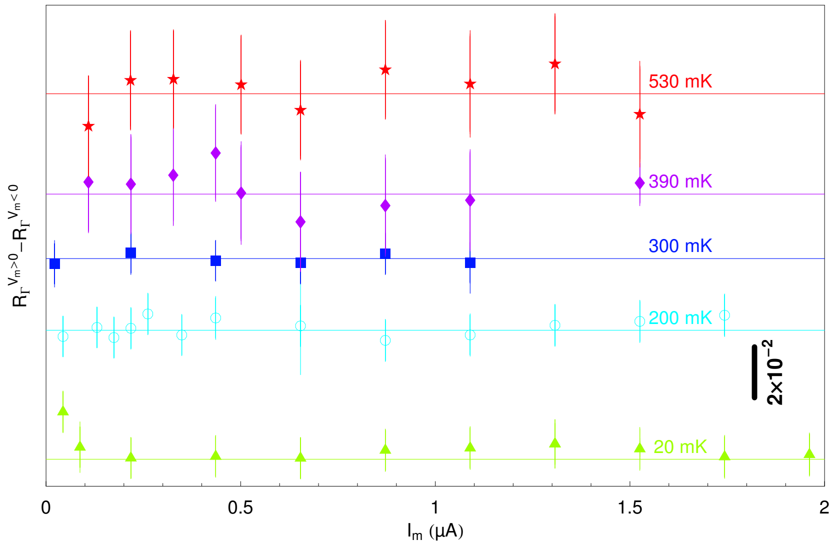

Fig. 7.18. For several refrigerator temperatures, the average difference between the offsets R_Γ calculated using both methods $V_m > 0$ and $\pm V_b$ or $V_m < 0$ and $\mp V_b$ is plotted as a function of the current $\langle I_m \rangle$. The data were shifted for clarity and the zero corresponding to each temperature is indicated by a line. The error bar is calculated using Eq. (7.27).

connected to the batteries in the voltage source V_m and the ground should be extremely small (in our setup, the resistance leakage is estimated by a lower bound of 100 GΩ). The signal, which is a difference between the two groups of curves, is characterized by the relative difference in the rates $R_\Gamma(s)$ between pairs of curves of Fig. 7.17:

$$\boxed{R_\Gamma \equiv \Gamma_+(s)/\Gamma_-(s) - 1}, \tag{7.28}$$

where $\Gamma_+(s)$ (respectively $\Gamma_-(s)$) is the switching rate in case V_b and V_m are of the same sign (respectively opposite sign). Then, the condition (7.25) is equivalent to having R_Γ unchanged whether it is calculated using $V_m > 0$ and the two rates at $\pm V_b$ or using $V_m < 0$ and the two rates at $\mp V_b$. The difference of these two offsets $R_\Gamma^{V_m>0} - R_\Gamma^{V_m<0}$ should thus be zero. On Fig. 7.18, the difference between these two determinations is plotted for different values of

---

After each set of ten thousands measurements, $\Delta\Gamma$ is compared to a maximum value set by the operator. If it is too large, another set of ten thousands measurements is repeated with the same parameters, and so on.

the current $\langle I_m \rangle$ and for several temperatures. The distance from zero is much smaller than the signal R_Γ itself (see Fig. 7.18), thus strongly supporting the validity of our measurements. Notice that the uncertainty on the measurement of R_Γ is given by (see Eq. (7.27)):

$$\Delta R_\Gamma = 2\frac{\Delta \Gamma}{\Gamma} = -2\sqrt{\frac{P}{N(1-P)}}\frac{1}{\ln(1-P)} \tag{7.29}$$

Measuring the asymmetry in the switching rates

On Fig. 7.17, it is clear that for opposite signs of $V_b \times V_m$, the switching rates take different values. Curves like the ones shown on Fig. 7.17 were measured as a function of s for several values of $\langle I_m \rangle$ and of the refrigerator temperature. From those curves, the asymmetry factor R_Γ was calculated as a function of s. Choosing the range of s on which these measurements are performed was done by maximizing the uncertainty on R_Γ, and by limiting the acquisition of a set of 6 points to 10 minutes (as the uncertainty depends strongly on s near $s = 0$ or $s = 1$, the acquisition time can grow very fast in those regions). In the experiment, we chose the range of s so that $P_{\text{min}} = 0.25$ and $P_{\text{max}} = 0.987$ where $\Delta R_\Gamma \approx 4/\sqrt{N}$.

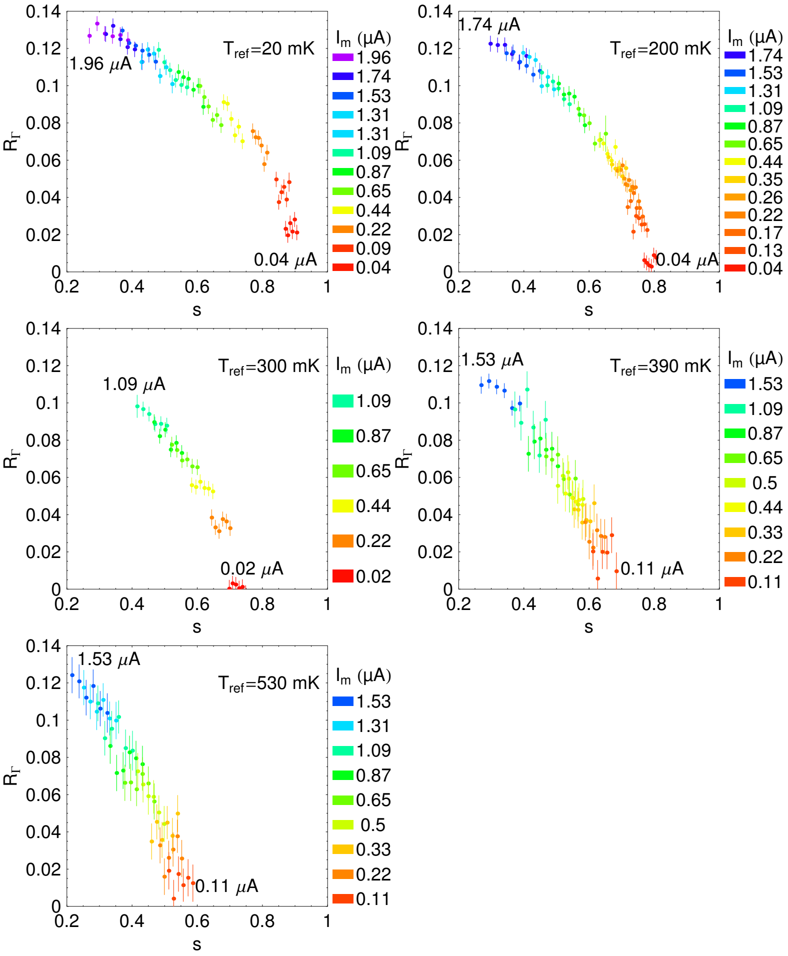

Fig. 7.19. On each panel, the dots represent the measured $R_\Gamma = \Gamma_+(s)/\Gamma_-(s) - 1$ as a function of s for several values of the current $\langle I_m \rangle$ indicated by the color of the dot. To each dot corresponds an error bar calculated using Eq. (7.27). Each panel corresponds to a single temperature of the refrigerator indicated on the top right corner. To each single dot of Figs. 7.13 corresponds a set of 6 dots with different values for s.

7.4 Classical escape dynamics of a Josephson junction in presence of non-Gaussian noise

7.4.1 Numerical simulations

In order to get some insight on the effect of noise on the switching of a Josephson junction, Xavier Waintal, a theorist from our physics department (SPEC, CEA Saclay), performed numerical simulations of the classical dynamics of the phase in a potential well in presence of non-Gaussian noise. Similar simulations were performed long ago [187, 191, 154] in the case of thermal noise and confirmed the predictions of the escape dynamics theory in the classical regime discussed in 5.2.1. In the simulations performed by Xavier Waintal, the total noise was taken as the sum of a thermal noise and of a noise with a Poisson distribution of the currents. In the following, we use the reduced units of Table. 7.2. With these notations, Eq. (7.9) reads

Reduced unit	Translation
$\tilde{t}$	$\omega_{p0}t$
χ	$\langle I_m\rangle/(e\omega_{p0})$
α	$e\omega_{p0}/I_0$
$\tilde{T}$	$k_BT/(\varphi_0 I_0)$
s	I_b/I_0

Table 7.2. Table of the reduced notations used in the numerical simulations.

$$\frac{\mathrm{d}^2\gamma}{\mathrm{d}\tilde{t}^2}+\frac{1}{Q_0}\frac{\mathrm{d}\gamma}{\mathrm{d}\tilde{t}}+\sin\gamma-s=\delta s(\tilde{t}) \tag{7.30}$$

The noise term $\delta s(\tilde{t})$ contains two parts:

- a Gaussian noise due to the Johnson-Nyquist noise of the circuit at temperature T_{th}. The correlator of this noise is (7.11)

$$\langle\delta s(\tilde{t})\delta s(0)\rangle=\frac{2\tilde{T}_{\mathrm{th}}}{Q_0}\delta(\tilde{t}) \tag{7.31}$$

  where $\tilde{T}_{\mathrm{th}}$ is be related in our experiment to the temperatures $\tilde{T}_1$ and $\tilde{T}_2$ by Eq. (7.17):

$$\tilde{T}_{\mathrm{th}}=\frac{\tilde{T}_1/R_1+\tilde{T}_2/R_2}{1/R_1+1/R_2+1/R_t} \tag{7.32}$$

- The second part is due to the mesoscopic current $\langle I_m \rangle$ flowing through the tunneling junction.

$$\delta s(\tilde{t}) = \mathrm{sgn}(\chi) \sum_i \alpha \delta(\tilde{t} - \tau_i) \tag{7.33}$$

where the random variables τ_i are given by $\tau_{i+1} = \tau_i + w$ with the Poisson distribution law $p(w) = \chi e^{-\chi w}$.

The simulations are straightforward step by step numerical resolutions of Eq. (7.30), with time steps of $10^{-3}\omega_{p0}^{-1}$. At each step, the current fluctuation δs is calculated according to the above conditions. When the phase reaches a position beyond 1 rad past the top of the barrier potential $\gamma_{\max}$, the time is acquired and appended to the switching histogram. This procedure is repeated $N_{\mathrm{data}} = 10^5$ times so that the histogram has enough points to extract the switching rate Γ.

At the time of this writing, no calculations were performed using the same parameters as in the experiment.

7.4.2 Perturbative calculation

In order to predict the outcome of our experiments, Joachim Ankerhold, theorist from Freiburg University (Germany), developed a theory for the escape rate of a Josephson junction in the classical regime in presence of non-Gaussian noise [60]. In this section, we present the main results of his derivation and compare them to our experimental data.

The derivation is based on an effective Fokker Planck equation, valid in the following conditions:

- the cumulants of the current fluctuations are rapidly decreasing with their order
- the current autocorrelation time is much smaller than ω_{p0}^{-1}
- the exponent B is much higher[11] than the quality factor Q

Solving this Fokker-Plank equation for the population of the phase as a function of the time, position and velocity, one finds the rate at which the population inside the well decreases.

Main results

The switching rate calculated with this method reads (up to an approximate value of the prefactor)

---

[11] This is not true in our experiment where $B \approx 10$ and $Q \approx 15$ at its minimum (when $s \approx 0.9$). This condition must be fulfilled for a correct calculation of the prefactor in the switching rate formula. But this might have implications on R_Γ too.

$$\mathit{\Gamma}(s, I_m) = \frac{\omega_p(s)}{2\pi}\lambda(Q(s)) \exp\left[\frac{4\sqrt{2}}{3}\varphi_0 I_0 \frac{(1-s)^{2/3}}{k_B T_{\mathrm{esc}}}(1 - g(s, \langle I_m \rangle))\right] = A\mathrm{e}^{-B(1-g)} \tag{7.34}$$

where A and B correspond to the definitions of section 5.2.1 and where

$$g(s, \langle I_m \rangle) = \frac{1}{4}\frac{Q(s)^2}{5 + Q(s)^2}\left(\frac{\hbar\omega_{p0}}{k_B T_{\mathrm{esc}}}\right)^2 \frac{\langle I_m \rangle}{I_0}(1 - |s|)^{11/6}. \tag{7.35}$$

Therefore, at first order, $R_\mathit{\Gamma} = 2B \times g$ which gives

$$\boxed{R_\mathit{\Gamma} = \frac{2\sqrt{2}}{3}\frac{Q(|s|)^2}{5 + Q(|s|)^2}\frac{\varphi_0 \hbar^2 \omega_p(|s|)^2 \langle I_m \rangle}{(k_B T_{\mathrm{esc}})^3}(1 - |s|)^2 (1 + |s|)^{-1/2}} \tag{7.36}$$

Finite temperature case

At finite temperatures, we plotted the theoretical expression for $R_\mathit{\Gamma}$ (7.36) at constant exponent B as a function of $\langle I_m \rangle$ for several refrigerator temperatures (and using the measured escape temperatures T_{esc} from Fig. 7.13), it is clear that $R_\mathit{\Gamma} B^{-5/3}$ is independent on B. Therefore, at finite or at zero temperature, one has

$$R_\mathit{\Gamma} \propto B^{5/3}. \tag{7.37}$$

Actually, there is another scaling law:

$$\boxed{R_\mathit{\Gamma} \propto B^{5/3} \langle I_m \rangle T_{\mathrm{esc}}^{-4/3}}. \tag{7.38}$$

This scaling is consistent with preliminary zero temperature results of numerical simulations in the exponent of B, as in this case $T_{\mathrm{esc}} \propto \langle I_m \rangle$.

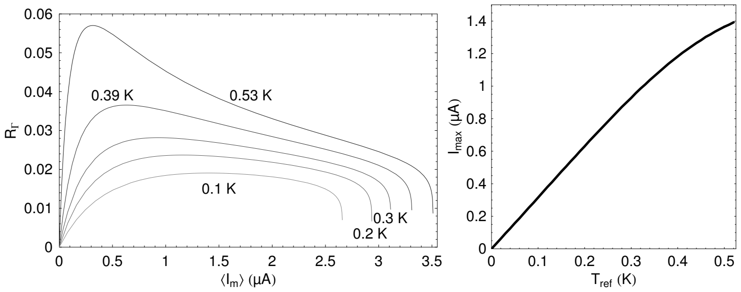

Fig. 7.20. Left panel: theoretical curves for various values of the temperatures of the environment ($T_1 = T_2$) using Eqs. (7.36,7.17) for a value of s leading to a constant switching rate corresponding to the lowest experimentally accessed rate $\Gamma = 5.7$ kHz. Right panel: calculated average current $\langle I_m \rangle$ at which the asymmetry R_Γ is maximal with our experimental parameters as a function of the temperature of the environment.

7.5 Comparison between theory and experiment

Using the definition of the exponent B in (7.8):

$$B \equiv -\ln(2\pi\Gamma_+(s)/[\omega_p(s)\lambda(Q(s))]), \tag{7.39}$$

R_Γ is plotted on Fig. 7.21 as a function of $\langle I_m \rangle$ for several values of B. For all temperatures and values of B, R_Γ increases with $\langle I_m \rangle$.

Our data do not verify the scaling law (7.37) as shown on Fig. 7.22 where the curves do not fall on a single one.

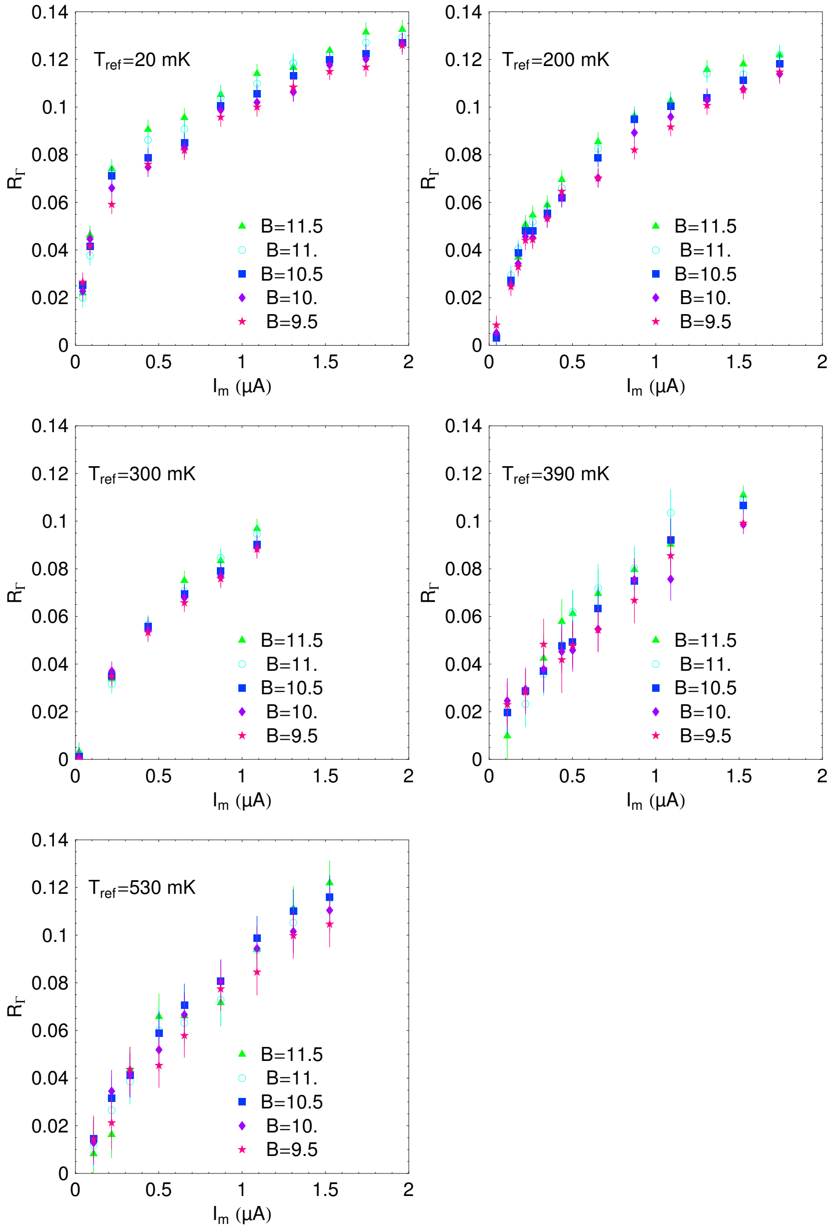

Fig. 7.21. The dots are the measured offset $R_\Gamma = \Gamma_+(s)/\Gamma_-(s) - 1$ as a function of the current $\langle I_m \rangle$ obtained for a value of the bias current pulse sI_0 leading to a value of $B(s)$ indicated by the color of the dot. The error bars are plotted as lines. Each panel corresponds to a single temperature of the refrigerator indicated on the top left corner.

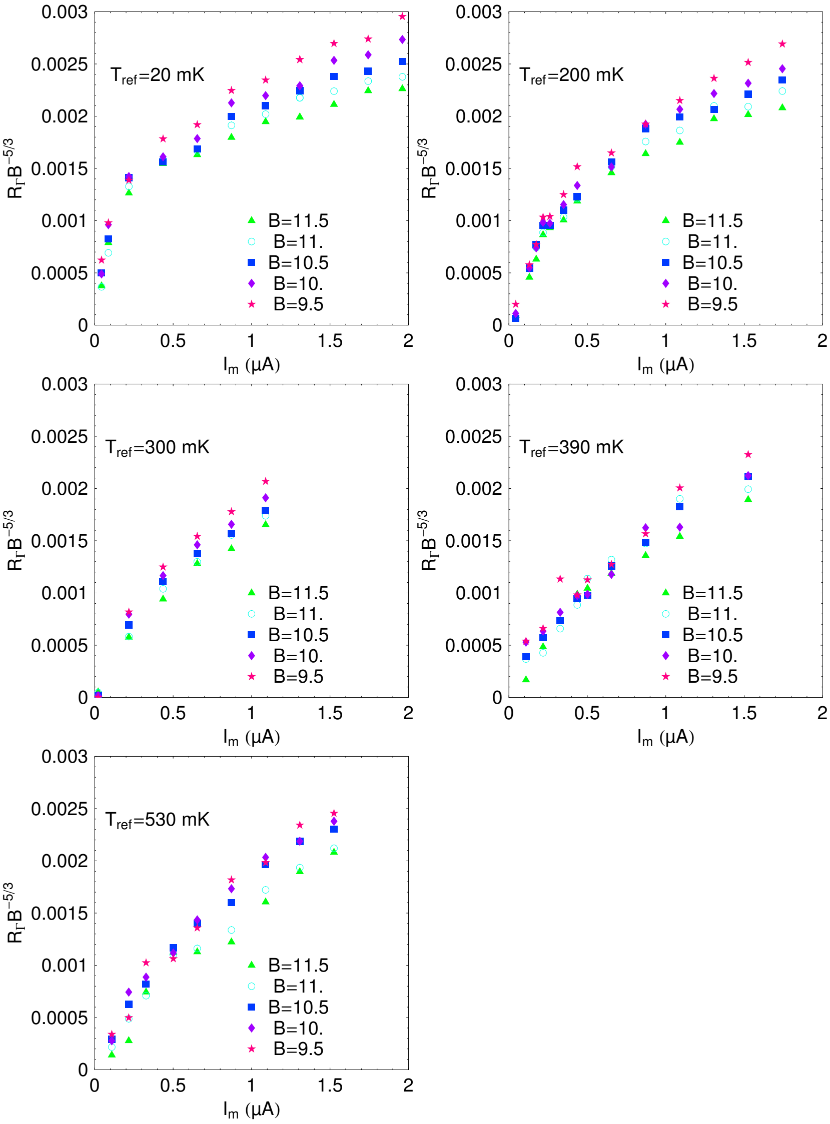

Fig. 7.22. Each panel corresponds to a single temperature of the refrigerator indicated on the top left corner. The dots are the measured offset R_Γ times $B^{-5/3}$ as a function of the current $\langle I_m \rangle$ obtained for a bias current sI_0 such that $B(s)$ is given by the value indicated by the color of the dot.

An empirical scaling law can still be found, and it seems from Fig. 7.23 that

$$R_\Gamma \propto B^{2/3} \tag{7.40}$$

since all the curves at a given temperature are superimposed.

It is clear that the theory does not reproduce our data. On the contrary, for low temperatures, it seems that the experimental offset R_Γ scales along the empirical expression (see Fig. 7.24-b):

$$R_\Gamma \approx 1.43 \times 10^{-42} \left(\frac{\langle I_m \rangle}{1\ \mu\mathrm{A}} \right) B^{2/3} \left(\frac{T_{\mathrm{esc}}}{1\ \mathrm{K}} \right)^{-3/4} + 10^{-3} \tag{7.41}$$

where T_{esc} is the measured escape temperature of Fig. 7.13. It seems that the theoretical prediction has the good dependences on B and on the current $\langle I_m \rangle$ but a wrong exponent in T_{esc} (see Eq. (7.38)).

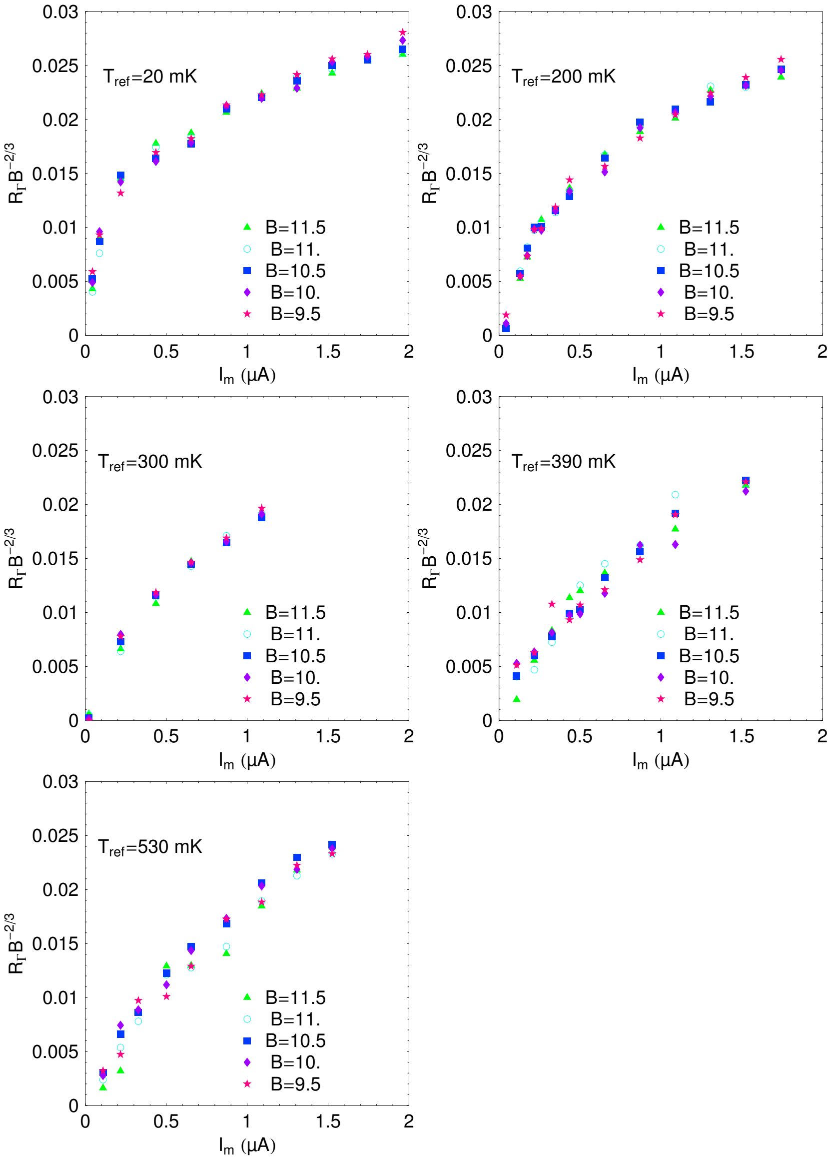

Fig. 7.23. Each panel corresponds to a single temperature of the refrigerator indicated on the top left corner. The dots are the measured offset R_Γ times $B^{-2/3}$ as a function of the current $\langle I_m \rangle$ obtained for a bias current sI_0 such that $B(s)$ is given by the value indicated by the color of the dot.

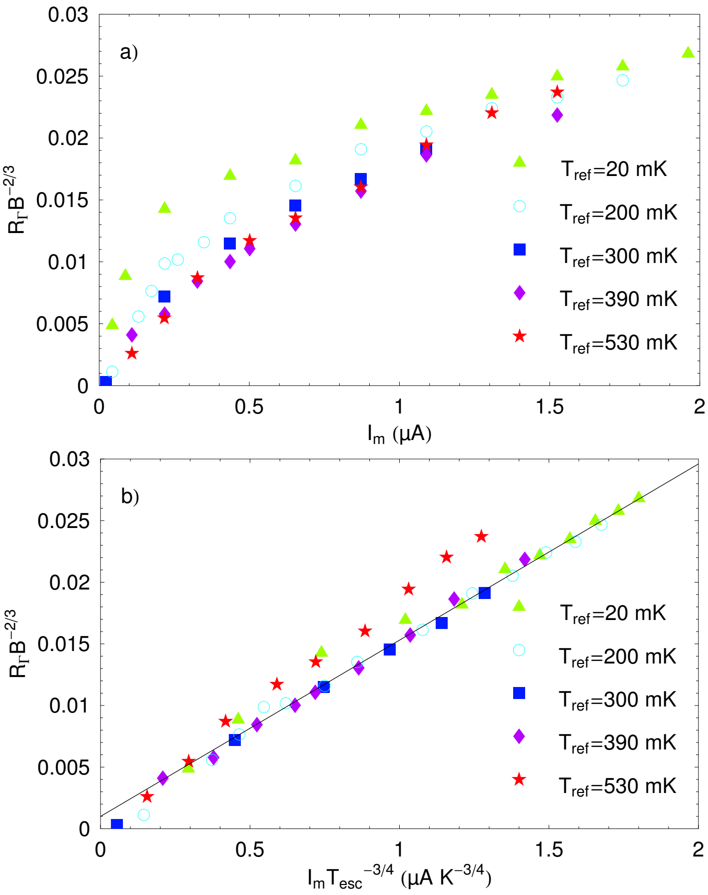

Fig. 7.24. Fig a): Average value of $R_\Gamma B^{-2/3}$ as a function of $\langle I_m \rangle$ for several refrigerator temperatures. Fig b): Average value of $R_\Gamma B^{-2/3}$ as a function of $\langle I_m \rangle T_{\mathrm{esc}}^{-3/4}$ for several refrigerator temperatures. The line is an empirical linear fit (7.41) for the dots at low refrigerator temperatures.

7.6 Conclusions

In this chapter, we have discussed an experiment in which a Josephson junction was used as a detector of current fluctuations. In particular, we showed how this detector can be sensitive to the non-Gaussian fluctuations of the noise.

The main results of this chapter are the following

- an experiment probing the effect of current noise through a tunnel junction on the switching dynamics of a Josephson junction was performed.
- the sensitivity of a Josephson junction to the current fluctuations was described theoretically at the first order (see Eq. (7.16)). It was found that the escape temperature depends linearly on the variance of the current fluctuations.
- the escape temperature was measured, and a quantitative comparison was made with Eq. (7.16) (see Fig. 7.14).
- when reversing the sign of the current through the noisy junction, it was found that the switching rates get slightly modified (see Fig. 7.19). Several tests were performed to rule out possible sources of asymmetry other than the asymmetry in the current noise in the tunnel junction itself (see Fig. 7.18).
- preliminary comparisons with numerical simulations and with a perturbative theory were discussed.

The discussion of the experimental data is still preliminary, and further work is currently in progress. From the experimental point of view, more experiments are needed to get rid of parasitic effects like heating of the dissipative environment of the junction, and other values of the quality factor should be scanned to test our understanding of the role of this parameter.

Part IV

Experimental techniques

Chapter 8

Sample processing

Contents

This chapter shows the various techniques used in the fabrication of the samples described in this thesis work.

8.1 Optical lithography

Optical lithography was used for designing patterns at a resolution above 1 μm. Several samples can easily be patterned in the same time on a single wafer.

8.1.1 Mask fabrication

Depending on the application, two techniques were used to fabricate the masks. For coarse patterns, like coplanar wave guides on the tenth of mm scale, an AutoCad drawing is printed on a transparency using a standard inkjet printer (HP Business inkjet 2250tn). The mask has the resolution of the printer (300 ppp) and is full of defects on the μm scale, but this does not affect macroscopic wave guides and it is fast and cheap. For more accurate patterns, a professional printer (high resolution printing with 8000 lines on A4 paper, MKM Electronique) was used. The resolution is better than 1 μm and the minimal width of the lines is about 10 μm. After printing, the drawing is transferred on a Cr coated mask using the following standard process:

- sandwiching the transparency between a clean glass and a glass coated with Cr and positive optical resist. The printed side of the transparency must be in contact with the Cr coated side for best resolution
- UV exposure of the resist during 12 s in a SUSS aligner (5 mW.cm^{-2})
- development of the resist in two successive baths of MF-319 for a total duration of 50 s at room temperature followed by water rinsing
- Cr etching during 110 s
- resist removal in acetone bath followed by isopropanol.

8.1.2 Metallic layers

Resist spinning

Prior to lithography, the substrate is cleaned in an ultrasonic acetone bath followed by isopropanol. Then, a primer is deposited on the wafer and is spun at 5000 rpm 30 s later. A resist (AZ5206 or AZ5214E) is spun on the substrate at 5000 rpm for 60 s then baked at 90°C on a hot plate for 3 min.

Exposure and development

The substrate is then exposed in a SUSS aligner through a Cr mask for 50 s. In order to strengthen the surface of the resist, so that the undercuts are more pronounced once developed, the substrate is dipped in 1,2-dichlorobenzene for 1 h, then dried under a nitrogen gas flow. Development follows in AZ351B diluted to 1:5 in water during about 10 min, then the wafer is water rinsed.

Metal deposition

Metals like Au, Ag, Cu, Ti or Al were evaporated in the same electron gun evaporator.

Lift-off

The remaining resist is removed in an acetone bath at 65°C, thus removing all the undesired metallic parts.

8.1.3 Dielectric layers

Three methods were used to fabricate patterned dielectric layers. The first one used a UV sensitive resist which once baked is a very good dielectric. The second one used oxidized aluminum. The third one used etching of a polyimide.

BCB resist

The first dielectric method used to fabricate capacitors uses the BCB (Cyclotene 4000, XU35 133.00) resist by DOW©. It can be very conveniently patterned because it is sensitive to UVs: it can be exposed and developed as a standard optical resist. The deposit of this resist is very similar to the AZ5206 (see 8.1.2) except that the primer is the AP3000, and that we used a spinning velocity of 3700 rpm. The wafer is baked for 2 min at 60°C on a hot plate before and after UV exposure during about 10 s. The resist which has not been exposed is removed in a development bath of DS3000 at 32°C for 50 s, followed by a stoping bath in the same solvent but at room temperature, for 60 s. Finally, the wafer is annealed at 350°C in vacuum (turbo pump) for 80 min.

At the end, the remaining BCB resist forms a dielectric with $\epsilon_r = 2.65$ and about 600 nm thick (approximately 40 $\mathrm{pF.mm^{-2}}$). After hot bake, it cannot be altered by acetone or any other chemical used in lithography. The profile of the edges of this resist is smooth at the scale of a few μm.

Polyimide

In experiments on atomic contacts, we used Polyimide as a dielectric. A solution of PI2611 (30 g (HD Microsystems PI2611)+30 mL N-methyl-2-pyrrolidone) is spun at 2000 rpm on a metallic wafer (polished brass) after an adhesion promoter (Ultradel A600). It is then baked for one hour in an oven at 180°C, and annealed for one hour at 350°C in a vacuum chamber under a residual pressure of 10^{-6} mbar. The final thickness of the layer is 1.6 μm and its permittivity is $\epsilon_r = 2.9$ (approximately 16 $\mathrm{pF.mm^{-2}}$). This dielectric can be dry etched isotropically. While being kept at 200°C the sample is exposed to a plasma formed in a flow[1] of 50 sccm O_2 and 2 sccm SF_6 at a total pressure of 0.3 mbar and an auto-polarization voltage of 25 V. The etching depth, monitored by laser interferometry, grows approximately linearly at about 200 nm/min.

---

[1] One standard cubic centimeter per minute (sccm) is a measure of the flow of gas at a pressure of 1 atm.

Alumina

The process based on dielectrics of alumina was developed in our group by François Nguyen. It involves strong oxidizing of patterned aluminum electrodes. In a subsequent fabrication step, other pairs of electrodes are deposited so that they overlap the aluminum electrode covered with alumina, thus forming two capacitors in series. The main asset of this method is that the capacitances obtained have very large values because the dielectric is very thin (a few nm). However, it is difficult to have a good control of the thickness and quality of the alumina layer.

In a first step, an aluminum electrode is fabricated by lithography. Then, the wafer is heated at 150°C during 4 min in presence of O_2 at a pressure of 1.2×10^{-2} mbar. An oxygen plasma at 0.2 mbar just follows for 10 s.

The dielectric coated electrodes are covered in a following step by a metallic Cu or Al electrode (it was observed that Ti or Au electrodes diffuse in the alumina and create short circuits). The obtained capacitances have values of about 15 $\mathrm{nF.mm^{-2}}$.

Technology	Present fabrication success ratio	Dispersion of the capacitances values	Direct patterning	Capacitance per area ($\mathrm{pF.mm^{-2}}$)
BCB resist	90%	up to 5%	Yes (with UV)	40
Polyimide	90%	up to 5%	No	16
Alumina	40%	up to 300%	No	15000

Table 8.1. Properties of the various techniques to fabricate capacitors.

8.2 E-beam lithography

E-beam lithography allows to design patterns with a resolution better than 100 nm.

8.2.1 Principle

Using electro-sensitive resists, one can use a scanning electron microscope to insolate the desired parts of a future mask. We used positive resists for which, exposed regions are dissolved during development. Multiple layers are used in case one needs to deposit metal in different spots in a single evaporation (see below and on Fig. 8.1).

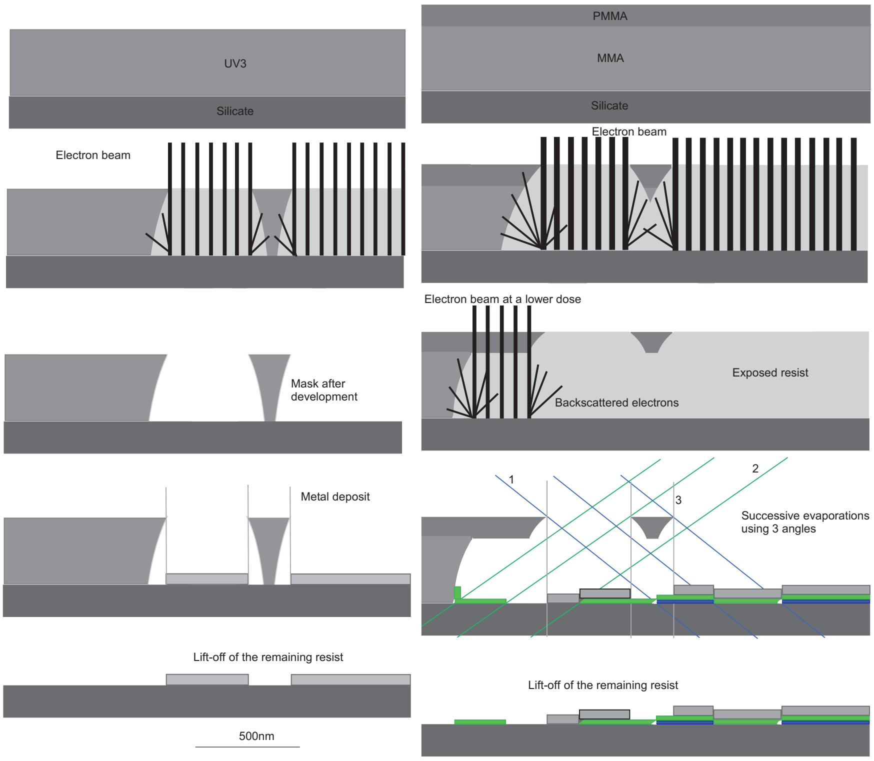

Fig. 8.1. Typical fabrication scheme. Left panel: monolayer resist (UVIII). Right panel: bilayer resist (PMMA/MAA).

8.2.2 Resists

UVIII$^{\mathrm{TM}}$

This resist is extremely sensitive to electronic exposure (12 μC.cm^{-2}), thus being a good choice for large area patterning. In our case, its main drawback was that we were never able to completely get rid of the resist in the exposed area after development. The process used starts with a primer spinning followed by a spinning of UVIII$^{\mathrm{TM}}$ at 2000 rpm and heating on a hot plate at 135°C for 1 min. The resulting layer is about 500 nm thick. Once exposed, it is developed in MEGAPOSIT MF CD-26 for 60 s and rinsed in water. The lift-off is performed with acetone at 65°C and followed by a rinse with isopropanol.

PMMA

The most standard electro-sensitive (about 200 μC.cm^{-2}) resist is the polymethyl-meta-acrylate (PMMA). We used a PMMA of molecular mass 950K diluted at 3% in anisole. It is either used as a monolayer or on top of a more sensitive resist. After spinning, it is baked on a hot plate at 140°C for 15 min[2]. Once exposed, it is developed in methyl-isobutyl ketone (MIBK) diluted 1:3 in volume with isopropanol for 35 s and rinsed in isopropanol. The lift-off is performed with acetone at 65°C and followed by a rinse in isopropanol.

PMMA/MAA

A resist often used as the bottom of bilayers is the electro-sensitive (about 100 μC.cm^{-2}) polymethyl-meta-acrylate/meta-acrylate acid (PMMA/MAA). The one we used is diluted in mass at 10% in ethyl-lactate and the molecular mass of the MAA is 8.5 K. This resist is spun directly on the silicon substrate and baked on a hot plate at 140°C for 7 min. Once exposed, it is developed at the same time as the top layer of PMMA.

LOR

The Lift-Off Resist 30B (LOR30B) by Microchem allows to obtain very thick bottom layers of bilayers for fabricating very wide undercuts. It is insensitive to electrons and is not altered by MIBK nor by acetone, which makes it particularly convenient to work with as a bottom layer under a PMMA mask. All areas of LOR30B which are not protected by PMMA get dissolved in MF-319, the undercut being determined by the time the sample stays in MF-319. For example, for the sample used in the experiment probing fluctuations of the current (chapter 7), the last step in the fabrication used a bilayer of LOR30B (spun at 3000 rpm and baked at 150°C for 4 minutes - 3 μm thick) covered by a PMMA layer. Once the top PMMA layer has been exposed and developed, it takes 13 s in MF-319 to get an undercut of 1.7 μm. LOR resists are removed with AZ400K at 80°C for 3 min (MF-319 also etches aluminum, so its use is not always an option).

8.2.3 Exposure

The exposure to electron beam was performed either at 35 kV in a JEOL 840A scanning electron microscope using Proxy Writer from Raith or at 25 kV in a Philips XL30 SFEG using Elphy Quantum from Raith. In both microscopes, the electron beam is steered on the areas of the resist one wants to expose. The time spent on each zone is calculated depending on the resist and on the current (see appropriate doses above). Large areas of the pattern in which the

---

[2] at temperatures higher than 150°C, we found that a 4 min bake was sufficient

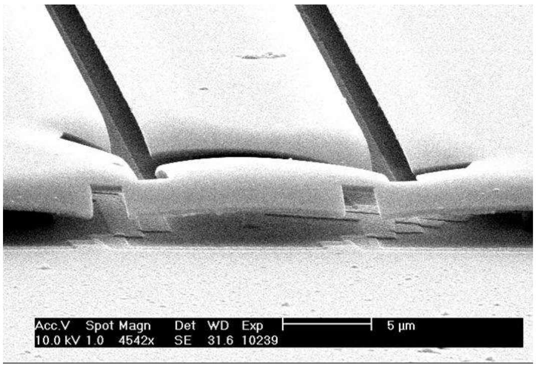

Fig. 8.2. Scanning electron microscope image at 45° of a sample coated by a bilayer LOR30B/PMMA covered with metal, after development, metal deposit and before lift-off. One clearly sees the wide undercut in the LOR30B resist, creating wide hanging PMMA structure, and allowing metallic evaporation at large angles.

resolution is not essential were patterned using a larger current, in order to gain exposure time. Typically, 15 pA for details and 10 nA for large areas. The finest wires we got were 80 nm wide.

8.3 Metal deposition

All metals used in our experiments (Au, Ag, Cu, Ti or Al) were evaporated in the same electron gun evaporator, which is free of magnetic materials, thus limiting pollution hazards. In the loadlock, where the sample sits, the pressure is as low as 10^{-6} mbar. The material sources are located in the lower chamber about 50 cm below the sample and in a 10^{-7} mbar vacuum. The rate of deposition is measured in real time from the resonance frequency of a crystal, and is tuned between 0.2 and 1 nm/s depending on the material.

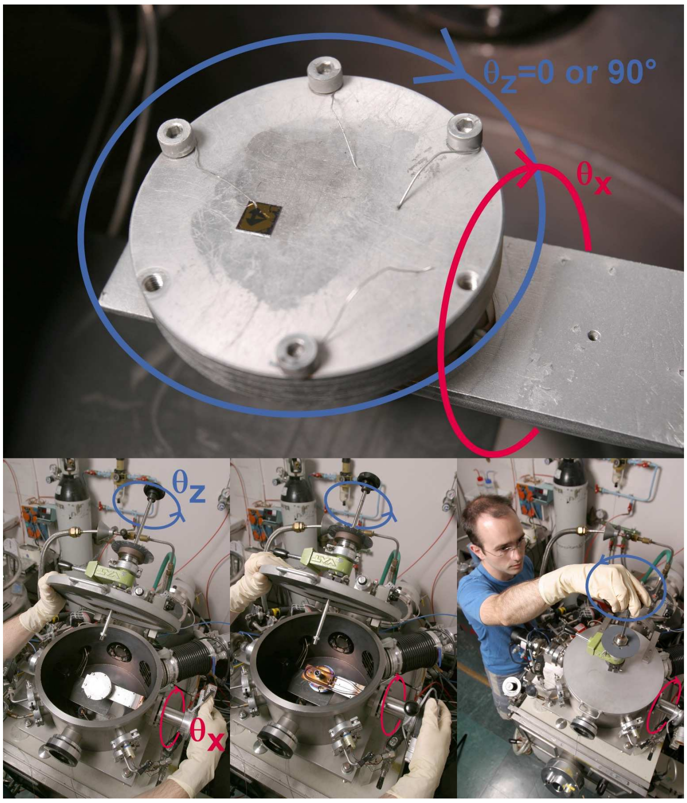

Fig. 8.3. Picture of the evaporator. The sample can be tilted along two rotation axes.

The sample holder is carried by a rotating arm, so that its angle with the direction of evaporation can be adjusted continuously between −90° and +90° around the X axis (see Fig. 8.3). We have additionally installed a mechanism that allows to rotate the sample holder on the arm by +90° around the Z

axis. We used this possibility for the samples of chapter 7, for which the three deposition directions needed not to be in the same plane.

8.3.1 Cleaning

When a metal has been in contact with air or some resist, its surface can be covered with a water layer, oxidized or polluted. It is then essential to clean it before depositing another metal on top if one wants reproducible contacts. We used ion milling with an argon plasma (about 10^{-4} mbar of Ar, $V = 500$ V and $I = 5$ mA during $5 - 7$ s) in the evaporator chamber. Resists are not altered significantly by this treatment.

8.3.2 Tunnel junctions

Fabrication of tunnel junctions requires 3 to 4 steps not necessarily done in the same vacuum:

- Deposition of the bottom electrode
- Deposition of a few nm Al layer (this step is skipped if the bottom electrode is in Al)
- Oxidation of the Al (in the evaporator loadlock)
- Deposition of the top electrode

Depending on the material and on the oxidizing parameters, the tunnel junctions of 100 nm × 200 nm exhibit resistances ranging from 100 Ω to hundreds of kΩ. The gas used for the 10 min oxidation is a mixture of 80% Ar and 20%O_2 at typical pressures ranging from 1 to 40 mbar.

8.4 Ion implantation

In experiments of chapters 2 and 3, Mn atoms were implanted in silver thin films. This section describes the implantation procedure.

8.4.1 Apparatus

The system used is the one described in [192] and was operated by S. Gautrot, O. Kaitasov and J. Chaumont at the CSNSM in Orsay University. Manganese atoms get ionized with a hot cathode into Mn^+ ions, the ions are first accelerated at 30 keV, then are selected in mass by a magnet, then re-accelerated up to 70 keV, and the resulting beam is focused and scanned on the sample holder. The sample holder is connected to ground through a current integrator. Hence, the number of Mn^+ ions that have reached the sample holder can be accessed. Besides, an “electron repeller” prevents electrons to scatter to the ground through other pathes (see Fig. 8.4).

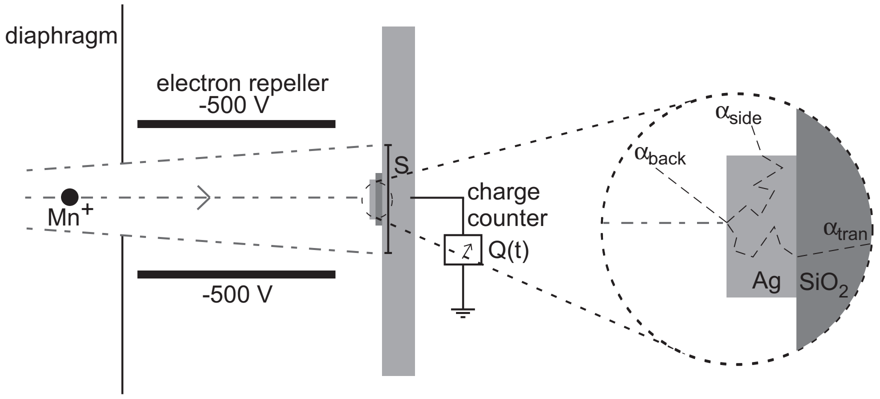

Fig. 8.4. Scheme of the ion implantation in the sample. Each Mn^+ ion has a finite probability of escaping the Ag wire as described in the text.

8.4.2 Calculation of the concentration

The part of Mn atoms which actually ends inside of the sample is not necessarily the one measured by the current integrator. In the following, we describe the calculation of the actual concentration of Mn in the particular example of the sample for the experiment on magnetic impurities in Ag wires. For this calculation, the path followed by an Mn^+ ion in the sample is numerically simulated using the SRIM software [129].

Total number of Mn^+ ions impinging on the sample

At the end of the implantation, the current integrator measures the total charge having reached the target $Q = N_{\mathrm{tot}}e$. However, the number of charges N_{tot} can be different from the number of Mn^+ ions impinging on the target because as a fraction α_{back} of the ions can be backscattered, then hit the electron repeller and emit secondary electrons that reach the sample holder. In order to evaluate this number of “fake events”, we calculate the fraction α_{back} of ions backscattered by the sample holder made of Dural (the surface covered by the sample itself is negligible. The SRIM software gives a few permils for $\alpha_{\mathrm{back}}^{\mathrm{dural}}$, therefore, we can finally safely neglect false events and consider that the total number of Mn^+ ions impinging on the target is just N_{tot}.

Finally, the density of Mn atoms impinging on the sample is obtained from the total charge $Q = 1.952\ \mu\mathrm{C}$ measured by the current integrator and the total area $S = 56.5\ \mathrm{cm}^2$ scanned by the ion beam:

$$\sigma_{\mathrm{tot}} = \frac{Q}{eS} \approx 2.16 \times 10^{15} m^{-2}. \tag{8.1}$$

Total number of Mn^+ ions deposited in the silver wire

Once a Mn^+ ion has hit the top side of the wire designed for our experiments (42 nm thick, 230 nm wide layer of Ag on top of silicon), it does not necessarily stop within the wire:

- it can be backscattered with a probability $\alpha_{\text{back}} = 0.045$, much higher than in Dural
- it can be transmitted through the Ag layer to the SiO_2 with a probability $\alpha_{\text{tran}} = 0.164$
- it can escape through the edges of the wire and finally end in the Substrate around the wire with a probability $\alpha_{\text{side}} = 0.061$
- it can stay in the wire.

The probabilities of the four possibilities are calculated using the SRIM software (see Fig. 8.4).

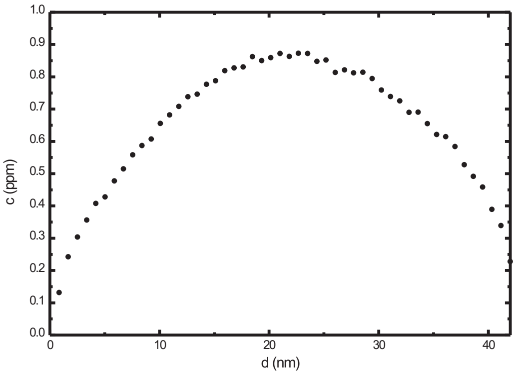

Fig. 8.5. Concentration profile of Mn atoms in Ag, according to the SRIM simulation of the implantation of Mn^+ ions at 70 kV in a 42 nm thick and 230 nm wide Ag wire on top of silicon. The dots show the concentration in parts per million (ppm) of Mn atoms in the wire, as a function of the depth (0 being the surface on which the Mn^+ ions hit the wire).

As a result, the density of Mn atoms in the wire after the implantation is

$$\sigma_{\text{wire}} = \sigma_{\text{tot}}(1 - \alpha_{\text{back}} - \alpha_{\text{tran}} - \alpha_{\text{side}}) \approx 1.60 \times 10^{15} m^{-2} \tag{8.2}$$

Given the density of the Ag wire $\rho = 5.86 \times 10^{28}$ m^{-3}, the average concentration of Mn impurities can be estimated as $c = 0.65$ ppm (parts per million).

These calculations introduce corrections in the reported values of the concentration of Mn impurities in [43]. The actual concentration of implanted

Mn atoms in the so-called Ag(5N)$c_{\mathrm{Mn0.3}}$ is 0.14 ppm and in the so-called Ag(5N)d_{Mn1} is 0.46 ppm.

Chapter 9

Low temperature measurements

Contents

9.1 Sample holder

9.1.1 Electron-electron interactions experiments

In the experiments of chapter 2 and 3, the sample were glued with silver paint on a copper plate fixed on a DIL$^{\text{TM}}$ connector. The sample was grounded to the copper plate with a gold ribbon glued with silver paint, and the other pads are bonded to the pins of the DIL connector with 50 μm gold wires.

9.1.2 Full counting statistics (FCS) experiments

In addition to the techniques used in the electron-electron interactions experiments, we designed (see Fig. 9.1) sample holders for microwave measurements

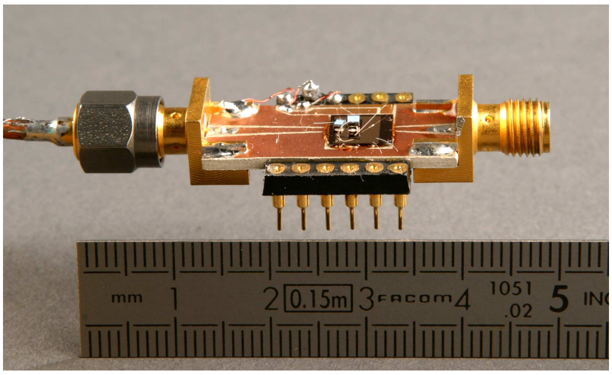

Fig. 9.1. Picture of the sample holder for the FCS experiment.

up to a few GHz. For the experiments of chapter 7, we connected SMC resistors (Vishay) directly on the chip with a conductive epoxy (CircuitWorks), without any bake.

9.1.3 Atomic contact experiments

To obtain contacts through a single atom, nanofabricated mechanically controlled break junctions [45] were used. The setup is the same as the one described in [21], except that in the latest version of this setup, the whole bending stage is made of copper, and the magnetic field generating coil is fixed inside the Cu pushing rod, so that electromagnetic noise from the coil is screened. The sample sits in an Al inner chamber to avoid magnetic noise.

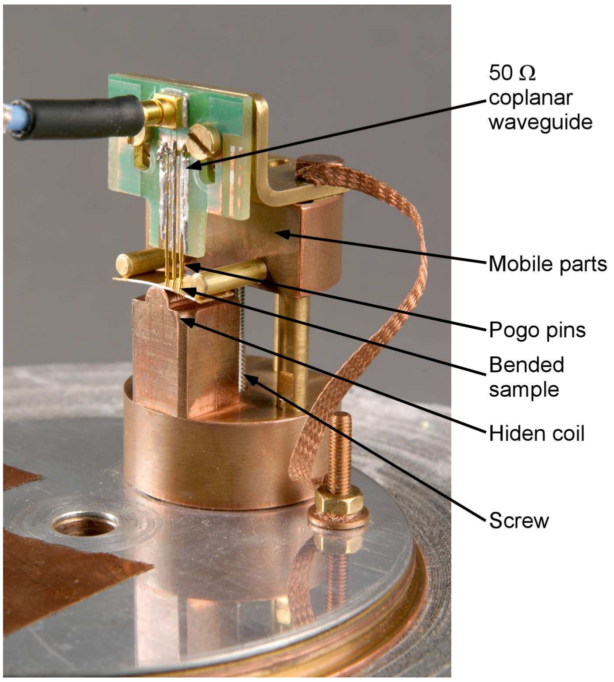

Fig. 9.2. Picture of the mechanical bending setup which allows one to break the nanopatterned metallic bridges in order to form atomic contacts. The screw is rotated by an electrically powered rotor. It then moves the mobile parts vertically and the sample is bent or unfolded. All the measurement lines go through the 50 Ω transmission line.

9.2 Noise filtering

In our experiments, electrical noise is a big issue. Indeed, the resolution in energy of the experiments is eventually limited by the temperature of the electrons in the electromagnetic environment of our sample. For phenomena occuring on a few tens of μV, the effective temperature of the electrons needs to be of the order of dilution refrigerator temperatures (around 20 mK). In order to perform experiments with such cold electromagnetic environments, the sample must be in good thermal contact with the lowest stage of a dilution refrigerator (a Kelvinox300 from Oxford Instruments or a home-made refrigerator depending on the experiment), and the Johnson-Nyquist noise must be correctly filtered. Here, we describe the filtering techniques used in our experiments.

9.2.1 Attenuating and amplifying a signal

Attenuating

Using strong signals at room temperature allows to have a good signal to noise ratio. Therefore, it is always preferable to attenuate strong signals than just propagating small signals. Yet, discrete attenuators are made of resistors, which themselves cause some Johnson-Nyquist current noise. In order to reduce this noise, one needs to cool the attenuators. However, if too much energy gets dissipated in the attenuators, the cooling power of the dilution refrigerator could become insufficient. As a consequence, a subtle balance needs to be found by placing a series of attenuators at various temperatures, each attenuating as much as allowed by the cooling power of the stage of the dilution refrigerator at which it is attached.

Amplifying

The voltages one needs to measure in the experiments are so low that one needs to amplify them before having them processed in various measurement appliances. We performed differential voltage measurements using lossy twisted pairs connected to a room temperature low noise voltage amplifier NF LI75A ($1.2\ \mathrm{nV}/\sqrt{\mathrm{Hz}}$ in 1 MHz bandwidth). Besides, the twisted pairs, which can be seen as RC distributed filters, have the advantage of also filtering the noise.

9.2.2 Band selection

Various filters were used in our experiments. Among them:

- MiniCircuits LC filters [193]
- Powder filters [194]
- RC distributed micro-engineered filters [195]
- Coiled filters. Those are made of a long manganin wire covered with an insulating resist which are coiled inside a tight screw threading. The capacitance between the wire and the threading can be very big thus producing a nice RC filter.

For further details, the reader should refer to Ref. [193].

9.3 Technical schemes and pictures of the circuits

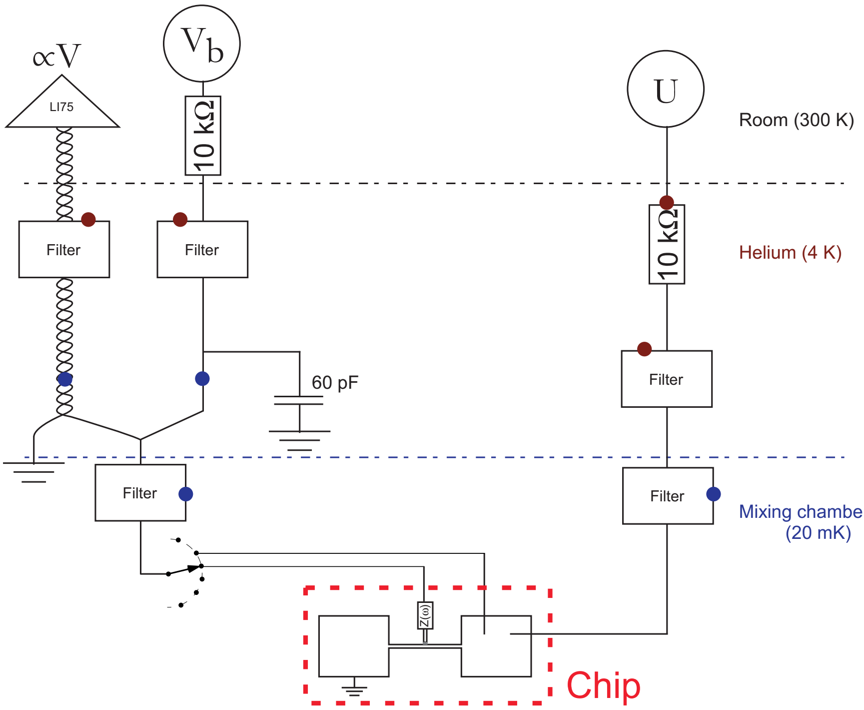

Fig. 9.3. Scheme of the wiring in the experiment on interactions between electrons for the sample called “implanted” (see chapters 2 and 3). The arrow represents a 12 port rotary switch which can be operated at low temperatures. All filters were either copper powder filters [194] or micro-engineered RC distributed ones [195]. Thick points mark points of thermal anchoring.

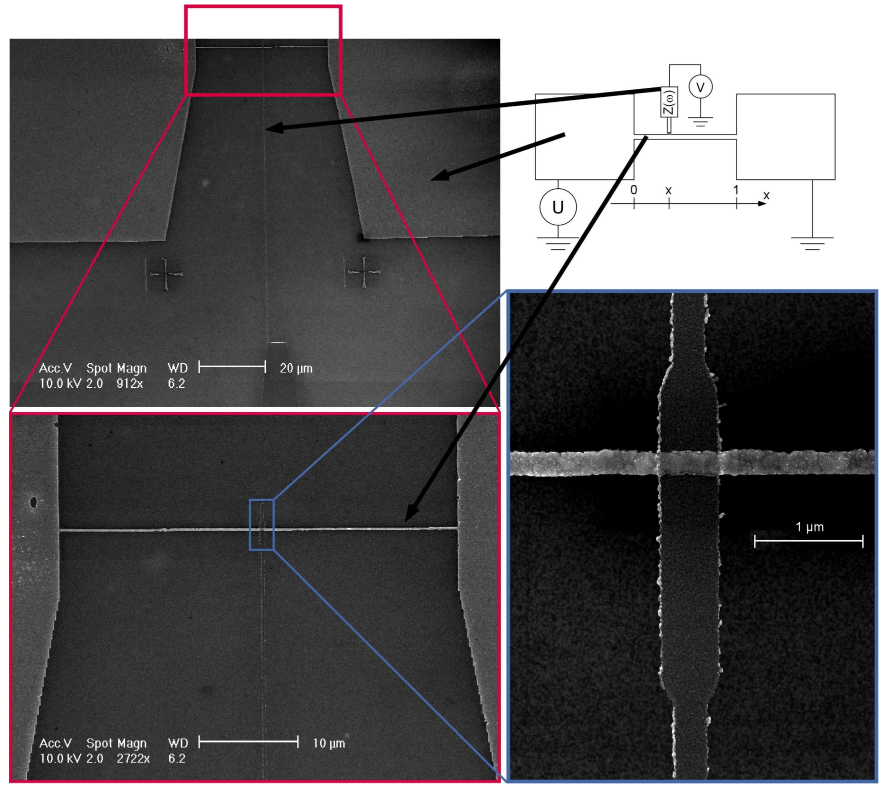

Fig. 9.4. Scanning Electron Microscope pictures of the *bare* wire and its environment. The scheme is the one of Fig. 3.4.

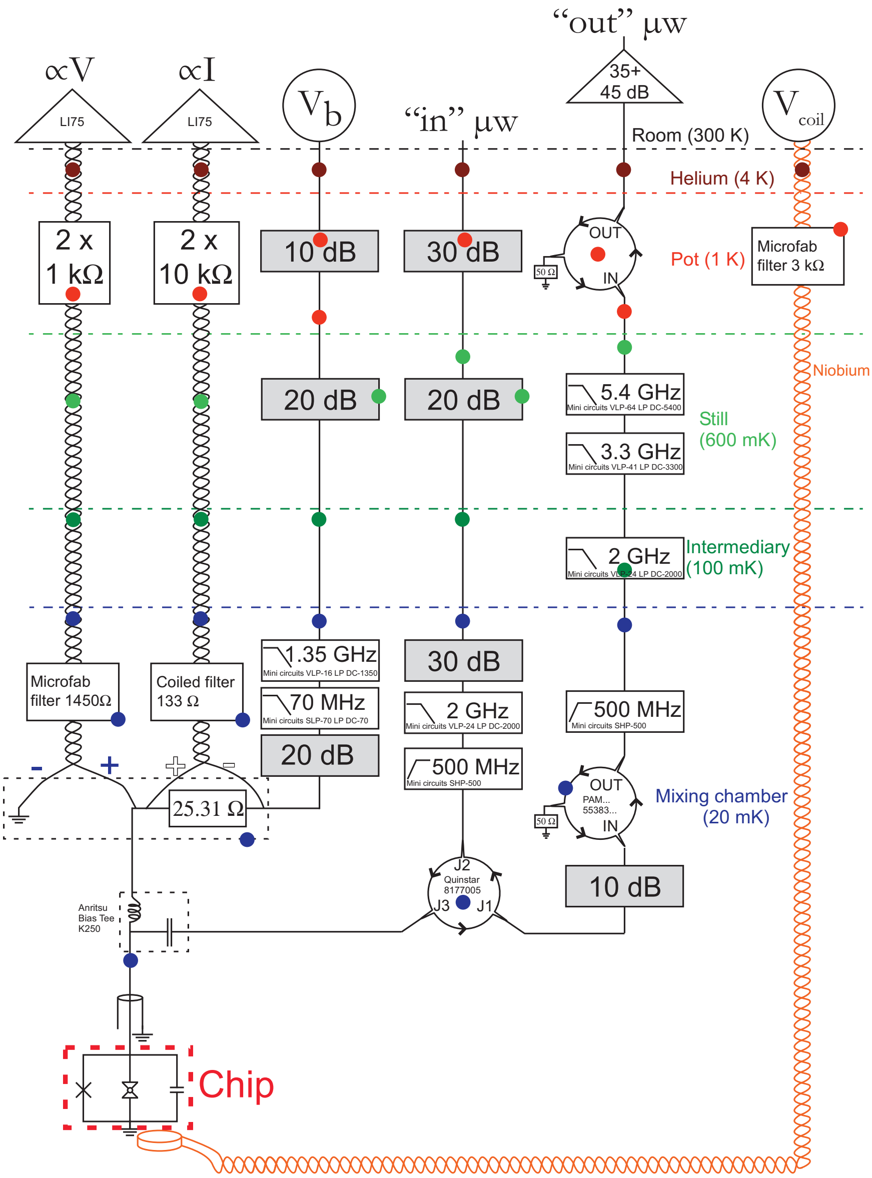

Fig. 9.5. Scheme of the wiring in the experiment on atomic contacts for the sample CP6 (see chapter 5). The three port circles are circulators. They break the time reversal symmetry in the propagation of the electrical signals so that a signal going in the opposite direction than the arrow is strongly attenuated.

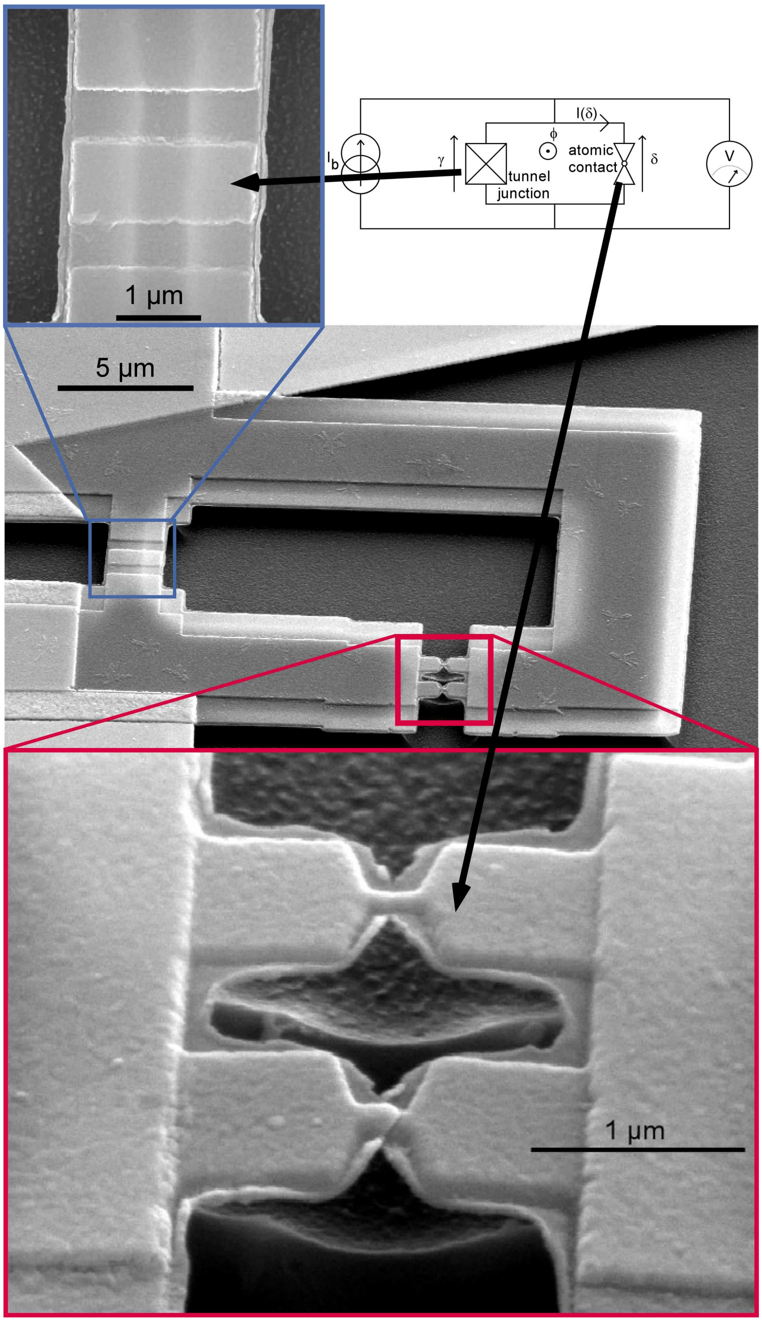

Fig. 9.6. Scanning Electron Microscope picture of the sample CP6. The sample was covered with a thin layer of gold in order to improve the contrast. The picture is taken at an angle of 45° so that one can distinguish that the polyimide layer has been etched underneath the bridges. The fact that two bridges are present instead of one is a result of the double-angle evaporation technique, and is of no importance as only one of them forms an atomic contact just before breakage.

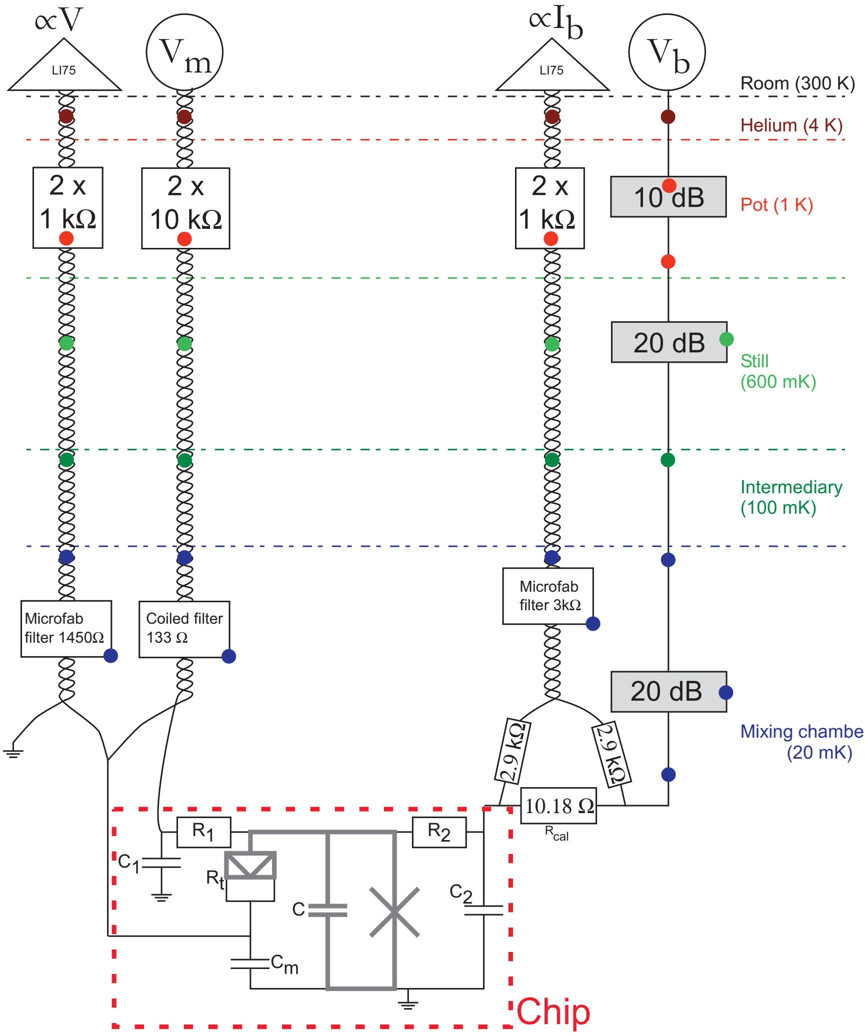

Fig. 9.7. Scheme of the wiring in the experiment on current fluctuations (see chapter 7).

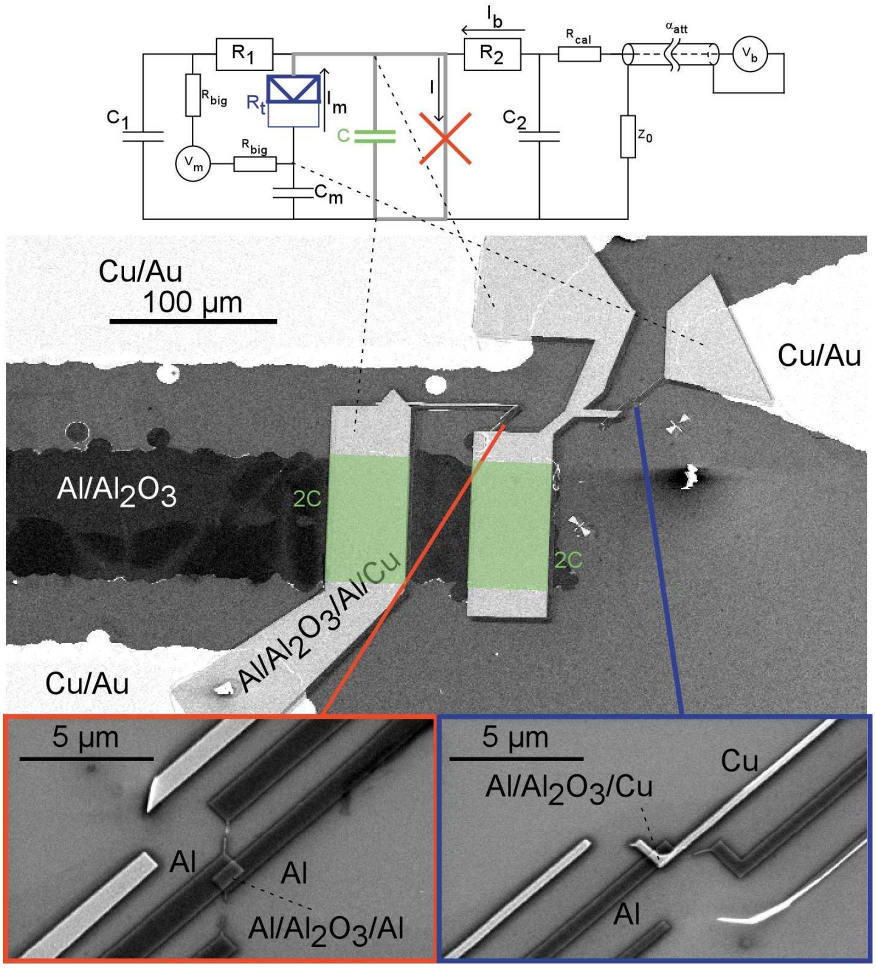

Fig. 9.8. Scanning Electron Microscope pictures of the sample used in the experiments discussed in chapter 7. The scheme is the one of Fig. 7.3.

9.4 Fabrication of each particular sample

9.4.1 Experiments of chapters 2 and 3

Here, we describe the fabrication procedure used for the *bare* and the *implanted* samples.

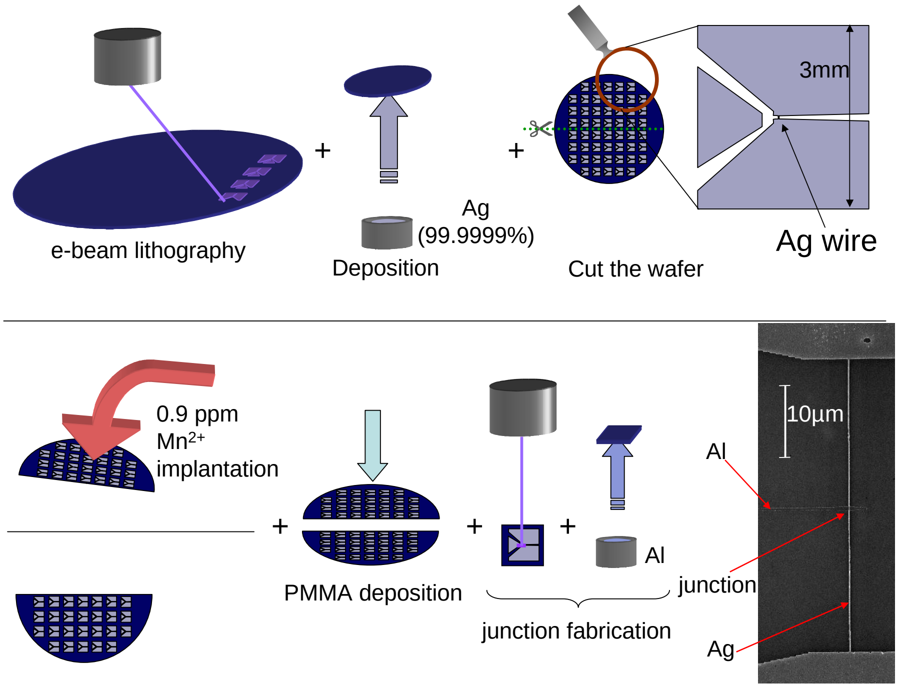

Fig. 9.9. Principle of the fabrication of the samples denoted as bare and implanted.

1. An oxidized silicon wafer is covered with UVIII resist and patterned by electronic lithography. A film of 45 nm of silver is then deposited on the developed surface using an electron gun evaporator with a 99.9999 % pure silver source. At the end of this step an array of diffusive wires and their pads is obtained.
2. The wafer is cut into two parts, containing the same amount of samples. One of the parts is implanted following the process described in section 8.4.2 with $c_{\mathrm{MI}} = 0.65$ ppm of Mn atoms.
3. Both parts are covered with a single layer of PMMA resist (spun at 5,000 rpm). Then the wafer is cut into individual samples containing only one silver wire each.

4. For each of the two samples used, a line crossing the wire at its middle position is then patterned by electronic lithography and the resist is developed. An ion milling is performed just before evaporating a flash of Al on the sample and oxidizing in order to fabricate a tunnel junction (see 8.3.2). This layer is then topped by 15.5 nm of Al.
5. Immediately after lift-off, the sample is mounted on its sample holder and cooled down.

9.4.2 Experiments of chapter 5

The sample CP6 were fabricated using the so-called Mechanically Controllable Break Junction (MCBJ) [45]. For details, please refer to Ref. [21].

1. A polished 0.3 mm-thick bronze wafer (about 1 μm roughness) is coated with a Polyimide layer, and annealed for 3 hours at 350°C in vacuum.
2. A PMMA layer is coated on top of a PMMA/MAA layer. Then an electronic lithography is performed to pattern the big connecting pads. A layer of 100 nm of Au on top of 1 nm of Ti is evaporated perpendicularly to the sample and the sample is lifted off..
3. A new PMMA layer is coated on top of a PMMA/MAA layer. Then an electronic lithography is performed to pattern the loop and the bridge shown on Fig. 9.6.
4. The sample is ion milled just before a layer of 70 nm of Al is evaporated with an angle $\theta_X = 20°$, oxidized to form a tunnel barrier and covered with a layer of 85 nm of Al with an angle of $\theta_X = -20°$.
5. After lift-off, the polyimide layer is dry-etched in a reactive ion etcher so as to suspend the breakable bridge.
6. The external pad of the sample is then scratched in order to contact the layer of bronze and the actual contact is performed using silver lake.

9.4.3 Experiments of chapters 7

The sample used in the experiment of chapter 7 was made using the following steps.

1. On a clear oxidized silicon wafer, a 25 nm-thin film of Al was patterned using optical lithography with the mask in the middle of Fig. 9.10. Then using the recipe described in 8.1.3, a thin alumina layer was formed on top of this film.
2. Still using optical lithography a bilayer of 54 nm of Cu topped by 10 nm of Au was patterned on top of the wafer with the left mask of Fig. 9.10.
3. Using a bilayer of LOR30B and PMMA, an electron-beam lithography was used to pattern the junctions and the counter electrodes of the capacitances whose dielectric is the alumina of the first step.

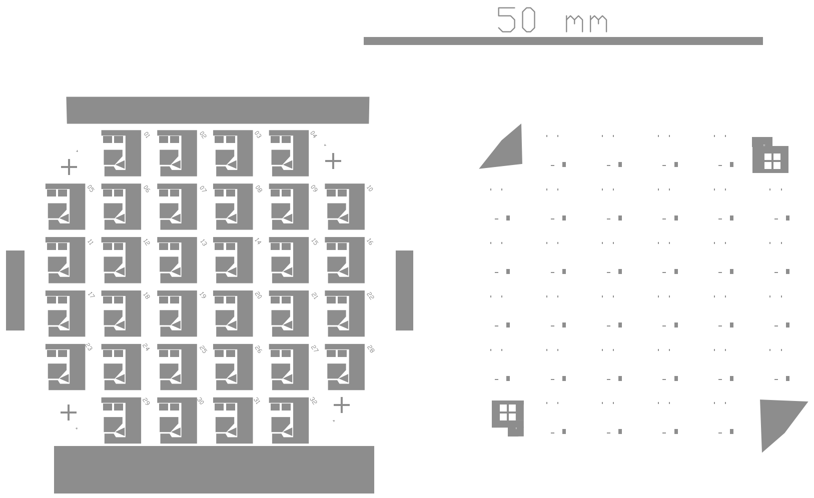

Fig. 9.10. Masks used for the optical lithography steps.

4. An ion milling was realized to clean the surface, then 40 nm of Al were evaporated at an angle $\theta_X = 0°$. After oxidizing the Al, a film of 60 nm was deposited at $\theta_X = -44°$, and after having rotated the sample by $\theta_Z = 90°$, a layer of 75 nm of Cu is evaporated at $\theta_X = 44°$.
5. Two SMC resistors are then surface mounted with conductive epoxy before cooling down the sample.

Appendix A

Fundamental constants and formula

A.1 Fundamental constants and material parameters

Constant name	Value
speed of light in vacuum	$c \approx 2.9979 \times 10^{8}$ m.s^{-1}
electron mass	$m_e \approx 9.109 \times 10^{-31}$ kg
reduced Planck constant	$\hbar = \frac{h}{2\pi} \approx 1.0546 \times 10^{-34}$ J.s
elementary charge	$e \approx 1.602 \times 10^{-19}$ C
Boltzmann constant	$k_B \approx 1.381 \times 10^{-23}$ J.K^{-1}
Avogadro number	$N_A \approx 6.022 \times 10^{23}$ mol^{-1}
electric constant	$\epsilon_0 \approx 8.854 \times 10^{-12}$ F.m^{-1}
magnetic constant	$\mu_0 = 4\pi \times 10^{-7}$ N.A^{-2}
Bohr magneton	$\mu_B \approx 9.274 \times 10^{-24}$ J.T^{-1}

Table A.1. Fundamental constants of nature [196]

Material	Z number	Configuration	Density (nm^{-3})	ν_F (J^{-1}m^{-3})	v_F (m.s^{-1})	E_F (eV)
silver (Ag)	47	[Kr]4d^{10}5s^{1}	59	1.03×10^{47}	1.39×10^{6}	5.6
copper (Cu)	29	[Ar]3d^{10}4s^{1}	147	1.56×10^{47}	1.57×10^{6}	7.0
gold (Au)	79	[Xe]4f^{14}5d^{10}6s^{1}	59	1.14×10^{47}	1.39×10^{6}	5.53
aluminum (Al)	13	[Ne]3s^{2}3p^{1}	60	2.15×10^{47}	2.03×10^{6}	11.7

Table A.2. Material parameters used in this paper [197, 198].

silver	copper
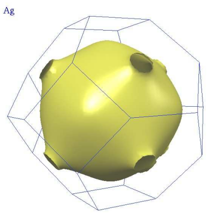	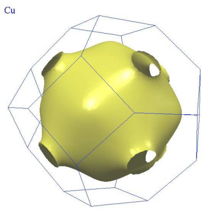
gold	aluminum
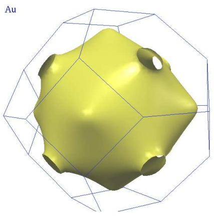	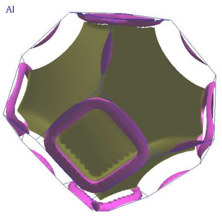

Table A.3. Fermi surfaces of some metals. [199].

A.2 Useful formula

A.2.1 Spin calculations

With the notations of section 2.1.4, we have

$$\langle T_0|(\sigma^{\circlearrowleft} + \sigma^{\circlearrowright})^2|T_0\rangle = 0 \tag{A.1}$$

$$\forall i \in \{1,2,3\}; \langle T_i|(\sigma^{\circlearrowleft} + \sigma^{\circlearrowright})^2|T_i\rangle = 8 \tag{A.2}$$

$$\sum_{s_t \in \pm} \sum_{i=1}^{3} \langle s_t| \otimes \langle s_0|T_i\rangle\langle T_i|s_0\rangle \otimes |s_t\rangle = \frac{3}{2} \tag{A.3}$$

$$\sum_{s_t \in \pm} \langle s_t| \otimes \langle s_0|T_0\rangle\langle T_0|s_0\rangle \otimes |s_t\rangle = -\frac{1}{2} \tag{A.4}$$

A.2.2 Fermi functions

If $f(x) = \left(1 + \mathrm{e}^{\beta x}\right)^{-1}$, then

$$\int_{-\infty}^{+\infty} f(x)(1 - f(x+y))\mathrm{d}x = \frac{y}{1 - \mathrm{e}^{-\beta y}} \tag{A.5}$$

$$\int_{-\infty}^{+\infty} f(x)(1 - f(x))\mathrm{d}x = 1/\beta \tag{A.6}$$

$$\int_{-\infty}^{+\infty} x^2 f(x)(1 - f(x))\mathrm{d}x = \frac{\pi^2}{3\beta^3} \tag{A.7}$$

Appendix B

Specific calculations

B.1 Heat equation

B.1.1 Electrons temperature in a hot wire

Knowing that $f_x(E)$ is a Fermi function $[1+\exp\left(\frac{E-eU(1-x)}{k_BT_{\text{eff}}(x)}\right)]^{-1}$,

$$\int \frac{\partial f_x(E)}{\partial x} E\mathrm{d}E = \int \frac{\partial f_x(E)}{\partial x}(E-eU[1-x])\mathrm{d}E + \int \frac{\partial f_x(E)}{\partial x} eU(1-x)\mathrm{d}E \tag{B.1}$$

Using now the fact that

$$\begin{aligned} \tfrac{\partial f_x(E)}{\partial x} &= [E-eU(1-x)]\tfrac{k_BT'_{\text{eff}}(x)}{(k_BT_{\text{eff}}(x))^2} f_x(E)[1-f_x(E)] \\ &\quad -\tfrac{eU}{k_BT_{\text{eff}}(x)} f_x(E)[1-f_x(E)] \end{aligned} \tag{B.2}$$

Then, for parity reasons, we have

$$\begin{aligned} \int \frac{\partial f_x(E)}{\partial x} E\mathrm{d}E = \int & \frac{k_BT'_{\text{eff}}(x)f_x(E)(1-f_x(E))}{k_B^2T_{\text{eff}}^2(x)}(E-eU(1-x))^2\mathrm{d}E \\ & -\int \frac{f_x(E)(1-f_x(E))}{k_BT_{\text{eff}}(x)}(eU)^2(1-x)\mathrm{d}E \end{aligned} \tag{B.3}$$

hence, using Eq. (A.6, A.7),

$$\int \frac{\partial f_x(E)}{\partial x} E\mathrm{d}E = \frac{\pi^2}{6} k_B^2 \frac{\mathrm{d}T_{\text{eff}}^2}{\mathrm{d}x} + \frac{(eU)^2}{2}\frac{\mathrm{d}(1-x)^2}{\mathrm{d}x} \tag{B.4}$$

B.1.2 Heating of the pads

The energy conservation states that the radial heat flow $\mathbf{j_T} = \kappa\nabla T$ verifies the heat equation:

$$\nabla.\mathbf{j_T} + \rho_T = 0 \tag{B.5}$$

with ρ_T the local incoming power density. If only the electron-phonon interaction was present [111, 36, 190],

$$\rho_T = -\Sigma(T^5 - T_{\mathrm{ph}}^5) \tag{B.6}$$

with T_{ph} the phonon temperature and $\Sigma = 24\zeta(5)\nu_F\kappa_{\mathrm{e-ph}}k_B^5 \approx 10^9$ W.m^{-3}K^{-5} is expressed here using the parameter $\kappa_{\mathrm{e-ph}}$ entering in Eq. (3.69). The Wiedemann-Franz law states that the thermal conductivity reads $\kappa = \sigma\mathcal{L}T$, with σ the electric conductivity and $\mathcal{L} = \frac{1}{3}\left(\frac{\pi k_B}{e}\right)^2 \approx 2.4 \times 10^{-8}$ V^2.K^{-2} the Lorentz number. Introducing the notation:

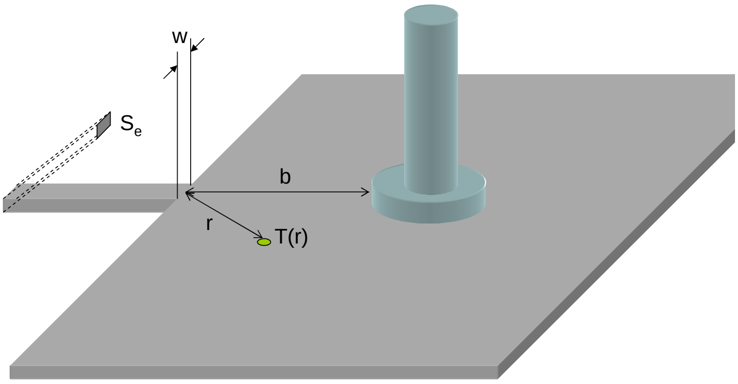

Fig. B.1.

$$v(r) = \left(\frac{k_B T(r)}{eU}\right)^2 \tag{B.7}$$

the heat equation reads, where r is in units of $w/2$,

$$\nabla.\nabla v(r) = \frac{\mathrm{d}}{r\mathrm{d}r}\left(r\frac{\mathrm{d}v(r)}{\mathrm{d}r}\right) = \frac{w^2}{2^2}\Sigma\left(\frac{e}{k_B}\right)^5\frac{U^3}{\sigma}\frac{6}{\pi^2}\left(v(r)^{5/2} - v_{\mathrm{ph}}^{5/2}\right) \tag{B.8}$$

where v_{ph} corresponds to the phonon temperature T_{ph} (base refrigerator temperature). In order to find the appropriate boundary conditions, we consider the heat flux on a circular ribbon, whose width is the thickness t of the pad and radius is r. We have:

$$\int \mathbf{j_T}.\mathrm{d}\boldsymbol{S} = \dot{Q} \tag{B.9}$$

Close to the wire, at $r = 1$, this flux is just half the power dissipated in the R resistive wire, hence the last equation reads

$$\pi \frac{w}{2} t\sigma \mathcal{L} T(r) \frac{\nabla T(r)}{w/2} = \int \mathbf{j_T}.\mathrm{d}\boldsymbol{S} = \dot{Q} = -\frac{U^2}{2R} \tag{B.10}$$

Hence,

$$\nabla v(r = 1) = -\frac{3\pi^3 w}{L} \tag{B.11}$$

Then, two cases might occur:

Non-superconducting bonding wire

Then, the temperature at bonding wire ($r = 2b/w$) is the phonon temperature. The boundary conditions then read

$$\nabla v(r = 1) = -\frac{3\pi^3 w}{L} \text{ and } v(r = 2b/w) = v_{\mathrm{ph}} \tag{B.12}$$

Superconducting bonding wire

Then, no "hot" quasiparticle can escape through the bonding wire (assuming $k_B T \ll \Delta$) and the derivative of T at the edges of the pads ($r \approx 6b/w$) is zero. The boundary conditions then read

$$\nabla v(r = 1) = -\frac{3\pi^3 w}{L} \text{ and } \nabla v(r = 6b/w) = 0 \tag{B.13}$$

B.2 Sensitivity of the Relax experiments

In section 3.4.7, it was claimed that the best fitting value of κ_{ee} was $\kappa_{ee} = 0.05$ ns^{-1}meV$^{-1/2}$ for the whole set of data shown on Fig. 3.29. In this section we show the results of the same calculation using $\kappa_{ee} = 0.02$ and 0.08 ns^{-1}meV$^{-1/2}$. Recall that using the theoretical expression (3.56), one gets $\kappa_{ee}^{\mathrm{AAK}} = 0.016$ ns^{-1}meV$^{-1/2}$. The bad agreement between theory and experiment on both figures B.2 and B.3 clearly demonstrate that there are more interactions than just $\kappa_{ee}^{\mathrm{AAK}}$, as was already claimed in section 3.4.3.

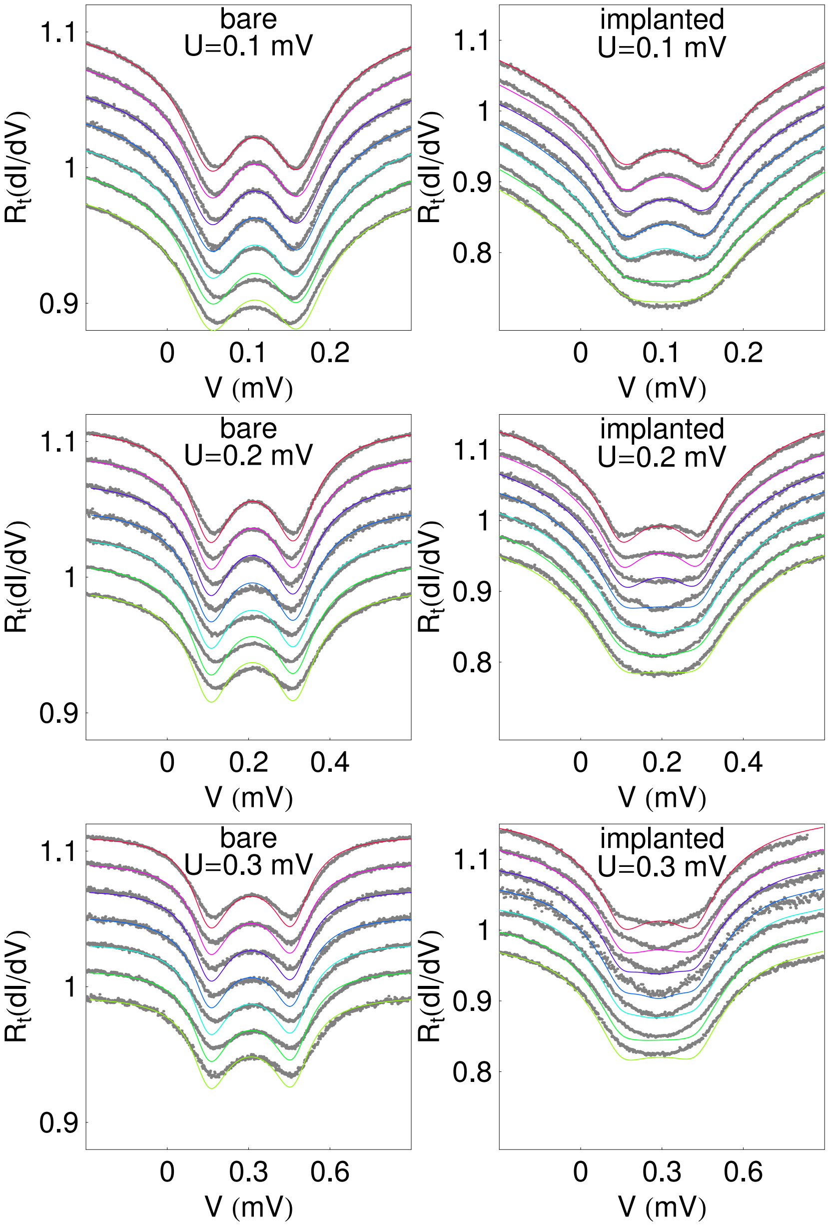

Fig. B.2. Same plot as Fig. 3.29 but for $\kappa_{ee} = 0.02$ ns^{-1}meV$^{-1/2}$.

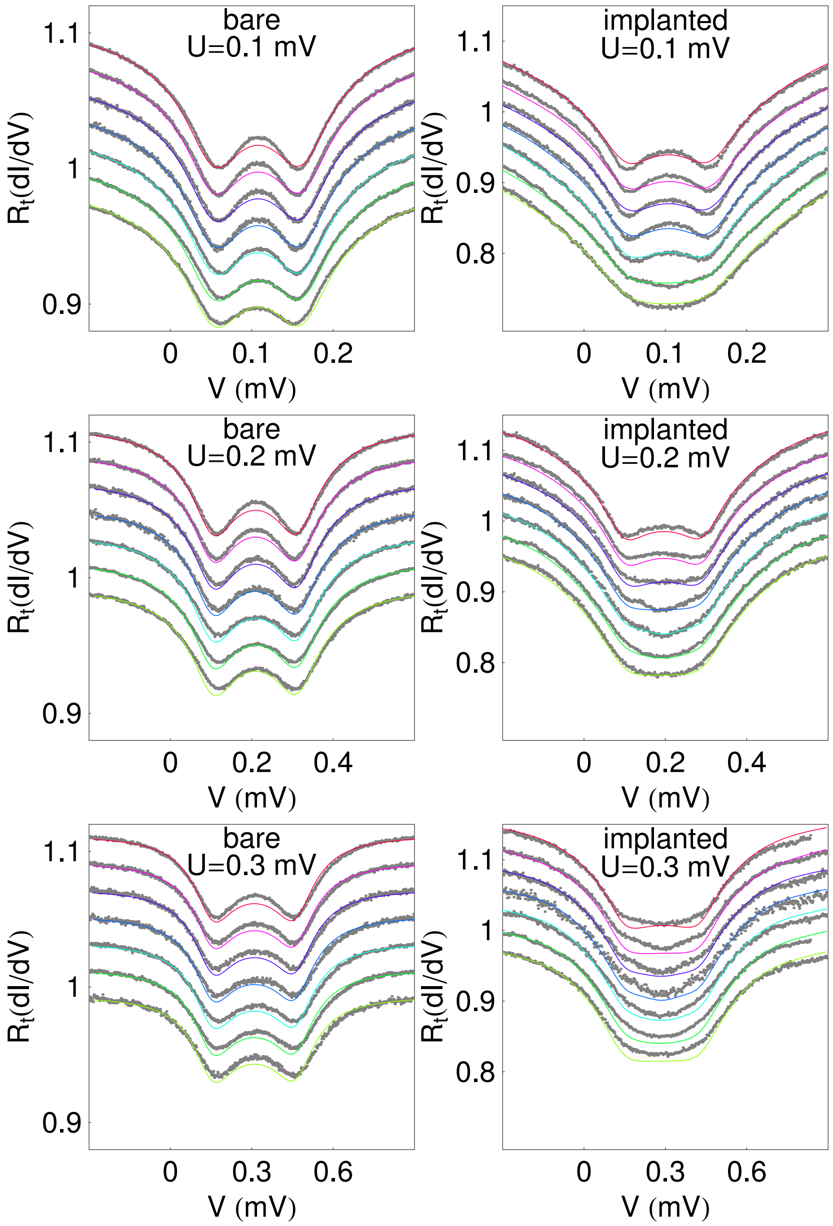

Fig. B.3. Same plot as Fig. 3.29 but for $\kappa_{ee} = 0.08\ \text{ns}^{-1}\text{meV}^{-1/2}$.

B.3 Diffusive conductor transmissions

Random matrix theory leads to the distribution of the transmissions in a diffusive conductor

$$P(\tau) \propto \frac{1}{\tau\sqrt{1-\tau}}$$

with a cutoff at low τ. To find the exact prefactor, one has to calculate the value of the conductance using this distribution and compare it to the Drude value. But first, let us find the link between the cutoff at small τ and the prefactor.

$$\begin{aligned} 1 &= \int_0^1 P(\tau)\mathrm{d}\tau \\ &= \int_{\tau_{\mathrm{cutoff}}}^1 \alpha \frac{\mathrm{d}\tau}{\tau\sqrt{1-\tau}} \\ &= \alpha \ln\left(\frac{(1+\sqrt{1-\tau_{\mathrm{cutoff}}})^2}{\tau_{\mathrm{cutoff}}}\right) \\ &\approx \alpha \ln\left(\frac{4}{\tau_{\mathrm{cutoff}}}\right) \end{aligned} \tag{B.14}$$

Hence,

$$\tau_{\mathrm{cutoff}} = 4\mathrm{e}^{-1/\alpha} \tag{B.15}$$

Therefore, the conductance reads

$$\begin{aligned} G &= M\frac{2e^2}{h}\int_0^1 P(\tau)\tau\mathrm{d}\tau \\ &= M\frac{2e^2}{h}\int_{4\mathrm{e}^{-1/\alpha}}^1 \alpha\frac{\mathrm{d}\tau}{\sqrt{1-\tau}} \\ &= M\frac{2e^2}{h}\alpha 2\sqrt{1-4\mathrm{e}^{-1/\alpha}} \\ &\approx M\frac{4e^2}{h}\alpha \end{aligned} \tag{B.16}$$

Besides, the number of transverse channels M is just the ratio between the occupied area in k space (πk_F^2) and the elementary space occupied by a state ($(2\pi)^2/S_e$) where S_e is the cross-section area of the wire. Thus, using

$$D = v_F l_e/3 \; ; \; \sigma = e^2 D\nu_F \; ; \; G = S_e\sigma/L \; ; \; v_F\nu_F = \frac{k_F^2}{\pi^2\hbar} \tag{B.17}$$

one gets

$$\alpha = \frac{2l_e}{3L}. \tag{B.18}$$

We thus recover Eq. (4.5).

B.4 Critical current through a short conductor

B.4.1 Single channel

In a single channel conductor of transmission τ, the maximal value of the current $I(\delta)$ is found for

$$\delta = \delta_{\max} = \arccos(-[1 - \sqrt{1-\tau}]^2/\tau)$$

and reads

$$I_{\max}(\tau) = I(\delta_{\max}) = \frac{e\Delta}{2\hbar}\sqrt{\frac{\tau^2 - (1-\sqrt{1-\tau})^4}{\sqrt{1-\tau}}} \tag{B.19}$$

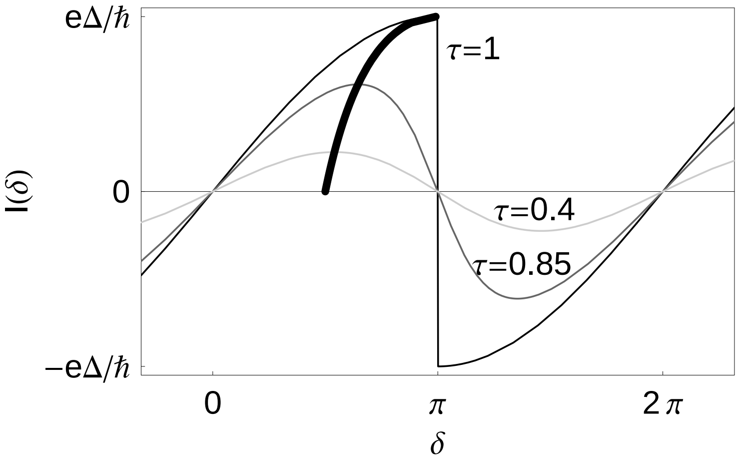

Fig. B.4. The thick line shows the position of the maximal current using Eq. (B.19).

B.4.2 Diffusive conductor

The maximum value of $I(\delta)$, obtained by Eq. (5.35), is nearly $I_{\max} \approx 2.08\frac{G\Delta}{e}$ which agrees with Ref. [200]. One shows [201] that the sample to sample fluctuations of the critical current $I_{\max}$ can be obtained using the Universal Conductance Fluctuation [202, 203]. And since the rms (root mean square) value of the conductance is [61]

$$\overline{G^2} - \overline{G}^2 = \frac{2\sqrt{2}}{\sqrt{15}}\frac{e\Delta}{h},$$

the fluctuations of the critical current reads

$$\overline{I^2_{\max}} - \overline{I_{\max}}^2 = \frac{4\pi\sqrt{2}}{3\sqrt{15}}\frac{e\Delta}{h}. \tag{B.20}$$

In a recent work, the length dependence of $I_{\max}$ was calculated [204]. The maximal current $I_{\max}$ is predicted to decay very rapidly with the ratio of the length of the constriction to the superconducting coherence length ξ.

B.5 Switching current at first order

This section is a proof of the first order relation between the switching current of the SQUID and the current-phase relation of the atomic contact.

Starting from Eq. (5.55),

$$U^{(-)}(\gamma) = -\varphi_0 I_0 \cos(\gamma) - \varphi_0 I_b \gamma - |\Delta| \sum_i \sqrt{1 - \tau_i \sin^2\left(\frac{\gamma+\phi}{2}\right)} \tag{B.21}$$

The switching rate is given by the classical expression (5.43)

$$\mathit{\Gamma}(I_b) = \frac{\omega_p^{(-)}(I_b)}{2\pi} \mathrm{e}^{-\Delta U^{(-)}(I_b)/k_B T} \tag{B.22}$$

where the barrier height can be obtained from the potential $U^{(-)}(\gamma)$ and the plasma frequency is given by $\omega_p^{(-)}(I_b) = 1/\sqrt{L^{(-)}(I_b)C}$, where $L^{(-)}(I_b)$ is the effective Josephson inductance

$$L^{(-)}(I_b) = \varphi_0^2 \left(\left.\frac{\partial^2 U^{(-)}(\gamma)}{\partial \gamma^2}\right|_{\gamma=\gamma_{\min}} \right)^{-1} . \tag{B.23}$$

The phase $\gamma_{\min}$ ($\gamma_{\max}$ respectively) is the phase at which the potential well is locally minimal (maximal, see Fig. 5.9). The larger the switching rate, the smaller the barrier height $\Delta U^{(-)} = U^{(-)}(\gamma_{\max}) - U^{(-)}(\gamma_{\min})$. As the barrier height goes to zero, the phase difference $\delta\gamma = \gamma_{\max} - \gamma_{\min}$ goes to zero. Therefore for large enough values of I_b, the barrier height entering in the switching rate reads

$$\begin{aligned} \Delta U^{(-)} &\approx \frac{\partial U}{\partial \gamma}(\gamma_0)\delta\gamma + \sum_i \frac{\partial E_{|\tau_i -\rangle}}{\partial \delta}(\delta = \gamma_0 + \varphi)\delta\gamma \\ \frac{\Delta U^{(-)}}{\varphi_0 \delta\gamma} &\approx I_0 \sin(\gamma_0) - I_b + \sum_i I_{|\tau_i -\rangle}(\gamma_0 + \varphi) \end{aligned} \tag{B.24}$$

where $\gamma_0 = (\gamma_{\max} + \gamma_{\min})/2$. In the experiment, we measure the bias current $I_b^{\mathit{\Gamma}_{\exp}}(\varphi)$ for which the switching rate is a constant $\mathit{\Gamma}_{\exp}$ when varying the flux. Given the exponential dependence of the rate on the barrier height, we can make the good approximation that a constant rate means a constant barrier height. Now, if the contribution of the atomic contact to the potential $U^{(-)}$ is negligible[1], the phase difference $\delta\gamma$ is nearly identical to the one corresponding to the tunnel junction alone. Therefore, if $\Delta U^{(-)}$ remains constant, $\delta\gamma$ also does, and therefore at constant switching rate,

---

[1] For a few channels, the contribution of the Andreev energy term to the total potential $U^{(-)}$ can be treated pertubatively if $|\Delta| \lesssim \varphi_0 I_0$. Using Eq. (5.32), this condition is equivalent to $R_N \lesssim R_K/8$, where R_N is the resistance of the Josephson junction in the normal state.

$$I_0 \sin(\gamma_0) - I_b^{\Gamma_{\mathrm{exp}}} + \sum_i I_{|\tau_i -\rangle}(\gamma_0 + \varphi) = \mathrm{cste}'. \tag{B.25}$$

Hence, the bias current at constant switching rate reads

$$I_b^{\Gamma_{\mathrm{exp}}}(\varphi) = \mathrm{cste} + \sum_i I_{|\tau_i -\rangle}(\gamma_0 + \varphi). \tag{B.26}$$

Therefore, measuring the SQUID switching current $I_b^{\Gamma_{\mathrm{exp}}}(\varphi)$ is a good measurement of the current-phase relation of the atomic contact (at least for large rates Γ_{exp}).

B.6 Reflectometry transition

Starting from Eqs. (5.84, 5.85), one can write

$$Z = \frac{iL_{\|}\omega - rL_{\|}C\omega^2}{1 - L_{\|}C\omega^2 + irC\omega} \tag{B.27}$$

then

$$Z \pm Z_0 = \frac{iL_{\|}\omega - rL_{\|}C\omega^2 \pm Z_0 \mp L_{\|}CZ_0\omega^2 \pm irZ_0C\omega}{\mathrm{denom.}} \tag{B.28}$$

hence,

$$\mathcal{R} = \frac{L_{\|}C\omega^2(Z_0 - r) - Z_0 + i\omega(L_{\|} - rZ_0C)}{-L_{\|}C\omega^2(Z_0 + r) + Z_0 + i\omega(L_{\|} + rZ_0C)}. \tag{B.29}$$

Taking the modulus squared of this expression,

$$|\mathcal{R}|^2 = \frac{[L_{\|}C\omega^2(Z_0 - r) - Z_0]^2 + \omega^2(L_{\|} - rZ_0C)^2}{[L_{\|}C\omega^2(Z_0 + r) - Z_0]^2 + \omega^2(L_{\|} + rZ_0C)^2}. \tag{B.30}$$

Taking the derivative with respect to ω^2:

$$\frac{\mathrm{d}|\mathcal{R}|^2}{\mathrm{d}\omega^2} = \frac{\omega^2(\omega^2 - [L_{\|}C - L_{\|}^2/(\sqrt{2}Z_0)^2 - r^2C^2/2]^{-1})}{\mathrm{denom.}} \tag{B.31}$$

The minimum of $|\mathcal{R}|$ is obtained for

$$\omega = \frac{1}{\sqrt{L_{\|}C}} \left(\sqrt{1 - \frac{L_{\|}}{2CZ_0^2} - \frac{r^2C}{2L_{\|}}} \right)^{-1} \tag{B.32}$$

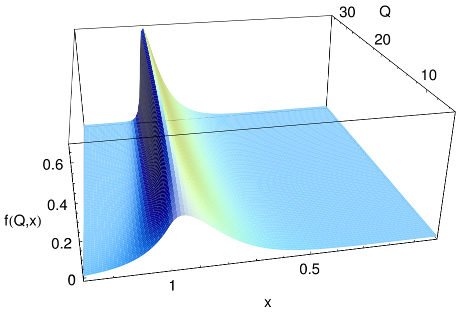

Fig. B.5. Function $f(x,Q)$.

B.7 Resonant activation

B.7.1 Function f(Q,x)

In this section, we report the resonant activation formula from Ref. [187] useful for our experiment.

$$f(x,Q) \approx \begin{cases} 8Q(81-4Q^2)^{-2}[(5.5-Q)(4.5+Q)^2 \mathrm{e}^{2Q(x-1)} & \\ +0.01Q\mathrm{e}^{9x}(x[1-0.049Q^2]+0.074Q^2-1.72)] & \text{if } x \leq 1 \\ & \\ \mathrm{e}^{-2Q(x-1)}Q(11+2Q)(9+2Q)^{-2} & \text{if } x > 1 \end{cases} \tag{B.33}$$

B.8 Amplitude of the micro-wave current as a function of the power

The RF source is connected to the bias line at room temperature. Therefore, the RF signal goes through a series of attenuators before actually getting to the circuit which can be schemed as Fig. B.6. The link between current and voltage representations is

$$I_{\mathrm{RF}} = \frac{V_{\mathrm{RF}}}{Z_0 + R_b} \; ; \; R_{\mathrm{eq}} = \frac{(Z_0 + R_b)R_d}{Z_0 + R_b + R_d}. \tag{B.34}$$

As the impedance seen from the source is that of the attenuators ($Z_0 = 50\ \Omega$), the voltage $V_{\mathrm{RF}}^{(source)}$ delivered by the source on the first attenuator is given by

$$V_{\mathrm{RF}}^{(source)} = \sqrt{Z_0 10^{P_{\mathrm{RF}}/10} \times 1\mathrm{mW}} \tag{B.35}$$

where P_{RF} is expressed in dBm. The voltage V_{RF} delivered on our circuit by the last attenuator is given by

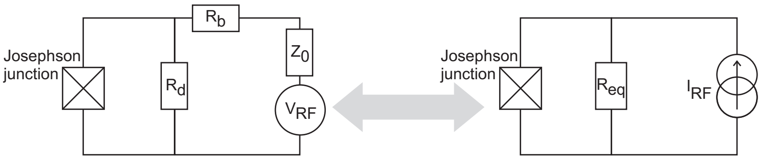

Fig. B.6. Thevenin-Norton transformation.

$$V_{\mathrm{RF}} = V_{\mathrm{RF}}^{(source)} \frac{2 \times 10^{\alpha_{\mathrm{att}}/20}}{|1 + Z_0/Z|} \tag{B.36}$$

where α_{att} is the total attenuation in dB on $Z_0 = 50\ \Omega$, and Z is the impedance to the ground seen by the last attenuator:

$$Z = R_b + \left(\frac{1}{R_d} + \frac{1}{jL_{\mathrm{JJ}}\Omega_{\mathrm{RF}}} + jC\Omega_{\mathrm{RF}}\right)^{-1} \tag{B.37}$$

where $L_{\mathrm{JJ}} = (1 - s^2)^{-1/2}\varphi_0/I_0$ is the Josephson inductance. Eventually,

$$I_{\mathrm{RF}}^2 = \frac{Z_0 10^{P_{\mathrm{RF}}/10} \times 1\mathrm{mW}}{(Z_0 + R_b)^2} \frac{4 \times 10^{\alpha_{\mathrm{att}}/10}}{|1 + Z_0/Z|^2} \tag{B.38}$$

Then, to get the RF current, one just has to plug in the measured parameters of the experiment: $R_b \approx 0.212$ kΩ, $R_d \approx 0.20$ kΩ and $I_0 = 0.49\ \mu$A.

B.9 Full Counting Statistics for a coherent metallic wire

B.9.1 Normal leads (N-wire-N)

We consider a normal metal diffusive wire of length L connected to normal leads at both ends. The notations are those of chapter 2. If the counting time t is bigger than the diffusion time $\tau_D = L^2/D$, one can use Eq. (6.30) to get the generating function of the diffusive wire at any temperature. We will make use of the formula

$$\int_0^1 \mathrm{d}\tau \frac{1}{\tau\sqrt{1-\tau}} \ln(1 + \tau x) = 2\mathrm{asinh}^2(\sqrt{x}) = \frac{1}{2}\mathrm{acosh}^2(2x + 1) \tag{B.39}$$

Thus, one finds

$$\begin{aligned}\mathcal{F}_c^{\mathrm{NN}}(\xi, t) = \frac{tR_K}{4hR} \int_{-\infty}^{+\infty} \mathrm{d}E\mathrm{acosh}^2 \big[&2f_T(E)(1 - f_T(E + eV))(\mathrm{e}^{-i\xi} - 1)+ \\ &2f_T(E + eV)(1 - f_T(E))(\mathrm{e}^{i\xi} - 1) + 1\big]\end{aligned} \tag{B.40}$$

where $f_T(E)$ is the Fermi function at temperature T: $f_T(E) = (1+\mathrm{e}^{E/k_BT})^{-1}$

Zero temperature, N-wire-N

In case $T = 0$, $f_0 = 1 - \theta$ with $\theta(E)$ the Heavyside function. Hence, if $E > |eV|$, the term inside the integral is zero and

$$\mathcal{F}_c^{\mathrm{NN}}(\xi,t) = \frac{tR_K e|V|}{4hR}\mathrm{acosh}^2(2\mathrm{e}^{-i\mathrm{sgn}(V)\xi} - 1) = \frac{|\langle \hat{N}(t)\rangle|}{4}\mathrm{acosh}^2(2\mathrm{e}^{-i\mathrm{sgn}(V)\xi} - 1) \tag{B.41}$$

Now, we can calculate the cumulants of $\hat{N}$ in this non interacting, low temperature, long counting times limit by the same method used for tunnel junctions.

$$\mathcal{F}_c^{\mathrm{NN}}(\xi,t) = \underset{\substack{\downarrow \\ |\langle\langle \hat{N}(t)\rangle\rangle|}}{|\langle \hat{N}(t)\rangle|}\ \xi/i + \underset{\substack{\downarrow \\ |\langle\langle \hat{N}^2(t)\rangle\rangle|}}{\tfrac{1}{3}|\langle \hat{N}(t)\rangle|}\ \tfrac{(\xi/i)^2}{2!} + \underset{\substack{\downarrow \\ |\langle\langle \hat{N}^3(t)\rangle\rangle|}}{\tfrac{1}{15}|\langle \hat{N}(t)\rangle|}\ \tfrac{(\xi/i)^3}{3!} + O(\xi^4) \tag{B.42}$$

B.9.2 One superconducting lead (N-wire-S)

Now, we consider the same normal diffusive wire with a superconducting metal in perfect contact at one end. In such a case, one has to solve the Usadel equation to take into account proximity effect in the wire. The techniques engineered by Nazarov to calculate the generating function are particularly convenient to directly use the solution of the Usadel equation. The drawback of this method is that it can only calculate the generating function at long times.

The result of the calculation is exactly the same as in the normal lead case when one replaces everywhere ξ by 2ξ (because 2 charges are transferred instead of one) and τ by $\rho = \frac{\tau^2}{(2-\tau)^2}$ (probability of Andreev reflexion). Besides, one can easily check that

$$\frac{1}{2\tau\sqrt{1-\tau}}\mathrm{d}\tau = \frac{1}{4\rho\sqrt{1-\rho}}\mathrm{d}\rho$$

hence, the generating function in the SN case is related to the one in the NN case by

$$\mathcal{F}_c^{\mathrm{NS}}(\xi,t) = \frac{1}{2}\mathcal{F}_c^{\mathrm{NN}}(2\xi,t) \tag{B.43}$$

Zero temperature, N-wire-S

At $T = 0$,

$$\mathcal{F}_c^{\mathrm{NS}}(\xi,t) = \frac{|\langle \hat{N}(t)\rangle|}{6}\mathrm{acosh}^2(2\mathrm{e}^{-2i\mathrm{sgn}(V)\xi} - 1) = \frac{|\langle \hat{N}(t)\rangle|}{2}\mathrm{acosh}^2(\mathrm{e}^{-i\mathrm{sgn}(V)\xi}) \tag{B.44}$$

And the cumulants are

$$\mathcal{F}_c^{\mathrm{NS}}(\xi,t) = \underset{\substack{\downarrow \\ |\langle\langle\hat{N}(t)\rangle\rangle|}}{|\langle\hat{N}(t)\rangle|} \; \xi/i + \underset{\substack{\downarrow \\ |\langle\langle\hat{N}^2(t)\rangle\rangle|}}{\tfrac{2}{3}|\langle\hat{N}(t)\rangle|} \; \frac{(\xi/i)^2}{2!} + \underset{\substack{\downarrow \\ |\langle\langle\hat{N}^3(t)\rangle\rangle|}}{\tfrac{4}{15}|\langle\hat{N}(t)\rangle|} \; \frac{(\xi/i)^3}{3!} + O(\xi^4) \tag{B.45}$$

Appendix C

Experimental stuff

C.1 Electrical properties of the discrete elements in the counting experiment

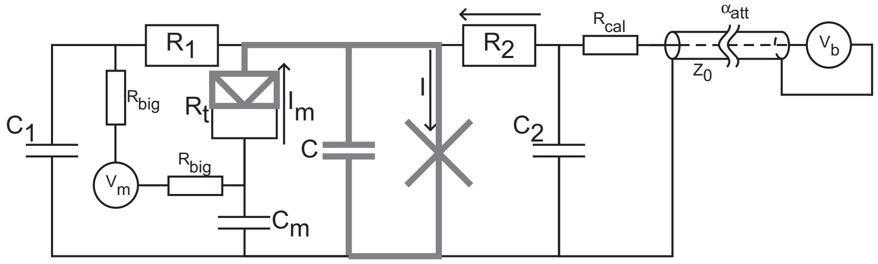

Fig. C.1. Scheme of the electromagnetic environment of the Josephson junction. Apart from the tiny drawings and letters, all the circuit is made on the silicon chip. Besides, all the gray parts are made of aluminum, which is superconducting at the temperatures of the experiment. The transmission line on the right has a characteristic impedance $Z_0 = 50\ \Omega$ and is interrupted by attenuators whose total attenuation is denoted by α_{att}.

The four capacitors represented on Fig. 7.3 are made using alumina as a dielectric (see 8.1.3). Three of them could be measured at room temperature before fabricating the remaining of the circuit:

$$C_m \approx 0.85\ \mathrm{nF}\ ;\ C_1 \approx 0.13\ \mathrm{nF}\ ;\ C_2 \approx 0.13\ \mathrm{nF}. \qquad \text{(C.1)}$$

When the refrigerator was running at its base temperature (20 mK), the resistances R_2, R_{cal} and R_{big} could be measured by a standard four probe measurement which gave

$$R_2 \approx 202.1\ \Omega\ ;\ R_{\mathrm{cal}} \approx 10.18\ \Omega\ ;\ R_{\mathrm{big}} \approx 10573\ \Omega. \tag{C.2}$$

Moreover, the resistors R_1 and R_2 are nominally exactly identical. They are Surface Mounted Components (SMC) made by Vishay (series number P 0603 Y 2000 DB). They consist of thin films of Cu/Ni enclosed in a cage with two connectors made in SnPb. Finally, the attenuation of the transmission line could be measured at low frequency (330 Hz).

$$\alpha_{\mathrm{att}} \approx 50.0\ \mathrm{dB}. \tag{C.3}$$

C.2 Plasma frequency of a Josephson junction as a function of s

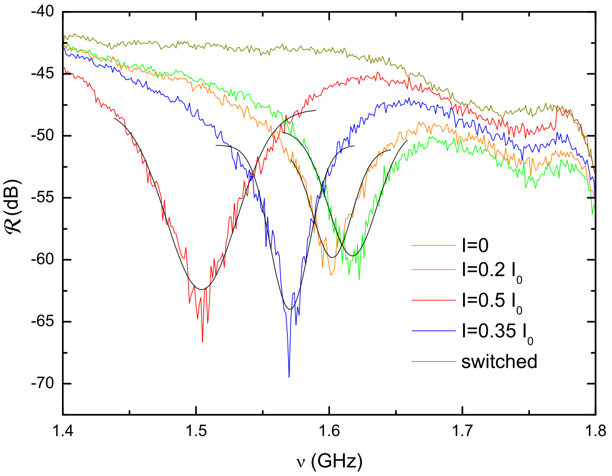

Fig. C.2. Colored lines (color online): reflection coefficient $|\mathcal{R}|$ as a function of the frequency ν (see section 5.3.1 for measurement details) for various values of the current I in the Josephson junction alone. Black lines: Lorentzian fit of the dips in order to determine the minimal frequency for each value of the current.

Using the measurements of Fig. C.2 and others, one may determine the plasma frequency of the Josephson junction alone as a function of s. The results are reported on Fig. C.3

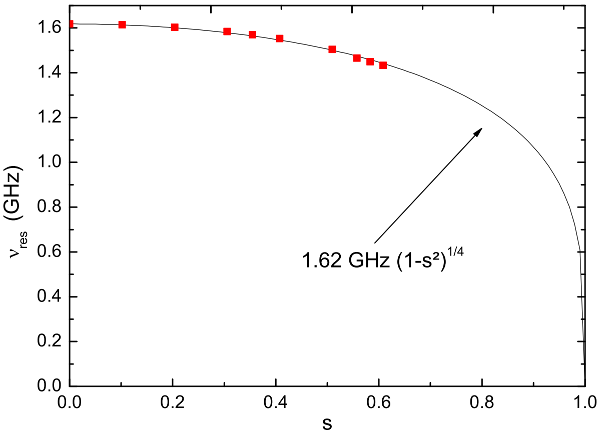

Fig. C.3. Dots: minimum of the reflection curves of Fig. C.2 as a function of $s = I/I_0$. Line: best fit using Eq. (5.46). The plasma frequency is thus 1.62 GHz, as reported on Table. 5.1.

C.3 Small field effect on the conductance of an NIS junction

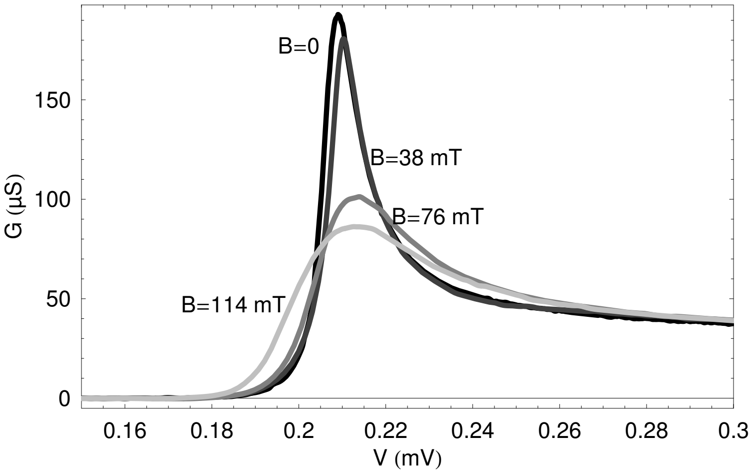

Fig. C.4. Lines: measured differential conductance of a tunnel junction located at position $x = 1/2$ of the *implanted* wire at a bias voltage $U = 0$ for various magnetic field B.

Appendix D

Translation between the notations of this work and previous ones

Sample in this work	Sample in the notebook
CP1	MAS5
CP2	MAS11
CP3	MAS4re
CP4	MAS17
CP5	MAS22
CP6	MAS26
CP7	JonctionTest
bare	DB38
implanted	DB4le retour

References

1. B. Altshuler and A. Aronov, *Electron-Electron Interaction in Disordered Conductors* (Elsevier, Amsterdam, 1985), p. 1.
2. B. Altshuler, A. Aronov, and D. Khmelnitsky, J. Phys. C **15**, 7367 (1982).
3. R. Landauer, IBM J. Res. Dev. **1**, 223 (1957).
4. R. Landauer, Philos. Mag. **21**, 863 (1970).
5. B. J. van Wees *et al.*, Physical Review Letters **60**, 848 (1988).
6. D. A. Wharam *et al.*, Journal of Physics C: Solid State Physics **21**, L209 (1988).
7. M. Reznikov, M. Heiblum, H. Shtrikman, and D. Mahalu, Physical Review Letters **75**, 3340 (1995).
8. A. Kumar, L. Saminadayar, D. C. Glattli, Y. Jin, and B. Etienne, Physical Review Letters **76**, 2778 (1996).
9. K. Nagaev, Phys. Lett. A **169**, 103 (1992).
10. Y. Naveh and D. V. Averin, Physical Review Letters **82**, 4090 (1999).
11. J. C. Cuevas, A. Martín-Rodero, and A. L. Yeyati, Physical Review Letters **82**, 4086 (1999).
12. A. H. Steinbach, J. M. Martinis, and M. H. Devoret, Physical Review Letters **76**, 3806 (1996).
13. M. Henny, S. Oberholzer, C. Strunk, and C. Schonenberger, Physical Review B (Condensed Matter and Materials Physics) **59**, 2871 (1999).
14. R. Cron, M. F. Goffman, D. Esteve, and C. Urbina, Physical Review Letters **86**, 4104 (2001).
15. B. Josephson, Phys. Lett. **1**, 251 (1962).
16. P. W. Anderson and J. M. Rowell, Physical Review Letters **10**, 230 (1963).
17. E. Bratus', V. Shumeiko, and G. Wendin, Physical Review Letters **74**, 2110 (1995).
18. D. Averin and A. Bardas, Physical Review Letters **75**, 1831 (1995).
19. M. Hurd, S. Datta, and P. Bagwell, Physical Review B (Condensed Matter and Materials Physics) **54**, 6557 (1996).
20. J. Cuevas, A. Martin-Rodero, and A. Levy Yeyati, Physical Review B (Condensed Matter and Materials Physics) **54**, 7366 (1996).
21. M. Chauvin, *The Josephson effect in superconducting atomic contacts (available on the website* `tel.ccsd.cnrs.fr`*)*, PhD thesis, Université Paris 6, 2005.
22. L. Levitov and G. Lesovik, JETP Lett. **58**, 230 (1993).

23. B. Reulet, J. Senzier, and D. Prober, Physical Review Letters **91**, 196601 (2003).
24. Y. Bomze, G. Gershon, D. Shovkun, L. S. Levitov, and M. Reznikov, Physical Review Letters **95**, 176601 (2005).
25. S. Gustavsson *et al.*, Physical Review Letters **96**, 076605 (2006).
26. T. Fujisawa, T. Hayashi, R. Tomita, and Y. Hirayama, Science **312**, 1634 (2006).
27. J. Tobiska and Y. V. Nazarov, Physical Review Letters **93**, 106801 (2004).
28. D. Pines and P. Nozières, *The Theory of Quantum Liquids* (Perseus Books, Cambridge, Massachusetts, 1966).
29. N. Ashcroft and D. Mermin, *Solid State Physics* (Sauders College, Philadelphia, 1976).
30. A. F. Ioffe and A. R. Regel, Prog. Semicond. **4**, 237 (1960).
31. E. Wigner, Phys. Rev. **46**, 1002 (1934).
32. S. Wind, M. Rooks, V. Chandrasekhar, and D. Prober, Physical Review Letters **57**, 633 (1986).
33. P. Mohanty, E. Jariwala, and R. Webb, Physical Review Letters **78**, 3366 (1997).
34. H. Pothier, S. Guéron, N. O. Birge, D. Esteve, and M. H. Devoret, Physical Review Letters **79**, 3490 (1997).
35. F. Pierre, H. Pothier, D. Esteve, and M. H. Devoret, J. Low Temp. Phys. **118**, 437 (2000).
36. F. Pierre, Ann. Phys. (Paris) **26**, No. 4 (2001).
37. A. Kaminski and L. Glazman, Physical Review Letters **86**, 2400 (2001).
38. J. Kondo, Prog. Theor. Phys. **32**, 37 (1964).
39. G. Göppert, Y. Galperin, B. Altshuler, and H. Grabert, Physical Review B (Condensed Matter and Materials Physics) **66**, 195328 (2002).
40. A. Anthore, F. Pierre, H. Pothier, and D. Esteve, Physical Review Letters **90**, 076806 (2003).
41. A. Anthore, *Decoherence mechanisms in mesoscopic conductors (available on the website* `tel.ccsd.cnrs.fr`*)*, PhD thesis, Université Paris 6, 2003.
42. R. P. Peters, G. Bergmann, and R. M. Mueller, Phys. Rev. Lett. **58**, 1964 (1987).
43. F. Pierre *et al.*, Physical Review B (Condensed Matter and Materials Physics) **68**, 085413 (2003).
44. S. Shapiro, Physical Review Letters **11**, 80 (1963).
45. J. van Ruitenbeek *et al.*, Rev. Sci. Instrum. **67**, 108 (1996).
46. N. Agrait, A. Levy Yeyati, and J. van Ruitenbeek, Phys. Rep. **377**, 81 (2003).
47. E. Scheer, P. Joyez, D. Esteve, C. Urbina, and M. Devoret, Physical Review Letters **78**, 3535 (1997).
48. R. Cron, *Atomic Contacts: a Test-Bed for Mesoscopic Physics (available on the website* `tel.ccsd.cnrs.fr`*)*, PhD thesis, Université Paris 6, 2001.
49. M. F. Goffman *et al.*, Physical Review Letters **85**, 170 (2000).
50. M. Chauvin *et al.*, Physical Review Letters **97**, 067006 (2006).
51. F. Hekking, G. Schön, and D. Averin, Mesoscopic superconductivity, in *Proceedings of the NATO Advanced Reseach Workshop on Mesoscopic Superconductivity*, 1994.
52. Y. M. Blanter and M. Buttiker, Phys. Rep. **336**, 1 (2000).
53. J. Cuevas and W. Belzig, Physical Review Letters **91**, 187001 (2003).

54. W. Belzig and Y. V. Nazarov, Physical Review Letters **87**, 197006 (2001).
55. K. Nagaev, Physical Review Letters **86**, 3112 (2000).
56. S. Pilgram, K. E. Nagaev, and M. Buttiker, Physical Review B (Condensed Matter and Materials Physics) **70**, 045304 (2004).
57. A. N. Jordan and E. V. Sukhorukov, Physical Review B (Condensed Matter and Materials Physics) **72**, 035335 (2005).
58. P. Hänggi, P. Talkner, and M. Borkovec, Rev. Mod. Phys. **62**, 251 (1990).
59. J. P. Pekola *et al.*, Physical Review Letters **95**, 197004 (2005).
60. J. Ankerhold, Detecting charge noise with a josephson junction: A problem of thermal escape in presence of non-gaussian fluctuations (preprint cond-mat/0607020), 2006.
61. E. Akkermans and G. Montambaux, *Mesoscopic Physics of Electrons and Photons (to be published)* (Cambridge University Press, 2007).
62. B. L. Altshuler, A. G. Aronov, and A. Y. Zyuzin, JETP **59**, 415 (1984).
63. G. Bergmann, Sol. Stat. Com. **42**, 815 (1982).
64. S. Chakravarty and A. Schmid, Phys. Rep. **140**, 193 (1986).
65. B. Huard, A. Anthore, N. O. Birge, H. Pothier, and D. Esteve, Physical Review Letters **95**, 036802 (2005).
66. A. A. Abrikosov and L. P. Gor'kov, JETP **15**, 752 (1962).
67. R. Meservey and P. M. Tedrow, Physical Review Letters **41**, 805 (1978).
68. P. Lee, A. D. Stone, and H. Fukuyama, Physical Review B (Condensed Matter and Materials Physics) **35**, 1039 (1987).
69. G. Zala, B. Narozhny, and I. Aleiner, Physical Review B (Condensed Matter and Materials Physics) **64**, 214204 (2001).
70. G. E. Grechnev, N. V. Savchenko, I. V. Svechkarev, M. J. G. Lee, and J. M. Perz, Phys. Rev. B **39**, 9865 (1989).
71. V. Y. Butko, P. W. Adams, and I. L. Aleiner, Physical Review Letters **82**, 4284 (1999).
72. I. Aleiner, private communication.
73. B. Narozhny, G. Zala, and I. Aleiner, Physical Review B (Condensed Matter and Materials Physics) **65**, 180202 (2002).
74. J. Ziman, *Electrons and phonons* (Oxford: Clarendon, 1960).
75. M. Y. Reizer and A. Sergeev, JETP Lett. **65**, 1291 (1987).
76. A. Sergeev and V. Mitin, Physical Review B (Condensed Matter and Materials Physics) **61**, 6041 (2000).
77. A. Sergeev and V. Mitin, Europhys. Lett. **51**, 641 (2000).
78. J. Lin and J. Bird, J. Phys.: Cond. Matt. **14**, R501 (2002).
79. T. Micklitz, A. Altland, T. A. Costi, and A. Rosch, Physical Review Letters **96**, 226601 (2006).
80. A. Hewson, *The Kondo Problem to Heavy Fermions* (Cambridge University Press, 1993).
81. C. van Haesendonck, J. Vranken, and Y. Bruynseraede, Physical Review Letters **58**, 1968 (1987).
82. M. Vavilov and L. Glazman, Physical Review B (Condensed Matter and Materials Physics) **67**, 115310 (2003).
83. M. Vavilov, L. Glazman, and A. Larkin, Physical Review B (Condensed Matter and Materials Physics) **68**, 075119 (2003).
84. G. Zaránd, L. Borda, J. von Delft, and N. Andrei, Physical Review Letters **93**, 107204 (2004).

85. M. Ruderman and C. Kittel, Phys. Rev. **96**, 99 (1954).
86. T. Kasuya, Prog. Theor. Phys. **16**, 45 (1956).
87. K. Yosida, Phys. Rev. **106**, 893 (1957).
88. F. Schopfer, C. Bäuerle, W. Rabaud, and L. Saminadayar, Phase coherence in mesoscopic kondo wires, in *Advances in Solid State Physics* Vol. 43, pp. 181–192, Springer Berlin / Heidelberg, 2003.
89. V. Fal'ko, JETP Lett. **53**, 340 (1991).
90. J. Korringa, Physica (Amsterdam) **14**, 601 (1950).
91. O. Újsághy, A. Jakovac, and A. Zawadowski, Physical Review Letters **93**, 256805 (2004).
92. G. Zaránd, private communication.
93. A. J. Heeger, *Solid State Physics* (Academic, New York, 1969), p. 283.
94. P. W. Anderson, Phys. Rev. **124**, 41 (1961).
95. O. Újsághy, A. Zawadowski, and B. L. Gyorffy, Physical Review Letters **76**, 2378 (1996).
96. D. Shaltiel and J. H. Wernick, Phys. Rev. **136**, A245 (1964).
97. C. M. Hurd, J. Phys. Chem. Solids **30**, 539 (1969).
98. G. M. Alzoubi and N. O. Birge, Phase coherence of conduction electrons below the kondo temperature (preprint cond-mat/0607168), 2006.
99. F. Mallet *et al.*, Scaling of the low temperature dephasing rate in kondo systems (preprint cond-mat/0607154), 2006.
100. I. Aleiner and Y. Blanter, Physical Review B (Condensed Matter and Materials Physics) **65**, 115317 (2001).
101. A. Schmid, Z. Phys. **271**, 251 (1974).
102. J. Rammer, *Quantum Transport Theory* (Perseus Books, Reading, MA, 1998).
103. K. E. Nagaev, Physical Review B (Condensed Matter and Materials Physics) **52**, 4740 (1995).
104. W. Press, S. Teukolsky, W. Vetterling, and B. Flannery, *Numerical Recipes in C++ (found on* `http://www.library.cornell.edu/nr/cbookcpdf.html`*)* (Cambridge University Press).
105. G.-L. Ingold and Y. Nazarov, *Single Charge Tunneling* (Plenum, New York, 1992), .
106. H. Pothier, *Blocage de Coulomb et transfert d'électrons un par un (in english)*, PhD thesis, Université Paris 6, 1991.
107. M. H. Devoret *et al.*, Physical Review Letters **64**, 1824 (1990).
108. A. Finkelstein, Sov. Phys. JETP **57**, 97 (1983).
109. G. Montambaux and E. Akkermans, Physical Review Letters **95**, 016403 (2005).
110. B. Altshuler, JETP **48**, 670 (1978).
111. F. C. Wellstood, C. Urbina, and J. Clarke, Physical Review B (Condensed Matter and Materials Physics) **49**, 5942 (1994).
112. B. Huard *et al.*, Solid. State Comm. **131**, 599 (2004).
113. S. Hikami, A. Larkin, and Y. Nagaoka, Prog. Theor. Phys. **63**, 707 (1980).
114. P. Echternach, M. Gershenson, H. Bozler, A. Bogdanov, and B. Nilsson, Physical Review B (Condensed Matter and Materials Physics) **48**, 11516 (1993).
115. G. Bergmann, Phys. Rep. **107**, 1 (1984).
116. S. Chakravarty and A. Schmid, Phys. Rep. **140**, 19 (1986).
117. I. Aleiner, B. Altshuler, and M. Gershenson, Waves Random Media **9**, 201 (1999).

118. V. I. Kozub and A. Rudin, Physical Review B (Condensed Matter and Materials Physics) **52**, 7853 (1995).
119. M. Henny *et al.*, Appl. Phys. Lett. **71**, 773 (1997).
120. B. Altshuler and B. Simon, *Mesoscopic Quantum Physics* (Elsevier Science B.V., 1994), .
121. Y. Blanter, private communication.
122. O. Újsághy and A. Zawadowski, private communication.
123. B. Diu, C. Guthmann, D. Lederer, and B. Roulet, *Éléments de Physique Statistique* (Hermann, 1989).
124. M. Garst, P. Wolfle, L. Borda, J. von Delft, and L. Glazman, Physical Review B (Condensed Matter and Materials Physics) **72**, 205125 (2005).
125. G. Göppert and H. Grabert, Physical Review B (Condensed Matter and Materials Physics) **68**, 193301 (2003).
126. G. Göppert and H. Grabert, Physical Review B (Condensed Matter and Materials Physics) **64**, 033301 (2001).
127. J. Kroha and A. Zawadowski, Physical Review Letters **88**, 176803 (2002).
128. O. Ùjsàghy and A. Zawadowski, Physical Review B (Condensed Matter and Materials Physics) **57**, 11598 (1998).
129. J. F. Ziegler, computer code srim-2003.26 (`www.srim.org`).
130. P. Santhanam, Physical Review B (Condensed Matter and Materials Physics) **35**, 8737 (1987).
131. M. Maple, *Magnetism, vol.5* (Academic, New York, 1973).
132. P. Joyez and D. Esteve, Physical Review B (Condensed Matter and Materials Physics) **56**, 1848 (1997).
133. P. Joyez and D. Esteve, Physical Review B (Condensed Matter and Materials Physics) **58**, 15912 (1998).
134. G. Brodale, R. Fisher, N. Phillips, and K. Matho, J. Magn. Magn. Matter. **54**, 194 (1986).
135. C. Beenakker, Rev. Mod. Phys. **69**, 731 (1997).
136. M. de Jong and C. Beenakker, Sub-poissonian shot noise in a diffusive conductor, in *XXIXth Rencontres de Moriond on Coulomb and Interferences Effects in Small Electronic Structures (edited by D.C. Glattli and M. Sanquer, Frontières, France)*, 1994.
137. O. N. Dorokhov, Solid State Communications **51**, 381 (1984).
138. E. Scheer *et al.*, Nature (London) **394**, 154 (1998).
139. B. van Wees *et al.*, Physical Review Letters **60**, 848 (1988).
140. D. Wharam *et al.*, J. Phys. C **21**, L209 (1988).
141. P. de Gennes, *Superconductivity of Metals and Alloys* (Addison-Wesley, New York, 1989).
142. A. Andreev, Sov. Phys. JETP **19**, 1228 (1964).
143. A. Andreev, Sov. Phys. JETP **22**, 455 (1966).
144. V. Ambegaokar and A. Baratoff, Physical Review Letters **10**, 486 (1963).
145. G. Blonder, M. Tinkham, and T. Klapwijk, Physical Review B (Condensed Matter and Materials Physics) **25**, 4515 (1982).
146. G. B. Arnold, Journal of Low Temperature Physics **68**, 1 (1987).
147. E. Scheer *et al.*, Nature **394**, 154 (1998).
148. A. Bauer *et al.*, Physical Review Letters **92**, 217001 (2004).
149. M. C. Koops, G. V. van Duyneveldt, and R. de Bruyn Ouboter, Physical Review Letters **77**, 2542 (1996).

150. A. Barone and G. Paterno, *Physics and Applications of the Josephson effect* (Wiley, New York, 1982).
151. D. Vion, Josephson quantum bits based on a cooper pair box, in *Quantum entanglement and information processing, session LXXIX (Proceedings of the Les Houches Summer School)*, 2003.
152. V. I. Mel'nikov, Physics Reports **209**, 1 (1991).
153. H. Grabert, Phys. Rev. Lett. **61**, 1683 (1988).
154. S. Linkwitz, H. Grabert, E. Turlot, D. Esteve, and M. H. Devoret, Physical Review A (Atomic, Molecular, and Optical Physics) **45**, R3369 (1992).
155. M. H. Devoret *et al.*, *Quantum Tunneling in Condensed Media"* (Elsevier Science Publishers, 1992), chap. Macroscopic quantum effects in the current-biased Josephson junction, p. 313.
156. D. Vion, M. Götz, P. Joyez, D. Esteve, and M. H. Devoret, Physical Review Letters **77**, 3435 (1996).
157. V. Lefevre-Seguin, E. Turlot, C. Urbina, D. Esteve, and M. H. Devoret, Physical Review B (Condensed Matter and Materials Physics) **46**, 5507 (1992).
158. E. V. Bezuglyi, A. S. Vasenko, E. N. Bratus, V. S. Shumeiko, and G. Wendin, Physical Review B (Condensed Matter and Materials Physics) **73**, 220506 (2006).
159. T. Holst, D. Esteve, C. Urbina, and M. H. Devoret, Physical Review Letters **73**, 3455 (1994).
160. A. Zazunov, V. S. Shumeiko, G. Wendin, and E. N. Bratus', Physical Review B (Condensed Matter and Materials Physics) **71**, 214505 (2005).
161. J. Lantz, V. S. Shumeiko, E. Bratus, and G. Wendin, Physica C: Superconductivity **368**, 315 (2002).
162. L. Levitov and G. Lesovik, JETP Lett. **55**, 555 (1992).
163. M. Kindermann, *Electron Counting Statistics in Nanostructures*, PhD thesis, Universiteit Leiden, 2003.
164. P.-E. Roche, B. Derrida, and B. Douçot, The European Physical Journal B - Condensed Matter and Complex Systems **43**, 529 (2005).
165. N. van Kampen, Physica **74**, 215 (1973).
166. J. Marcinkiewicz, Math. Z. **44**, 612 (1939).
167. A. K. Rajagopal and E. C. G. Sudarshan, Phys. Rev. A **10**, 1852 (1974).
168. Y. Nazarov, Ann. Phys. (Leipzig) **8**, SI (1999).
169. A. Kamenev, *Proceedings of the Les Houches Summer School, Session LXI, edited by* (Elsevier, Amsterdam,, 2005), chap. 3, p. 177.
170. K. E. Nagaev, Physical Review B (Condensed Matter and Materials Physics) **66**, 075334 (2002).
171. S. Pilgram, A. N. Jordan, E. V. Sukhorukov, and M. Buttiker, Physical Review Letters **90**, 206801 (2003).
172. W. Belzig, Full counting statistics in quantum contacts, in *Proceedings of Summer School/Conference on Functional Nanostructures, Karlsruhe*, 2003.
173. W. Belzig, *Quantum noise in mesoscopic physics* (NATO Science Series, Kluwer Academic Publishers, Dordrecht Boston London, 2003), p. 494.
174. B. A. Muzykantskii and D. E. Khmelnitskii, Physical Review B (Condensed Matter and Materials Physics) **50**, 3982 (1994).
175. J. Cuevas and W. Belzig, Physical Review B (Condensed Matter and Materials Physics) **70**, 214512 (2004).
176. M. Kindermann and Y. V. Nazarov, Physical Review Letters **91**, 136802 (2003).

177. A. V. Andreev and E. G. Mishchenko, Physical Review B (Condensed Matter and Materials Physics) **64**, 233316 (2001).
178. D. A. Bagrets and Y. V. Nazarov, Physical Review Letters **94**, 056801 (2005).
179. M. Kindermann and B. Trauzettel, Physical Review Letters **94**, 166803 (2005).
180. F. Pistolesi, Physical Review B (Condensed Matter and Materials Physics) **69**, 245409 (2004).
181. A. Romito and Y. V. Nazarov, Physical Review B (Condensed Matter and Materials Physics) **70**, 212509 (2004).
182. J. Tobiska and Y. V. Nazarov, Physical Review B (Condensed Matter and Materials Physics) **72**, 235328 (2005).
183. A. Braggio, J. Konig, and R. Fazio, Physical Review Letters **96**, 026805 (2006).
184. S. Pilgram, Physical Review B (Condensed Matter and Materials Physics) **69**, 115315 (2004).
185. D. Bagrets, Y. Utsumi, D. Golubev, and G. Schön, Full counting statistics of interacting electrons (preprint cond-mat/0605263), 2006.
186. D. B. Gutman and Y. Gefen, Physical Review B (Condensed Matter and Materials Physics) **68**, 035302 (2003).
187. M. H. Devoret, D. Esteve, J. M. Martinis, A. Cleland, and J. Clarke, Physical Review B (Condensed Matter and Materials Physics) **36**, 58 (1987).
188. S. Guéron, *Quasiparticles in a diffusive conductor: Interactions and pairing*, PhD thesis, Université de Paris 6, 1997.
189. P. Lafarge, *Macroscopic Charge Quantization in Metallic Nanostructures*, PhD thesis, Université de Paris 6, 1993.
190. F. Giazotto, T. T. Heikkila, A. Luukanen, A. M. Savin, and J. P. Pekola, Reviews of Modern Physics **78**, 217 (2006).
191. J. M. Martinis and R. L. Kautz, Physical Review Letters **63**, 1507 (1989).
192. J. Chaumont, F. Lalu, M. Salome, A.-M. Lamoise, and H. Bernas, Nucl. Instr. and Meth. **189**, 193 (1981).
193. K. Bladh *et al.*, Review of Scientific Instruments **74**, 1323 (2003).
194. J. M. Martinis, M. H. Devoret, and J. Clarke, Physical Review B (Condensed Matter and Materials Physics) **35**, 4682 (1987).
195. D. Vion, P. F. Orfila, P. Joyez, D. Esteve, and M. H. Devoret, Journal of Applied Physics **77**, 2519 (1995).
196. P. Mohr and B. Taylor, Rev. Mod. Phys. **77**, 1 (2005).
197. H. Ibach and I. Luth, *Solid-State Physics, an Introduction to Principles of Material Science (The volumic density of states at the Fermi level ν_F is inferred from the experimental value of the calorific capacity $C = \gamma T$ related to ν_F through the equation $\gamma = \pi^2 k_B^2 \nu_F/3$)* (Springer, Berlin, 1966).
198. N. Simon, E. Drexler, and R. Reed, NIST Monograph **177** (1992).
199. T.-S. Choy, J. Naset, J. Chen, S. Hershfield, and C. Stanton, Bulletin of The American Physical Society **45(1):L36**, 42 (2000).
200. I. O. Kulik and A. N. Omel'yanchuk, JETP Lett. **21**, 96 (1975).
201. C. Beenakker, Physical Review Letters **67**, 003836 (1991).
202. B. Altshuler, JETP **41**, 648 (1985).
203. P. Lee and A. Stone, Physical Review Letters **55**, 1622 (1985).
204. A. Levchenko, A. Kamenev, and L. Glazman, Singular length dependence of critical current in sns bridges (preprint cond-mat/0601177), 2006.

Index

Abstract : This thesis discusses three experiments on the properties of electronic transport at the mesoscopic scale. The first one allowed to measure the energy exchange rate between electrons in a metal contaminated by a very weak concentration of magnetic impurities. The role played by magnetic impurities in the Kondo regime on those energy exchanges is quantitatively investigated, and the global measured exchange rate is larger than expected. The second experiment is a measurement of the current-phase relation in a system made of two superconductors linked through a single atom. We thus provide quantitative support for the recent description of the mesoscopic Josephson effect. The last experiment is a measurement of the asymmetry of the current fluctuations in a mesoscopic conductor, using a Josephson junction as a threshold detector.

Résumé : Cette thèse décrit trois expériences portant sur les propriétés du transport électronique à l'échelle mésoscopique. La première a permis de mesurer le taux d'échange d'énergie entre électrons dans un métal contenant une très faible concentration d'impuretés magnétiques. Nous avons validé la description quantitative du rôle des impuretés magnétiques dans le régime Kondo sur ces échanges énergétiques et aussi montré que le taux global d'échange est plus fort que prévu. La seconde expérience est une mesure de la relation courant-phase dans un système constitué de deux supraconducteurs couplés par un seul atome. Elle nous a permis de conforter quantitativement la récente description de l'effet Josephson mésoscopique. La dernière expérience est une mesure de l'asymétrie des fluctuations du courant dans un conducteur mésoscopique en utilisant une Jonction Josephson comme détecteur de seuil.